Tracking Chemical Reactions with Ultrafast X-ray Spectroscopic Techniques

Dissertation

zur Erlangung des Doktorgrades
des Fachbereichs Physik
der Universität Hamburg

vorgelegt von

Tadesse Abebaw Assefa, M. Sc.
aus Estie, Ethiopia

Hamburg
2016

Gutachter der Dissertation	Prof. Dr. Christian Bressler Prof. Dr. Markus Drescher
Gutachter der Disputation	Prof. Dr. Christian Bressler Prof. Dr. Markus Drescher Prof. Dr. Henning Moritz Prof. Dr. Michael Rübhausen Prof. Dr. Michael Thorwart
Datum der Disputation	December 16, 2016
Vorsitzende des Prüfungsausschusses	Prof. Dr. Michael Rübhausen
Vorsitzender des Promotionsausschusses	Prof. Dr. Wolfgang Hansen
Dekan der Fakultät für Mathematik, Informatik und Naturwissenschaften	Prof. Dr. Heinrich Graener

DECLARATION

I, Tadesse Abebaw Assefa, declare that this thesis titled, *Tracking Chemical Reactions with Ultrafast X-ray Spectroscopic techniques* and the work presented in it are my own. This thesis is a presentation of my original research work. Wherever contributions of others are involved, every effort is made to indicate this clearly, with due reference to the literature, and acknowledgement of collaborative research and discussions. The work was done under the guidance of Prof. Dr. Christian Bressler, European XFEL facility and University of Hamburg, Germany.

Signed:

Date:

Abstract

Chemical reactions in transition metal complexes can be triggered with light, which results in structural and electronic changes. These changes can be visualised by measuring the geometric and electronic structure of a complex in real-time during a chemical reaction pathway. Time-resolved (TR) X-ray Absorption and Emission Spectroscopy (XAS and XES) delivers information about the geometric (via XANES and EXAFS) and electronic (via XES) transient changes when used in synchronisation with an ultrafast laser in a pump-probe scheme. Element specificity and sensitivity to the local structure of X-ray spectroscopic tools around the absorbing atom allows us to look at the photoexcited changes of transition metal complexes.

We studied aqueous ferrocyanide ($[\mathrm{Fe^{II}(CN)_6}]^{4-}$) following photoexcitation with UV laser light which results in two photoproducts namely $[\mathrm{Fe^{II}(CN)_5H_2O}]^{3-}$ and $[\mathrm{Fe^{III}(CN)_6}]^{3-}$ [1]. Picosecond-resolved XANES measurements after 266 nm excitation show both photoproducts and the ratio of extracted excited state fractions is consistent with quantum yield measurements reported by Shirom *et al.*[1, 2]. TR XES was used to look at the spin state and ligand environment changes with the core-to-core (K$\beta_{1,3}$) and valance-to-core (vtc) (or K$\beta_{2,5}$) emission lines of the central Fe atom. Furthermore, we investigated the ultrafast ligand dissociation of aqueous ferrocyanide ions upon irradiation of 355 nm laser light. Based on a comparison of the simulated pre-edge peaks of 1s→3d transition and the experimental data, we concluded that the reaction pathway commences via ligand detachment followed by the formation of the long-lived photoaquated complex. TR XES reveals the spin state of the intermediate complex. Combining these finding we interpret that the aquation process happens from a non-singlet potential energy surface and takes about 13 ps.

Also, we characterised the molecular structure of photoexcited $[\mathrm{Fe^{II}(terpy)_2}]^{2+}$ molecule via TR EXAFS. The data analysis in energy space used two structural model expansions which are the representations of DFT predicted ^{5}E and ^{5}B$_2$ quintet high spin states. After statistical evaluation of the two models, ^{5}E high spin state model is in better agreement with experimental data. The transient EXAFS fitting implemented here can be used to characterise molecular structures of other spin crossover complexes.

Kurzfassung

Chemische Reaktionen von Übergangsmetallkomplexen können durch Licht induziert werden, dies wird von Veränderungen in der geometrischen und der elektronischen Struktur begleitet. Das Messen dieser Strukturen gewährt die Möglichkeit den Reaktionsweg in Echtzeit zu charakterisieren. Röntgenabsorptions- sowie Röntgenemissionsspektroskopie (XAS und XES) sind übliche Messmethoden um Informationen über diese Strukturen zu erhalten. XAS nahe der Absorptionskante (XANES) sowie die Feinstruktur über der Kante (EXAFS) gibt dabei Aufschluss über die geometrische Struktur sowie die elektronische Struktur der unbesetzten Zustände. Die elektronische Struktur der besetzten Zustände kann mit XES untersucht werden. In Kombination mit einem ausreichend schnell gepulsten Laser können die Veränderungen zeitaufgelöst (TR) betrachtet werden. Die elementspezifische Eigenschaft der Röntgenstrahlung sowie ihre Sensitivität auf die lokale Struktur werden bei der Röntgenabsorptionsspektroskopie ausgenutzt um die Photoinduzierten Veränderungen von Übergangsmetallkomplexen sichtbar zu machen.

Als Teil dieser Arbeit wurde Ferrocyanid ($[Fe(CN)_6]^{4-}$) in wässriger Lösung gemessen. Durch Anregung mit Laserlicht bei 266 nm entstehen zwei Photoprodukte, $[Fe(CN)_5H_2O]^{3-}$ und $[Fe^{III}(CN)_6]^{3-}$ [1]. Beide Photoprodukte konnten mittels zeitaufgelöster XANES im Picosekunden-Regime nachgewiesen werden. Ihr quantitatives Verhältnis deckt sich mit den Quanteneffizienz-Messungen von Shirom *et al.*[1, 2]. Veränderungen des Spins und der Ligandenumgebung wurden mit TR-XES gemessen. Dafür wurde die Fluoreszenz des $K\beta_{1,3}$ sowie des $K\beta_{2,5}$ Übergangs des zentralen Eisenzentrums genutzt. Im Weiteren wurde die Abspaltung eines (CN^-) Liganden durch Anregung mit 355 nm Laserlicht gemessen. Der Vergleich unserer Messdaten mit Simulationen des 1s→3d Übergangs in der XANES Vorkante legt nahe, dass die Reaktion mit der Abtrennung eines Liganden beginnt und sich anschließend unter Einbindung eines Wassermoleküls ein langlebiger Komplex bildet. Über TR-XES konnte zusätzlich der Spin-Zustand des Übergangzustands gemessen werden. Diese Ergebnisse zeigen, dass der Prozess der Wassereinbindung von einem nicht-Singulett Spinzustand ausgeht und in etwa 13 ps dauert.

Außerdem wurde die optisch induzierte Strukturänderung von $[Fe^{II}(terpy)_2]^{2+}$ Molekülen, mittels TR-EXAFS charakterisiert. Für die Analyse der Daten wurde die Ausgleichsrechnung für transiente EXAFS Daten durch zwei von DFT vorhergesagte Quintett Highspin-Zustände, ^5E und $^5B_2$, erweitert. Die Simulation des ^5E-Spinzustands liegt dabei in deutlich besserer Übereinstimmung mit den Messdaten. Die implementierte Methode zur Untersuchung transienter EXAFS Daten kann zukünftig als Werkzeug zur Charakterisierung der molekularen Struktur anderer Spincrossover-Komplexe bei zeitaufgelösten Messungen genutzt werden.

List of papers

In addition to the results presented in this thesis, here I include list of publications during my graduate school at "SFB 925" the University of Hamburg. The topics presented in these papers are only marginally part of this dissertation. Manuscripts in preparation are not included in the list.

1. A. M. March, **T. A. Assefa**, Ch. Boemer, Ch. Bressler, A. Britz, M. Diez, G. Doumy, A. Galler, M. Harder, D. Khakhulin, Z. Németh, M. Pápai, S. Schulz, S. H. Southworth, H. Yavas, L. Young, W. Gawelda and G. Vanko, "Probing Transient Valence Orbital Changes with Picosecond Valence-to-Core X-ray Emission Spectroscopy", J. Phys. Chem. C, (Accepted), January 17,10.1021/acs.jpcc.6b12940, (2017).

2. A. Britz, **T. A. Assefa**, A. Galler, W. Gawelda, M. Diez, P. Zalden, D. Khakhulin, B. Fernandes, P. Gessler, H. S. Namin, A. Beckmann, M. Harder, H. Yavas and Ch. Bressler, "A Multi-MHz Single Shot Data Acquisition Scheme with High Dynamic Range: Pump-Probe X-Ray Experiments at Synchrotrons" J Synch, Rad., 23(6),(2016).

3. E Biasin, Tim Brandt van Driel, K S. Kjær, A O. Dohn, M Christensen, T Harlang, P Chabera, Y Liu, J Uhlig, M Papai, Z Nemeth, R Hartsock, W Liang, R Alonso-Mori, M Chollet, J M. Glownia, Silke Nelson, D Sokaras, **T A. Assefa**, A Britz, A Galler, W Gawelda, C Bressler, K J. Gaffney, H T. Lemke, K B. M, M M. Nielsen,V Sundstrom, G Vanko, K Warnmark, S E. Canton, and K Haldrup "Femtosecond X-ray scattering study of ultrafast photoinduced structural dynamics in solvated $[Co(terpy)_2]^{2+}$" Phys. Rev. Lett. 117, 13002 (2016).

4. A. M. March, **T. A. Assefa**, G. Doumy, M. Pápai, E. Rozsályi, Z. Németh, E. P. Kanter, S. H. Southworth, C. Bressler, W. Gawelda, L. Young, and G. Vankó "Valence-to-core X-ray emission spectroscopy for tracking chemical dynamics in solutions" J. Phys. Chem. C, 119, 14571 (2015).

5. G. Vankó, A. Bordage, M. Pápai, K. Haldrup, P. Glatzel, A. M. March, G. Doumy, A. Galler, A. Britz, **T. A. Assefa**, D. Cabaret, A. Juhin, T. B. van Driel, K. S. Kjaer, A. O. Dohn, K. B. Moller, E. Gallo, M. Rovezzi, Z. Németh, E. Rozsályi, T. Rozgonyi, J. Uhlig, V. Sundström, M. M. Nielsen, L. Young, S. H. Southworth, C. Bressler and W. Gawelda "Detailed characterization of a nanosecond-lived excited state: X-ray and theoretical investigation of the quintet state in photoexcited $[Fe(terpy)_2]^{2+}$" J. Phys. Chem. C, 119, 5888 (2015).

6. G. Coslovich, C. Giannetti, F. Cilento, S. Dal Conte, **T. Abebaw**, D. Bossini, G. Ferrini, H. Eisaki, M. Greven, A. Damascelli, and F. Parmigiani, “Competition Between the Pseudo-gap and Superconducting States of $Bi_2Sr_2Ca_{0.92}Y_{0.08}Cu_2O_{8+\delta}$ Single Crystals Revealed by Ultrafast Broadband Optical Reflectivity”, Phys. Rev. Lett., 110, 107003 (2013).

Contents

Chapter 1

Introduction

To track chemical reactions at the level of individual atoms, experimental methods with spatial and temporal resolution are necessary. Scientists have used different experimental techniques to follow reactions at the microscopic (atomic) level. With the advent of femtosecond laser sources, experts implement pump-probe techniques to follow chemical reactions in real-time by monitoring optical transient changes. Ahmed H. Zewail (1946-2016) won a Nobel Prize in Chemistry in 1999 for his pioneering works on chemical reaction dynamics with femtosecond time resolution, which opened a new field called Femtochemistry [3]. Since then scientists have implemented a pump-probe technique to follow chemical reactions in real-time. During this process, the first optical pump pulse triggers the reaction and the second probe pulse follows the evolution of the chemical reaction in time. However, optical spectroscopy is sensitive to transitions in the valence states and the relation to the structure of an observable phenomenon is not straightforward.

Synchrotron-based X-ray probe tools (such as X-ray crystallography, X-ray diffuse scattering, X-ray absorption, and emission spectroscopy) have been applied to understand chemical reactions in combination with optical lasers in a time-resolved fashion. Anfinrud, Schotte *et al.* used the structural resolving capability of X-ray crystallography to look at the trans-to-cis photoisomerization of a chromophore during a signaling protein function process [4, 5]. X-ray crystallography techniques showed tremendous success in resolving protein structure in a crystal form. Also, Ihee, Wulff *et al.* used time-resolved X-ray diffuse scattering to study the biological activity of proteins in a solution such as myoglobin [6, 7]. However, XDS mainly gives the precise global structure of the protein but is not straight forward to decouple the solvent and solute response from the measured total scattering signal. In this case, X-ray absorption and emission spectroscopic techniques become valuable since they provide information on electronic and structural changes around the absorbing atom (solute). The implementation of time-resolved X-ray absorption spectroscopy Chen *et al.* [8], Bressler and Chergui [9, 10] allowed the researchers to follow structural evolution of an observable during a chemical reaction. Similarly, time-resolved X-ray emission spectroscopy techniques have been used by Vanko and Bressler *et al.* to look at spin state changes in a photoinduced chemical dynamics [11]. The emergence of ultrashort X-ray pulses from X-ray Free-Electron Laser (XFEL) sources further enabled researchers to observe chemical reactions in real-time with an atomic spatial resolution, down to a few femtoseconds of time resolution [12, 13].

In this thesis, a suite of time-resolved X-ray spectroscopic techniques have been used to follow photoinduced chemical reactions in an aqueous solution (natural environment). Two model systems, namely $[Fe^{II}(terpy)_2]^{2+}$ and $[Fe^{II}(bpy)_3]^{2+}$, both underwent an increase in the bond length upon excitation with a green laser light. Here the high-quality TR EXAFS data of $[Fe^{II}(terpy)_2]^{2+}$ allowed us to identify the possible excited state among two candidates. The analysis used two reaction coordinate expansion methods instead of the one used in the $[Fe^{II}(bpy)_3]^{2+}$ case [14, 9]. The other model system studied was the $[Fe^{II}(CN)_6]^{4-}$ (ferrocyanide) molecule which underwent both a ligand exchange and charge transfer upon excitation with a UV laser light [15, 1, 2]. Charge transfer, bond breaking and making processes are common in many biologically relevant systems. For this reason, model systems have been studied to sharpen the experimental tools used here which will enable us to probe more complex molecules.

Although the ferrocyanide molecule is a model system, upon photoexcitation it undergoes a charge transfer and ligand exchange mechanism. The ligand exchange mechanism studied here has similarities to the $Fe^{III}(CO)_5$ studied by Wernet *et al.* [16] which undergoes ultrafast ligand dissociation. The charge transfer mechanisms are also common in photocatalytic electron acceptor complexes. The open question in the ligand exchange mechanism of ferrocyanide molecules is whether it proceeds via one of the following mechanisms; dissociative with pentacoordinated intermediate, associative with heptacoordinated intermediate or dissociative interchange where the bond breaking and making process happens at the same time.

Studies of the ligand exchange mechanism process in the $[Fe^{II}(CN)_5(NH_3)]^{3-}$ [17, 18] and $[Fe^{II}(CN)_5(SO_3)]^{5-}$ [19] complexes suggest the exchange mechanism proceeds via the dissociative pathway which results in a reactive $[Fe^{II}(CN)_5]^{3-}$ intermediate state. The breaking of the metal-to-ligand bond is the reaction rate-determining step in the ligand exchange process [20]. A similar study by Finston *et al.* suggested a dissociative interchange mechanism for the photoaquation of the ferrocyanide molecule, whereby the Fe-CN bond breaking and Fe-OH2 bond formation occurs simultaneously[21]. In the present study, the our findings concerning the ligand detachment and attachment process in the ferrocyanide molecule will be presented.

The charge transfer dynamics in ferrocyanide complexes have been studied by Pommeret *et al.* with optical pump-probe techniques [22, 23] and it was determined that the charge separation from the ferrocyanide molecule was almost instantaneous. By monitoring the optical absorption band centred at 719 nm (assigned to the hydrated electron)[24], a fully solvated electron e^- appears with a time constant of 510 fs. Similarly, the radical $[Fe^{III}(CN)_6]^{3-}$ which has an absorption band centred at 422 nm appears almost instantaneously. Recently, studies by Reinhard observed that the transient features of $[Fe^{III}(CN)_6]^{3-}$ are around 150 fs whereas the solvated electron is approximately 500 fs [25]. Flash photolysis studies by Shirom and

Stein[1, 2] showed that upon photoexcitation ($\lambda < 313$ nm) both charge transfer and photoaquation channels demonstrated no straightforward way to disentangle these two competing relaxation channels. In addition to the reported optical studies, X-ray spectroscopy tools have been used to study the ferrocyanide molecule. X-ray studies by Rose-Petruck *et al.*[26] claimed that the radical $[\mathrm{Fe^{III}(CN)_6}]^{3-}$ is observed by looking at the iron K-edge shift. Similarly, Reinhard *et al.* [27] recently reported picosecond-resolved X-ray absorption spectroscopy (XAS) results, which showed the formation of ferricyanide complex within 70 ps. In the XAS spectrum below the iron, K-edge is the pre-edge, which shows sensitivity to symmetry changes around the absorbing atom [28, 29]. Westre *et al.* [30] also demonstrated the sensitivity of X-ray absorption pre-edges to the change in symmetry around the iron. In like manner, the present study has exploited this knowledge in order to examine the details of the photoaquation process.

The scope of this thesis is to track chemical reactions using ultrafast X-ray spectroscopic tools. To present a coherent story, the thesis is organised in the following way: in Chapter Two the photochemistry of transition metal complexes are examined by emphasising the charge transfer and ligand exchange processes. The general electronic properties and crystal structure of the relaxation processes of aqueous ferrocyanide, $[\mathrm{Fe^{II}(terpy)_2}]^{2+}$ and $[\mathrm{Fe^{II}(bpy)_3}]^{2+}$ are discussed in detail as well. Chapter Three describes the principles of X-ray spectroscopic techniques along with the information contents that can be extracted from each tool. Theoretical tools used in this thesis are also described. In Chapter Four the experimental methods used for the data collection at 7ID-D Advanced Photon source-USA and SACLA-Japan are presented. Chapter Five examines the results of the picosecond-resolved X-ray absorption spectroscopy (XAS) used to disentangle the two simultaneous relaxation channels (such as photooxidation and ligand exchange processes) following 266 nm laser excitation. In Chapter Six TR X-ray emission spectroscopy (XES) results (Kβ and valence-to-core) used to monitor electronic changes that occur after 266 nm and 355 nm laser excitation of aqueous ferrocyanide molecule are discussed. In Chapter Seven the femtosecond resolved XAS and XES results of the ligand detachment and attachment process are presented, and the pentacoordinated intermediate state which lives for 12 ps before the nearby solvent is ligated is characterized. Chapter Eight employs a novel approach to analyse the TR extended X-ray absorption fine structure (EXAFS) of high-quality data. The method is used to identify the possible high spin excited state among the two likely candidates of the $[\mathrm{Fe^{II}(terpy)_2}]^{2+}$ molecule. This analysis is extended further to examine the $[\mathrm{Fe^{II}(bpy)_3}]^{2+}$ EXAFS data, which has been published. The end result from the analysis shows the excited state fraction estimation with this method, and thus demonstrates good agreement with the XES techniques. Chapter Nine concludes the thesis with a final summary and presents an outlook for future research.

Chapter 2

Photochemistry of transition metal complexes

Transition metal (TM)[1] complexes are an important class of compounds in chemistry and studied as model molecular systems for complex interactions involving electronic, spin and structural degrees of freedom in catalysis, material synthesis, photochemistry and biology[31, 32]. In all cases, these molecules consist of a central transition metal bound to another group of ions or molecules called ligands[2]. The most common transition metals are Cr, Mn, Fe, Co, Ni, and Ru, whereas the common ligands are CN^-, CO, and pyridine[3]. In TM complexes the metal ion forms a fixed number of bonds with the neighbouring atoms which are often referred to as coordination number. The chemical reactivity of complexes depends mainly on its electronic properties which will be discussed in later section (see Sec. 2.1).

Photochemistry of transition metal complexes can often be triggered by irradiation of visible light which generates a Franck-Condon excited state. Afterwards, the molecule undergoes relaxation into lower excited states involving charge transfer such as spin dynamics[13, 34], bond length change[10], bond breaking and making[16]. The time scale for the different molecular processes depends on the reaction pathways and the competing processes (see Fig.2.1).

Biological functions[35, 36] and chemically relevant processes[31, 32] often undergo charge transfer and ligand rearrangement dynamics. In order to understand these type of fundamental reaction steps two model systems namely iron(II) hexacyanide or ferrocyanide ($[Fe^{II}(CN)_6]^{4-}$) and iron(II) bis-terpyridine ($Fe^{II}(terpy)_2]^{2+}$)[4] are investigated in this thesis. Upon laser excitation, the aqueous ferrocyanide molecule undergoes charge transfer and ligand dissociation mechanisms[15, 37, 1, 2]. In aqueous $Fe^{II}(terpy)_2]^{2+}$ molecule, laser excitation results in charge transfer from iron to the terpy ligands. Later it decays into a high-spin excited state through

---

[1] Transition metal elements are elements having a partially filled d or f subshell. Transition metal elements are most commonly refers to as the d-block transition elements.

[2] Ligand is an ion or molecule that forms a bond to a central metal atom [33]

[3] Pyridine is an organic compound with the chemical formula of C_5H_5N and structurally similar to benzene with one CH_2 group replaced by a nitrogen atom

[4] terpy: 2,2′:6′,2″-terpyridine

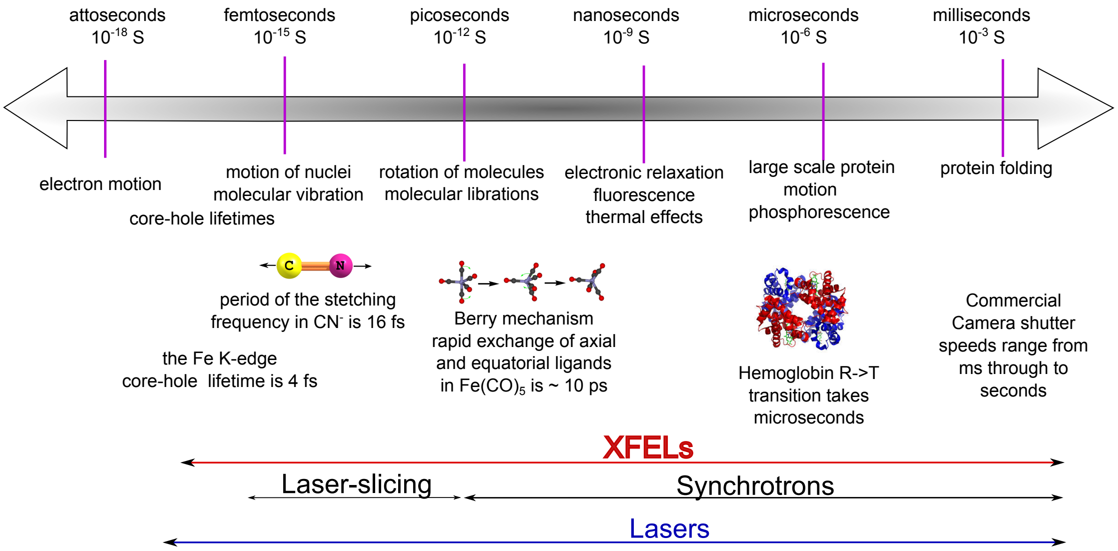

Figure 2.1.: Time scales of various electronic and structural dynamics which occur during a course of a chemical reaction. The suitable light sources that can be used to access the different time scales are shown with an arrow.

intermediate states [38, 31]. The detailed electronic and structural properties of these complexes will be discussed in the later part of this chapter (see Sec. 2.4 and 2.5).

This chapter is organised in the following way: the first Section contains the description of the general electronic properties of transition metal complexes and introduces crystal-field and ligand-field theory. In the second Section, the excited state dynamics of transition metal complexes will be discussed using the Jablonski diagram. In the third Section, the role of spin in the relaxation process of photoexcited transition metal complexes will be presented. The description of the electronic, crystal structure and photochemical processes of solvated iron hexacyanide complexes such as ferrocyanide and iron(III) hexacyanide or ferricyanide ($[\mathrm{Fe}^{\mathrm{III}}(\mathrm{CN})_6]^{3-}$) will be discussed in detail. As one focus point of this thesis the details of photochemical reaction pathways such as ligand exchange mechanism and photooxidation processes including the quantum yield measurements under different experimental conditions. As a second model system of this thesis the ground state electronic structure and the excited state processes of the $[\mathrm{Fe}^{\mathrm{II}}(\mathrm{terpy})_2]^{2+}$ molecule will be described.

2.1. Electronic structure of transition metal complexes

Historically, two different theories namely crystal-field and the ligand-field theories [39] are used to explain the electronic structure of transition metal complexes.

Crystal-field theory (a.k.a. Electrostatic theory) emerged from analysing the spectra of TM solids and, strictly speaking; crystal field theory applies to TM ions in a crystal. In this theory, the ligand and the metal centre with fully unoccupied d-orbitals are treated as negative and positive charges respectively. The electrostatic interaction results in an electric dipole with a dipole moment directed towards the ligand. In the presence of an *octahedral crystal field* the d orbitals of the metal center split into threefold degenerate e_g and twofold degenerate t_{2g} set of orbitals (see Fig.2.2).

Ligand-field theory arises from the application of molecular orbital theory[40]. It describes bonding and orbital arrangements in a transition metal complex. Here the electrons are placed in molecular orbitals formed as a linear combination between the metal (3d, 4s and 4p) and ligand (σ, π, σ^* and π^*) orbitals. Orbital hybridization between the orbitals of the metal and the ligand depends on their symmetry. Totally symmetric orbitals of the ligand interact with 4s orbital, single nodal plane orbitals interact with 4p orbitals and the rest interacts with 3d_{z^2} and $3\text{d}_{x^2-y^2}$ orbitals. Each interaction between asymmetric orbitals of the ligand and an atomic orbital of the metal gives rise to a bonding or antibonding orbital. The former are more stable than the orbitals concentrated primarily on the ligands or the metal [40].

Interaction of d orbital electrons from the metal center with ligands in an octahedral field are splitted into threefold degenerate e_g and twofold degenerate t_{2g} set of orbitals (see Fig. 2.2). The electrons in the d_{z^2} and $d_{x^2-y^2}$ orbitals of symmetry type e_g are concentrated close to the ligands whereas electrons in the d_{xy}, d_{xz} and d_{yz} orbitals of symmetry type t_{2g} are located between the ligands. The orbitals of e_g symmetry experience strong Coulomb repulsion compared to the orbitals of t_{2g} symmetry; as a result t_{2g} orbitals will have lower energy compared to the e_g orbitals. The separation between t_{2g} and e_g orbitals is called *ligand field splitting parameter* (Δ_o) and it's value depends on the type of ligands, the identity of the central metal ion and the number of electrons in the d-orbital [41].

In a complex, all d orbitals are not degenerate in the presence so octahedral crystal field. As a result, the electron filling will follow *Pauli exclusion principle*[5]. The first three electrons will occupy the lower t_{2g} orbitals, but the next two electrons could occupy either the upper e_g (with parallel spin as lower ones) or all the three could occupy the t_{2g} with opposite spin. The pairing energy (P) which is strong Coulomb repulsion between electrons in same orbital and the ligand field splitting parameter (Δ_o) are the determining factors. The weak field case ($\Delta_o <$ P) will result $t_{2g}^4 e_g^2$ electronic configuration which results in high-spin (HS) with total spin of **S**= 2. In case $\Delta_o >$ P, electronic configuration becomes t_{2g}^6 and results low-spin (LS) with **S**= 0. Most transition metal complexes are in the low-spin state. In some cases in non-perfect octahedral symmetry, the above electronic configuration does not hold. Contraction or elongation of metal-ligand bond lengths will lead to

---

[5] Pauli exclusion principle states that two electrons of the same spin can not have identical quantum energy states

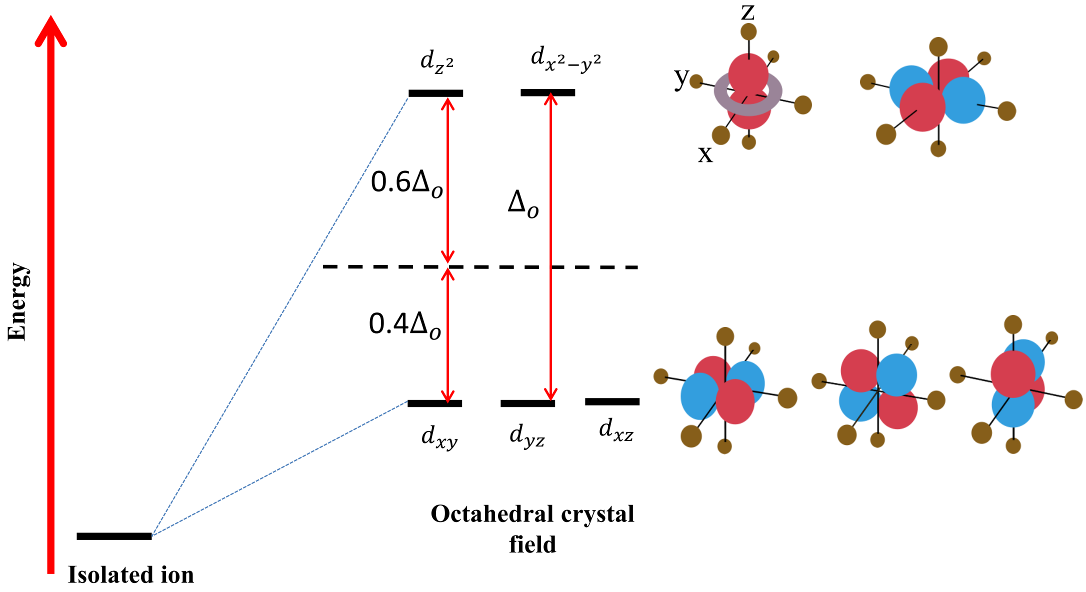

Figure 2.2.: Splitting of d-orbitals in the presence of octahedral crystal field. For clarity, the TM d orbitals shown in red and blue and ligands in dark orange spheres.

a *Jahn-Teller distortion* [6]. This results in splitting of the t_{2g} and e_g orbitals to a different orbital ordering see Fig.2.3.

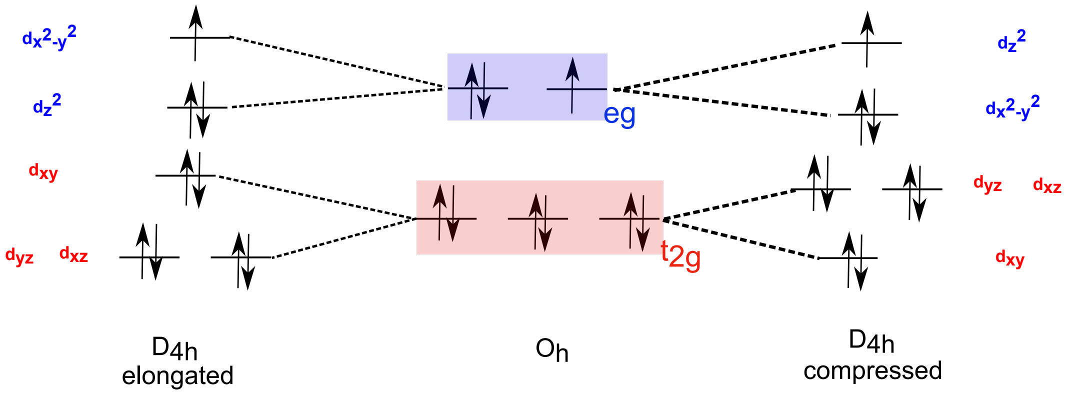

Figure 2.3.: Diagram showing the two possible Jahn-Teller splittings of the d-energy levels in an octahedral $[\mathrm{CuL}_6]^{2+}$ complex. The orbital ordering of the t_{2g} and e_g states change depending on the structural distortion happening [42].

Crystal field theory treats ligands as point charges or dipoles and does not take into account overlapping of metal and ligand orbitals. *Molecular orbital theory*

---

[6] Jahn-Teller distortion is an effect when the electronic configuration of a non-linear molecular system is orbitally degenerate, and in the presence of has an asymmetric field, the complex distorts to remove the degeneracy.

builds up molecular orbital (MO) energy levels from the metal centre and the symmetry-adapted linear combination of ligand orbitals. In Sec.2.4.1 and 2.5.1 the description of the electronic structure of ferrocyanide complex using the molecular orbital theory to understand better and visualise involving ligand orbitals in the electronic structure of the molecule will be given.

2.2. Excited state dynamics

The coupling strength of an electron which makes a transition from an initial ψ_i to a final state ψ_f is determined by the transition dipole moment which is defined by the integral:

$$\mu_{fi} = \int \psi_f^* \mu \psi_i dr, \tag{2.1}$$

where $\mu = -er$ is the electric dipole operator. The intensity of the transition is proportional to the square of its dipole moment. A transition can be allowed or forbidden depending on the integral of the transition dipole moment. If the integral is non-zero, the transition is allowed. If the integral is zero, the transition is forbidden. However, forbidden transitions still occur in a spectrum, if the assumptions on which the transition dipole moment calculated are invalid. One example is a complex having a lower symmetry than assumed. Electronic transitions with a change of spin multiplicities are also forbidden, but can be observed in a spectrum. For example transition from singlet (S=0) to triplet (S=1) is not possible. However, the coupling between the spin and orbital angular momentum can relax the spin selection rule and transition may occur. In octahedral complexes such as $[\mathrm{Fe^{II}(CN)_6}]^{4-}$ transitions between d-orbitals are forbidden. The Laporte selection rule states that in centrosymmetric complex, the only allowed transitions are those accompanied by a change in parity. The only possible transitions are between g (gerade) and u (ungerade) states. Since s and d orbitals are gerade, whereas p and f orbitals are ungerade it means that s-p, p-d and d-f transitions are allowed. Transitions such as s-s, p-p, d-d and f-f transitions are forbidden. The reason why d-d transition still occur in the centrosymmetric complex such as $[\mathrm{Fe^{II}(CN)_6}]^{4-}$ is caused by small distortions in its ground state structure, and asymmetric vibration destroys its centre of inversion.

The electronic transition which leads to an excited state should obey the Franck-Condon principle [43]. The most favoured transitions are to vibrational levels where the nuclear positions differ only by minimal value from the ground state. If the transition to the Franck-Condon region ends up in a high vibrational level of the excited state, it relaxes to the lowest vibrational state of the excited state through radiationless deactivation and/or internal conversion (IC). The vertical transitions are from the lowest vibrational ground state to some vibrational states of an electronically excited state which result in Franck–Condon region. As shown in Fig. 2.4 electronic transitions can be from the ground state to many vibrational levels of an excited electronic state which result in broadband in the ultraviolet-

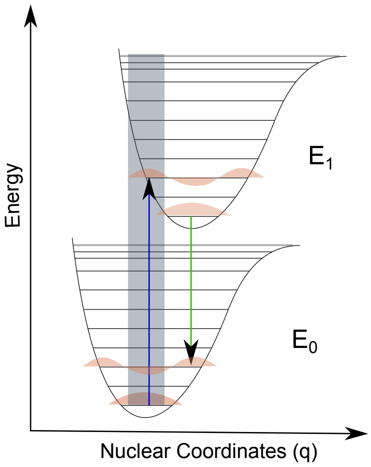

Figure 2.4.: The schematic representation which shows an electronic transition from a ground state (E_0) to an excited electronic state (E_1) in the Franck-Condon region.

visible (UV-vis) spectrum.

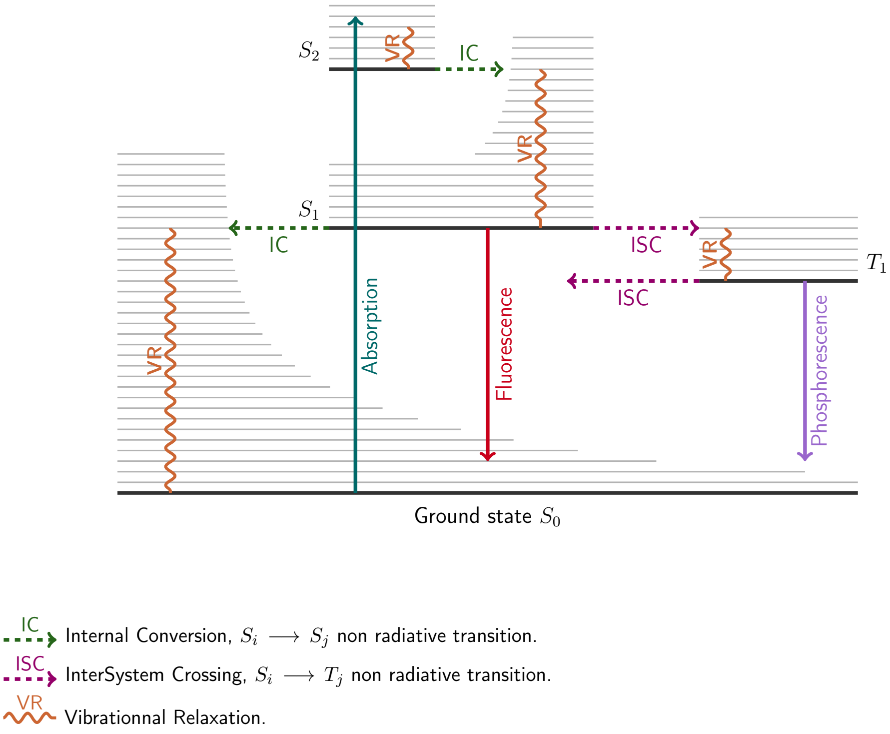

Figure 2.5.: Jablonski diagram showing relaxation of an exited state through fluorescence, phosphorescence and vibrational relaxation. Figure from [44].

The excited state can return to the ground state through luminescence if it emits radiation or nonradiative decay by thermal degradation of energy to the surroundings internally. As a result, luminescence has to compete with nonradiative decay.

There are two types of luminescence: a fast decaying luminescence called **fluorescence**, happens if both the ground and excited states have the same spin multiplicity. Fluorescence half-lives are typically in nanoseconds. If the luminescence persists after exciting illumination is called **phosphorescence**. Phosphorescence is also a radiative decay from a state of different spin multiplicity from the ground state. The mechanism of phosphorescence involves **intersystem crossing**, nonradiative conversion from initial excited state to another excited state with different spin multiplicity. The second state serves as the energy reservoir for the radiative decay to the ground state. Phosphorescence is due to a spin-forbidden transition. However, spin-orbit coupling allows the intersystem crossing to occur because it breaks down the spin selection rule. Phosphorescence is a slow decay and can typically survive to milliseconds (see Fig. 2.5).

2.3. The role of spin in excited state processes

Vanquickenborne *et al.* claims the ligand substitution, isomerization, and racemization are possible if there is a spin state change along the reaction coordinate [45]. Most Fe(II) octahedral complexes undergo ligand rearrangement reactions in two ways. The first one is an intra-molecular twist via a trigonal prism transition state. The second one is a complete dissociation of one ligand; this results in a *square pyramidal* symmetry which can rearrange itself to form a *trigonal bipyramidal* symmetry. For ligand substitution reactions, the substituting ligand attacks on the equatorial plane of the trigonal bipyramidal symmetry. According to Vanquickenborne *et al.* [45] ligand reorganisation takes place to form a trigonal bipyramidal (D_{3h}) before a new ligand attacks the square pyramidal. For this reorganisation to happen the energy barrier between D_{3h} and C_{4V} should be low. The 3d orbital and electronic state correlation diagrams for angular displacement of two ligands to make a transition from C_{4V} to D_{3h} and vice versa (see Fig. 2.6). During this transition the $3d_{yz}$ is the most strongly destabilised orbital, developing from π-antibonding orbital into a predominantly σ-bonding orbital. As a consequence, the $^1A_1$ ground state increases in energy to the extent of 200 kJ/mol ($\cong$ 2 eV). If the ligand attachment to D_{3h} symmetry molecule does not happen in a singlet potential surface and it must happen through the level crossing.

According to Spees *et al.* [46] octahedral Fe(II) complexes have a singlet ground state. Except in strong field ligands such as CN^-, when Fe(II) and Co(III) complexes undergo dissociation the D_{3h} symmetry of the same complex will have a quintet excited state, ^5E" instead of the singlet excited state, $^3A_{2'}$. After dissociation of one ligand, the reordering of 3d orbitals results in quintet spin state for the lowest excited state [45] (see Fig. 2.7). For the reaction mechanisms studied in this thesis (see Sec. 2.4.3), if the attachment of the water molecule happens from the D_{3h} symmetry, according to what is presented so far, the reaction will be slow. The slow process is the result of intersystem crossing that the molecule has to pass through before ligand attachment. In the case of ferrocyanide, if the

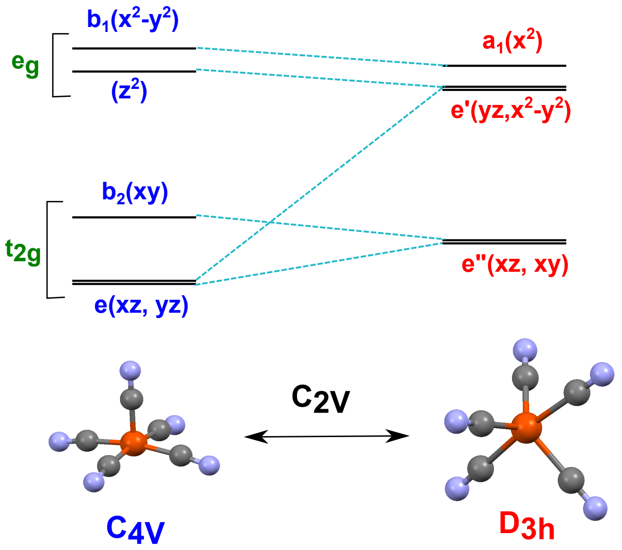

Figure 2.6.: 3d orbital ordering and correlation diagrams for the transition between C_{4V} and D_{3h} symmetries. Adapted from [45].

aquation takes place through a complete dissociation, then a spin-flip is inevitable. A recent time-resolved resonant inelastic X-ray scattering study by Wernet *et al.* [16] on $Fe^{III}(CO)_5$ at the Linac Coherent Light Source (LCLS), suggest that the ligation of ethanol (EtOH) to $Fe^{III}(CO)_4$ from the triplet excited state takes 50-100 ps. On the other hand, they suggest that $[Fe^{III}(CO)_4(EtOH)]$ complex formation from a singlet excited state happens in sub-picosecond time scales.

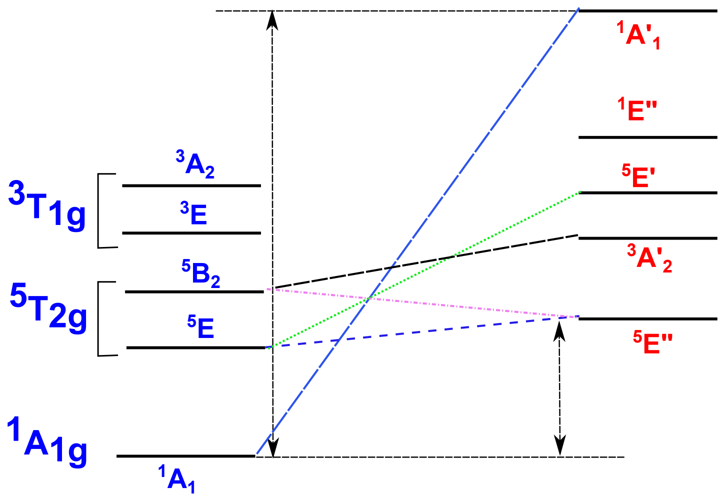

Figure 2.7.: Spin state rearrangement for a transition between C_{4V} and D_{3h} symmetries in $[Co(CN)_6]^{3-}$ complexes. Adapted from [45].

2.4. Iron(II) hexacyanide

2.4.1. Electronic structure of ferro and ferricyanide ions

In this Section, the electronic structure of iron hexacyanide molecules will be described starting from the UV-Vis spectrum shown in Fig. 2.9. The different absorption bands centred at different wavelengths can be explained by using the molecular orbital diagram energy shown in Fig. 2.8. The molecular orbital diagram energy levels of ferrocyanide and ferricyanide molecules are similar (see Fig. 2.8).

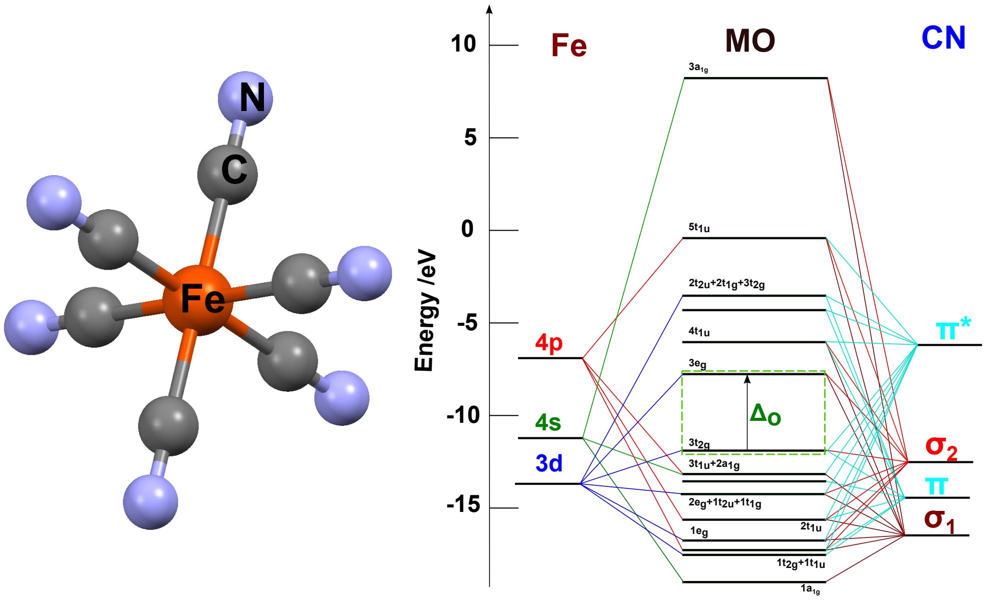

Figure 2.8.: Molecular orbital (MO) diagram of Iron(II) hexacyanide molecule for $[\mathrm{Fe}^{\mathrm{II}}(\mathrm{CN})_6]^{4-}$ in O_h crystal field symmetry. The MO diagram is the result of interaction between the six cyanide (CN^-) ligands and Fe metal center. The $\sigma-$ and $\pi-$bonding orbitals shown on the right-hand side from the CN^- while the 3d, 4s and 4p atomic orbitals shown on the left-hand side originate from Iron. The green box shows the $d-d$ excitations with a crystal field splitting of Δ_o [47].

Ferrocyanide molecule has filled $2t_{2g}$ orbitals as a result; it has ${}^1A_{1g}$ ground state electronic configuration. As shown in Fig. 2.9(a) there is strong absorption band below 250 nm and it originates from $d \rightarrow d$ excitations of $2t_{2g} \rightarrow 3e_g$ transition. These transitions are ${}^1A_{1g}$ ground state to ${}^3T_{1g}$, ${}^1T_{1g}$, ${}^3T_{2g}$ and ${}^1T_{2g}$ excited states [47]. According to A. Gray *et al.* ferrocyanide ion has two MLCT bands centered at 218 nm and 200 nm. Other symmetry forbidden ligand-field ($d-d$) transition bands are also observed at 420, 322 and 270 nm [48] (see Tab.2.1).

Ferricyanide has one empty orbital in the $2t_{2g}$, as a result the ground state electronic configuration becomes $3t_{1u}^6 2t_{2g}^5 = {}^2T_{2g}$. Some of the observed transitions in ferricyanide molecule are centred at 420, 320, 301, 285, 260, 220 and 200 nm [47]. The first Laporte-allowed transition is centred at 420 nm which is a ligand to

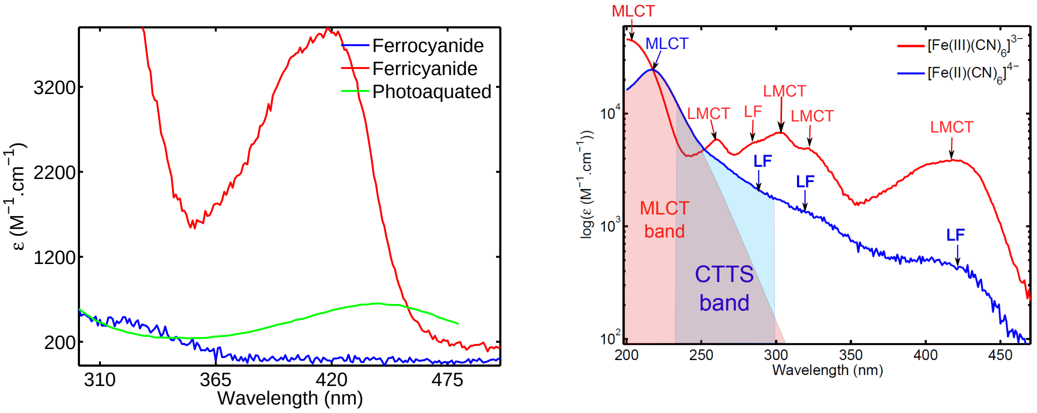

(a) (b)

Figure 2.9.: (a) The molar extinction coefficient spectra of ferro and ferricyanide measured in aqueous solution. (b) The logarithmic plot of extinction coefficient for ferro and ferricyanide ions in aqueous solution. Assignment of absorption bands is based on literature data[47, 48].

Table 2.1.: Summary of all ferrocyanide absorption bands and transition states identified after comparison with reported results [49, 47, 2, 48].

	λ(nm)	Transition	type
$[Fe(CN)_6]^{4-}$	218 nm	$^1A_{1g} \rightarrow ^1T_{1u}$	MLCT
	270 nm	$^1A_{1g} \rightarrow ^1T_{2g}$	LF
	322 nm	$^1A_{1g} \rightarrow ^1T_{1g}$	LF
	422 nm	$^1A_{1g} \rightarrow ^3T_{1g}$	LF

metal charge transfer (LMCT) transition. [50] (see Tab.2.2). To understand the photooxidation and ligand detachment processes, the ferro and ferricyanide ions are studied by excitation at two particular wavelengths such as 266 and 355 nm. The molar extinction coefficient at the two wavelength is summarised in Tab.2.3.

2.4.2. Structure of crystalline iron hexacyanides

The crystal structure of ferrocyanide and ferricyanide has been investigated with Neutron diffraction [51], Extended X-ray Absorption Fine Structure (EXAFS) and X-ray Absorption Near Edge Spectroscopy (XANES) techniques [52]. The crystal structure of $K_4Fe(CN)_63H_2O$ powder has been investigated using diffraction techniques which delivers a bond length of 1.929 Å for Fe−C, 1.1608 Å for C≡N and a bond angle of 179.21° for Fe−C≡N [51]. X-ray diffraction studies of $K_3Fe(CN)_6$ by Figgis *et al.*[53] report Fe−C bond length is 1.903 Å and C≡N is 1.133 Å. The two results show a slight difference of Fe−C and C≡N bond distances for complexes

Table 2.2.: Summary of all ferricyanide absorption bands and transition states identified after comparison with reported results [49, 47, 2, 48].

	λ(nm)	Transition	type
$[Fe(CN)_6]^{3-}$	200 nm	$^2T_{2g} \rightarrow ^2 T_{2u}$	MLCT
	220 nm	$^2T_{2g} \rightarrow ^2 T_{1u}$	MLCT
	260 nm	$^2T_{2g} \rightarrow ^2 T_{1u}$	LMCT
	285 nm	$^2T_{2g} \rightarrow ^2 E_g$	LF
	301 nm	$^2T_{2g} \rightarrow ^2 T_{2u}$	LMCT
	320 nm	$^2T_{2g} \rightarrow ^2 T_{1g}$	LF
	420 nm	$^2T_{2g} \rightarrow ^2 T_{1u}$	LMCT
	550 nm	$^2T_{2g} \rightarrow ^4 T_{1u}$	LMCT

Table 2.3.: Summary of the extinction coefficient (ε) of ferrocyanide and ferricyanide ions in aqueous solution at selected wavelengths.

$\lambda/\varepsilon(M^{-1}\ cm^{-1})$	$[Fe(CN)_6]^{4-}$	$[Fe(CN)_6]^{3-}$
266 nm	2921	4963
355 nm	114	1534

with K_3 and K_4 counter ions.

Structural analysis studies of ferro and ferricyanide in aqueous solution using EXAFS show slight differences in the Fe−C but no difference for the C≡N bond lengths. According to Hayakawa *et al.* in a solution Fe−C is 1.92 Å and 1.93 Å for ferrocyanide and ferricyanide complexes respectively. On the contrary the C≡N bond length is 1.18 Å in both cases [52]. Comparative EXAFS studies of these two complexes in crystalline and solution phases do not show any change in the bond lengths, while there is a slight difference in the Fe−C≡N bond angle [52]. Structural data optimisation with EXAFS fitting is done using DFT predicted atomic coordinates as an initial guess. However, DFT calculations do not include some important information such as crystal packing, solvation shell or the counter ions [26] which are a possible cause for slight differences in the reported values.

2.4.3. Photochemical reactions in iron hexacyanides

Upon irradiation of aqueous ferrocyanide ions depending on the energy of the incident photon energy can undergo ligand exchange and/or photooxidation mechanisms. Ligand exchange is when one solvent molecule (in this case is H_2O) replaces one of the CN^- ligands which results in a distorted octahedral molecule. On the contrary, photooxidation is when the iron metal centre loses an electron. Then the electron is transferred from the central iron to the solvent. At later times, the electron moves away from the parent molecule and is surrounded by solvent molecules to form a hydrated electron. As shown in Fig. 2.9(b) upon irradiation of

Table 2.4.: Summary of bond lengths and bond angles of ferrocyanide and ferricyanide complexes measured by using different structural techniques.

$[Fe(CN)_6]^{4-}$	EXAFS [52]	Diffraction [53, 51]
Fe−C (Å)	1.92	1.93
C≡N (Å)	1.16	1.16
Fe−C≡N (deg.)	177	179.21
$[Fe(CN)_6]^{3-}$		
Fe−C (Å)	1.93	1.903
C≡N (Å)	1.16	1.133
Fe−C≡N (deg.)	176	-

ferrocyanide molecule with λ <313 nm would allow us to access both the MLCT and higher ligand field excited states which would result in both ligand exchange and photooxidation processes [15, 1]. Whereas, if λ >313 nm only the lowest ligand field state which results ligand exchange mechanisms will be accessed [2].

Ligand exchange mechanisms

Ligand exchange mechanisms are a type of reaction which has to pass through a transition state before it forms the final complex [54] (see Fig.2.10). According to transition state theory the rate constant k is given by:

$$k = \frac{k_B T}{h} e^{-(\frac{\Delta G^o}{RT})}, \tag{2.2}$$

where ΔG^o is the Gibbs free energy of activation, k_B is the Boltzmann constant, h is the Planck constant and T is temperature. Gibbs free energy activation determines the rate of reaction and therefore reactions will be temperature dependent. In this section, the explanation of ligand exchange mechanism in a ferrocyanide molecule will be described.

Excitation of aqueous ferrocyanide ions with $\lambda > 313$ nm laser results in a **ligand substituted**, photoaquated complex ($[Fe(CN)_5H_2O]^{3-}$) as the only photoproduct [2]. The reaction mechanism is shown in Eq.(2.3). Shirom *et al.* concluded from flash photolysis measurements that photoaquated complex is formed in less than 7 ns which is within the time resolution of their experiment [55]. The result was obtained by looking at the absorption band of the photoaquated complex which is centred around 440 nm [2]. The formation of photoaquated complex occurs via singlet $^1T_{1g}$ excited state [47, 56]. If the excitation wavelength is below 313 nm the photoaquated complex formation happens in competition with a transition from the short-lived higher singlet state to a charge transfer to solvent (CTTS) state yielding a hydrated electron [15]. The photochemical reaction cycle have been discussed in Reinhard *et al.* and it will be described in the results section using the UV-vis spectra.

The photoaquated complex formation evolves through the $^1T_{1g}$ excited state

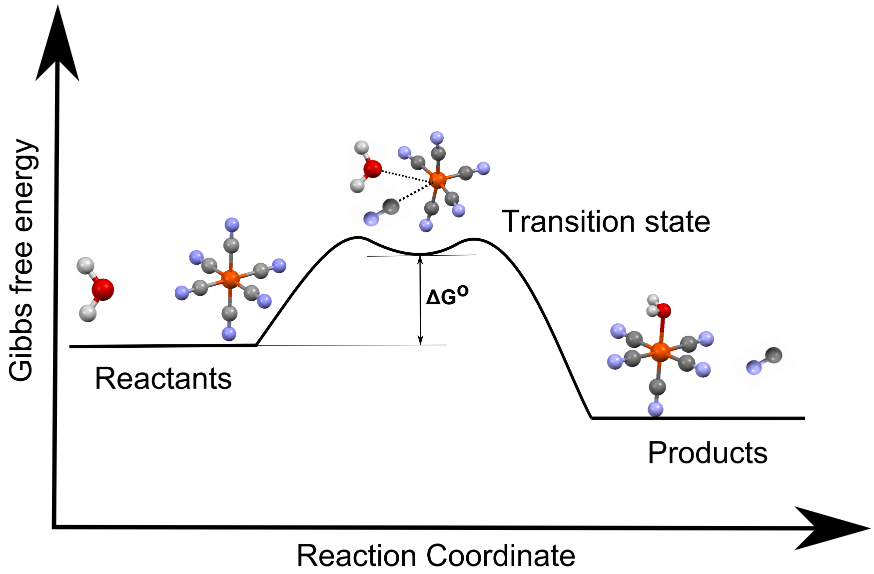

Figure 2.10.: Reaction coordinate diagram for ligand substitution reaction between ferrocyanide and water molecule in aqueous solution. The ligand substitution reaction in ferrocyanide complex has a single intermediate transition state which is pentacoordinated before the photoaquated formation as a final product.

potential surface, but there is no clear evidence whether the intermediate decays to ${}^3T_{1g}$ potential surface through intersystem crossing before the photoaquated complex formation. Another open question where previous studies also fail to answer is whether the ligand exchange mechanism proceeds via a reduced, or an enhanced coordination number.

$$[\mathrm{Fe(CN)_6}]^{4-} + \mathrm{H_2O} \xrightarrow{h\nu} [\mathrm{Fe(CN)_5H_2O}]^{3-} + \mathrm{CN^-} \tag{2.3}$$

Depending on the intermediate/meta-stable state, the ligand exchange mechanism in TM complexes can be one of the following [39]:

1. **Associative pathway (A)** occurs when the intermediate has temporarily increased its coordination number via:

$$\mathrm{ML_6} + \mathrm{Y} \longrightarrow [\mathrm{ML_6}{-}{-}\mathrm{Y}]^{\ddagger} \longrightarrow \mathrm{ML_5}{-}\mathrm{Y} + \mathrm{L} \tag{2.4}$$

2. **Dissociative pathway (D)** occurs when the first dissociation results in reduced coordination number followed by attachment of the solvent molecule via:

$$\mathrm{ML_6} + \mathrm{Y} \longrightarrow [\mathrm{ML_5}]^{\ddagger} \longrightarrow \mathrm{ML_5}{-}\mathrm{Y} + \mathrm{L} \tag{2.5}$$

3. **Interchange pathway (I)** is when the exchange occurs in a one-step process [57].

$$\mathrm{ML_6 + Y \longrightarrow [L{-}{-}ML_5{-}{-}Y]^{\ddagger} \longrightarrow ML_5{-}Y + L_;} \tag{2.6}$$

Where, M is the transition metal center, L is the ligand in the transition metal complex and Y is the nearby solvent. The ligand exchange process in $[\mathrm{Fe(CN)_6}]^{4-}$, exchange of a $\mathrm{CN^-}$ with $\mathrm{H_2O}$ molecule could take place in an associative (A), dissociative (D) or interchange (I) pathway. Depending on the reaction pathway it follows, their can be either penta-coordinated or hepta-coordinated as a transient intermediate state. If the intermediate state is pentacoordinated state it can adopt either square pyramidal (C_{4V}) or trigonal bipyramidal (D_{3h}) symmetry. According to Spees *et al.* [46], if the excitation wavelength (activation energy) is comparable to the crystal field stabilisation energy (CFSE), then it is possible to predict the intermediate or transition state. With an over-simplified model, they have predicted that a model with an enhanced coordination number of C_{2V} symmetry fits the data best for Cr(III) complexes. While a model with reduced coordination number of C_{4V} symmetry fits the data best for Co(III) complexes. The ligand exchange mechanism of iron(II) hexacyanide is not studied thoroughly, and there is no clear evidence whether the reaction proceeds via a complete dissociation or association mechanism. Recently Reinhard *et al.*[25] studied this reaction mechanism using TR optical spectroscopies and claim, that the exchange mechanism proceeded via a complete dissociation of one cyanide molecule and replaced with one solvent molecule. According to their claim, the spectral signatures of the photoaquation complex starts to appear within 500 fs. In this thesis, we will investigate how the details of the ligand substitution reaction process take place, for this our results collected from different X-ray techniques such as TR X-ray Emission Spectroscopy (TR-XES) and TR X-ray Absorption Spectroscopy (TR-XAS) will be presented (see Ch.5,6 and 7.).

Photooxidation mechanism

Photoexcitation of ferrocyanide ions below $\lambda < 313$ leads to a formation of a hydrated electron from ${}^1T_{1u}$ or ${}^1T_{2g}$ states (see Eq.(2.7)) in competition with internal conversion to the lowest excited state ${}^1T_{1g}$ which results photoaquation (see Eq.(2.3)) [1, 47]. The absorption band centered around 218 nm is responsible for these two reaction channels to happen.

$$[\mathrm{Fe(CN)_6}]^{4-}_{\mathrm{aq}} \xrightarrow{\mathrm{h}\nu} [\mathrm{Fe(CN)_6}]^{4-*} \longrightarrow [\mathrm{Fe(CN)_6}]^{3-}_{\mathrm{aq}} + \mathrm{e^-(aq)} \tag{2.7}$$

The hydrated electron formation is a two-step process; the first step is the formation of an excited state of ferricyanide ions, followed by the ejection of an electron from the parent complex to the solvent. According to Shirom *et al.* the quantum yield of hydrated electron formation at 253.7 nm is 0.65, and this is in good agreement with the results of Airey *et al.* and Waltz *et al.* [58, 59]. Solvated electron formation from an excited state is due to a CTTS. Environmental effects such as temperature, the type of solvent (cage effect) and the amount of solute determine the spectrum of the solvated electron. As discussed above the hydrated electron formation is from $^1T_{1u}$ or $^1T_{2g}$ excited states competes with an internal conversion to the lowest $^3T_{1g}$ excited state which only yields photoaquation. For the hydrated electron formation to happen with high quantum yield it has to be very fast to win over an internal conversion. Shirom *et al.* claim the hydrated electron formation in ferrocyanide ions happens below the limit of their experimental time resolution of 1 ns [1, 60].

Pommeret *et al.* assign the spectrum between 450 nm and 550 nm as the CTTS band of the ferrocyanide ion [23, 1]. The absorption band centred around 760 nm is assigned to the hydrated electron. The result concludes that the pre-solvated state appears within the experimental resolution of 60 fs, and the fully solvated state appears within 510 fs. The experiment was done by exciting the ferrocyanide ion with 267 nm laser light [23]. Similar studies were done by Gauduel *et al.* [61] and Ohno *et al.* [62] by exciting ferrocyanide with 310 nm laser light; the pre-solvated state formation has a time constant of 110 fs and followed by fully solvated electron formation within a 240 fs life time.

The hydrated electron formation reaction pathway has been studied by TR-XAS techniques [27, 26] and TR infrared spectroscopy [22] as well. Photoexcitation of ferrocyanide in aqueous solution with laser wavelength between 200–300 nm leads to simultaneous photochemical pathways i.e. photoelectron and photoaquated complex [1, 2]. This reaction pathway has been investigated by Reinhard *et al.* [27] using TR-XAS but they did not show how to disentangle these simultaneous reaction pathways. In Chapters 5 and 6 the recent picosecond-resolved XAS and XES results will be presented respectively.

Quantum Yield measurements of iron(II) hexacyanides

In TR experiments, one of the bottlenecks in analysing a measured spectrum is to know exactly the fraction of excited state molecules. The determining factor for this is the quantum yield of the reaction mechanism investigated. In spin-crossover complexes, each incident laser photon excites one molecule resulting a quantum yield of 1. However, in ferrocyanide molecules, this is not the case. Quantum yield (ϕ) is defined as the ratio of number of absorbed photons to number of reactants produced:

$$\phi = \frac{number\ of\ reactants\ photoionized = n}{number\ of\ photons\ absorbed\ = n^{'}}, \tag{2.8}$$

where $n^{'}$ is the number of photons with energy $h\nu$ absorbed by the reactant. The quantum yield values reported for the photooxidation and photoaquation processes is summarised in Tab.(5.2), but there are many discrepancies among the literature published.

Table 2.5.: Quantum yield(QY) of photo-oxidation and photoaquated of ferrocyanide molecule at a different wavelength. Where ϕ_e is the quantum yield for photoelectron production and ϕ_{aq} is the quantum yield for the photoaquated product. pH is a measure of acidity/basicity of a given solution. The pH scale ranges from 0 - 14, with seven being neutral. Mathematically, pH=-log[H^+], where [H^+] is the concentration of hydrogen ion in the solution.

QY	254 nm/pH	366 nm/pH	365 nm/pH	313 nm/pH
ϕ_e	0.35/nat.pH [62] 0.65/nat.pH [59, 58]		0.0 [15]	0.1 [58, 59, 1]
ϕ_{aq}	0.1-0.2/6.8-9.9 [2] 0.1/nat.pH [63]	0.52/0.65 [56] 0.89/4.0 [56] 0.36/10.0 [63]	0.2/nat.pH [63]	0.35/10 [63] 0.4/6.8-9.9 [2]

2.5. Spin crossover complexes

In this Section first the general properties of pseudo-octahedral Fe(II) spin crossover (SCO) complexes and the relaxation dynamics will be presented. After that the ground state electronic structure and photoexcited relaxation pathways of $[\mathrm{Fe(terpy)_2}]^{2+}$ will be described.

2.5.1. General properties of SCO complexes

As discussed in Sec.2.1 in a perfect octahedral crystal field the five d-orbitals of a transition metal ion are split into two subsets. The first subset contains d_{xy}, d_{yz} and d_{zx} which are the basis of the irreducible representation t_{2g} and the second subset contains d_{yz} and d_{zx} which are the basis of the irreducible representation e_g in octahedral symmetry [64]. The splitting between the two sets is called ligand field splitting ($10\mathrm{D}_q$), and it depends on the metal-ligand distance as $1/\mathrm{r}^n$ with n = 5-6 and r being the metal-ligand bond distance [64]. As a result, the potential surfaces of the possible electronic states has to be plotted along the breathing mode which corresponds to the variation of $10\mathrm{D}_q$.

Electron-electron interaction between the d-electrons of the metal results from a series of states characterised by their spin-multiplicity 2S+1 and their orbital moment L, which is denoted by the term symbol ^{2S+1}L is called Russel-Saunders coupling [67]. The energies of the different electronic states are calculated as a function of Racah parameters of electron-electron repulsion, B, and C [65]. The Tanabe-Sugano diagram of $3d^6$ complexes is shown in Fig. 2.11 and it illustrates how the different electronic states of the free metal ion split under the additional influence of an octahedral ligand field [68, 69]. According to Hund's rule ^5D, is the ground state of the free ion. When the ligand field is applied ^5D state splits into ^5E (purple line) and $^5T_2$ (black line). The $^5T_2$ high-spin (HS) state remains the

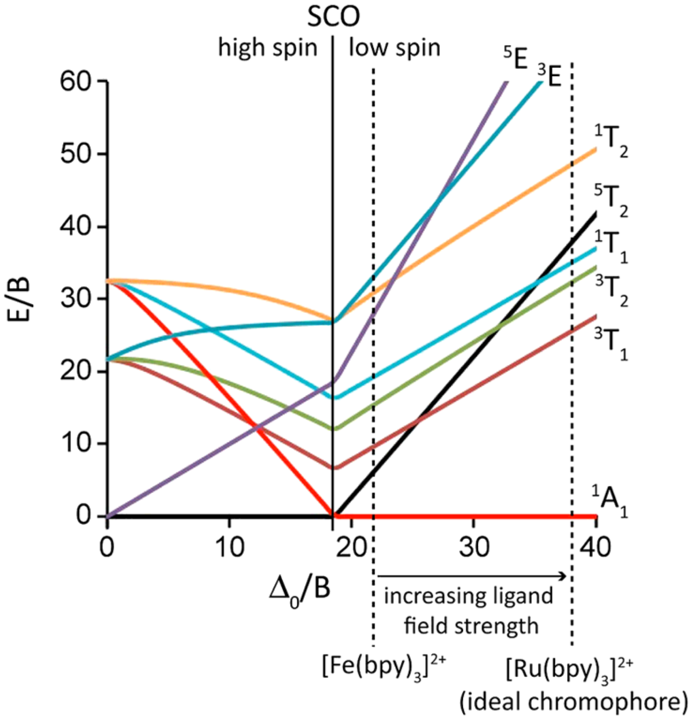

Figure 2.11.: Tanabe-Sugano diagram for transition metal complexes with six electrons in octahedral symmetry. Where Δ_o is the ligand field splitting parameter, E is the energy. The Recah parameters used for preparing the diagram are C = 4774 cm^{-1} and B = 1080 cm^{-1} given in [65]. The vertical dotted line shows for $[Fe(bpy)_3]^{2+}$ complex. The figure is adapted from [66].

ground state upto a critical value of the ligand field strength, where $10D_q$ is equal to the spin pairing energy P = $20\Delta_0/B$. Above this value, the $^1A_1$ low spin(LS) state is relatively stabilised, and it becomes the ground state. The maxima of d-d transitions absorption bands correspond to vertical transitions in the Tanabe-Sugano diagram. The value of $10D_q$ depends on the ligand type and the metal to ligand bond distance. For all spin crossover complexes, the HS state has larger metal to ligand bond lengths than LS state complexes. Because the HS state has two electrons in the antibonding e_g orbitals whereas the LS state has all six electrons in the non-bonding t_{2g} orbitals.

Octahedral and pseudo-octahedral TM complexes with completely unoccupied d orbitals of d^4–d^7 electronic configuration are classified into three depending on the ligand-field strength and the mean spin-pairing energy [70, 38].

i **Strong ligand field case**: low-spin (LS) state

ii **Weak ligand field case**: high-spin (HS) state and

iii **Intermediate ligand field case**: thermal spin crossover between HS↔LS

The SCO phenomenon can happen upon an application of external perturbation such as temperature, light, pressure and magnetic field [70, 71, 72, 73]. Bistability is a major factor in their application for sensors and switches [64]. Another possible and realistic application of Fe(II) polypyridine complexes is their potential to serve as light harvesters in dye-sensitized solar cells (DSSCs).

The LS→HS spin state change in transition metal complexes is always accompanied by significant changes in the metal coordination environment due the different electronic configuration i.e. $t_{2g}^4 e_g^2$. As a result, the total spin state change is ΔS=2 and the metal-donor atom bond length is increased by roughly 0.2 Å or 10%, for $[Fe(terpy)_2]^{2+}$ and $[Fe(bpy)_3]^{2+}$ complexes [74, 75].

2.5.2. Relaxation dynamics

Optically excited SCO Fe(II) complexes switched from the LS state to a metastable HS state from which it relaxes back to the ground state (with a single exponential decay)[73]. This phenomenon is referred to as light-induced excited spin state trapping (LIESST). Buhks *et al.* proposed a model which describes this phenomena which is called *radiationless nonadiabatic multiphonon process* [76]. The model describes the reaction rate between the two spin states which are characterised by different nuclear configurations and the energy barrier should be proportional to k_BT [7]. The temperature dependent relaxation rate is given by Eq.(2.9). The formula is derived from Fermi's Golden rule (for details refer to [76]).

$$k_{HL}(T) = \frac{2\pi}{\hbar^2\omega}\beta_{HL}^2 F_m(T) \tag{2.9}$$

Where β_{HL} is the electronic coupling matrix element provided by second order spin-orbit coupling, $\hbar\omega$ is the vibrational energy of the active vibrational mode, which is the metal-ligand breathing mode and F_n(T) is thermally averaged Franck-Condon factor and given by Eq.(2.10). For SCO complexes with ΔS=2, a typical value of β_{HL} is 150 cm^{-1} and $\hbar\omega$ is 250 cm^{-1} [73].

$$F_n(T) = \frac{\sum_m |\langle\chi_{m+n}|\chi_m\rangle|^2 e^{\frac{-m\hbar\omega}{k_B T}}}{\sum_m e^{\frac{-m\hbar\omega}{k_B T}}} \tag{2.10}$$

The sum goes over all vibrational levels m of the high spin state with reduced energy gap n = $\Delta E_{HL}/\hbar^2\omega$ being the dimensionless measure of the vertical displacement of the potential walls. At low temperatures (as T→0) electrons will occupy only the lowest vibrational state and the relaxation rate constant becomes:

$$k_{HL}(T) = \frac{2\pi}{\hbar^2\omega}\beta_{HL}^2 |\langle\chi_n|\chi_0\rangle|^2, \tag{2.11}$$

---

[7] k_BT is the product of Boltzmann constant k_B and temperature T. At room temperature, T = 298 K, k_BT is equal to 25.7 meV.

The Franck-Condon factor is the square of an overlapping integral between two slightly displaced electronic potential surfaces (i.e. HS and LS) and it simplifies to:

$$|\langle \chi_n|\chi_0\rangle|^2 = \left|\int \chi_n\chi_0 d^3r\right|^2 = \frac{S^n e^{-S}}{n!} \tag{2.12}$$

Where S$\propto$ $\Delta Q_{HL}^2/\hbar\omega$ is the Huang-Rhys factor and the horizontal displacement is given by $\Delta Q = \sqrt{6}\Delta r_{HL}$. For a strong vibronic coupling and below 50 K temperature the HS → LS relaxation process is temperature independent, and pure tunneling process governs it. The tunneling process has been observed experimentally by Xie *at al.* [77]. At higher temperatures the relaxation process is thermally activated, and the energy barrier becomes less than at room temperature.

The LIESST phenomenon makes SCO complexes ideal for TR studies. The relaxation dynamics of SCO compounds such as $[\mathrm{Fe(bpy)_3}]^{2+}$ has been studied using TR optical spectroscopy [14, 34]. The experimental work was able to follow the full relaxation process from the MLCT to the HS state. A time-resolved X-ray emission spectroscopy study by Kelly Gaffney *et al.* showed rather the relaxation has to happen through triplet spin state[78]. A combination of picosecond-resolved X-ray probe tools (i.e. EXAFS, XES and XDS) are also used to study the relaxation processes of $[\mathrm{Fe(bpy)_3}]^{2+}$ complex [79]. EXAFS give the 0.2 Å change of Fe-N bond length, XES give the ΔS =2 spin state change, and the XDS give the change in solvation of $[\mathrm{Fe(bpy)_3}]^{2+}$ complex the following conversion to the HS state. In this thesis, previously published EXAFS data [79] and analysed newly implemented energy-space EXAFS fitting is used to characterise and extract structural information of the excited high spin state (see Ch.8).

2.5.3. Fe(II)-bis-terpyridine

This Section introduces $[\mathrm{Fe(terpy)_2}]^{2+}$ as one of the SCO complex investigated in this thesis. $[\mathrm{Fe(terpy)_2}]^{2+}$ is one of the most studied SCO complexes with a potential application for making a magnetic memory device [31, 70]. Like other SCO complexes the ground state of $[\mathrm{Fe(terpy)_2}]^{2+}$ has a LS ground state with all six electrons occupying the non-bonding t_{2g} d-orbitals (see Fig. 2.12). The ground state structure obtained using different experimental and theoretical methods will be presented and discussed. Studies by Hauser *et al.* showed that upon photoexcitation with UV-visible light the molecule is excited to the metal-to-ligand charge transfer state and afterwards decays to the HS quintet ($^5T_2$) spin state through a triplet intermediate state. At room temperature the $^5T_2$ HS state decays to the ground state in 2.61 ns (see Sec. 2.5.3) [31, 38].

Ground state structure

As shown in Fig.2.13(b) is the $[\mathrm{Fe(terpy)_2}]^{2+}$ molecule has two terpyridine ligands. The six nitrogen atoms form bonds with the metal centre. The bonds are cat-

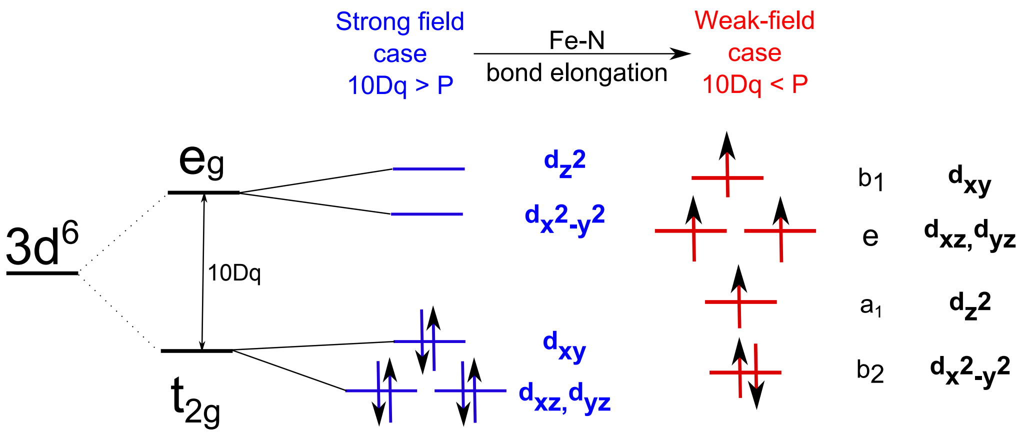

Figure 2.12.: Schematic energy level diagram for $3d^6$ electronic configuration of the low-spin ground state and high-spin excited state of $[Fe(terpy)_2]^{2+}$ molecule in pseudo-octahedral crystal field. Where p is the strong Coulomb repulsion energy and 10Dq is the ligand-field strength [74].

egorised into two groups, with two nitrogen atoms in the axial (ax.) and four nitrogen atoms in the equatorial (eq.) plane. The ground state of $[Fe(terpy)_2]^{2+}$ molecule shown in Fig.2.13(a) has a D_{4h} symmetry with a ligand field strength parameter of $10D_q = 2$ eV.

The crystal structure of $[Fe(terpy)_2]^{2+}$ complex at room temperature solved by Figgis *et al.* in 1983 using X-ray diffraction technique[80]. The experimental results for the bond length of $Fe-N_{ax.} = 1.891$ Å, $Fe-N_{eq.} = 1.988$ Å and NNN angle is 102.8°. Later the experimental data form Baker *et al.* were used as initial input and the structures are optimized using DFT. The structural results from DFT are $Fe-N_{ax.} = 1.886$ Å, for $Fe-N_{eq.} = 1.985$ Å and NNN angle is 102.6° is in a good agreement with the experimental data reported earlier. In our recent paper [74] of Fourier transform EXAFS analysis we reported bond distances of $Fe-N_{ax.} = 1.874 \pm 0.004$ Å and $Fe-N_{eq.} = 1.969 \pm 0.004$ Å. The slight disagreement between the EXAFS and other techniques could be due to the fact that the NNN angle distortion is not optimized in our EXAFS fitting.

Relaxation dynamics

Both experimental [31] and theoretical [81] studies indicates that the full LS-HS dynamics of this molecules do not follow a single configurational coordinate (SCC) breathing mode similar to the $[Fe(bpy)_3]^{2+}$ molecule rather it shows two vibrational modes involved for the switching mechanism. As shown in the Fig.2.14(b) upon photoexcitation the $[Fe(terpy)_2]^{2+}$ molecule is excited to metal-centered (MC) or metal-to-ligand charge transfer (MLCT) excited states and then decays to the quintet HS state via intersystem crossings through the participation of intermediate states [82, 83, 84].

As explained in Sec. 2.5.2 the lifetime of excited HS state is determined by ΔE_{HL}

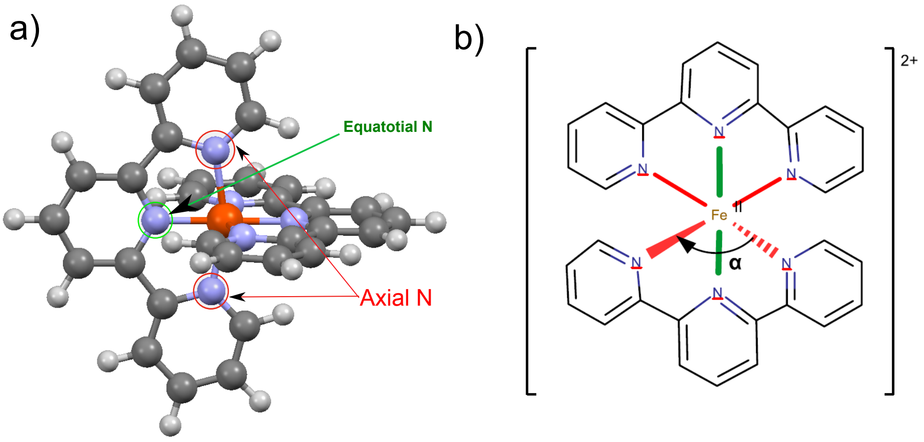

Figure 2.13.: a) Ball and stick representation of $[Fe(terpy)_2]^{2+}$ molecule. b) $[Fe(terpy)_2]^{2+}$ molecule, where red Fe-N bonds are equatorial nitrogen atoms and the green ones are axial nitrogen atoms. Where α is called a bite angle for $[Fe(terpy)_2]^{2+}$ molecule it is 161° [66].

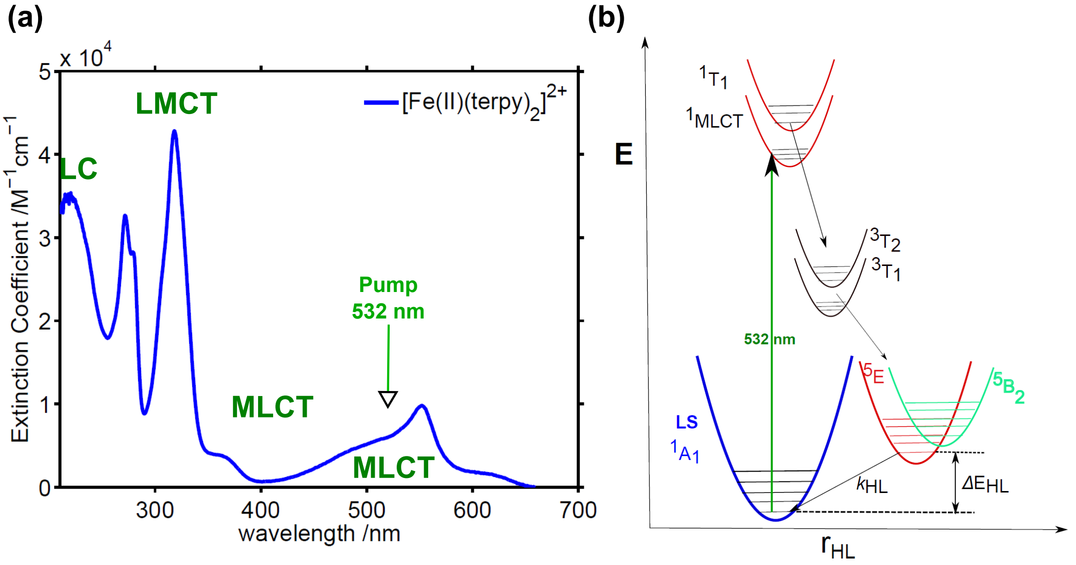

Figure 2.14.: (a) Static UV-VIS absorption spectrum of aqueous $[Fe(terpy)_2]^{2+}$ complex. The green arrow shows the excitation wavelength used for the TR measurements reported in this work. (b) A possible mechanism of light-induced excited spin state trapping and the relaxation dynamics in $[Fe(terpy)_3]^{2+}$ molecule. The concept of the figure is adapted from [81, 74].

and Δr_{HL}, this has been shown by earlier works of Hauser and *et al.* [38, 85, 31]. The LS↔HS switching mechanism has been studied using TR techniques in spin crossover complexes with ΔE_{HL} is between 0.35 eV - 0.7 eV. In our recent study [74] which combines an arsenal of TR X-ray spectroscopic and scattering tools is used to characterise the excited state structure of optically prepared HS state. Due to the excellent quality of EXAFS data we able to identify the suitable HS excited state among the two closely lying possible states predicted by DFT [86]. In this thesis, the same EXAFS data published [74] is analyzed with the newly implemented energy-space EXAFS fitting to characterize and extract structure of the possible HS state (see Ch. 8).

Chapter 3

Principles of X-ray spectroscopy

This chapter describes the principles of X-ray spectroscopic probe tools used to follow chemical reaction dynamics. For a better understanding of the X-ray spectroscopic techniques, first the interaction of radiation with matter, particularly X-rays will be presented. The second Section contains the principles of X-ray absorption spectroscopy (XAS) and the information content of XAS spectrum both X-ray Absorption Near Edge Structure (XANES) and Extended X-Ray Absorption Fine Structure (EXAFS) with the multiple scattering theory. Computer-based ab-initio programs such as FEFF[1] and ORCA[2] used to calculate the XAS spectrum will be described briefly. Then the X-ray emission spectroscopy and its information content that can be extracted will be discussed.

3.1. Interaction of X-rays with matter

When a beam of X-ray photons interacts with matter one or both of the following scenarios can be observed: the photons can be absorbed and disappear, or scattered and change direction. The different kinds of physical processes are Thomson (coherent) scattering, Compton (incoherent) scattering and photoelectric effect[87, 88]. The cross-sections of these physical process is shown as a function of energy is shown in Fig. 3.1. For the elastic Thomson scattering the incident photon energy is transferred to an oscillating electron and the oscillating electron emits a photon with the same frequency. For the inelastic Compton scattering a photon with energy and momentum interacts with a free electron at rest and after the collision, the photon is scattered at an angle with a different photon energy and momentum. Also, the electron is ejected at an angle with certain energy and momentum. The photoelectric effect is observed when the incident X-ray photon is absorbed and as a result, photoelectrons are emitted with a certain kinetic energy. The emitted photoelectron kinetic energy depends on the incident photon energy, not on the intensity. If the incident photon energy is higher than the binding energy of the

---

[1] FEFF 9.0 is developed by the group of J. J. Rehr *et. al.* from University of Washington, USA

[2] ORCA is developed by the group of Frank Neese *et. al.* from Max-Planck-Institute for Chemical Energy Conversion, Germany.

electron, then the kinetic energy of the photoelectron is the difference between the incident photon energy and the binding energy of the electron. This phenomenon can be interpreted with a mathematical formula proposed by Einstein (3.1):

$$E_k = h\nu - E_b, \tag{3.1}$$

where hν is the incident X-ray photon energy, E$_k$ is the kinetic energy of the photoelectron and E$_b$ is the binding energy of an electron within the atom.

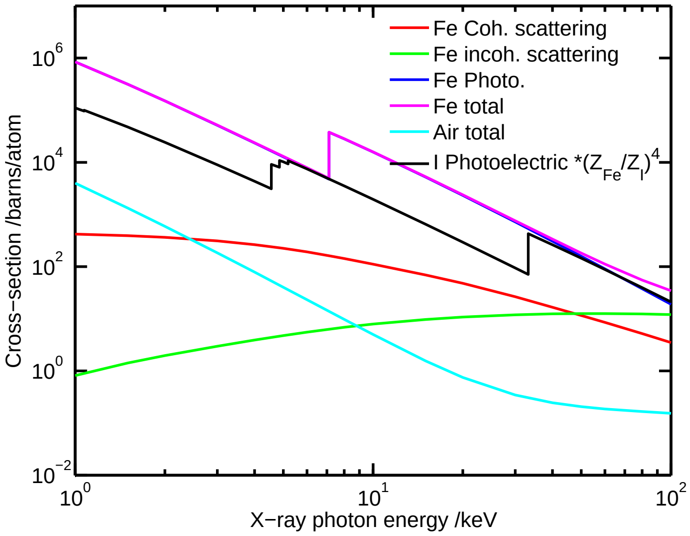

Figure 3.1.: Logarithmic plot of cross-sections for the different processes contributing to the total X-ray cross-section. The photoelectric cross-section of Fe and I in barns/atom are displayed. The jumps in the photoelectric cross-section are absorption K-edges of iron (Fe) and iodine (I) at 7.112 keV and 33.169 keV respectively. Similarly, the L$_{1,2,3}$-edges of I at 5.188 keV, 4.852 keV, and 4.557 keV are shown. Photoelectric cross-section of I shown in the plot is multiplied by $\frac{Z_{Fe}}{Z_I}$. The data of this plot is from [89].

3.1.1. Theory of X-ray interactions with matter

The total Hamiltonian of a molecule without an external electromagnetic field is given by Eq.(3.2):

$$\begin{cases} \hat{H}_{at} = \hat{T}_{NN} + \hat{V}_{NN} + \hat{H}_{el} \\ \hat{H}_{el} = \hat{T}_{ee} + \hat{V}_{en} + \hat{V}_{ee} = \hat{H}_0 + \hat{V}_{ee}, \end{cases} \tag{3.2}$$

where $\hat{T}_{NN}$ is the kinetic energy of nuclei, $\hat{V}_{NN}$ is pair-wise nucleus-nucleus repulsion and $\hat{H}_{el}$ is the electronic Hamiltonian of the atom. The electronic part of the Hamiltonian contains the kinetic energy of electrons $\hat{T}_{ee}$, the electrostatic interaction of electrons with the nucleus $\hat{V}_{en}$, and the electron-electron repulsion $\hat{V}_{ee}$. Using Born-Oppenheimer's (BO) adiabatic approximation (named after Max Born and J. Robert Oppenheimer) proposed 1927, the electronic and nuclear part of the Hamiltonian can be split and solved separately. The BO approximation assumes that the motion of atomic nucleus is slow compared to the motion of electrons; thus, both operators can be separated. In the presence of an electromagnetic field, the electronic part of the Hamiltonian shown in Eq.(3.2) can be rewritten as:

$$\hat{H}_{tot} = \left(\hat{H}_{EM} + \hat{H}_{at}\right) + \hat{H}_{int} = \hat{H}_0 + \hat{V}_{ee} + \hat{H}_{int} \quad , \tag{3.3}$$

where $\hat{H}_{EM}$ is an electromagnetic field of the free external field and $\hat{H}_{int}$ is the perturbation interaction of electrons with an external electric field and $\hat{H}_0$ is the unperturbed part of the Hamiltonian. Solving Eq.(3.3) exactly is impossible but approximate solutions can be obtained using *perturbation theory* approach. Using the eigenfunctions of the Hamiltonian the Schrödinger Equation can be solved and yields the eigenvalues. The Hamiltonian $\hat{H}_{EM}$ results quantized energy of the applied electromagnetic field. $\hat{H}_0$ is the same for all electrons and can be solved with orbital eigenfunctions for a certain electronic configuration and results in the average energy of the configuration. The energies depend on the principal quantum number (n = 1, 2, 3, ...), the angular momentum quantum number (l = 0,1,2,..,n-1) and the magnetic quantum number (m =-l,-(l-1),...,0,1,..l). As a result, the energetic ordering of electron shells in an atom becomes as follows:

$$1s < 2s < 2p < 3s < 3p < 4s < 3d < 4p..., \tag{3.4}$$

In spectroscopy, shells corresponding to the main quantum numbers n = 1, 2, 3, ... are denoted as K, L, M, N, ... The principal quantum number specifies the number of electrons in each shell for a given atom or ion and its electronic configuration. The ground state configuration is usually found by progressively adding electrons from the energetically lowest to higher lying shells according to Eq.(3.4) called *Aufbau principle.* At the same time, the configuration should follow the Pauli exclusion principle[3].

The $\hat{H}_{int}$ part of the Hamiltonian describes the interaction of an external field with electrons. Due to the interaction with the external electromagnetic field, the electrons start oscillating and therefore excited from an initial to a final state. The transition probability Γ_{if} of an electron from an initial state ψ_i to a final state ψ_f until the second-order perturbation is given by Fermi's golden rule via:

---

[3] No two electrons in an atom or ion can have identical quantum numbers

$$\Gamma_{if} = \frac{2\pi}{\hbar}\delta(E_f - E_i - h\nu)|\left\langle\psi_i\right|\hat{H}_{int}\left|\psi_f\right\rangle + \sum_m \frac{\left\langle\psi_i\right|\hat{H}_{int}\left|\psi_m\right\rangle\left\langle\psi_m\right|\hat{H}_{int}\left|\psi_f\right\rangle}{E_i - E_m + i\epsilon} + ...|^2, \tag{3.5}$$

which is divided into two parts: first-order and second-order perturbation theory. The transition can happen only if the energy of the final state equals the energy of initial state plus the energy of the applied electromagnetic field. This energy conservation rule is taken care by the Dirac delta function.

In the hard X-ray energy range the photoexcitation of electrons is the dominant mechanism (see Fig. 3.1). Incoherent scattering is negligible in comparison to the photoelectric effect, and pair production is almost zero in the energy range shown. As a result of this and due to the weak interaction of the electromagnetic field only a first-order perturbation of the applied electromagnetic field needs to be taken into account. The Fermi's golden rule shown in Eq.(3.5) can be rewritten as:

$$\Gamma_{if} = \frac{2\pi}{\hbar}\delta(E_f - E_i - h\nu)|\langle\psi_i|\mathbf{p}\cdot\mathbf{A(r)}|\psi_f\rangle|^2, \tag{3.6}$$

where $\mathbf{p}$ is the momentum operator and $\mathbf{A(r)}$ is the vector potential of the incident electromagnetic field, which is described by a classical wave with polarization $\hat{\epsilon}\perp\hat{k}$. Using a plane wave description the vector potential can be written as $\mathbf{A(r,t)}\cong \hat{\epsilon}A_0e^{i\mathbf{k}.\mathbf{r}}$. The exponential part of the function can be expanded as:

$$e^{i\mathbf{k}\cdot\mathbf{r}} = 1 + i\mathbf{k}\cdot\mathbf{r} + ... = \sum_{n=0}^{\infty}\frac{(i\mathbf{k}\cdot\mathbf{r})^n}{n!}, \tag{3.7}$$

where the first two terms are called the dipole approximation. Transitions are allowed if the difference in the angular momentum between the final and initial state wave function is ±1 ($\Delta l = \pm 1$). As a result, only transitions from s→p, p→d, d→f ... and vice versa are allowed. The second term in Eq. (3.7) accounts the electric quadrupole transitions with the selection rule $\Delta l = \pm 2$ this results in a transition from s→d. The quadrupole transition matrix elements are smaller compared to the dipole transition matrix elements by a factor of the order of the fine structure constant; $\alpha \sim 1/137$ [90, 91, 92].

The initial (ψ_i) and final (ψ_f) state wave functions used in Fermi's golden rule(Eq. (3.6)) are not exactly known. Therefore, one has to make a few assumptions to get an approximate and meaningful wave functions. The first assumption is that X-ray absorption is a single electron excitation process. Based on this the initial state wave function can be just the core wave function, and the final state as a free electron wave function. The second assumption is that all other electrons do not participate in the X-ray induced transition. The X-ray intensity I_{XAS} will be then proportional to $M^2\rho$, with M being the one electron dipole transition matrix element and ρ the density of empty states derived from the Dirac delta function [93]. The X-ray absorption cross-section σ is the ratio between X-ray absorption rate Γ_{if} and X-ray photon flux J_p [94].

$$\sigma = \frac{\Gamma_{if}}{J_p} \tag{3.8}$$

The SI unit of the cross-section is m^2 but usually expressed in units of barn (1 barn = 10^{-30} m^2).

3.2. Principles of X-ray absorption spectroscopy

X-ray Absorption Spectroscopy (XAS) measures the absorption of X-rays as a function of the incident energy E. When an X-ray beam with incident intensity I_0 passes through a material of thickness x the intensity will be decreased by an amount determined by the absorption characteristics and length of the material being irradiated (see Fig. 3.2).

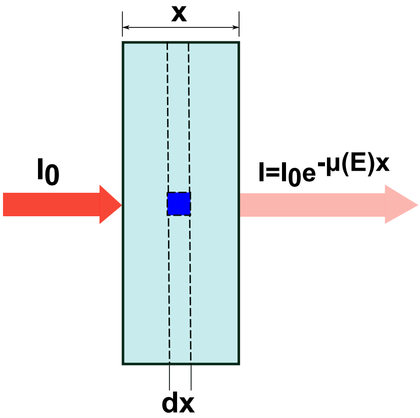

Figure 3.2.: A schematic view of X-ray absorption. The incoming X-ray beam I_0 loses its intensity due to absorption processes within the irradiated material. The intensity loss depends on the absorption coefficient $\mu(E)$ of the material, which is an intrinsic property of the material.

The change of incident X-ray intensity, dI when passing through an infinitesimal material of thickness dx is given by the following Eq.(3.9):

$$\frac{dI}{I} = -\mu(E)dx \tag{3.9}$$

After integrating both sides of the equation, for the intensity from I_0 to I_t and for the path length from zero to x, will result in a formula for the transmitted intensity. The transmitted intensity depends on the absorption coefficient $\mu(E)$ and the path length which is given by Eq.(3.10).

$$I_t = I_0 e^{-\mu(E)\cdot x} \tag{3.10}$$

Fig. 3.3 shows the X-ray absorption coefficient multiplied by the sample thickness (100 μm) as a function of incident photon energy E for ferrocyanide molecule.

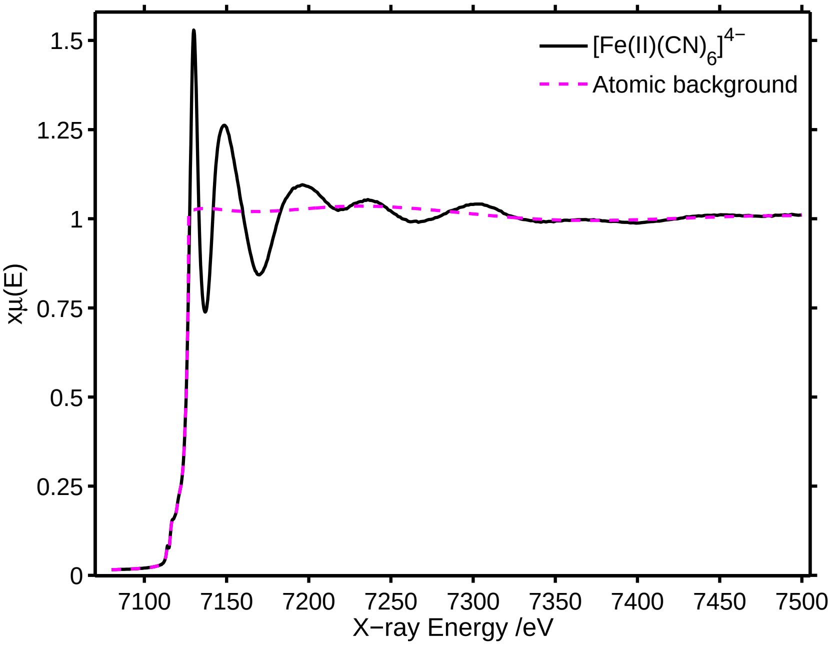

Figure 3.3.: X-ray absorption coefficient of 50 mM aqueous ferrocyanide sample as a function of the incident X-ray energy. The step function represents the atomic background.

When the incident X-ray energy (hν) is higher than the binding energy of the electron, the core level electrons gets excited to the continuum. The difference between the incident X-ray energy and the binding energy of the electron will be converted to the kinetic energy of the photoelectron. At the absorption edge E_{edge} the kinetic energy of the photoelectron E_k is equal to E_0 which is defined as the zero-point energy. The relation between the incident X-ray photon energy $h\nu$, the photoelectron kinetic energy E_k and the binding energy E_b of core level electrons is given by Eq.(3.11).

$$E_k = h\nu - E_b; \tag{3.11}$$

The outgoing photoelectron with energy-dependent wavevector k can be represented as a spherical wave with de Broglie wavelength λ using Eq.(3.12).

$$k = \frac{2\pi}{\lambda} \tag{3.12}$$

and

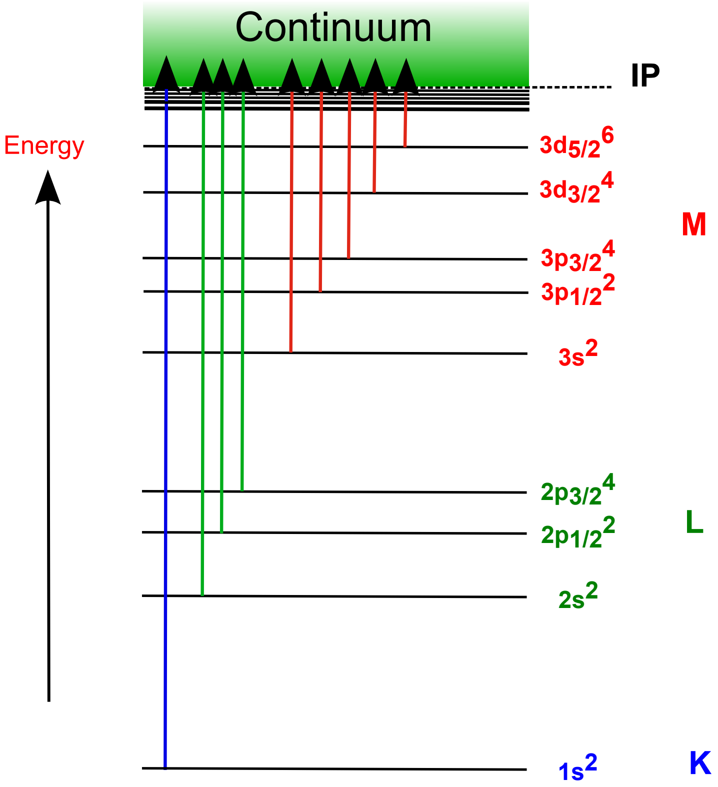

Figure 3.4.: Schematics of X-ray absorption edges and corresponding core-level electrons. The different K, L, M absorption edges are shown. All the transition from the core-level to the unoccupied states above the ionization potential (IP), in addition to the bound-bound transitions.

$$k^2 = \frac{2m_e}{\hbar^2}(E_k) = \frac{2m_e}{\hbar^2}(h\nu - E_b) \tag{3.13}$$

Where $\hbar$ is the Planck's constant and m$_e$ is mass of electron which results in the photoelectron wavevector, k.

$$k = 0.512 \cdot \sqrt{\frac{h\nu - E_b}{eV}}(\mathring{A}^{-1}) \tag{3.14}$$

The XAS spectrum shown in Fig.3.3 shows two distinct features; a sharp rise around the energy point of 7112 eV, called *absorption edge* and an oscillatory structure above the absorption edge. In general, the XAS spectrum is classified into three regions: the pre-edge, X-ray Absorption Near Edge Structure (XANES) and Extended X-ray Absorption Fine Structure (EXAFS) (see Fig.3.5). The part of the spectrum below the edge is dominated by bound-bound transitions in the vicinity of the Fermi level (see the inset of Fig.3.5). In Section 3.2.4 the information content that can be extracted from the pre-edge region will be discussed by comparing the experimental data with simulated ORCA calculations. The oscillatory part of the spectrum is further classified into two parts, i.e. XANES and EXAFS. Roughly up to 30 eV above the absorption edge is called XANES and the region beyond 30 eV of the edge is called EXAFS [91]. The origin of the oscillation is due to constructive and destructive interference between the outgoing and the backscattering photoelectrons. In the next Sec.3.2.1 the theories used to interpret the EXAFS spectrum will be presented.

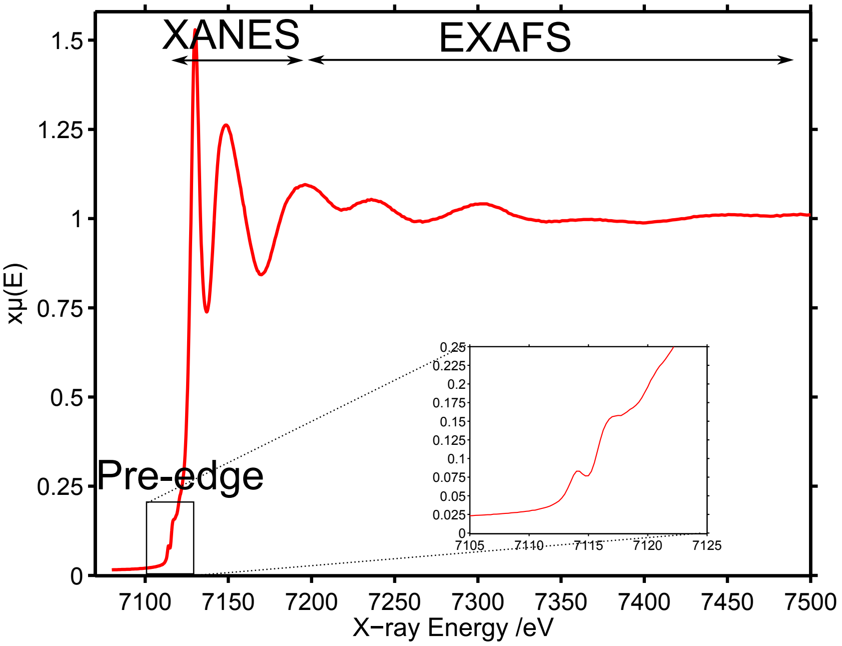

Figure 3.5.: X-ray absorption spectrum measured around the Fe K-edge of 50 mM aqueous ferrocyanide solution as a function of the incident X-ray energy. The classification of the XAS spectrum indicated is based on [10]. The inset is the zoom-in the pre-edge part of the spectrum.

The absorption edge is what makes XAS element specific because every element in the periodic table has an absorption edge at a different particular energy which is unique. The absorption edge is also sensitive to the oxidation state of the absorbing atom. Fig.3.6(a) shows the XAS spectrum around the K-edge of aqueous ferrocyanide and ferricyanide molecules measured at the same experimental conditions. As can be seen in Fig.3.6(a) the K absorption edge of the ferricyanide complex with Fe having +3 oxidation state is 1 eV blue shifted on a corresponding ferrocyanide complex with Fe having +2 oxidation state. The absorption edge is also sensitive to electronic, or bond length changes, for example in the case of $[Fe(terpy)_2]^{2+}$ upon irradiation with 532 nm laser light the molecule gets excited from the ground state with S=0 to an excited state with S=2, accompanied by Fe-N bond length expansion. The XANES spectra measured before and after excitation show differences due to this effect. This shows the absorption edge of the excited state spectrum is red shifted by 1.5 eV on the ground state spectrum (see Fig.3.6(b)).

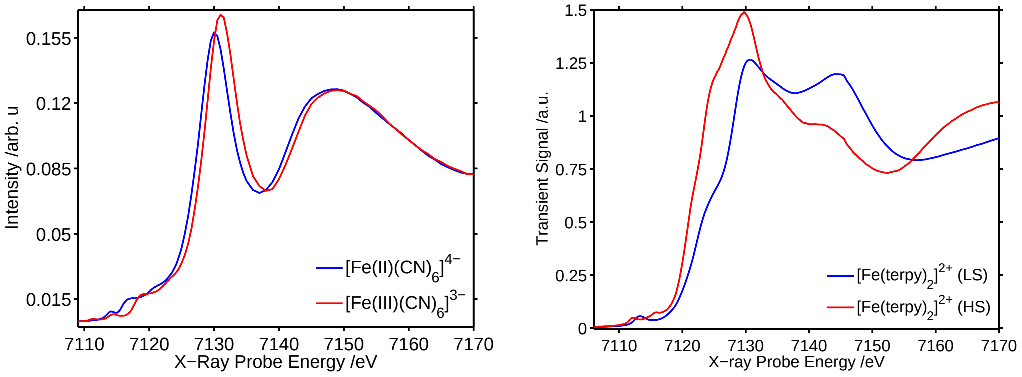

(a) (b)

Figure 3.6.: (a) XANES spectrum measured around Fe K-edge for ferricyanide (red) and ferrocyanide (blue) ions in aqueous solution. (b) XANES spectrum measured around Fe K-edge for ground state $[Fe(terpy)_2]^{2+}$ (blue) and excited state $[Fe(terpy)_2]^{2+}$ (red) molecules in aqueous solution.

Below the absorption edge is the bound-bound transitions, also called pre-edges are observed (see inset of Fig.3.5). These transitions are from core level to bound unoccupied levels. In 3d transition metal complexes, the origin is due to 1s to 3d transitions which are quadrupole allowed transitions [95]. In metal K-edge XAS the pre-edge (1s to 3d excitations) gives information about oxidation state and the symmetry of the ligand environment around the metal centre [30, 96, 28].

3.2.1. Extended X-ray absorption fine structure

Extended X-ray absorption fine structure (EXAFS) is the oscillatory part of the X-ray absorption spectrum which is beyond 30 eV of the absorption edge. This part of the spectrum gives the details of the atomic structure also delivers electronic and some vibrational fingerprints (through the Debye-Waller factor) around the absorbing atom. This makes EXAFS a suitable tool to probe materials and helps us to acquire knowledge of local atomic structure in the fields of biology, chemistry, geophysics, materials science, etc. However, extracting structural information is often complicated and not straight forward. To interpret and understand the measured EXAFS spectrum, one has to know the theory of EXAFS.

The first EXAFS theory is formulated based on single-scattering plane wave approximation. This theory relies on the following approximations: the photoelectron is viewed as a plane wave rather than a spherical wave and the atomic radii are much smaller than the interatomic distances. As a result, the theory is valid only for higher k-values ($k > 3$ Å). In this theory, the photoelectron is scattered once before it comes back to the absorbing atom. This simplification allows describing the EXAFS signals which are dominated by single scattering events [97, 98]. The theory was later modified by Rehr and Albers to include the contribution from equivalent multiple scattering paths [99]. The EXAFS Equation $\chi(E)$, is due to the scattering of an outgoing photoelectron from neighbouring atoms and can be written using a phenomenological Equation (3.15):

$$\chi(E) = \frac{\mu(E) - \mu_0(E)}{\Delta\mu_0(E)}, \tag{3.15}$$

where $\mu_0(E)$ is atomic-like background absorption and $\Delta\mu_0(E)$ is the normalization factor which is the net increase in the atomic background absorption edge. The EXAFS function $\chi(E)$, is a summation over all interference patterns scattered from the neighboring atoms around the absorbing atom [99].

$$\chi(k) = \sum_{i=1}^{shells} \frac{N_i}{kR_i^2} S_0^2 F_i(k) e^{-2k^2\sigma_i^2} e^{\frac{-2R_i^2}{\lambda(k)}} \sin(2kR_i - \phi_i(k)) \tag{3.16}$$

$$R_i = R_0 + \Delta R \tag{3.17}$$

$$k = \sqrt{\frac{4\pi m_e}{h^2}(E - E_b)} \tag{3.18}$$

$$\phi_i(k) = 2\phi_{abs}(k) + \phi_{scatter}(k) \tag{3.19}$$

Where N_i contains the coordination number or degeneracy of path, S_0^2 is an amplitude reduction factor representing many-body effects such as central atom shake-up and shake-off due to relaxation processes after the creation of the core hole. E_b is the binding energy and ΔR is the change of the half-path length. σ_i^2 is the mean square displacement which is due to the fluctuations in the path length due to thermal motion or structural disorder (also called Debye-Waller (DW) factor). $F_i(k)$ is the effective backscattering amplitude which is photoelectron specific and primarily responsible for the magnitude of EXAFS signal. $\phi_i(k)$ is effective scattering phase shift which reflects the quantum-mechanical wavelike nature of backscattering. $\lambda(k)$ is the mean-free path and R_0 is the initial path length [100].

The exponential term which contains the mean-free path of the photoelectrons accounts for the finite lifetime (including core-hole lifetime) of the excited state. This factor is largely responsible for the relatively short range (generally a few tens of Å) in a material probed by EXAFS experiment. The strength of the reflected interfering waves depends on the type, and a number of neighbouring atoms through the backscattering amplitude, F(k) (see Fig.3.7(a)), and hence is primarily responsible for the magnitude of the EXAFS signal.

The formula shown in Eq.(3.16) consists of two parts, the amplitude and sine function describing the interference pattern. As shown in Fig.3.8 the EXAFS oscillations are originated from constructive and destructive interference between the outgoing and backscattered waves. The EXAFS oscillation gives information about the local structure around the absorbing atom such as coordination number, and bond distances[101]. XANES part of the spectrum is dominated by multiple scat-

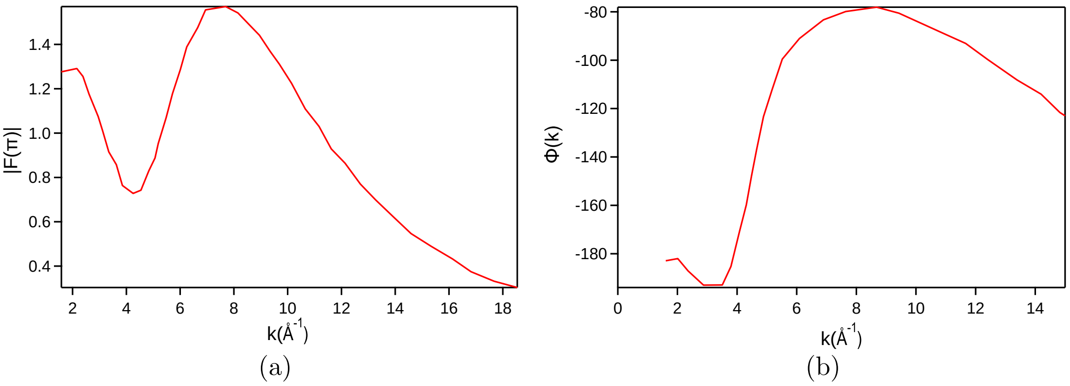

Figure 3.7.: (a) Dependence of effective backscattering amplitude F(k) on the photoelectron wavevector for a plane wave approximation. (b) Dependence of the phase on the photoelectron wavevector ϕ(k) for a plane wave approximation. The Figure is adapted from [91].

tering paths while single scattering paths dominate the EXAFS (see Fig.3.8). The XANES part of the spectrum is sensitive also to the coordination number around the absorbing atom, to the bond distance between the absorber and scatterer, bond angles and oxidation state of absorber [10].

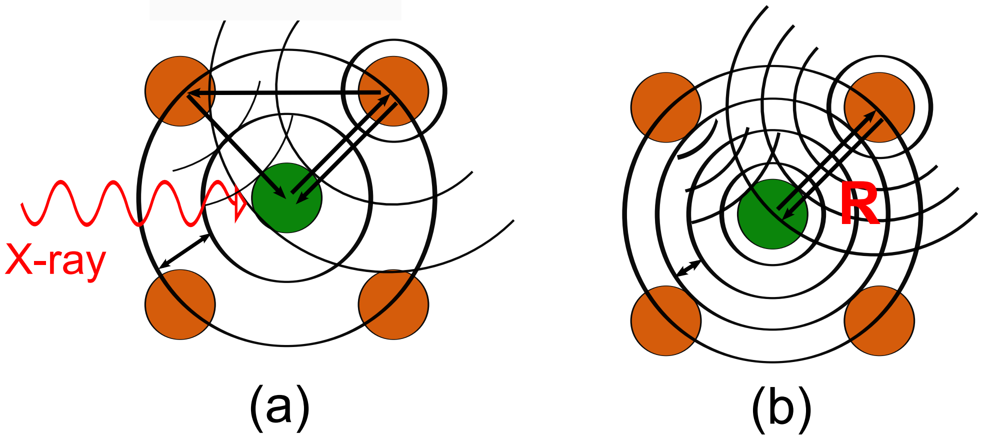

Figure 3.8.: (a) Multiple scattering of an outgoing electron wave from neighboring atoms. The incident X-ray is absorbed by the green atom then the outgoing photoelectron is diffracted first from the top right atom and successively to the top left atom (shown in orange), the successive outgoing spherical wave becomes weaker. (b) Single scattering of a photoelectron from the central atom to the nearest neighbors. It provides information about the bond distance between the nearest neighbors.

3.2.2. Multiple scattering theory

When an atom absorbs an incident X-ray, the photon is annihilated, and a core level electron is excited into a high-lying unoccupied state. As discussed in Sec.3.2, when the energy of the incident X-ray beam is increased, at some point its energy equals the binding energy of a core level electron of one of the atoms. When the incident energy is above the ionisation potential or in the continuum level the probability of the photon to be absorbed increases dramatically. The probability function includes an energy dependent oscillatory part yielding the fine structure which depends on the details of the local electronic and atomic structure in the vicinity of the absorbing atom. The fine structure is analysed to yield structural information about the sample. In a single electron picture the measured X-ray absorption coefficient is proportional to the transition rate given by Fermi's golden rule which is based on the one-electron approximation:

$$\mu(E) \propto \sum_{f}^{E>E_F} |\langle f|\,\hat{\varepsilon}\cdot\overrightarrow{r}\,|i\rangle|^2 \delta(E_f - E_i - h\nu), \tag{3.20}$$

where $\hat{\varepsilon}\cdot\overrightarrow{r}$ is the dipole operator which represents the interaction of an incident X-ray beam with the atom and the summation extends over all energies above the Fermi energy. The initial state $|i\rangle$ can be core-level electrons that are typically 1s, 2s, or 2p states although transitions from higher orbitals are also possible.

There are two different methods to solve Eq.3.20. The first is, to represent accurately both the initial $|i\rangle$ and the final $\langle f|$ states and then explicitly evaluate the integral implied by the Fermi-golden rule. This approach is implemented in Molecular Orbital (MO) theories [102]. This method requires a precise representation of the final state functions.

The second strategy is called multiple scattering (MS) theory which rewrites Eq.3.20 using Green's function [91, 99]. In this method, the potential is described regarding scattering regions with a potential δV and the flat interstitial regions with constant potential V_{int}. As a result the total effective single-electron Hamiltonian can be expressed as $\mathrm{H} = \mathrm{H}_0 + \mathrm{V}_{int} + \delta\mathrm{V}$. Both the spherical potential centred on each atom and a constant value in the interstitial region between the atom are approximated by muffin-tin geometry. Fig.3.9 shows the schematic representation of muffin-tin approximation implemented in FEFF and MXAN ab-initio based computer based programs.

The muffin-tins provide atomic scattering centres that are described entirely by atomic phase shifts, which are calculated from spherically symmetric atomic like potentials inside the muffin tins. Green's function propagators are employed to connect these scattering centres. The propagation of the interacting photoelectron as a quasiparticle with energy E and in the presence of the scattering potential is written by the one-particle Green's function.

$$G(E) = 1/(E - H + i\Gamma) \tag{3.21}$$

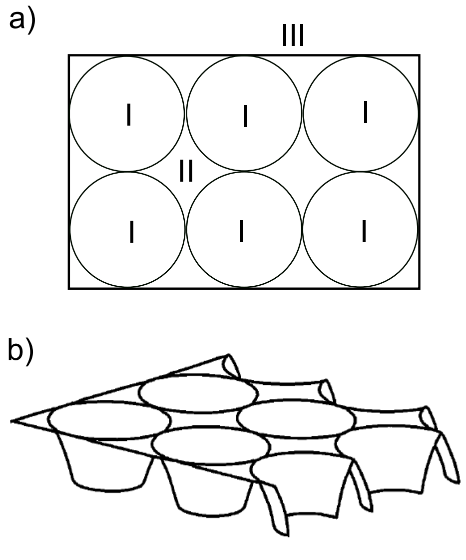

Figure 3.9.: Schematic representation of the muffin-tin potentials. (a) Top view of atoms where region I indicating the atomic potentials, region II flat interstitial regions with constant potential and region III. (b) 3d representation of muffin-tin potentials. Figure b) adapted from [91].

Where $\mathit{\Gamma}$ is the lifetime of a core-hole state including the intrinsic and extrinsic losses [103]. The operator from the Green's function is given by:

$$\sum_{f} |f\rangle G(E) \langle f| = (-1/\pi) Im G(E) \tag{3.22}$$

As a result, Eq.(3.20) can be rewritten by using Eq.(3.22) as:

$$\mu(E) \propto \frac{1}{\pi} Im \langle i|\hat{\varepsilon}^{*} \cdot \overrightarrow{r'} G(r', r; E) \hat{\varepsilon} \cdot \overrightarrow{r} |f\rangle \theta(E - E_F), \tag{3.23}$$

where θ is the Heaviside step function to make sure that the photoelectric cross-section is non-zero only above the Fermi energy E_F. The full one electron propagator G in the presence of the scattering potential is connected with the non-interacting free-electron propagator $G^0 = 1/(E - H_0 + i\mathit{\Gamma})$ by means of the Dyson equation $G = G^0 + G^0\ T\ G^0 + ...$, where $T = V + VG(E)T$ is the full atomic scattering matrix[104]. The T matrix can be expanded regarding single site scattering matrices t as $T = t + tG^0t + tG^0tG^0t + ...$ these allow us to express the interacting propagator as a geometric series:

$$G = G^0 + G^0 t G^0 + G^0 t G^0 t G^0 + ... = G^0 (1 - G^0 t)^{-1} \tag{3.24}$$

The Multiple scattering fine structures can then be obtained by taking an appropriate trace over the matrix elements in G for the XANES spectrum, and it includes the absorbing atom and the angular momentum of the photoelectron of the final state [105]. Each term in Eq.(3.24) describes the order of scattering. As an example the term G^0tG^0 describes all the possible single scattering paths. Whereas, $G^0tG^0tG^0$ describes double scattering paths. This implies that Eq.(3.24) contains all the contribution from all orders of scattering paths. An example of some of the possible scattering paths is schematically shown in Fig.3.10. Since Eq.(3.24) calculates all the possible scattering paths, it is called full multiple scattering (FMS). As a result, full multiple scattering calculations are computationally expensive. The size of the matrices of G^0 and t are determined by the number of atoms, angular momenta, and magnetic quantum numbers, $l = \{l, m\}$ required for each atom. For the i^{th} atom the number of angular momenta results in $l = l_{max}(l_{max}+1)$ and therefore the size of the matrix yields $\sum_i l_{max}(l_{max}+1)$. The l_{max} is reasonably limited by centrifugal barrier, $l_{max} \backsimeq kR_{MT}$, where k is the number of photoelectrons and R_{MT} is the muffin tin radius of the atoms [106, 107]. The most commonly used value of $l_{max} = 3$ results in $l = 12$. As the matrices of G^0 and t becomes higher which also increases computation time.

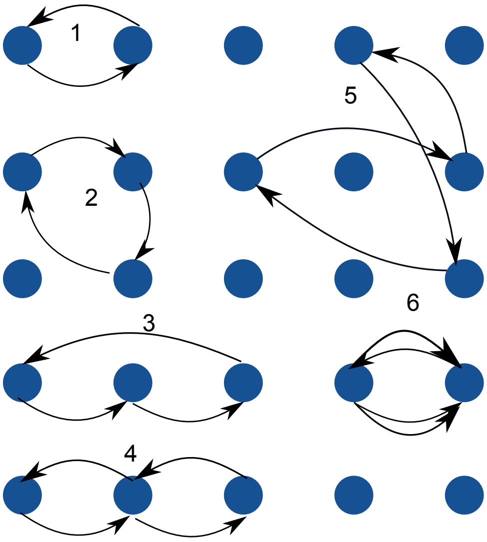

Figure 3.10.: Schematic representation of plain of atoms with various kinds of scattering paths. Path 1 is a single scattering path with two legs. Paths 2 and 3 are an example of double scattering paths with three legs. Paths 4, 5, and 6 are an example of triple scattering paths with four legs.

3.2.3. Theoretical XAS spectrum calculation

Nowadays there are various computer programs which are ab-initio based software to calculated XAS (i.e. XANES and EXAFS), and XES spectra of atoms and molecules. Some examples are TT-multiplets a MATLAB based code developed by Frank de Groot used to calculate XAS of K-, L-, and M-edges and XES spectra

[93]. FEFF 9.0 is a computer program for ab initio multiple scattering calculations of XAS (EXAFS and XANES) spectra for atoms or molecules [91]. ORCA is also an ab-initio based computer program for calculating XAS (pre-edge region), XES, UV-vis spectra calculation for atoms and molecules [108]. There are also other computer based programs such as ADF, Gaussian, MXAN, Quantum ESPRESSO and others [109]. However, this thesis FEFF for EXAFS and XANES spectra calculations and ORCA for pre-edge and XES spectra calculation of molecules are used. For this reason, only the description of FEFF and ORCA is included.

FEFF

FEFF 9.0 uses an *ab initio* self-consistent multiple scattering approaches including polarisation dependence, core-hole effects, and local field corrections based on self-consistent spherical muffin-tin scattering potentials. XAS spectra calculation is based on all-electron real space relativistic Green's function formalism with no symmetry requirements. The code includes both inelastic losses and vibrational effects regarding GW self-energy and correlated Debye-Waller factors, respectively. FEFF starts the calculation of XAS spectrum with potentials followed by scattering phase shifts. The scattering path and phase shifts are then used to calculate the scattering amplitudes using an explicit enumeration and summation for the EXAFS part and using implicit summation for XANES region. The FEFF program is controlled by a set of input cards which are user defined and can be set in the input file ”feff.inp” (see Appendix A). The code yields scattering amplitudes and phases used in many modern EXAFS analysis codes, as well as various other properties.

ORCA

ORCA is an *ab initio* approach that uses density functional theory (DFT) based on a semi-empirical self-consistent field molecular orbital picture. It can be used to calculate both X-ray absorption and emission spectra. The XAS spectra calculation in ORCA is based on Fermi's golden rule described in Eq.(3.20). Calculation of XAS spectra in ORCA requires the final state wave function, and Molecular-orbital DFT approach is used to calculate the final state. Similar to FEFF, ORCA-based calculations are controlled by a set of input parameters which are placed before the XYZ atomic coordinates and define the outcome of the calculation (see Appendix B). An advantage of ORCA over FEFF is for transition metal complexes such as ferrocyanide and ferricyanide in aqueous solution solvent effects can be considered effectively by the COSMO solvation model.

3.2.4. Time dependent density functional theory (TD-DFT)

In this thesis, the Fe K-edge XAS pre-edge features are calculated using TD-DFT approach implemented in the ORCA quantum chemistry package [110]. This region of the XAS spectrum is a powerful probe of the electronic and geometric structure of iron sites in inorganic transition metal complexes [111, 112, 113, 114, 115]. First, the ground state and excited state geometries are optimised with the B3LYP hybrid functional. Then the pre-edge XAS calculations were performed allowing only excitations from the Fe-1s core orbitals. For the calculations B3LYP (B3LYP with a hybrid functional with 15% exact exchange contribution) was used [116] in a combination of def2-TZVP [117] basis set. Calculations were carried out in a dielectric continuum using the conductor-like screening model in an infinite dielectric[118].

In Section 3.2 the XANES spectra for ferro and ferricyanide molecules measured in aqueous solution is reported. The spectrum of $[\mathrm{Fe^{II}(CN)_6}]^{4-}$ shows two pre-edge peaks at 7114.09 eV and at 7116.83 eV, according to DeBeer *et al.* [114] the first peak is due to the $1\,\mathrm{s} \rightarrow \mathrm{e_g}$ transition and the second peak due to a $1\,\mathrm{s} \rightarrow \pi^*$ transition or charge transfer from the 1s core to the π^* ligand orbitals. $[\mathrm{Fe^{III}(CN)_6}]^{3-}$ shows three peaks at 7111.3 eV, 7114.39 eV and 7118.91 eV, since $[\mathrm{Fe^{III}(CN)_6}]^{3-}$ has one open orbital in the t_{2g} d orbital the first peak is a transition from $1\,\mathrm{s} \rightarrow \mathrm{t_{2g}}$. The second peak is a transition from 1s core to the open e_g orbitals ($1\,\mathrm{s} \rightarrow \mathrm{e_g}$) and the third peak is assigned to a transition from 1s to π^* ligand orbitals. In Fig.3.11 theoretically simulated TD-DFT spectra is shown in comparison with the measured experimental data. With the level of DFT functional used all the experimentally observed pre-edge peaks are reproduced.

Table 3.1.: DFT optimized structural parameters for ferro and ferricyanide complexes used for TD-DFT pre-edge calculation shown in Fig. 3.11.

	$[\mathrm{Fe(CN)_6}]^{4-}$	$[\mathrm{Fe(CN)_6}]^{3-}$
Fe-C (Å)	1.970	1.918
C≡N (Å)	1.191	1.207
Fe Ox. state	+2	+3

As discussed in the proceeding section, upon photoexcitation of ferrocyanide molecule with 355 nm laser, it undergoes a ligand exchange mechanism, where one cyanide ($\mathrm{CN^-}$) ligand is replaced by a water molecule. If the ligand exchange mechanism happens through a complete dissociation, it results in a pentacoordinated complex either with square pyramidal C_{4V} or trigonal bipyramidal D_{3h} symmetries. The geometries of these possible intermediate states are optimised in ORCA, and structural parameters are summarised in Tab.3.2. The pre-edge calculations of all the possible intermediate states are reported in Fig. 3.2.4. The low energy pre-edge peaks of both the possible pentacoordinated complexes are red-shifted compared to the photoaquated complex. In later Chapter, this result will be used to interpret the femtosecond XANES data measured at SACLA, XFEL facility.

In Section 3.2 the XANES spectrum of the $[\mathrm{Fe(terpy)_2}]^{2+}$ molecule measured in aqueous solution is reported. In addition to the red shift of the excited state spectrum, new pre-edge peaks are observed which does not exist in the ground state spectrum. Figure 3.13 shows experimentally measured data of the ground

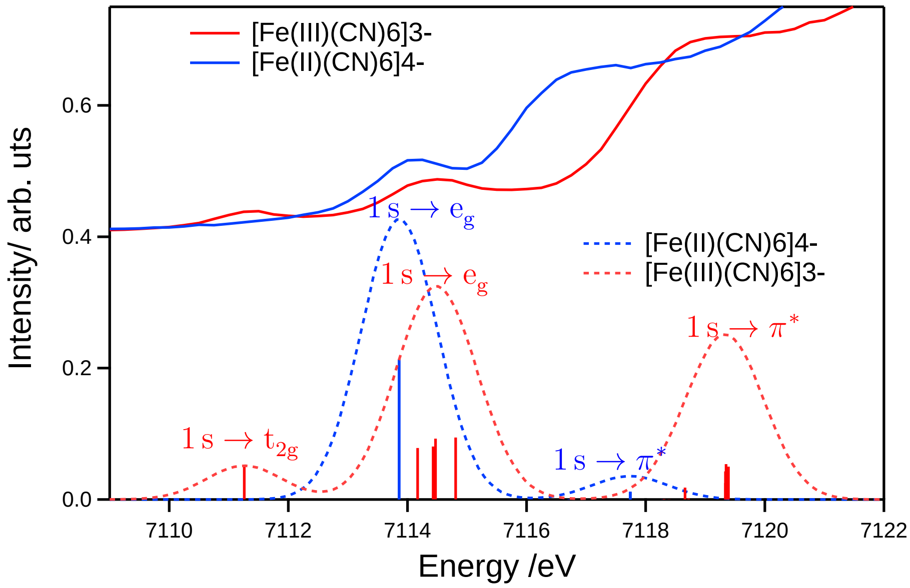

Figure 3.11.: Solid lines represent the experimental data which is a zoom in the pre-edge region of the Figure shown in 3.6(a). Dotted lines shown are TD-DFT calculated spectra for ferricyanide (red), ferrocyanide (blue). The calculation is done with B3LYP hybrid function in combination with def2-TZVP basis set and the calculated transitions shown in sticks are broaden by 1.5 eV. After the spectrum is calculated a constant shift of 160 eV is applied to all the calculated spectra. Assignment of calculated peaks has also been discussed in previous studies [114].

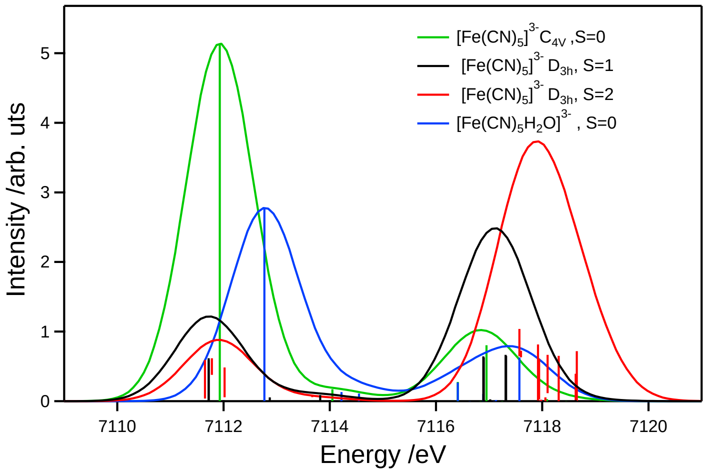

Figure 3.12.: Calculated pre-edge spectra for the possible intermediate states of ferrocyanide molecule formed after photoexcitation. All the calculated spectra are shifted by 160 eV and 1.5 eV broadening is applied.

Table 3.2.: DFT optimized structural parameters for pentacoordinated and photoaquated complexes used for TD-DFT pre-edge calculation shown in Fig.3.2.4. Where ax = axial and eq = equatorial atoms.

	$[Fe(CN)_5]^{3-}$	$[Fe(CN)_5]^{3-}$	$[Fe(CN)_5]^{3-}$	$[Fe(CN)_5(H_2O)]^{3-}$
Symmetry	C_{4V}	D_{3h}	D_{3h}	Dist. O_h
Fe-C (Å)	1.852^{ax}	1.992^{ax}	2.392^{ax}	1.842^{ax}
	1.944^{eq}	2.101^{eq}	2.231^{eq}	1.910^{eq}
C≡N(Å)	1.190^{ax}	1.173^{ax}	1.172^{ax}	1.187^{ax}
	1.187^{eq}	1.172^{eq}	1.169^{eq}	1.185^{eq}
Fe−O(Å)				2.189
Fe Ox. state	+2	+2	+2	+2
Spin state(S)	0	1	2	0

and excited state spectra including the TD-DFT calculated pre-edge peaks using DFT optimised atomic coordinates.

Table 3.3.: DFT optimized structural parameters for ground state (LS) and for the two possible high spin excited states of $^5B_2$, ^5E. Where α is the bite angle between the two nitrogen atoms in the equatorial plane (See Fig.2.13).

	LS	$^5B_2$	^5E
Fe-N (Å)	1.889^{ax}	$2.160\ ^{ax}$	2.107^{ax}
	1.984^{eq}	2.191^{eq}	2.203^{eq}
$\alpha(°)$	161.92	147.68	149.99

To compare the experimental measured XAS data with simulated spectra, the experimental data is deconvoluted. The result of the deconvolution is reported in Tab.3.4. First, the edge is fitted using an arctangent function which is indicated by red dashed line then three pseudo-Voigt profiles centred at different positions are used to have a reasonable fit of the ground state spectrum (see Fig. 3.14(a)). Similarly, an arctangent function is used for the edge and three pseudo-Voigt profiles to get the fit shown in Fig.3.14(b). The goal of this analysis is to assign the possible excited state among the two candidates predicted by DFT i.e. ^5E and $^5B_2$. From the experimental reconstructed excited state data, peak 1, peak 2 and peak 3 are obtained at 7112.15 eV, 7113.89 eV and 7115.8 eV as peak positions respectively. For simulated ^5E state peak 1, peak 2 and peak 3 are obtained at 7111.9 eV, 7113.1 eV and 7115.1 eV peak positions respectively. Whereas for $^5B_2$ state peak 1, peak 2 and peak 3 are obtained at 7112 eV, 7115 eV and 7117 eV peak positions respectively. Comparing the peak positions it is ambiguous to conclude whether the possible excited state is ^5E or $^5B_2$. For this reason, a full structural EXAFS analysis is necessary by fitting directly the transient EXAFS spectrum and the result of this analysis will be presented in Chapter 8.

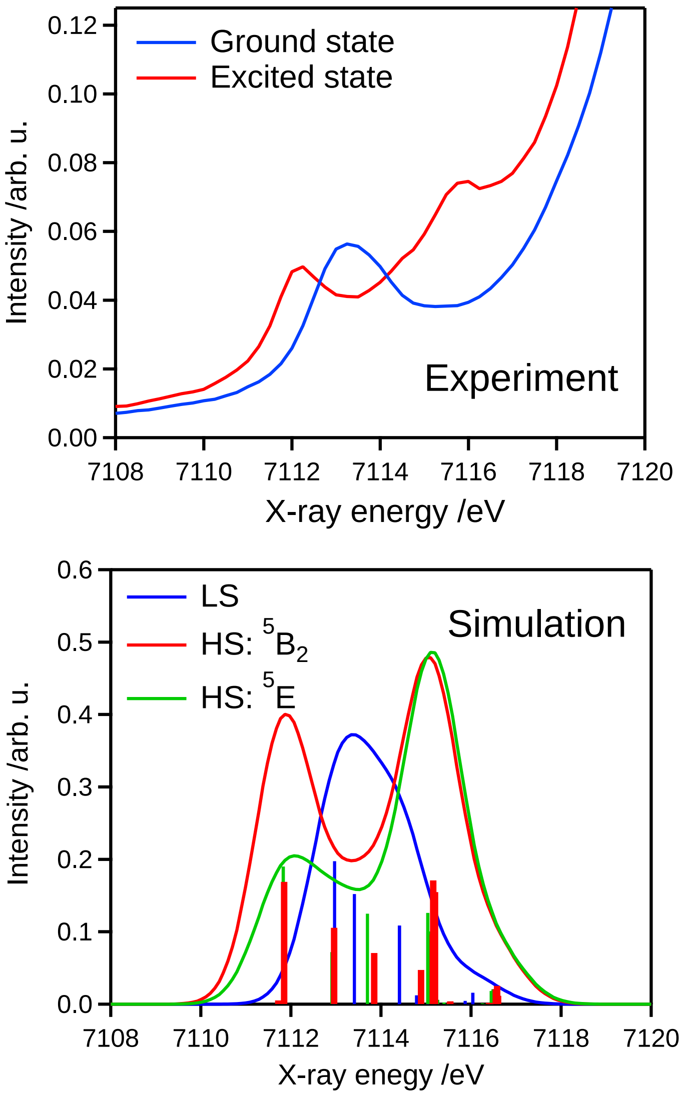

Figure 3.13.: Solid lines are the zoom around the pre-edge region of XAS spectra shown in Figure 3.6(b). Dashed lines are calculated spectra for the ground and the two possible excited states of $[\mathrm{Fe(terpy)_2}]^{2+}$ molecule. Calculations are done using ORCA with B3LYP hybrid function in combination of def2-TZVP basis set, and calculated transitions broaden with 1.5 eV and a constant shift of 160.2 eV for the ground state (LS) and 159.2 eV for the excited state spectra. Sticks are the possible transitions calculated before broadening. Some of the important structural parameters are summarised in Tab.3.3.

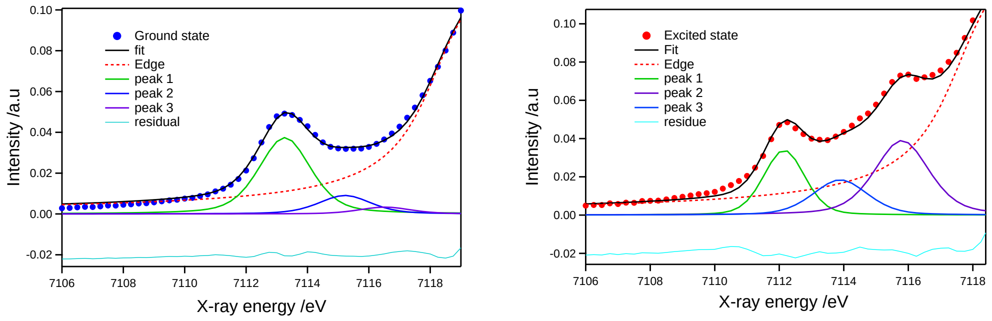

(a) (b)

Figure 3.14.: (a) Convoluted pre-edge peak fit for the ground state XAS spectra measured on $[Fe(terpy)_2]^{2+}$ molecule. Ground state spectrum (blue dots), arctangent, used to fit the edge (red dash line) and three pseudo-Voigt peaks to represent the different transitions. The fit is a convolution of the edge and the three peaks. (b) Convoluted pre-edge peak fit for the reconstructed excited state XAS spectra measured on $[Fe(terpy)_2]^{2+}$ molecule after 100 ps of 532 nm laser excitation. Excited state spectrum (red dots), arctangent, used to fit the edge (red dash line) and three pseudo-Voigt peaks to represent the different transitions. The fit is a convolution of the edge and the three peaks.

Table 3.4.: Summary of data extracted after deconvolution of the experimental and simulated spectra. Where LS and ES stands for low spin state and excited state respectively. *the unit for peak Area is eV units.

Experimental results

	Peak 1		**Peak 2**		**Peak 3**	
	Position (eV)	Area (*)	Position (eV)	Area (*)	Position(eV)	Area (*)
LS	7113.26	9.5x10^{-2}	7115.22	2.3x10^{-2}	7116.52	9x10^{-3}
ES	7112.15	6x10^{-2}	7113.89	4.5x10^{-2}	7115.8	9.9x10^{-2}

ORCA Simulation results

	Position (eV)	Area (*)	Position (eV)	Area (*)	Position(eV)	Area (*)
LS	7113.2	0.573	7114.5	0.425	7115.7	0.023
^5E	7111.9	0.275	7113.1	0.153	7115.1	1.07
$^5B_2$	7112	0.678	7115	1.33	7117.5	0.174

3.3. Relaxation process

In the preceding Section, photoionization of an atom due to an incident X-ray photon and the transition which is governed by Fermi's golden rule was presented [119]. As shown in Fig.3.15 the core-hole resulted from excitation to the higher level results relaxation of the energy levels due to the new effective nuclear charge. Through the uncertainty principle, any state has a finite lifetime (width), and it can be described very well with a Lorentzian line shape. The core-hole lifetime of an atom is in the order of few eV (or few femtoseconds). For example the 1s core-hole lifetime of iron (Fe) atom is 1.25 eV [120]. As a result of this finite lifetime, an excited atom relaxes through either fluorescence emission of an X-ray photon (see next section) or Auger processes through emission of an electron [90]. Tab.3.5 shows the absorption and the different fluorescence emission lines with the corresponding width.

Table 3.5.: Summary of the X-ray absorption and emission energies with the corresponding natural line widths of Iron atom [121].

K-shell series					
	absorption (eV)	**emission lines (eV)**			
		Kα_1	Kα_2	K$\beta_{1,3}$	K$\beta_{2,5}$
	7112	6404	6391	7058	7105
width (eV)	1.25	1.61	1.62		

Fluorescence transition occurs when higher-lying electrons fall into a lower-lying orbital and emit photons as radiative transitions. Auger transition occurs when the core-hole is filled with a shallow core electron; as a result, another core electron is emitted. Auger transition is a two-electron non-radiative process. The kinetic energy of the electron excited in an Auger decay is the difference between the energy level of the first core hole and energy level of the second electron [93]. These two described decay processes are competing processes [121]. For shallow core-hole Auger decay is the dominant process and has many advantages in atomic and molecular spectroscopy. This thesis will focus only the different fluorescence X-ray emission processes.

3.3.1. X-ray emission spectroscopy

The core-hole created by absorption of a photon has a finite lifetime. One way of the decay process is when the core-hole is filled with an electron from the outer shell and as a result, a photon is emitted. The emitted photon has an energy equal to the difference between the energy level of the outer electron and 1s energy level. The transition is *dipole allowed* when the electron originates from 2p or 3p level and

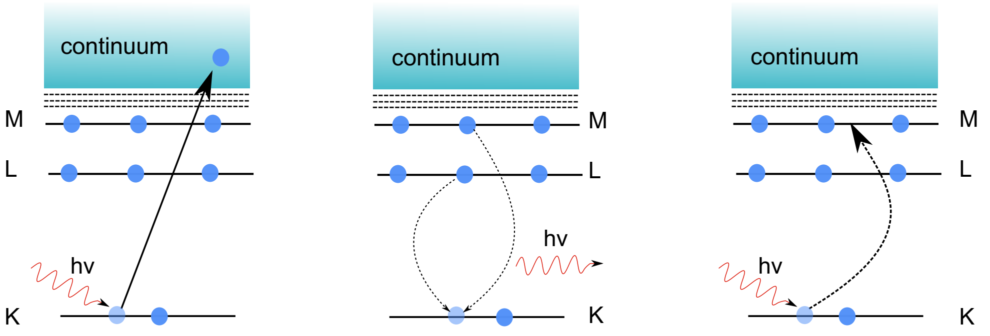

a) Photoionization b) X-ray emission c) Bound-bound transition

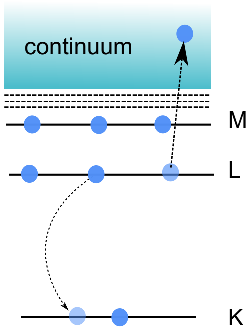

d) Auger decay

Figure 3.15.: A simplified illustration of: a) the photoionization process due to an incident X-ray photon. b) The relaxation of a photoexcited atom and subsequent relaxation through X-ray emission. c) Bound-bound transition when the incident energy is enough to excite the core electron to higher level empty state. d) The Auger process which occurs when an outer core electron fills the core-hole and as a result, another core electron is emitted.

dipole forbidden or *quadrapole allowed* if the electron originates from 3d to 1s level. The Kα fluorescence line results from the 2p to 1s transition. The Kβ fluorescence line results from the 3p to 1s transition and K$\beta_{2,5}$ fluorescence line results from 3d to 1s transition. The most probable emission line after the 1s core-hole creation is the Kα fluorescence emission. It is eight stronger than the Kβ and 100-500 times stronger than the K$\beta_{2,5}$ fluorescence.

The spectral line shapes of Kα and Kβ fluorescence lines are sensitive to the dipole moment in the 3d orbital due to an overlap between the 2p, 3p with 3d wave functions [102]. As a result, the emission line spectra are sensitive to the metal oxidation and spin state as well as the local geometry. The ratio between the intensities of Kα and Kβ has been used to estimate the electrons occupancy of 3d complexes [123, 124]. A detailed discussion can be found in references [90, 93, 125, 126]. X-ray emission experimental results reported in this thesis were measured at the *Advanced Photon Source (APS)* 7ID-D beamline in Chicago, USA

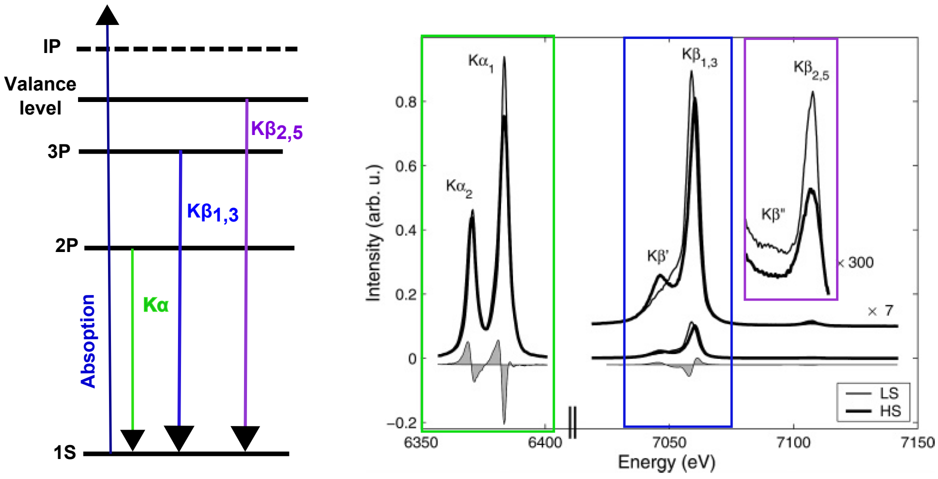

(a) (b)

Figure 3.16.: A simplified illustration of photoionization and relaxation processes after core-hole creation. (a) Shows absorption and the subsequent fluorescence X-ray emission lines when the empty core-hole is filled by an electron from the higher level. (b) Kα, Kβ and valence-to-core emission spectra recorded on [Fe^{II}(phen)$_2$(NCS)$_2$] (phen = 1,10-phenantroline) sample, high-spin (HS) and low-spin (LS) states are achieved by changing the temperature of the sample. The LS and HS are achieved at 80 K and 300 K respectively. Figure (b) is adapted from [122].

and the experimental setups used for the measurement will be discussed in Chapter 4.

Kα emission lines

Due to the spin-orbit coupling, the Kα fluorescence emission consists of two spectral features Kα_1 and Kα_2. The Kα_1 is the transition from the 2p$_{3/2}$ to 1s, and Kα_2 is from the 2p$_{1/2}$ to 1s state. The relative intensities $I_{K\alpha_1}/I_{K\alpha_2} \sim 2$ is determined by the occupancies of the 2p$_{1/2}$ and 2p$_{3/2}$ orbitals [127]. The spectral line shape of Kα_1 fluorescence emission line is proportional to the number of unpaired 3d electrons and can be explained by multiplet theory by neglecting the angular momentum. Therefore, the spectral line shape is solely determined by the (2p,3d) exchange interaction. Based on the work by Kawai *et. al.*[128] the exchange interaction is proportional to the nominal unpaired 3d electrons. As a result, the FWHM of Kα_1 is proportional to the net electron spin or the number of unpaired electrons. With the two approximations; i.e. the 3d angular momentum is zero and energy splitting arises from the exchange interaction between the 2p core-hole and 3d electrons which are set to be proportional to the nominal number of unpaired electrons. The theory works well for octahedral transition metal complexes, such as $[\mathrm{Fe^{II}(CN)_6}]^{4-}$ and $[\mathrm{Fe(CN)_6}]^{3-}$. However, for iron oxides, it does not work at all [128] because it does not include effects of different geometry of complexes which could also contribute to the line shape. A recent study by Vanko *et al.* [122] shows that the linear proportionality between the effective number of unpaired electrons and FWHM Kα_1 works very well for spin-cross over complexes.

Kβ emission lines

Similar to the Kα, the Kβ fluorescence emission spectrum consists of two peaks split by the exchange interaction. The first one is main Kβ (K$\beta_{1,3}$) and the second one which is located in the lower energy part of the spectrum is the Kβ' satellite peak [129]. For iron based transition metal complexes both the main Kβ and the satellite peak shows chemical dependence like the Kα fluorescence emission spectrum. As described in [130], the ~1 eV blue shift of the $K\beta_{1,3}$ peak of $[\mathrm{Fe^{III}(CN)_6}]^{3-}$ with respect to $[\mathrm{Fe^{II}(CN)_6}]^{4-}$ shows sensitivity to the change in oxidation state of the metal center (see Fig.3.17). The intensity of the $K\beta_{1,3}$ shifts to the satellite peak, as a result, the Kβ' peak intensity increases.

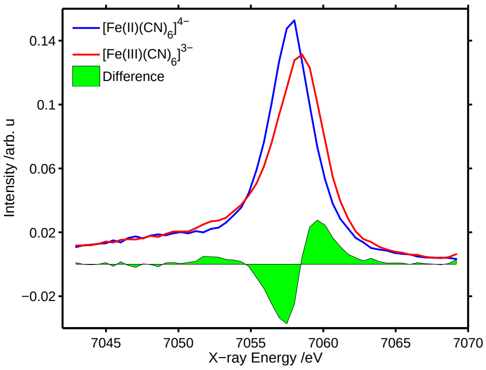

Figure 3.17.: K$\beta_{1,3}$ emission spectra measured for 0.4 M aqueous solution of ferricyanide (red), ferrocyanide (blue) and the difference between the two spectra (green).

In the case of iron-based spin-cross over complexes as described in papers [74, 131] the K$\beta_{1,3}$ peak shifts to the higher fluorescence energy for a higher effective number of unpaired 3d electrons because the exchange splitting is increased (see Fig. 3.18).

Valence-to-core emission line

Valence-to-core (vtc) fluorescence emission spectrum arises from the transition from higher occupied core or valence orbitals to the 1s core-hole. Since the spectrum represents transitions from ligand molecular orbitals, it is sensitive to the metal-ligand bonding character [78, 130]. Vtc XES has two features: the Kβ" which is the weaker and lower in energy part peak which involves a transition of the ligand s

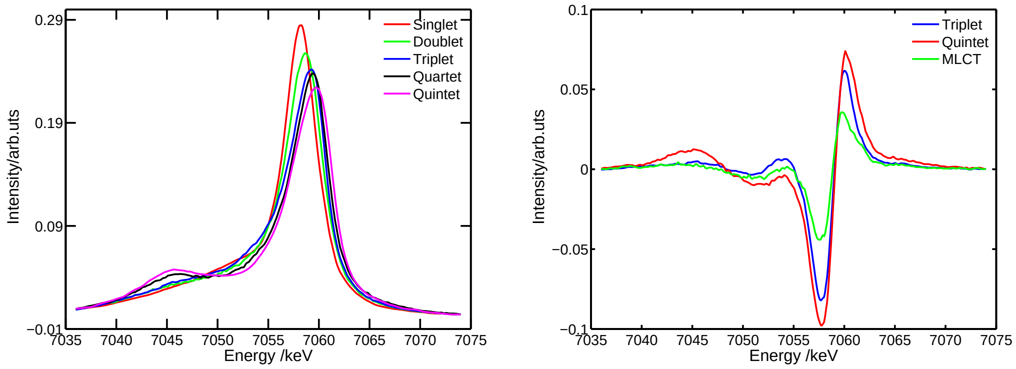

(a) (b)

Figure 3.18.: (a) K$\beta_{1,3}$ fluorescence spectra of ground state iron complexes with different spin moments: singlet $[\mathrm{Fe}^{\mathrm{II}}(\mathrm{bpy})_3]^{2+}$ (red), doublet $[\mathrm{Fe}^{\mathrm{III}}(\mathrm{bpy})_3]^{3+}$ (green), triplet (Fe(II) phthalocyanine (blue), quartet Fe(III) phthalocyanine chloride (black), and quintet $[\mathrm{Fe(phenanthroline)}_2(\mathrm{NCS})_2]$ (magenta). (b) Model difference spectra for the ^{1,3}MLCT, ^{3}T and $^5T_2$ excited states reconstructed by subtracting the singlet model complex spectrum from the doublet, triplet and quintet model spectra shown in Figure 3.18(a). The data is adapted from [13].

molecular orbitals. The second part of the spectrum is K$\beta_{2,5}$ which is stronger and found in the higher energy part. It involves ligand p molecular orbitals. The energy splitting between Kβ" and K$\beta_{2,5}$ peaks is roughly represented by the binding energy difference between the ligand s and p orbitals and these two parts of the spectrum are used to represent ligand identification [132]. Bergmann *et al.* describe that the vtc XES is a powerful tool to discriminate different ligand types [133]. Similarly [134] demonstrated that vtc XES can be used to identify different ligand types in titanium (Ti), iron (Fe) [135], and chromium (Cr) based complexes [136] which is hard to identify in EXAFS. In this spirit, our recent time-resolved vtc XES shows the TR vtc can be a powerful tool to study and identify intermediate states of a chemical reaction [130].

As shown in Figure 3.19 is the K$\beta_{2,5}$ emission line measurements for ferricyanide and ferrocyanide complexes. The result shows a blue shift of the ferricyanide spectrum on ferrocyanide which is similar to what is observed in K$\beta_{1,3}$ emission line.

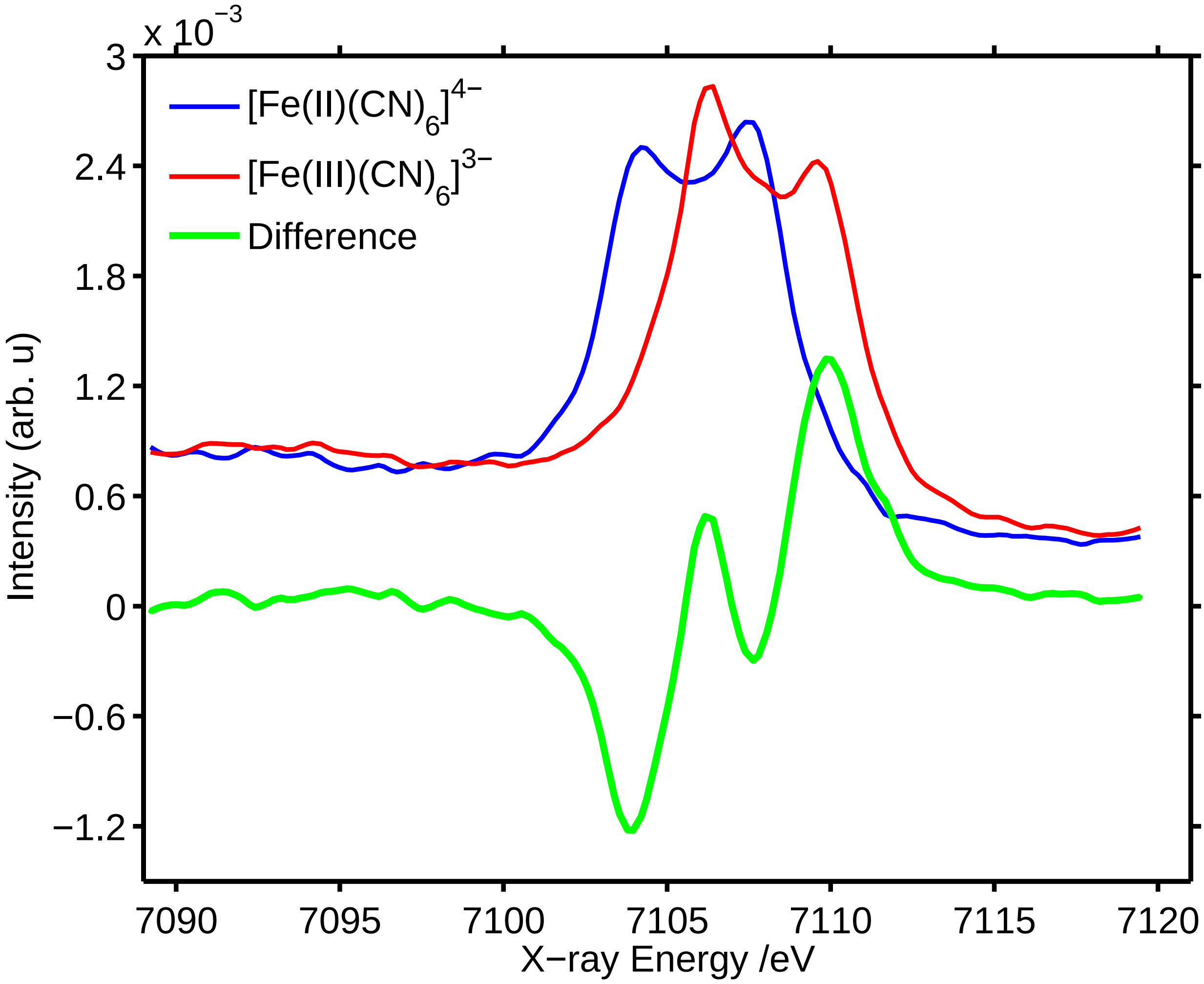

Figure 3.19.: K$\beta_{2,5}$ emission spectra measured for 0.4 M aqueous solution of ferricyanide (red), ferrocyanide (blue) and the difference between these spectra.

Chapter 4

Experimental Setups

This Chapter is dedicated to the description of experimental setups used at both the Advanced Photon Source (APS) and SACLA light sources. The first section starts with a brief introduction of synchrotron radiation, more specifically undulator based synchrotron radiation. Then the APS synchrotron radiation source working principle, timing modes of operation, the high repetition rate laser system and synchronisation used for time-resolved experiments will be presented. Following that, sector 7 beamline including the main beamline components will be described.

The femtosecond resolved XAS and XES data reported are measured at SACLA XFEL facility. For this reason in the second Section, the X-ray Free Electron Laser (XFEL) description more specifically SACLA will be presented. A comparison of the different existing and upcoming XFEL sources will be will also be described. In the third Section, the experimental methodology which combines an arsenal of complementary X-ray tools for structural and electronic studies will be explained. The basic aspects of XAS experiment i.e. transmission and fluorescence yield and the description of XES experimental setup including two different types of spectrometers the Johann and the von Hamos type will also be presented. In the last Sections time-resolved optical-pump X-ray probe setup including the data acquisition systems, the different X-ray detectors and the liquid jet setup used for our measurement will be presented.

4.1. Synchrotron radiation

A typical 3^{rd}-generation synchrotron radiation source is shown in Fig.4.1. It consists of an electron gun, linear accelerator (LINAC), a booster ring, a storage ring, multiple beamlines and End station. First, the electron gun produces electrons from a heated hot cathode which then enters the LINAC. Then electrons are accelerated close to the speed of light with high energy (several MeVs). The electrons are then transferred to the booster ring, where their energy is further increased and finally the electron enter the storage ring. Here electrons are circulated in the storage ring by a series of magnets separated by either straight sections of insertion devices such as undulators, wigglers or bending magnets. Bending magnet use a single magnet to bend the electron bunch, resulting a X-ray radiation around the bend whereas, Wiggers and undulators are periodic magnetic structures force the electron to oscillate due to the Lorentz force and resulting the electron to radiate in a narrow cone along the axial direction.

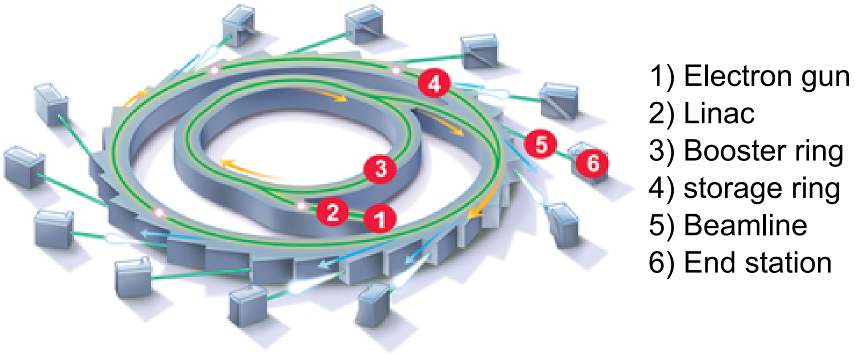

Figure 4.1.: Generic view of a synchrotron radiation source. Adapted from [137].

Compared laboratory based X-rays sources, 3^{rd}-generation synchrotron sources gives many orders of magnitude higher than intensity and brightness [138]. Recently, the 4^{th}-generation X-ray sources are in operation [139, 140] or in the final stages of design and construction phase [141, 142] increase the brightness even further which will be discussed in the next section. The X-ray beams generated in 3^{rd} and 4^{th}-generation sources have the following properties; high brilliance, wide energy spectrum, tunable X-ray energy range, highly polarized and emitted in very short pulses. All these aspects can be represented in single quantity called *Brilliance* [94].

$$Brilliance = \frac{photons/second}{(mrad)^2(mm^2)(0.1\%BW)} \tag{4.1}$$

Where $photons/second$ is the intensity of the monochromatic radiation, $mrad^2$ is the vertical and horizontal angular divergence, mm^2 is the source size and $0.1\%BW$ is the relative bandwidth of the monochromatic radiation in the 0.1%. Brilliance as a function of photon energy produced and is the quantity used to compare the different X-ray sources. Fig.4.2 shows a comparison between the various 3^{rd} and 4^{th} generation X-ray sources. The brilliance of 3^{rd} generation X-ray sources is approximately 10^{10} times higher than those of the laboratory-based X-ray sources.

4.1.1. Undulator radiation

Magnetic structures are common ways to generate synchrotron radiation when a relativistic electrons are accelerated in the magnetic field. There are three types of magnetic structures used to generate synchrotron radiation namely undulator, wiggler, and bending magnet. The later use a single magnet to bend the electron

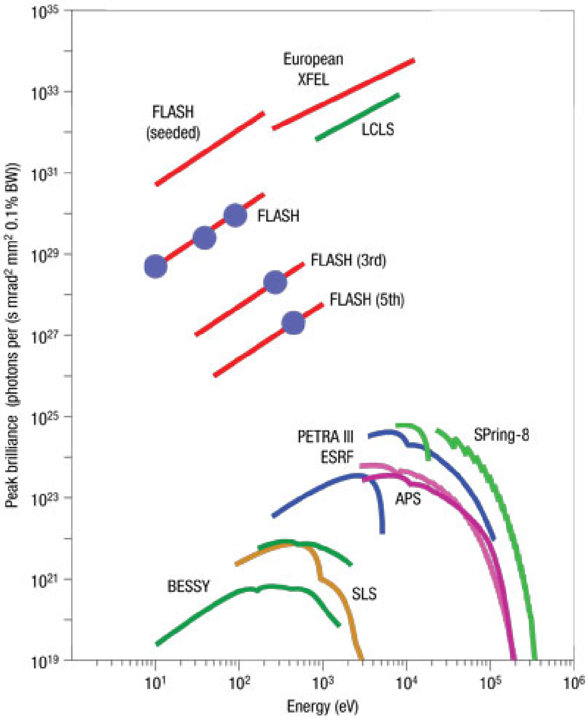

Figure 4.2.: Comparison of various 3^{rd} and 4^{th} generation accelerator-based X-ray sources based on peak spectral brightness (brilliance) as a function of photon energy. Blue points shown in the figure represent measurements. The Figure is adapted from [143].

bunch, resulting a fan of radiation around the bend. Wiggers and undulators are periodic magnetic structures with 2-3 cm gap and inserted in straight sections of the storage ring. The periodicity causes the electrons to experience an oscillation and acceleration due to the Lorentzian force as they move in the axial direction, resulting the electron to radiate in a narrow cone along the axial direction (see Fig.4.3).

The radiation in the forward direction is very intense and highly monochromatic. It is composed of a narrow spectral line at a well-defined frequency and its odd higher harmonics. Even harmonics will be radiated off-axis. The spectrum of an undulator is much narrower compared to other magnetic structures. The radiation wavelength λ of the nth harmonics from an undulator is described by Eq.(4.2).

$$\lambda_n = \frac{\lambda_0}{2n\gamma^2}\left(1 + \frac{K^2}{2} + \gamma^2\theta^2\right) \tag{4.2}$$

and

$$\gamma = \frac{E}{m_e c^2} \tag{4.3}$$

$$K = \frac{eB_u\lambda_0}{2\pi m_e c} = 0.9336 B_u[T]\lambda_0[cm] \tag{4.4}$$

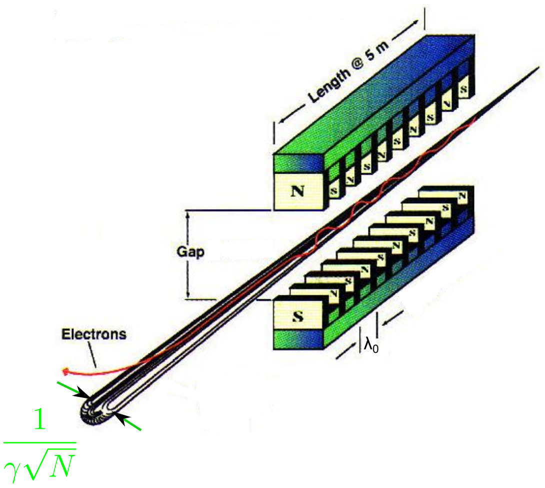

Figure 4.3.: Schematic diagram of undulator insertion device at the APS. The length of the undulator at 7ID is 2.4 m and one period of the magnetic array is 3.3 cm. The picture is adapted from [144].

Where λ_0 is the is the magnetic period and θ is the angle between the undulator axis and the direction of the center of the beam. γ is the Lorentz factor with E the electron energy and K is the undulator parameter. m_e the electron rest mass with e being the elementary charge. B_u is the strength of the magnetic field and c the speed of light in vacuum.

The radiation cone will have an angular divergence of $\theta = \frac{1}{\gamma\sqrt{N}}$, where N is the number of magnetic periods. The relative spectral bandwidth will be proportional to $\frac{1}{\sqrt{N}}$. Increasing the magnetic field and the number of magnetic periods will decrease the central cone angle. The monochromaticity ($\frac{\Delta\lambda}{\lambda}$) of the radiation from an undulator is inversely proportional to the number of magnetic periods and the harmonics index n.

$$\frac{\Delta\omega}{\omega} = \frac{\Delta\lambda}{\lambda} \approx \frac{1}{nN} \tag{4.5}$$

For the fundamental harmonics, n=1, the typical value yields $\frac{\Delta\lambda}{\lambda}$=$10^{-2}$. For the fundamental wavelength (n=1) at θ=0, the radiation wavelength becomes:

$$\lambda_1 = \frac{\lambda_0}{2\gamma^2}\left(1 + \frac{K^2}{2}\right) \tag{4.6}$$

Although the radiation from undulator is highly monochromatic, it is very broad for X-ray absorption and emission spectroscopy experiments. For this reason, the incoming X-ray beam of the undulator is monochromatized further with a double-crystal Si or diamond monochromator which defines the incoming X-ray energy with much narrower relative bandwidth of typical value of 10^{-4}. Tab.4.2 shows comparison of some of the 3^{rd} generation X-ray synchrotron sources.

Table 4.1.: Comparison of different synchrotron radiation sources at dedicated time-resolved end stations. Parameter values reported are adapted from APS [145], ESRF [146] and Petra III [147]. The brightness is calculated as (ph/s.)/(mrad^2.mm^2. 0.1% BW).

Synchrotron / filling pattern	APS / 24 bunch	ESRF/ hybrid	Petra III/ 40-bunch
Electron Energy(GeV)	7	6.03	6
Bunch charge(nC)	0.98	0.7	1.2
nominal current(mA)	100	200	100
Revolution frequency(MHz)	0.272	0.355	5.2
flux (photons/sec)	$3*10^{12}$ at 10 keV	$3.5*10^{11}$	$1*10^{13}$ at 7 keV
Brilliance	$2.3*10^{23}$	$2.3*10^{23}$	$2.3*10^{25}$

4.1.2. Advanced Photon Source (APS)

The APS consist of 5 main components namely the injector, the Booster, the LINAC, the storage ring and experimental halls (see Fig.4.4).

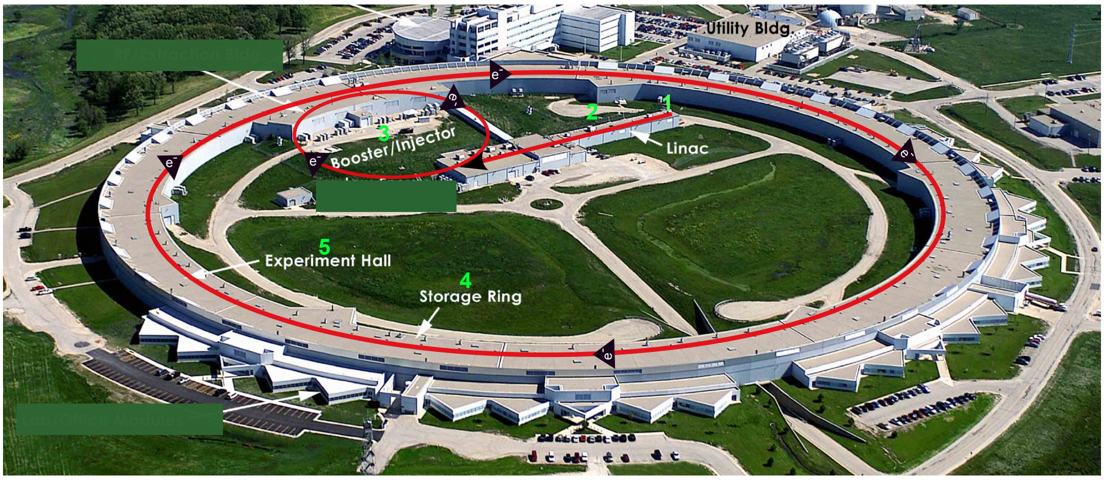

Figure 4.4.: The APS is a 3^{rd}-generation synchrotron radiation source. All the five essential components such as the injector, the Booster, the LINAC, the storage ring and experimental halls are labeled in the figure. The picture is adapted from [144].

The production of X-ray beams at the APS begins with electrons emitted from a cathode. Then the electrons are accelerated by high-voltage alternating electric fields in the LINAC. At this stage the electrons are relativistic, and they are traveling at 99.9999% of the speed of light. Afterwards the electrons are injected into the booster synchrotron and accelerated 7 GeV in one-half second. The accelerating force is supplied by electrical fields in four radio frequency (rf) cavities. To maintain the orbital path of the electrons, bending and focusing magnets increase the electron field strength in synchronization with the rf field. The electrons are then injected into the storage ring [144].

At the APS, the storage ring has 40 identical sectors, each of which consists of accelerator components and five meter long straight sections. Five of these straight sections are reserved for accelerator systems, one is to inject electrons into the ring, and four are dedicated to replenishing the electron energy loss through X-ray generation by using 16 radio-frequency accelerating cavities. The APS has 35 experimental sectors, and each of these can have at least two X-ray beamlines, one originating from a bending magnet in the storage ring lattice, the other from undulator.

4.1.3. Sector 7 beamline

The reported measurements were acquired at the APS sector 7 beamline. This sector consist of three X-ray experimental hutches namely 7ID-B, 7ID-C, and 7ID-D available for a wide variety of experimental setups (see Fig.4.5) and 7ID-A the optics hutch. For our measurements 7ID-D hutch is used which is dedicated to time-resolved X-ray spectroscopy and scattering experiments.

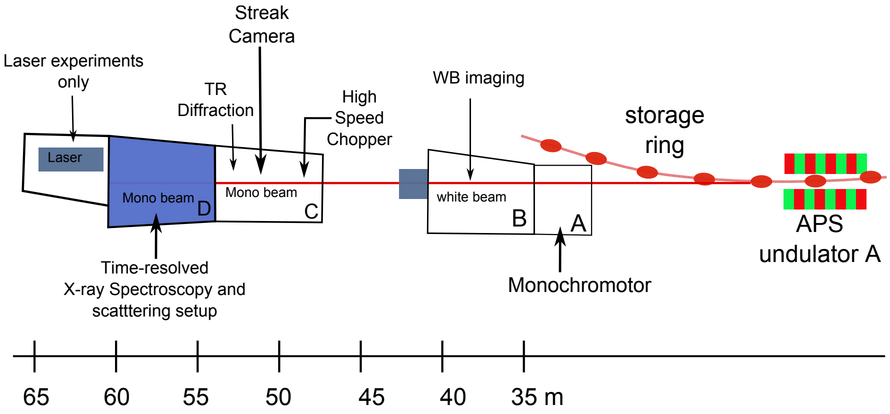

Figure 4.5.: The Sector 7 beamline layout, for the details, see the text below. (white beam(WB) and time-resolved(TR)). The Figure is loosely adapted from [148].

The X-ray source at 7ID is an APS Undulator A with a period of 3.3 cm and a length of 2.4 m [148]. The 7ID-A contains a double-crystal, water-cooled diamond (111) monochromator for delivering X-rays to the 7ID-C and 7ID-D hutches. The X-ray energy can be tuned in the range of 5 to 24 keV (see Fig.4.6) and the flux at 10 keV is 10^{12} photons/second/0.01% bandwidth in hutch D. The energy bandpass of the monochromator is $\Delta E/E$=5.4 x 10^{-5} measured at 9.887 keV. The short focal distance KB(Kirkpatrick and Baez) optics placed half a meter from the sample position allow us to achieve X-ray spot size of VxH= 3.5 x 7 μm^2.

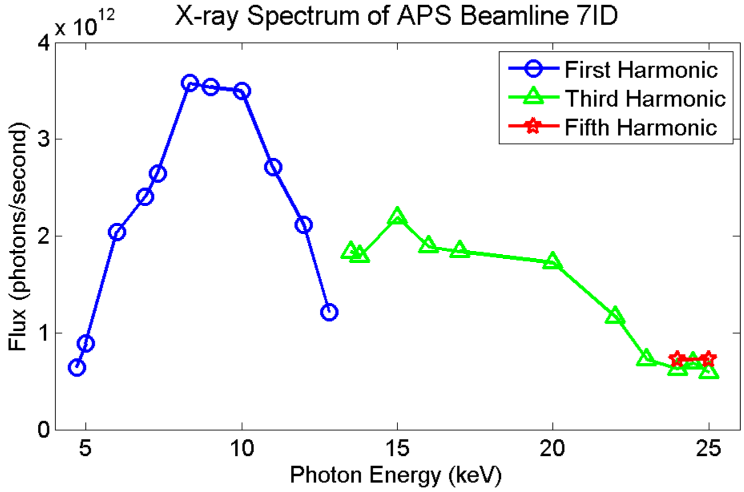

Figure 4.6.: The measured flux of the monochromatic beam on 7ID beamline. Figure adapted from [149].

4.1.4. Timing modes at APS

The timing structure of an X-ray source is an essential ingredient for time-resolved laser pump X-ray probe experiments. At the APS there are three available electron filling modes (see Fig.4.7). The 24-bunch mode has 24 equally spaced X-ray bunches and the time between consecutive bunches is about 153 ns, which makes it ideal for electronic gating and is suitable for time-resolved studies. In this mode, the X-ray pulse duration is about 80 ps [150]. The total current of 100 mA is distributed equally in all the bunches. The second electron filling mode is called the hybrid-singlet mode which consists of a single intense bunch of 16 mA together with a collection of 56 bunches crowded on the opposite side of the ring. There is a space of 1.594 μs before and after the single intense bunch. The X-ray pulse duration in this mode is 120 ps FWHM. The third timing mode is the 324-bunch mode with 11.2 ns between consecutive bunches.

4.1.5. High repetition laser system (DUETTO)

Laser systems with 1 kHz repetition rate have been used for pump-probe experiments at synchrotron facilities [151, 8, 152, 153]. The low repetition rates yields an inefficient use of the available X-ray flux and lead to dramatically longer data acquisition time and it's quality is even further decreased for low concentration liquid samples. At 7ID-D, the above drawback has been overcome by using a high repetition laser from *Time-Bandwidth Products* and single photon counting detectors. The high repetition rate allows us to study a range of complexes at MHz repetition rate. However, the choice of repetition rate depends on the lifetime of the excited state that will be investigated. Low repetition rate for complexes with long excited state lifetime and high repetition rate for complexes with the short excited lifetime.

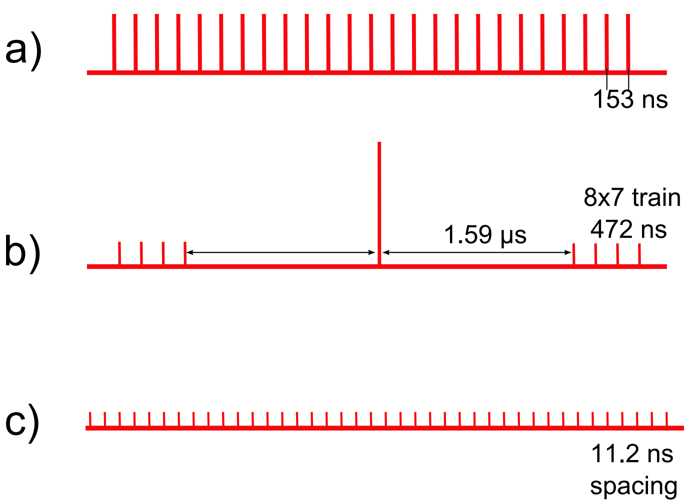

Figure 4.7.: The three available bunch patterns at APS. a) 24-bunch mode with 153 ns gap spacing between consecutive X-ray pulses which permits mechanical and electronic gating to provide variable repetition rate X-rays. b) Hybrid-singlet mode and c) 324-bunch mode.

The high repetition laser system used as a pump laser for the time-resolved measurements reported in this thesis is a customized master oscillator system from a *Time-Bandwidth Products* called Duetto. The central output wavelength is 1064 nm with a variable repetition frequency between 54 kHz and 6.52 MHz and 10 ps pulse duration. The oscillator operates at a customized 78.2 MHz, which is a $2/9^{th}$ of the 352 MHz of the storage ring rf frequency. The repetition rate is selected by specifying the rate at which pulses of the oscillator train are picked for amplification. The laser can operate at a frequency which is a submultiple of the oscillator frequency [150]. The details of harmonic generation are described in ref. [150].

4.1.6. Synchronization and delay control

The synchronization of pump and probe pulses is an integral part of a time-resolved experiment. For an optical pump-probe experiment synchronization is not necessary since both pulses are intrinsically synchronized to each other. However, this is not the case for laser pump and X-ray probe experiments. Therefore, the synchronization and control delays between the laser and X-ray pulses which are implemented at APS 7ID-D beamline will be described. For the detailed of the explanation please refer [150].

The synchronisation of the laser oscillator with the rf frequency of the APS storage ring and the delay control between the laser and X-ray pulses which is achieved electronically is depicted in Fig.4.8. The phase-lock-loop contains a clock synchronizer feedback system which allows the stabilisation of the laser and the X-ray pulses in time. First, the storage ring rf signal is down converted from 352

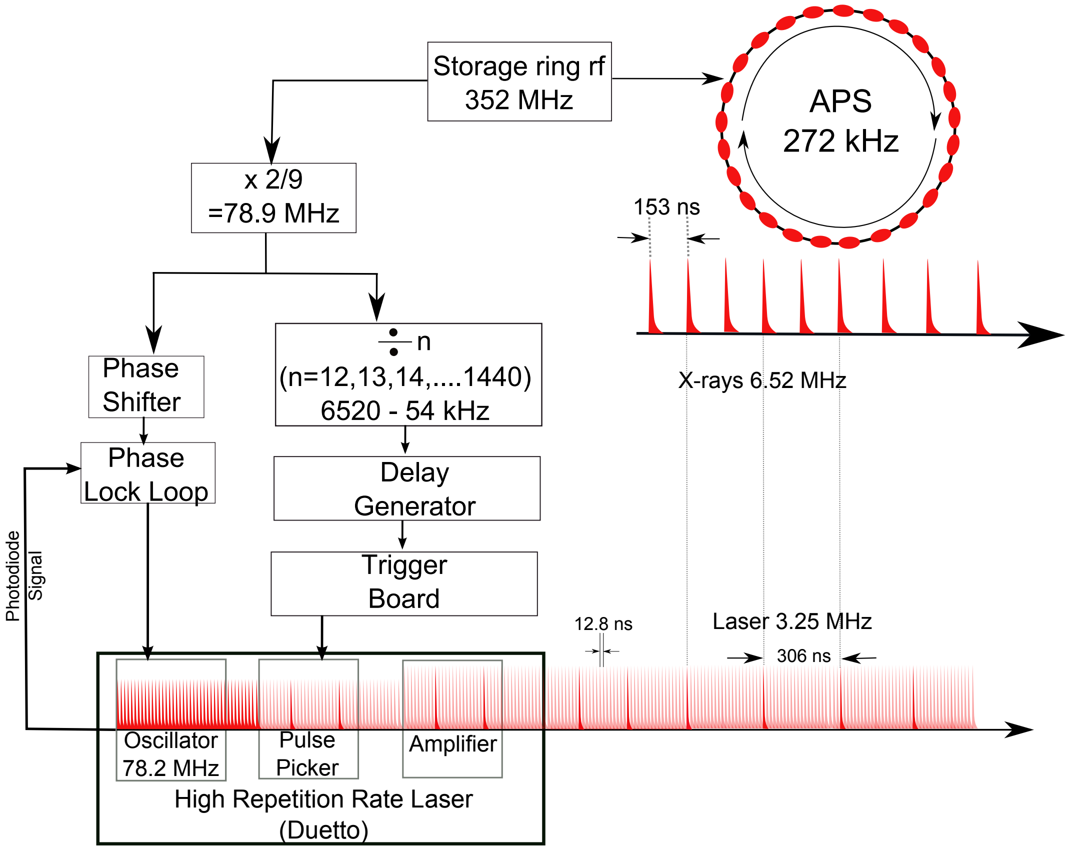

Figure 4.8.: Schematic of the synchronization and delay control of the laser pulses with respect to the X-ray pulses at the APS. The laser shown, is operating at 6.52 MHz (78.2 MHz ÷ 12) to match the X-rays in the standard 24 bunch mode. The red colored pulses separated by 12.8 ns illustrate other oscillator pulses that could be chosen for coarse delay of the laser relative to the X-ray pulses. Figure adapted from [150] (see the text for details).

MHz to 78.2 MHz using a frequency divider circuit. Then the signal is sent through a phase shifter to the laser, where the oscillator cavity length is adjusted by a piezo-actuated cavity mirror mount to lock the frequency of the oscillator. A photodiode signal from the laser oscillator is sent to a phase lock loop to keep the laser in phase to the rf signal. The oscillator pulse-to-pulse timing jitter with respect to the down-converted rf signal is stabilized. The 78.2 MHz signal mentioned above is sent through another frequency divider with a variable integer divisor value. This divided frequency is used to trigger the pulse picker. The divided signal is fed to the pulse picker for amplification. The details of synchronization and delay is described in ref. [150].

4.2. X-ray Free Electron Laser (XFEL)

X-ray free-electron lasers (XFELs) are 4^{th}-generation X-ray sources by offering new exciting features such as extremely short pulses roughly ∼10 fs, large number of photons $\sim 10^2$- 10^3 times higher than synchrotron and coherent X-ray pulses can be focused down to ∼0.1 µm. These properties of XFEL sources will enable us to unravel dynamics of complex molecular structures such as proteins with atomic resolution. Additionally, it will allow us to follow ultrafast chemical reactions with femtosecond time resolution.

An X-ray free electron laser is a device that transforms a beam of high energy electrons which travels at a relativistic speed into an X-ray radiation [154]. The two main components of an X-ray free-electron laser are a high-energy electron beam and undulator magnets (see Fig.4.9) [155].

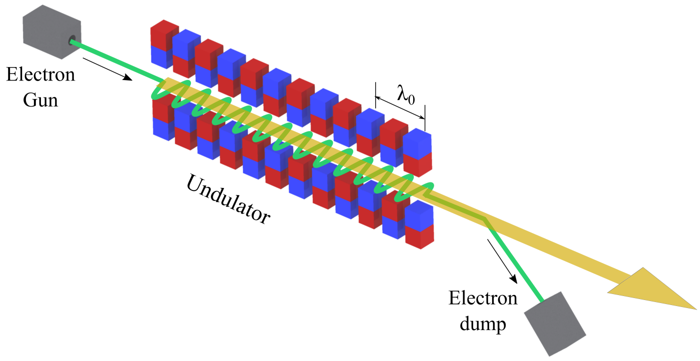

Figure 4.9.: Schematic representation of an undulator, at the core of a free-electron laser.

As the electron travels through an undulator, it experiences a Lorentz force from the magnetic lattice. After a certain distance, the electron also begins to respond to the radiation fields from the other electrons in the bunch. The interaction with the radiation field is spatially modulated with a period equal to the resulting X-ray wavelength, and will hence tend to modulate the electron density within the bunch into micro-bunches (see Fig. 4.10). Once this occurs the radiation enhances itself, as the radiation field increases rapidly as the electrons move downstream. This mechanism is called Self-Amplified Spontaneous Emission (SASE). The radiation field acting on the electrons has to be strong to create micro-bunching. The more localized the electron bunch is the more intense radiation field will be generated. For XFELs, this is solved by a LINAC which enables us to get smaller electron beams in the order of 100 μm in diameter.

The high energetic electrons generated from a photocathode acceleration by RF

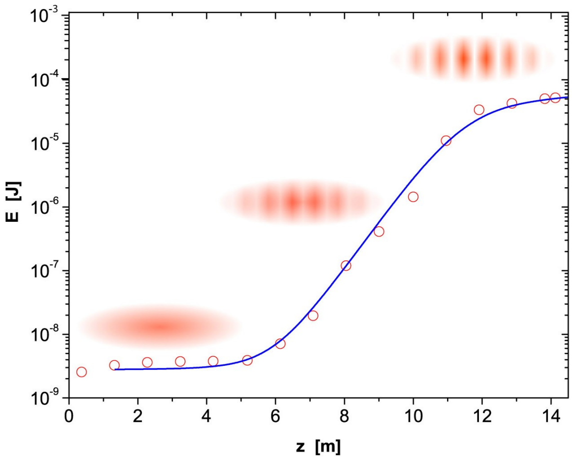

Figure 4.10.: The exponential growth of the FEL pulse energy E as a function of the length z travelled in the undulator. The data (open red circles) were obtained at the first stage of the SASE FEL at DESY; the electron energy was 245 MeV. The solid curve shows the theoretical prediction. The progress of microbunching is indicated schematically. Laser saturation sets in for z $\geq$ 12 m. Here the microbunches are fully developed, and no further increase in laser power can be expected. The depicted figure is the representation of an undulator, at the core of a free-electron laser. The Figure is adapted from [156].

cavities travel through an alternating magnetic field of period λ_0. Due to the magnetic field, the electrons move along an alternating sinusoidal trajectory and emit X-ray radiation in the forward direction with a narrow bandwidth around a resonance wavelength λ. The X-ray generated will have a wavelength λ given by:

$$\lambda = \frac{\lambda_0}{2\gamma^2}\left(1 + \frac{K^2}{2}\right) \tag{4.7}$$

Eq.(4.7) is similar to Eq.(4.2) indicates that increasing the electron beam energy results from a shorter wavelength of X-ray radiation. The emitted X-ray beam depends on the undulator period, the magnetic field strength and the electron beam energy. These quantities can be changed easily which makes FEL devices tunable over a large wavelength range. The cavity free self-amplified spontaneous emission results from intense X-ray generation in a single pass operation. Currently, XFELs which have the capacity of producing X-rays in the hard X-ray regime are LCLS-USA [139] and SACLA-Japan [140] and new ones under construction are European XFEL-Germany [142], SwissFEL-Switzerland [141] and PAL-XFEL-South Korea [157]. The comparison of existing and upcoming XFEL sources is shown in the table 4.2.

Table 4.2.: Comparison of hard X-ray Free-electron Laser sources. * means it is a nominal value, but it can be varied or smaller.

X-ray parameters	European XFEL [142]	LCLS [139]	SwissFEL [141]	SACLA [158]	PAL-XFEL [157]
Max. Electron energy (GeV)	17	14.3	5.8	8.5	10.1
* Bunch charge (nC)	1	1	0.2	0.3	0.2
Wavelength range (nm)	0.05 - 4.7	0.13 - 4.4	0.1 - 7	0.06 - 0.3	0.06 - 10
X-ray energy range (keV)	25 - 0.264	9.5 - 0.282	12.4 - 0.177	20.7 - 4.1	20.7 - 0.124
* FWHM pulse width (fs)	2	541	24	10	60
* Photons per pulse	$2 * 10^{12}$	$1.1 * 10^{12}$	$3.6 * 10^{10}$	$2 * 10^{11}$	$2 * 10^{11}$
X-ray flashes per second	27 000	120	100	60	60
*Photons per second	$5.4 * 10^{16}$	$1.32 * 10^{14}$	$3.6 * 10^{12}$	$1.2 * 10^{13}$	$1.2 * 10^{13}$
*Peak brilliance	$5 * 10^{33}$	$2 * 10^{33}$	$1 * 10^{33}$	$1.3 * 10^{33}$	$1 * 10^{33}$

4.2.1. Spring-8 Angstrom Compact Free Electron Laser (SACLA)

SACLA is one of the X-ray Free-electron laser sources which is currently open for users. X-ray generation at SACLA utilises a compact-scaled accelerator with a short-period undulator. This concept was first tested in the ultraviolet wavelength region before it was implemented at SACLA [159]. At SACLA the SASE undulator is kept in vacuum allowing the magnetic arrays to be placed in precision which yields smaller gap to achieve higher X-ray energies. The generated X-ray energy could be finely tuned by users by changing the parameter K with a precise adjustment of the undulator gap. The X-ray X-ray pulse at SACLA has a nominal X-ray pulse width of 10 fs. Although X-rays from FEL sources have a short pulse duration due to jitter the time resolution for the pump-probe experiment at SACLA was limited to roughly 600 fs at FWHM. To observe dynamics faster than 600 fs a timing tool has to be implemented to overcome to the X-ray jitter problem [160].

4.3. Experimental Layout

To measure a high quality of data, one has to make sure of choosing the right detection method, avoid from using detectors behaving non-linearly, X-ray beam stabilities and to ensure the reproducibility of successive energy scans. The experimental setup used to perform XAS, XES and XDS experiments is shown in Fig.4.11.

X-rays are produced from the APS Undulator A source and passed through a slit before striking the double-crystal monochromator. For XAS measurements, the

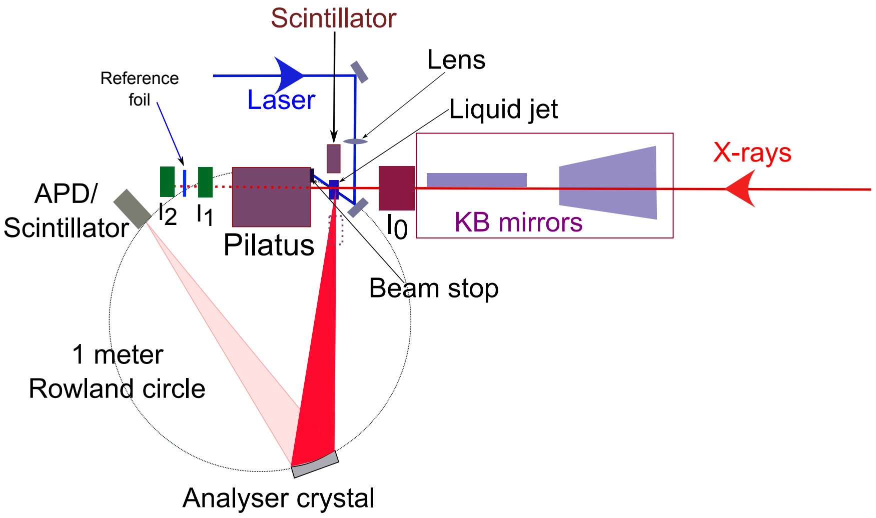

Figure 4.11.: Top view of the experimental setup used at 7ID-D beamline, APS for time-resolved XAS, XES, and XDS measurements. Laser and X-ray beams are focused and overlapped on a fast-flowing 100 µm thick sample sheet, and a Pilatus 100K detector collects scattered X-rays. The emitted X-ray photons are collected either directly by a scintillation detector for XANES using fluorescence detection or by an APD mounted in a 1 m Rowland circle dispersive setup within a He bag for XES measurements.

beam from the undulator is monochromatized and focused by KB mirrors on the sample position. An ion chamber is placed just before the sample to measure the incident X-ray intensity (I_0) used for normalization. For the experiment described in this thesis, the total fluorescence yield detection method is implemented for the XAS measurement. Concomitant to the X-ray absorption process by the sample unresolved Fe Kα and Kβ fluorescence was recorded by NaI scintillation detectors on either side of the liquid-jet (front or back side). The number of molecules in the probed region was $\sim 10^{11}$ and so the number of detected fluorescence photons per X-ray pulse was ~0.02 counts/pulse above the k-edge. The low number of photons allowed for the scintillator detector to be operated in single photon counting mode. In addition to that in front of the scintillator detector, we placed an aperture made of stainless steel with different sizes to avoid saturation of the detector. The scintillator detectors are placed orthogonal to the incoming X-ray beam to minimize the elastic scattering background measured by the detector. Aluminized mylar foil was used to block the scattered laser radiation from the sample. For each scan, an energy calibration measurement was done using a standard foil of the sample.

For the XES measurements presented in Chapter 6 we used a spherical analyzer which will be explained in Section 4.3.2. First, the incoming X-ray energy was set to 7.5 keV which is well above the Fe K-edge and fluorescence emission lines were collected with a spherically bent analyzer crystal of 10 cm diameter placed at 90° to minimize forward scattering.

4.3.1. XAS detection methods: transmission and total fluorescence yield

XAS spectrum can be measured either in transmission or total fluorescence yield (TFY) mode [161]. The transmission measurement technique is suitable for thick samples, sensitive to the bulk and has high background. On the contrary, the TFY measurement technique can be applied to samples of any thickness and has high sensitivity to the bulk. Additionally, is suitable for low concentrations and has a low background. Since we mostly deal with low concentration liquid samples, TFY was used for all measurements presented in this thesis.

Transmission mode

In transmission mode both the incoming (I_0) and transmitted (I_t) X-ray beams are measured by ion chambers when passing through a certain material with uniform thickness d. This process is governed by Lambert-Beer's law (Eq.4.8). The measured X-ray absorption spectrum (A) as a function of the incoming X-ray energy is related to the incident and transmitted X-ray beam intensity using the following equation:

$$\begin{aligned} A(E) &= \ln\left(\frac{I_0(E)}{I_t(E)}\right) \\ &= \mu(E) \cdot d \\ &= \sigma_a(E) \cdot \frac{\rho_m N_A}{M} d \end{aligned} \tag{4.8}$$

Where $\mu(E)$ is the total absorption coefficient, $\sigma_a(E)$ is the absorption cross-section per atom and N_A, ρ_m and M are Avogadro's number, the mass density, and the molar mass respectively. The total absorption coefficient includes both the absorber and all other atomic species present in the sample. Transmission mode measurements require concentrated samples such that the difference between I_0 and I_t is significantly larger than the variation due to the counting statistics. On top of that, samples which are prepared for a transmission measurement should be highly homogeneous and of constant thickness.

Total fluorescence yield mode

For all XAS measurements reported in this thesis, we used the TFY detection method. In this setup the intensity of the incoming X-ray beam (I_0) is measured using an ion chamber while the intensity of the characteristic fluorescence X-rays (I_F) is detected by a NaI scintillator detector placed at 90° on the incoming X-ray beam.

Within the first order of approximation, the absorption coefficient measured in fluorescence mode is proportional to the ratio between I_F and I_0 intensities,

$\mu(E) \propto I_F/I_0$. Systematic measurement errors in either I_F or I_0 will alter the measured EXAFS signal which makes TFY measurement prone to errors. Total fluorescence yield (TFY) measurements rely on the detection of the integrated intensity of all possible fluorescence channels I_F as a function of incoming photon energy E. On the contrary, energy discriminating detector can be used to detect specific fluorescence channel as a function of incoming photon energy E and is called partial fluorescence yield (PFY) [162].

The formula noted earlier, $\mu(E) \propto I_F/I_0$ is an oversimplified equation. The probability of fluorescence is proportional to the absorption probability but for the liquid jet the fluorescence intensity from the front end that we measure has to travel back through the sample to get to the detector. Since all matter attenuates X-rays, the fluorescence intensity, and therefore, the EXAFS oscillations can be damped due to this self-absorption effect. For our measurements we use a liquid-jet thickness of 100 μm, the self-absorption effect is insignificant. The measured fluorescence intensity by the detector as described in [163] yields:

$$I_F(E) = I_0(E)\frac{\epsilon\Omega}{4\pi}\frac{\mu_\chi(E)\left[1 - e^{-\left[\mu_{tot}(E)/\sin(\theta)+\mu_{tot}(E_f)/\sin(\phi)\right]d}\right]}{\mu_{tot}(E)/\sin(\theta) + \mu_{tot}(E_f)/\sin(\phi)}, \tag{4.9}$$

where Ω is the solid angle of the detector, ϵ is the fluorescence efficiency, E_f is the energy of the fluorescence X-ray photons, θ is the angle between incident X-ray and sample surface, ψ is the angle between fluorescence X-ray photons and the sample surface, $\mu_\chi(E)$ is the absorption from the element of interest, and $\mu_{tot}(E)$ is the total absorption in the sample: $\mu_{tot}(E) = \mu_\chi(E) + \mu_{other}(E)$. Eq.(4.9) has the following interesting limits that are common in XAS measurements [163]:

1. For **thin sample limit**: for which μd$\ll$1. Then the exponential term can be expanded using Taylor series as:

$$e^{-\left[\frac{\mu_{tot}(E)}{\sin(\theta)}+\frac{\mu_{tot}(E_f)}{\sin(\phi)}\right]d} = 1 - \left(\frac{\mu_{tot}(E)}{\sin(\theta)} + \frac{\mu_{tot}(E_f)}{\sin(\phi)}\right) + ... \tag{4.10}$$

   Keeping only the first two terms equation (4.9) reduces to:

$$I_F(E) = I_0(E)\frac{\epsilon\Omega}{4\pi}\mu_\chi(E)d \tag{4.11}$$

2. For **thick, dilute sample limit**: for which μd$\gg$1 and $\mu_\chi \ll \mu_{other}$. Now the exponential term goes to 0. Furthermore, for the sample that is a flat sheet liquid-jet tilted at 45° to the incoming X-ray beam, $\theta = \phi = 45°$, the angle dependence in equation (4.9) vanishes and reduces to:

$$I_F(E) = I_0(E)\frac{\epsilon\Omega}{4\pi}\frac{\sqrt{2}\mu_\chi(E)}{\mu_{tot}(E) + \mu_{tot}(E_f)} \tag{4.12}$$

Since $\mu_\chi(E) < \mu_{other}(E)$, we can ignore the energy dependence of μ_{tot} and equation (4.12) reduces to:

$$I_F(E) \propto I_0(E)\mu_\chi(E) \tag{4.13}$$

3. For **thick and concentrated samples**: for which the $\mu_\chi(E) \propto \mu_{other}(E)$ we can not ignore the energy dependence of μ_{tot}, representing the case of self-absorption. For this kind of samples, $\mu_{tot}(E) \approx \mu_\chi(E)$, the EXAFS oscillations are completely lost.

For XAS measurement reported in this thesis we used a 50 mM aqueous solution of the $[\mathrm{Fe(II)(CN)_6}]^{4-}$ molecule and we calculate μ_{tot}(E = 7.15 keV)$\cdot$ d and μ_{tot}(E = 6.404 keV).d to make a sanity check of the regime for our TFY measurements. Using the X-ray energy value reported in Table 3.5 and sample thickness of d = 100 μm/sin(45°) = 0.141 mm, the total absorption coefficient yields: $[\mu_{tot}(E) + \mu_{tot}(E_f)]$d= 0.06, using tabulated atomic absorption cross-section. The calculated value total absorption coefficient 0.06$\ll$1 which implies our measurements are fine. Normalizing the measured XAS spectrum will remove the constants which exist in the Eq.(4.11), such as Ωd/4π.

4.3.2. X-ray emission spectrometers: Johann and von Hamos

X-ray emission spectroscopy (XES) is a technique which probes occupied density of electronic states of material (see Ch.3). Similar to XAS, XES is also an element-specific and site-specific technique which makes it a powerful tool for determining detailed electronic properties of materials.

X-ray emission is a concomitant process of X-ray absorption. First, the core electron is excited by an incident X-ray photon and the excited state decays by emitting an X-ray photon to fill the core hole. By placing an energy-dispersive crystal, we can measure a specific spectra depending on the crystal type and angle. There are two commonly used spectrometers are Johann-type [164] and von Hamos type [165, 166] which will be described in the next section.

Johann type spectrometer

An incoming 7.5 keV X-ray photon energy is absorbed by the sample and resulting in a 1s core hole, then the sample relaxes through fluorescence emission. Using a crystal analyser arranged with sample and detector in a Rowland circle geometry (see Fig.4.12) the different fluorescence emission lines can be recorded by moving the crystal and detector in a controlled manner along the Rowland circle.

The Johann-type analyser crystal is bent to a radius R and the crystal planes lie parallel to the crystal surface. The crystals with a diameter of 10 cm were made of 0.15 mm thick single crystal wafer that is cut along the desired Miller plane. Then the wafer is glued onto a spherically bent shaped glass substrate with a radius of

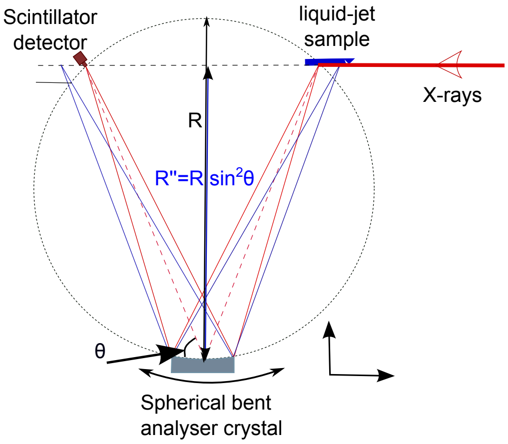

Figure 4.12.: The experimental setup arrangement at Advanced Photon Source (APS) with a spherically bent analyzer crystal of 10 cm diameter positioned at a 90° scattering angle and NaI scintillator detector at its focus. The sample-crystal analyzer-detector setup constituted a 1 m Rowland circle. Figure Adapted from [129].

curvature of R = 100 cm. We used Si(531) for and Ge(4,4,0) crystals for the XES spectra measurements. The solid angle Ω of a Johann crystal with area A and radius of curvature R are given by Eq.(4.14).

$$\Omega = \frac{A = (\pi(D/2)^2)}{R^2} \tag{4.14}$$

The solid angle captured by one of these crystals is 0.0078 sr[1] which covers $6.25{\cdot}10^{-4}$ of the total 4π sr solid angle. The fluorescence X-ray photons incident on the crystal are reflected provided that Bragg's law Eq.(4.15) holds true. The diffraction is defined by the parallel lattice planes with distances d between each other (see Eq.(4.16)) of the crystal.

$$2d\sin(\theta) = m\lambda \tag{4.15}$$

$$d = \frac{a}{\sqrt{\mathbf{h}^2 + \mathbf{k}^2 + \mathbf{l}^2}} \tag{4.16}$$

Where m is the order of diffraction, θ is the Bragg angle, a is the lattice parameter, **h**, **k**, and **l** are Miller indices, or coordinates defining the orientation of the intrinsic crystalline planes. Using the above equations for Si(531) at $\theta = 73.12°$ we get 7057 eV which is the maximum energy of the Fe K$\beta_{1,3}$ spectrum. At $\theta = 71.88°$ we get 7105 eV which is the maximum for Fe K$\beta_{2,5}$ spectrum. For Ge(440) at $\theta = 75.85°$ we get 6391 eV which is the maximum Fe Kα_1 spectrum.

For the Fe K$\beta_{1,3}$ XES spectra measurement the Si(531) analyzer crystal needs

---

[1] Steradian (sr) or sometimes called square radian is the SI unit of solid angle.

to be turned with a stepping motor so that the scanning Bragg angle sweeps from 72.52 to 73.12°, the NaI Scintillator detector needs to follow the reflected beam. The detector is mounted on a linear stage and turned by 27° with respect to the incident X-ray beam. A thin plastic bag filled with He was installed inside the Rowland circle, among the sample, analyzer, and detector.

Shielding is an integral part of the setup, and it helps a lot to minimize the background from the scattering. The plastic bag is constructed from thin plastic foil, and duct tape is used to fix at with anchoring it to the relevant parts of Scotch velcro tape. For overnight scans, the He-bag is connected to a large He cylinder tank with small He flow. The total energy resolution measured through the spectrometer has both intrinsic (the inherent resolution of the chosen reflection emission energy of the analyzer) and geometrical (source size, scanning procedure, finite sample size) contributions to the instrumental broadening of a spectrometer [129, 164].

von Hamos spectrometer

Unlike the Johann-type spectrometer, the von Hamos spectrometer has a crystal that is bent into a cylindrical surface. Due to the dispersive-type of diffraction, the von Hamos spectrometer geometry provides the possibility of a single-shot measurement with a total energy bandwidth ranging from a few tens to a few hundreds of eV. The von Hamos crystal diffracts fluorescence X-rays with different wavelengths according to Bragg's law. After diffraction from the crystal arc, each X-ray energy is focused to a point lying on the spectrometer axis and resulting in an XES spectrum.

The experimental setup with the von Hamos geometry implemented for the XES measurements at APS and SACLA is shown in Fig.4.13 (a). In this setup, the X-ray fluorescence from the sample is reflected by the cylindrically bent crystals and recorded by a single photon counting position sensitive detector (Pilatus 100K detector developed by SLS Detectors Group at PSI, Switzerland). On the detector plane, the diffracted X-rays create a 2D image. On the axis of dispersion, the position of detected X-rays is directly correlated to the energy of the XES spectrum. The energy range of the detected X-rays is determined primarily by the length of the crystal and the active area of the detector along the axis of dispersion (see Fig.4.13 (b)).

For the measurements at SACLA in 2014 two von Hamos crystals: Ge(440) with R = 70 mm with a Bragg angle of θ=27.23° and Si(531) with R = 250 mm with a Bragg angle of θ= 61.45° as shown in Fig.(4.14) are used. For both spectrometers, one single MPCCD detector (developed by Detector Group at SACLA, Japan) was used. This means at each XFEL shot we record Kα, K$\beta_{1,3}$ and K$\beta_{2,5}$ spectra simultaneously. The solid angle of single von Hamos crystal with radius of curvature

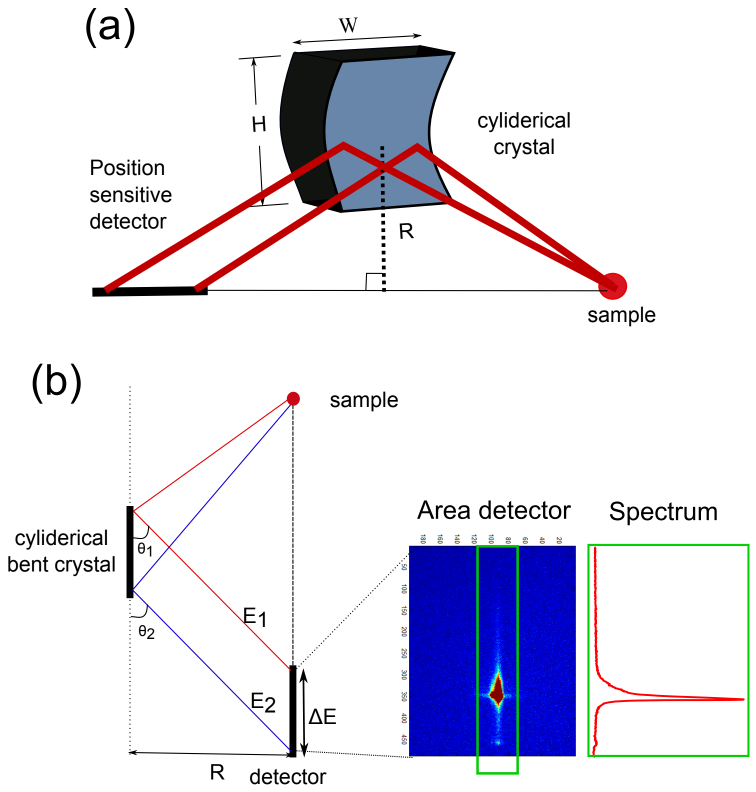

Figure 4.13.: (a) Schematic diagram of single concave crystal with von Hamos geometry at 7ID-D beamline APS. (b) Top view of the experimental setup or the projection along the axis of dispersion with $E_2 > E_1$. The color plot shown is the image collected with the Pilatus pixel detector. The red intense color shown in the figure is Iron $K\beta_{1,3}$ fluorescence emission line, and the faint peak in the high energy part is the vtc ($K\beta_{2,5}$) fluorescence emission line.

R, Bragg angle (θ), height (H) and width (W) is given by the following formula:

$$\Omega = \frac{H \cdot W}{R^2} \sin(\theta) \tag{4.17}$$

For any given configuration the average solid angle per 1 eV is given by the following formula:

$$\Omega_{1eV} \cong \frac{\Omega}{\Delta E} \tag{4.18}$$

For the setup at SACLA in 2015, two von Hamos crystals Ge(440) and Si(220) with a radius of curvature of 25 cm and 7 cm respectively were used. The total solid angle covered by Ge(440) (H=10 cm and W= 5 cm) for $\theta = 61.4°$ is 0.07 sr. The small Si(220) crystal (H=10 cm and W= 5 cm) for $\theta = 28°$ has a solid angle of 0.48 sr. The solid angle per 1 eV for Si(220) and Ge(440) is $1.85{*}10^{-4}$ sr and $1.85{*}10^{-4}$ sr per 1 eV respectively. The Si(220) crystal cover a larger solid angle than the

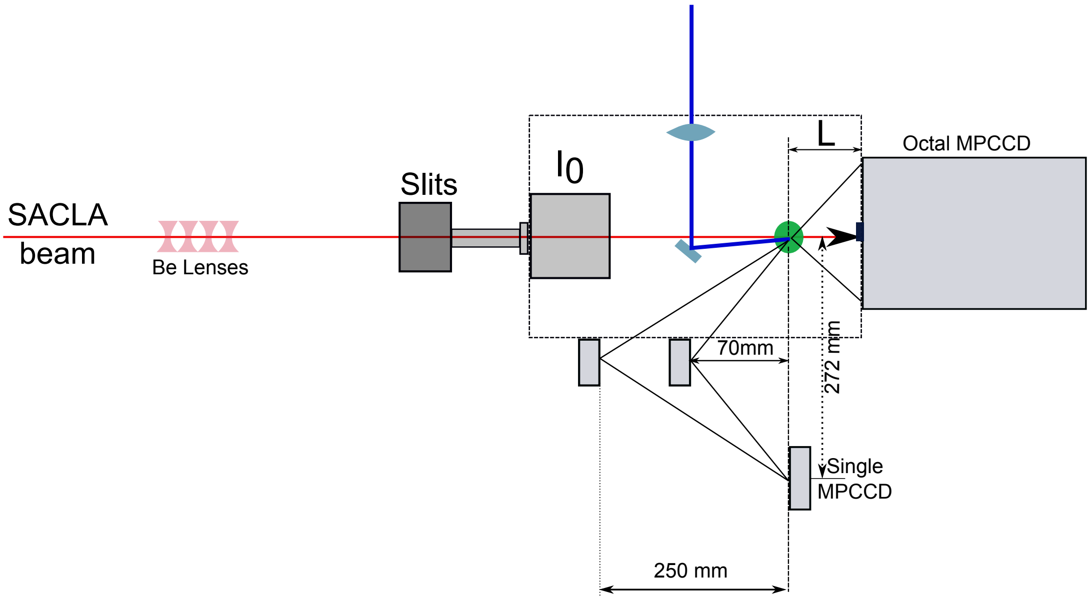

Figure 4.14.: Top view of the experimental setup at SACLA, Japan with two concave von Hamos crystals implemented for the X-ray emission spectroscopy with a pink beam.

Ge(440) crystal. On the contrary, a Si(220) crystal has 1 eV energy resolution whereas a Ge(440) crystal has resolution of 0.3 eV. Although the small radius of curvature increases the solid angle, and it comes at a cost of energy resolution. This will be improved much more by using a multi-crystal wavelength dispersive hard X-ray spectrometer which combines a high-energy resolution and large solid angle collection [165], will also shorten the measurement time and increase the data quality.

4.4. Time-resolved optical-pump X-ray probe setup

Time-resolved laser pump X-ray probe techniques with picosecond time resolution are well developed at different synchrotron sources. Since the early 2000's, synchrotron-based time-resolved optical laser pump and X-ray probe techniques have been used to investigate light-driven chemical reaction dynamics in solution but limited to picosecond resolution because of the 100 ps X-ray pulse width [8, 10]. At 7ID-D, the laser pump X-ray probe experiments have been implemented, and data acquisition is done at MHz repetition rates [150]. The description of the experimental setup used for time-resolved experiments at 7ID-D, APS will be presented here.

Figure 4.15 shows the top view of the time-resolved (TR) laser pump X-ray probe experimental setup. A tunable high repetition rate laser from *Time-Bandwidth Products* has a fundamental output wavelength of 1064 nm. Laser wavelengths of 532 nm, 355 nm, and 266 nm are available through frequency doubling (SHG), tripling (THG), and quadrupling (FHG) with a variable repetition rate. In TR experiments, the laser is used to initiate the light-driven chemical reaction followed by the X-ray photons from the APS used as a probe. Unlike kHz repetition rate laser sources, MHz repetition rate allows us to use almost all the incoming X-ray photons. This shortens the data acquisition time and improves the S/N ratio. The probe techniques are a suite of complementary X-ray tools such as X-ray absorption and emission spectroscopy (XAS and XES). As demonstrated in recent papers [74, 167] the different X-ray tools serve as the an ultrafast molecular camera which delivers structural and electronic information about the sample.

As discussed in Section 4.1.4 the APS has two suitable timing modes for our experiments. When the synchrotron is running in hybrid mode, the singlet bunch rotates the ring at 272 kHz repetition rate while the rest of the current is distributed among the eight multi-bunches. Then we set the repetition rate of the laser to 136 kHz, which is half the repetition rate of singlet X-ray bunch. The singlet bunch is then gated for experiment and every second bunch is the laser on signal. This allows us to measure laser on and laser off signals alternatively for both XAS and XES measurements. When the APS is running in the 24 bunch mode, the X-rays have a repetition rate of 6.53 MHz, in this mode, the laser can be tuned between 3.25 MHz to 130 kHz depending on the lifetime of the sample.

4.4.1. Pump-probe XAS signal

In Section 4.3.1 two of the different steady-state XAS methods and the formula for steady state XAS signals were presented. In time-resolved XAS measurements, we measure the difference between pumped (laser on or laser-excited) and unpumped (laser off or ground state) XAS spectra. In this Section, only the derivation of the pump-probe XAS signal which is recorded in TFY mode will be presented. For the transmission XAS transient signal, please refer the references [10]. According to [168], the laser induced transient XAS spectrum $\Delta I_f(E,t)$ measured in TFY mode is given by the following formula:

$$\Delta I_f(E,t) = \frac{I_f^{ON}(E,t) - I_f^{OFF}(E)}{I_0(E)} \tag{4.19}$$

where $I_f^{ON}(E,t)$ is the fluorescence intensity from the laser pumped sample and $I_f^{OFF}(E)$ is the fluorescence intensity from the unpumped sample. Using Eq.(4.13) for a thin-sample limit, Eq.(4.19) is reduced to:

$$\Delta I_f(E,t) = f(t)\frac{\epsilon\Omega}{4\pi}\Delta\mu_X(E)d \tag{4.20}$$

where $f(t)$ is the fraction of excited state molecules in the X-ray probe volume and ϵ is the fluorescence efficiency of the absorbing atom. According to [121], the fluorescence efficiency of iron (Fe) for the 1s core hole is 34 %. We are using a single photon counting detector with an efficiency of unity. The fraction of excited

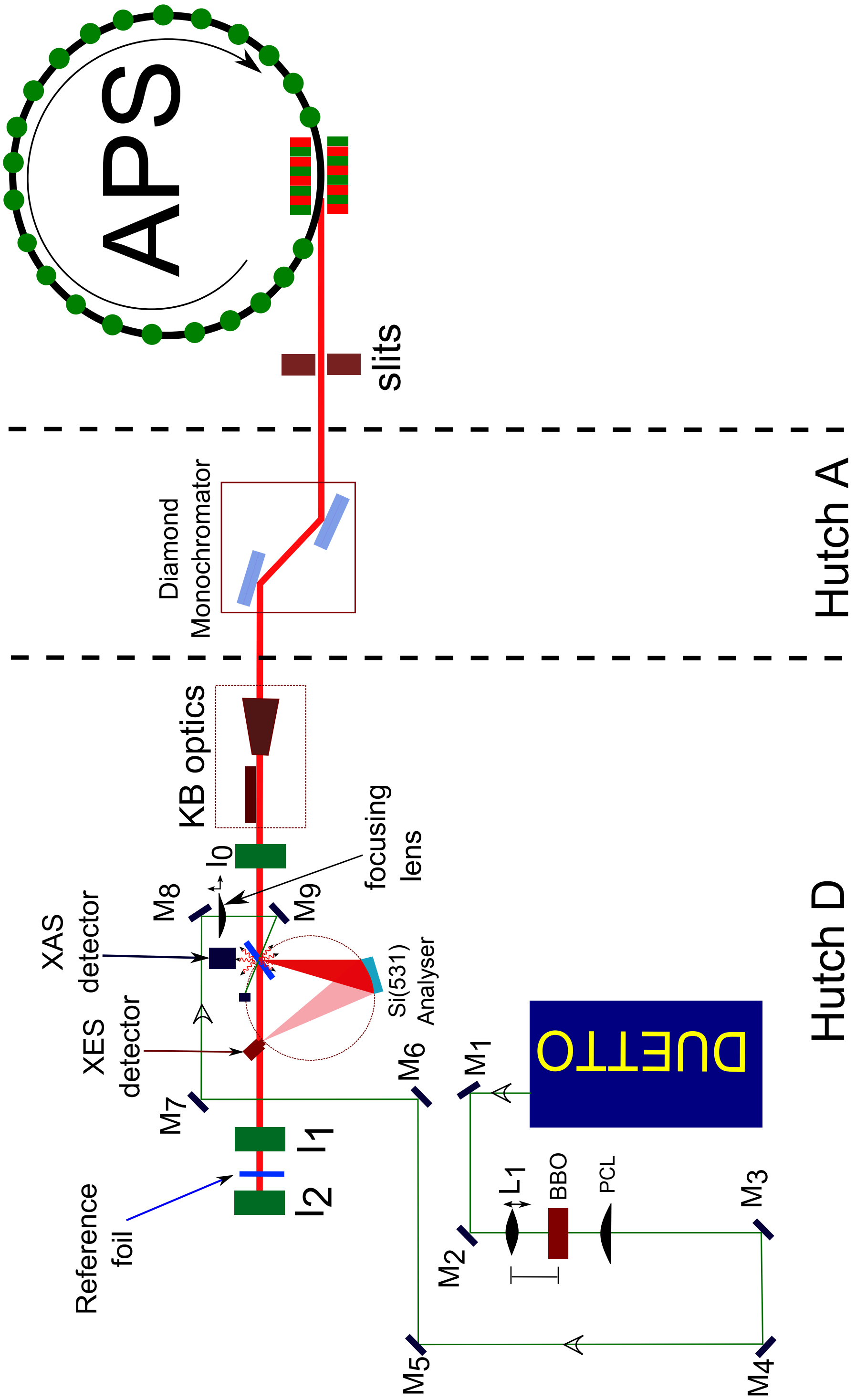

Figure 4.15.: Schematics of the time-resolved laser pump X-ray probe spectroscopy experimental set-up at APS, 7ID-D beamline. The figure only shows the 532 nm laser beam path but both THG and FHG laser wavelengths are also available for experiments. For the details see the text.

state molecules $f(t)$ can be estimated from the number of absorbed laser photons and spot sizes of the laser and the X-ray beams (see Section 4.4.2). The normalized transient signal is obtained by dividing by the edge jump and given as:

$$\begin{aligned}\Delta I_f^{norn}(E,t) &= f(t)\frac{\Delta I_f(E,t)}{\Delta I_f^{edge}} \\ &= f(t)\frac{\Delta\mu_f(E)}{\Delta\mu_0^{E_0}}\end{aligned} \tag{4.21}$$

Where ΔI_f^{edge} is the edge-jump magnitude of the steady-state fluorescence spectrum $I_f^{OFF}(E)/I_0(E)$. After normalization with the incoming X-ray intensity I_0 and edge-jump, the transient fluorescence signal $\Delta I_f^{norn}(E,t)$ can be compared to the theoretical transient spectrum $\Delta\mu(E)/\Delta\mu_0(E_0)$ provided that we know exactly the excited state fraction. This statement is used to analyze the time-resolved EXAFS data in Section 8.3.

4.4.2. Laser excitation process

One of the most important ingredients in analysing a time-resolved XAS data is to know the exact the fraction of excited state molecules. In this Section, the laser excitation process will be presented. For a linear optical photon absorption processes, the fraction of excited state molecules in the probe volume is given by the ratio between the number of absorbed laser photons N_{abs}^{ph} and the number of sample molecules in the volume [10]:

$$f = \frac{\phi N_{abs}^{ph}}{V_L c_{mol} \cdot N_A} \tag{4.22}$$

Where c_{mol} is sample concentration, V_L is volume covered by the pump laser and ϕ is the quantum yield of the laser excitation process. According to the Lambert-Beer law, the number of absorbed laser photons is given as:

$$N_{abs}^{ph} = N_0^{ph}(1 - 10^{-\varepsilon_\lambda c_{mol} d}) \tag{4.23}$$

Where ε_λ is the optical molar absorptivity (in $\mathrm{M}^{-1}\mathrm{cm}^{-1}$) at the laser wavelength. Inserting Eq.(4.23) into Eq.(4.22) yields us:

$$f = \frac{\phi N_0^{ph}}{V_L c_{mol} N_A}(1 - 10^{-\varepsilon_\lambda c_{mol} d}) \tag{4.24}$$

where N_A is Avogadro number and d is the sample thickness. Since the optical molar absorptivity of the laser excitation wavelength is known including the spot size of the pump laser, quantum yield of the excitation process and the concentration of the sample, it is possible to get an estimate of excited state fraction of molecules. According to the Eq.(4.24) to increase the f the optical density

(OD) value of $\varepsilon_{\lambda} c_{mol} d$ has to be higher. Which would result in all the incident laser photons need to be absorbed by the molecule. On the contrary for the XAS measurement in TFY mode the sample concentration has to be diluted to avoid background from the solvent and ligand molecules. At the APS 7ID-D beamline the higher excited state fraction is achieved by focusing the X-rays to a single digit micron spot size which allows us to probe uniformly excited part of the sample.

For the time-resolved XAS experiments reported in this thesis on ferrocyanide (with ε_{355nm}= 120 $M^{-1}cm^{-1}$), 50 mM concentration and the optical length of 100 μm. For the excitation wavelength of 355 nm with spot size of 26.5 x 22 μm^2 (VxH) and the optimum laser power of 0.3 μJ/pulse. Based on this condition the estimated the f= 8.3%. The value estimated here is comparable to the value obtained in Chapter 5.

4.5. Data acquisition system

In this Section will describe the data acquisition and electronic gating systems implemented at APS. For a time-resolved XAS spectrum measurement on a $[Fe(CN)_6]^{4-}$ sample in aqueous solution, we first set the time delay between the pump laser pulse and the probe X-ray pulse to the correct value not less than 100 ps. Then we collect the TFY signal using scintillator detector (from *Saint Gobain*) by scanning the incident X-ray energy across the Fe K edge using the monochromator. At each energy step the TFY counts are recorded and by using the MHz data acquisition system individual X-ray pulses can be distinguished utilizing the gate/delay units. Fig.4.16 shows the APS X-ray pulses running in 24 bunch mode (6.52 MHz) and pump laser frequency at 1.35 MHz. The gate enables us to count and discriminate between consecutive X-ray pulses.

Setting up the AMO Flexible Gate and how it works is beyond the scope of the thesis work so we will only describe it briefly. The versatile AMO Flexible Gate FPGA module allows us to set windows (or gates) with variable repetition rates, width, and delay around the detector signal. These windows are combined with a detector signal in OR, AND or XOR logic operations. The output of the logic operations is sent to scalers internal of the Flexible Gate to be counted. We have to set a two narrow windows to reduce noise in the signal. It is possible to have 12 logic operations that produce outputs to the 12 scalers. The laser ON gate selects the X-ray pulse that is overlapped with the laser, and the laser OFF signal is the gated 153 ns before the laser on a signal. The rest of the X-ray pulses can be gated as laser ON+1, laser ON+2 ...and so on.

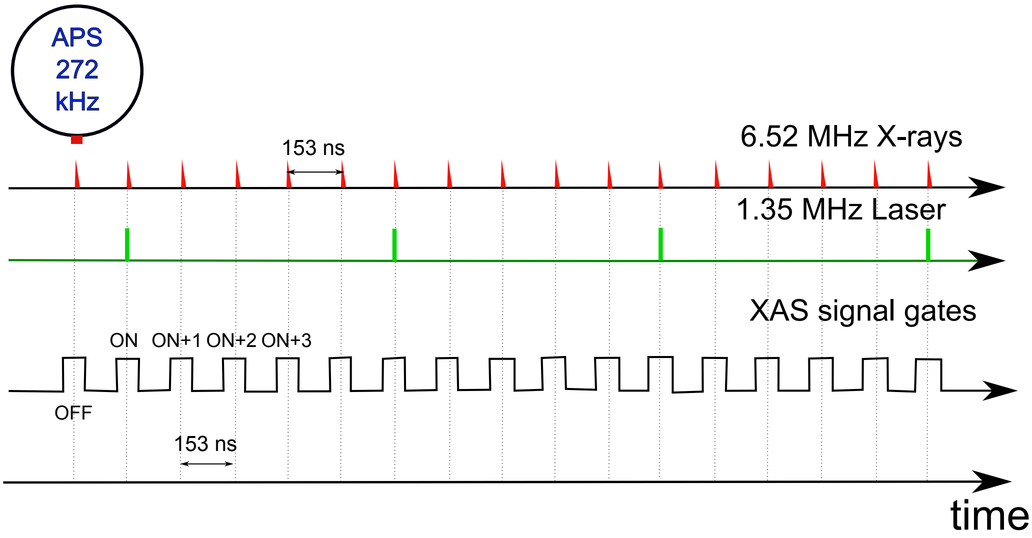

Figure 4.16.: Electronic gating scheme is shown when the laser is running at 1.35 MHz repetition rate. The APS is running in 24 bunch mode, the AMO flexible gate allows us to read all the signals from each bunch of X-rays.

4.6. Detectors

In this thesis 0D and 2D, detectors are used for XAS and XES measurements. For XAS measurement NaI scintillator detector for TFY detection and an Ion chamber for incident intensity measurement were used. When XES measurements were performed in Johann geometry the scintillator and APD detectors were used. For XES measurements with von Hamos geometry position sensitive detectors such as Pilatus and MPCCDs were used. In this Section, a brief description of some of the most often used detectors will be presented.

4.6.1. NaI(Tl) scintillation detector

A typical scintillator detector consist of a scintillation crystal and a photomultiplier tube which has a photocathode, a focusing electrode, dynodes, and an anode (see Fig.4.17). In our setup, a NaI(Tl) scintillator detector from *Saint Gobain* were used. It has a thin 1 mm thallium-activated sodium iodide and NaI(Tl) crystal of 25 mm in diameter assembled with an aluminum entrance window. When the X-rays strike the NaI(Tl) crystal, visible light is generated which strikes the photocathode of the photomultiplier results electrons emitted by the photoelectric effect. Then electrons are swept through a series of dynodes, and the initially small pulse of current is amplified. The counting rate without counting losses is calculated by $1/t_s$, where t_s is the minimum resolving time between two consecutive pulses. Scintillation detectors have a time resolution of about 1 μs. Thus, the counting rate is linearly proportional to the intensity of the incident X-ray beam for count rates up to

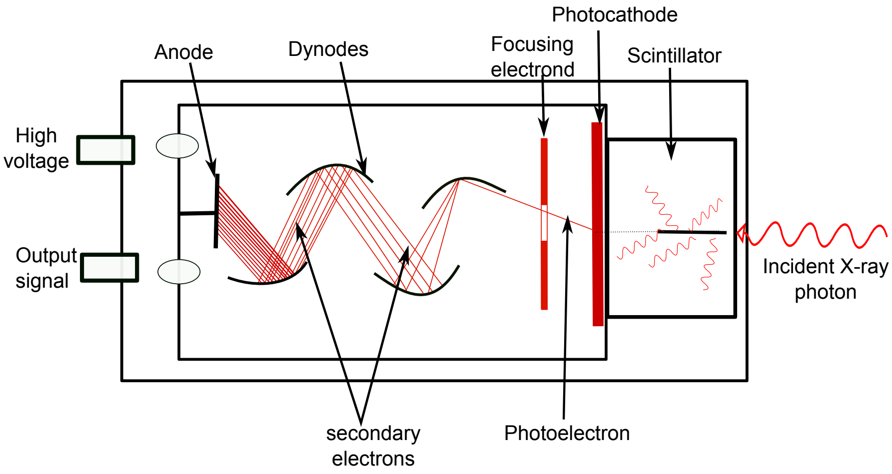

Figure 4.17.: Schematic showing an incident photon hitting a scintillating crystal, triggering the release of visible light photons are then converted into photoelectrons and further multiplied in the photomultiplier before reaching the anode and producing detectable signal.

approximately 10^6 counts per second. The NaI(Tl) scintillator detector covers a typical energy range of 10 to 200 keV with a detection efficiency of 100 % [169].

4.6.2. Ionization Chamber

Ionization chambers detect X-ray photons by measuring the ionization of the gas inside the chamber while a beam of X-rays is passing through. An Ionization chamber consists of two conducting metal plates (cathode and anode) in a sealed or open chamber filled with gas. When X-rays pass through the chamber, the gas becomes ionized, separating positive ions and negative electrons [169]. A high voltage (4 kV in our case) applied between two plates sweeps the electrons to the anode and the positive ions to the cathode. The resulting ionization current is directly proportional to the intensity of incident X-ray beam passing through. This detector is simple and reliable and is often used to measure the incident intensity of the X-ray beam on the sample. In the setup, three ionization chambers were used. The first one is before the sampe and the other two are after the sample. A reference foil is placed between the later placed chambers which allows us to get calibration measurement for every XAS spectra measured.

4.6.3. Avalanche photodiode (APD)

Certain limitations of NaI(Tl) scintillator and ionization chamber detectors, which both have low count rates, can be overcome by using Si-based avalanche photodiode (APD) detectors which offer a high count rate up to 108 photons per second. Avalanche photodiode (APD) from *FMB Oxford* is a system with an ultrafast detector suitable for experiments up to 20 keV with large dynamic ranges, time-resolved measurements and where fast photon counting is required. APDs have count rate up to 100 MHz, very low noise and efficiency of 95% at 6 keV 45% at 12 keV. APD detectors come with an **A**PD **C**ontroller **E**lectronics (ACE) box developed at the *European Synchrotron Radiation Facility, Grenoble* offers the user maximum flexibility. It supplies the bias voltage to the detector head and has an integrated counter/timer which can be operated in local (front panel) or remote (computer controlled) mode.

4.6.4. Position-sensitive detectors

Position Sensitive Detectors (PSD) are either 1D or 2D that can measure the position of an incident X-ray photon spot on the sensor surface. Although there are 1D position sensitive detectors this Section will be limited to a brief description of 2D Pilatus 100K detector from *DECTRIS Ltd., PSI.*

Pilatus 100 k is a single photon counting detector with hybrid pixel detector with a pixel size is 172 x 172 μm^2. The active area has 487 x 195 pixels with an active area size of 83.8 x 33.5 mm^2 and a count rate of 2 x 10^6 counts/s/pixel. The frame rate is >200 Hz and readout time of <2.7 ms. A proper operating temperature of this detector is 20 to 35 °C. The Pilatus detector can be gated for time-resolved experiments such as XES or RIXS measurements with von Hamos geometry.

4.7. Sample environment: Free flowing liquid jet

A free flowing flat liquid-jet flowed through a sapphire nozzle *Victor Kyburz AG* with a thickness of ~100 μm and a width of ~6 mm. The jet is placed at an orientation of 45° to the X-ray beam. The jet orientation is convenient to collect maximum fluorescence photons from the surface of the jet.

The jet speed can go up to 17 m/s and is adjustable depending on the sample being investigated (Fig.4.18). Adjusting the liquid jet speed is important to avoid multiple excitations of the same sample volume which will later result in an undesired transient signal. For samples with a long excited state lifetime we need to operate at higher speed and low repetition rate to clear out the sample before the next laser pulse hits the same spot. The integrity of the sample was checked by looking at the consecutive laser off scans.

For the results reported in Ch.5 were measured at a laser repetition rate of 283 kHz and a spot size of 26 x 22 μm^2 (VxH). The time separation between the consecutive laser pulses is given by 1/rep. rate = 1/283000 sec = 3.53 μsec. If the liquid jet speed is 25 m/s, the time needed to clear out the laser spot size is given by Eq.(4.25).

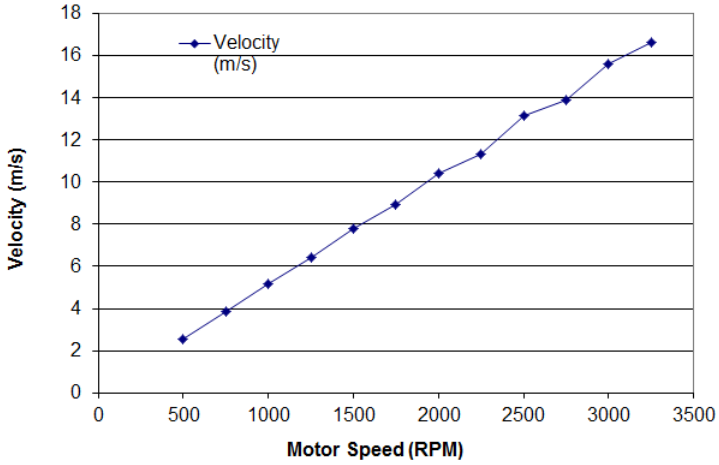

Figure 4.18.: Speed calibration measurement of 100 μm flat-sheet of a free-flawing liquid jet. The x-axis shows the RPM value of the pump controller and the y-axis is the velocity of the jet calculated.

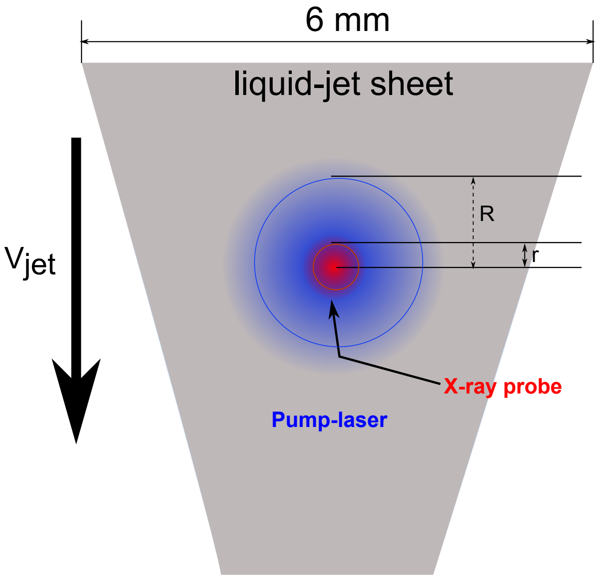

Figure 4.19.: The depicted drawing shows the pump laser and X-ray probe spot sizes on the liquid-jet, with R and r are the radius of the laser and X-ray spot sizes at the FWHM respectively.

$$\begin{aligned} t &= \frac{R}{V_{jet}} \\ &= \frac{13}{25}\mu s \cong 0.52\mu s \end{aligned} \tag{4.25}$$

The minimum liquid-jet speed needed to avoid multiple excitations with the laser repetition rate (rep. rate) is given by Eq.(4.26). For the set of measurements reported in Ch. 5 the liquid-jet speed was set higher than 3.7 m/s to avoid multiple excitations with the laser.

$$\begin{aligned} V_{jet} &= \frac{R}{t}, t = \frac{1}{rep.rate} \\ &= R * rep.rate \end{aligned} \tag{4.26}$$

4.8. Temporal and spatial overlap

Setting the delay time between pump and probe pulse is an integral part of the time-resolved experiment. Before starting doing the procedure of temporal overlap, we make sure the laser and X-ray overlap at the sample position. This helps later to have the laser and X-ray on the timing detector. We place the GaAs MSM detector from *Hammamatsu G4176-03* at the sample position. Then we connect the bias-tee and the MSM detector, to the oscilloscope (Lecroy, 400 MHz bandwidth, 4 input channel and 20 GS/s sample rate) and to the DC voltage supply (6 V).

We trigger the oscilloscope at the laser photodiode frequency, it could be any integer division of the laser frequency. Then we need to attenuate the laser beam with Neutral Density (ND) filters, start with ND=3 not to damage the detector. Then we can tweak the X- and Y- stages of the liquid jet holder to center the beam on the detector. Then the X-rays send onto the MSM detector along with the laser. If the APS is running in 24-bunch mode, there is no need to use X-ray filters, but it is necessary if the APS is running in hybrid singlet mode. Similarly, for XFEL sources using X-ray filters is necessary to use. We identify the laser and X-ray signals on the oscilloscope. Using the phase shifter, we can move the laser pulse to overlap to the nearest X-ray pulse.

For fine adjustment between the X-ray and laser pulses, we need to zoom in and center the overlapped laser and X-ray pulses on the oscilloscope. Then we run the oscilloscope in averaging traces and adjust the ND filter of the laser to have the same height signal of the laser and X-ray pulses. Block the laser and save the X-ray only trace on the scope. Next step is to block the X-ray and send the laser, then shift the laser in finer steps (minimum step of is 5 ps) using the phase shifter to match the laser and X-rays falling edge. This position of the laser is time-zero ("t0"). We save the reference signal on the oscilloscope and display the laser photodiode signal. Adjust the scope delay to center the photodiode signal and save the trace of the scope. Make sure to write down the delay value, later during the experiment it will be used as a marker for timing.

However, temporal overlap only does not grant a transient signal, for this reason, it is necessary to do a spatial overlap of the laser and X-ray pulse to make sure that we are probing the center of pumped sample area. We placed a tungsten pinhole (25, 35, 50, or 100 μm depending on the X-ray spot size) at the sample position and placed a slow PIN detector behind the pinhole to monitor the transmission signal. We scan the X- and Y- liquid jet stages to find the edges of the pinhole holder and set the X- and Y-liquid-jet stage positions to the center value. If there is a signal on the PIN diode, by scanning the X- and Y- liquid jet stages with finer steps about the center we can optimize the signal. Then set to X- and Y- liquid jet stage positions to the maximum of the PIN diode signal position. As a result, the X-rays is passing through the pinhole. Now we go inside the hutch and send the attenuated laser beam. Hold a white paper behind the pinhole and tweak the X- and Y- knobs of the last mirror to send the laser through the pinhole. To make sure the laser is centered on the pinhole, we should see diffraction like rings on the paper when the laser is going through the pinhole.

Once the spatial and temporal overlap is done a quick XANES scan is necessary. If there is a transient signal, it can be optimised by fine tuning the laser alignment, e.g. tweaking vertical and horizontal lens positions. After this procedure, another delay scan is necessary to set the right time delay and take note of the time-zero position. Fig.4.20 shows cross-correlation measurements between X-ray and synchronized pump laser at the APS 72.7±6.8 ps and at SACLA 798.13±56.71 fs. Normally, X-rays from XFEL sources have short pulse duration (in the order of few femtoseconds) the reason we have longer time resolution is due jitter.

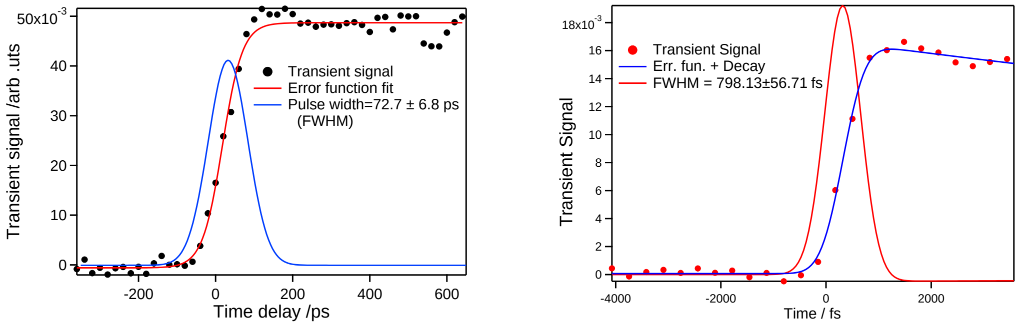

(a) (b)

Figure 4.20.: (a) Cross-correlation measurement of the 10 ps of the Deutto laser and 80 ps X-ray pulse width from APS, USA. The X-ray energy is fixed to 7113 eV to look at the maximum transient in $[Fe^{II}(CN)_6]^{4-}$ after 355 nm laser excitation. (b) Cross-correlation measurement of the 150 fs laser pulse width and X-ray of SACLA-XFEL. The X-ray energy is fixed to 7113 eV to look at the maximum transient in $[Fe^{II}(CN)_6]^{4-}$ after 355 nm laser excitation.

Chapter 5

Disentangling simultaneous reaction channels of aqueous ferrocyanide molecule using time-resolved X-ray absorption spectroscopy

Recent picosecond time-resolved Fe K-edge XAS studies by Reinhard *et al.*[27] reported the observation aquated of $[\mathrm{Fe^{II}(CN)_5(H_2O)}]^{3-}$ species following 355 nm laser excitation. Quantum mechanical theoretical simulations aided their interpretation of the enhanced pre-edge which was due to the distorted symmetry of aquated complex. On the other hand, excitation of ferrocyanide with 266 nm laser yields both ferricyanide and aquated species. Similarly, optical flash photolysis studies suggest predominantly ferricyanide formation after irradiation with 266 nm [15, 1]. According to Reinhard *et al.* [27], after subtraction of the ferricyanide component from the transient XANES measured after 266 nm excitation, the remnant photoproduct is identical to transient XANES measured after 266 nm excitation of ferricyanide complex. However, the measurement still has to treat multiple hit events of the same probed sample volume by the laser before it was cleared out of the area. We repeated the same experiment with experimental conditions that avoid multiple re-excitation of the sample. The results shown in this chapter are measured while the laser was operating at 283 kHz, laser spot size of 26 x 22 μm^2 and a liquid jet speed of 15 m/s to avoid repeatedly exciting the same sample. Hereby, the X-ray spot size of 4 x 5 μm^2 (V x H) allows us to probe only the uniformly excited centre of the laser-excited sample.

The reaction photocycle of aqueous ferrocyanide after laser excitation at two wavelengths 266 nm and 355 nm is summarised in the Fig.5.1. Excitation of aqueous ferrocyanide molecule with 266 nm laser light predominantly results in a branching towards ferricyanide and a small amount of the photoaquated photoproduct [15, 1]. Fe K-ege XANES results measured after 355 nm laser excitation and the static reference spectra are used to disentangle the simultaneous reaction channels measured after 266 nm laser excitation.

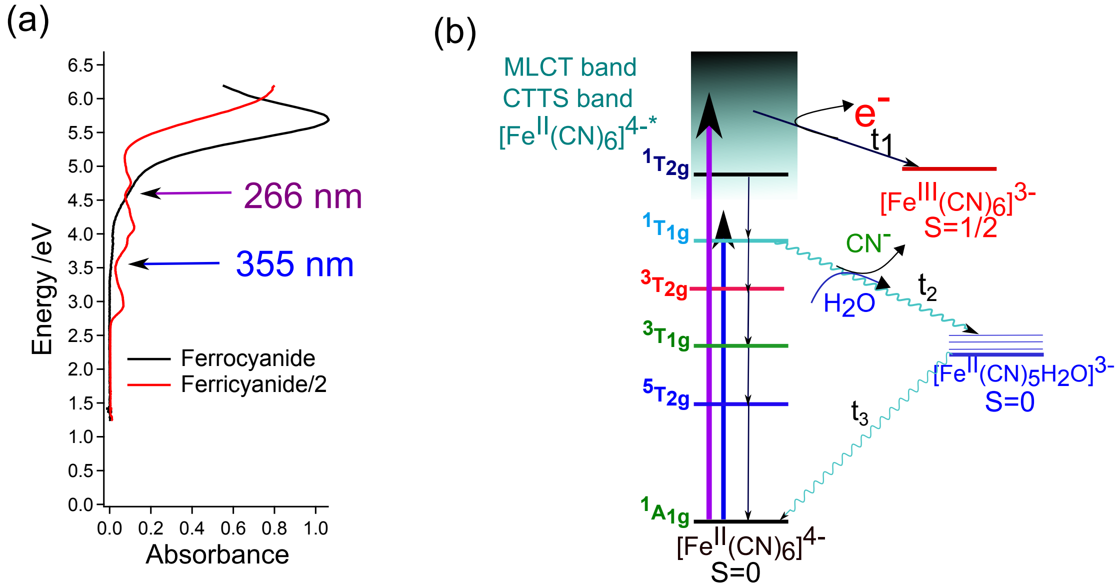

Figure 5.1.: a) The UV-Vis absorption spectra of ferro and ferricyanide molecules measured in aqueous solution. The arrows indicate the excitation wavelengths of 355 nm and 266 nm. b) Photochemical reaction pathways of ferrocyanide molecules after 266 nm and 355 nm excitation. The reaction photocycle is based on prior studies from [15, 1] and time scales extracted are from optical studies $\tau_1 = 150$ fs[170], $\tau_2 = 16$ ps [25] and $\tau_3 >> 1\ \mu$s [2]. The arrangement of electronic states are according to ref.[171].

5.1. Picosecond XAS results after 266 nm excitation

Shown in the Fig.5.2(a) is the iron K-edge XAS spectrum of 50 mM aqueous ferrocyanide solution. The solid black line is ground state spectrum, and the solid red line is measured after 100 ps following 266 nm laser excitation. Fig.5.2(c) is the transient signal measured at 100 ps which is the difference between laser ON and OFF spectra.

Both ferrocyanide and ferricyanide also exist as stable powder salts (*Sigma-Aldrich, Germany*), and 50 mM aqueous solution was prepared for each sample, and their static XAS spectrum is shown in Fig.5.2(b). We observe a 1 eV blue shift for the ferricyanide spectrum in agreement with earlier studies [27, 26]. The reason for the blue shift of ferricyanide XAS spectrum is due to the missing electron in the Fe(III) ion of ferricyanide versus Fe(II) ion in the ferrocyanide, which increases the effective nuclear charge shielding as a consequence, the electronic energy levels gain binding energy by about 1 eV per charge. The static difference signal derived from ferrocyanide and ferricyanide spectra represents 100 % conversion of the ferrocyanide molecule to ferricyanide molecule and will thus allow us to scale

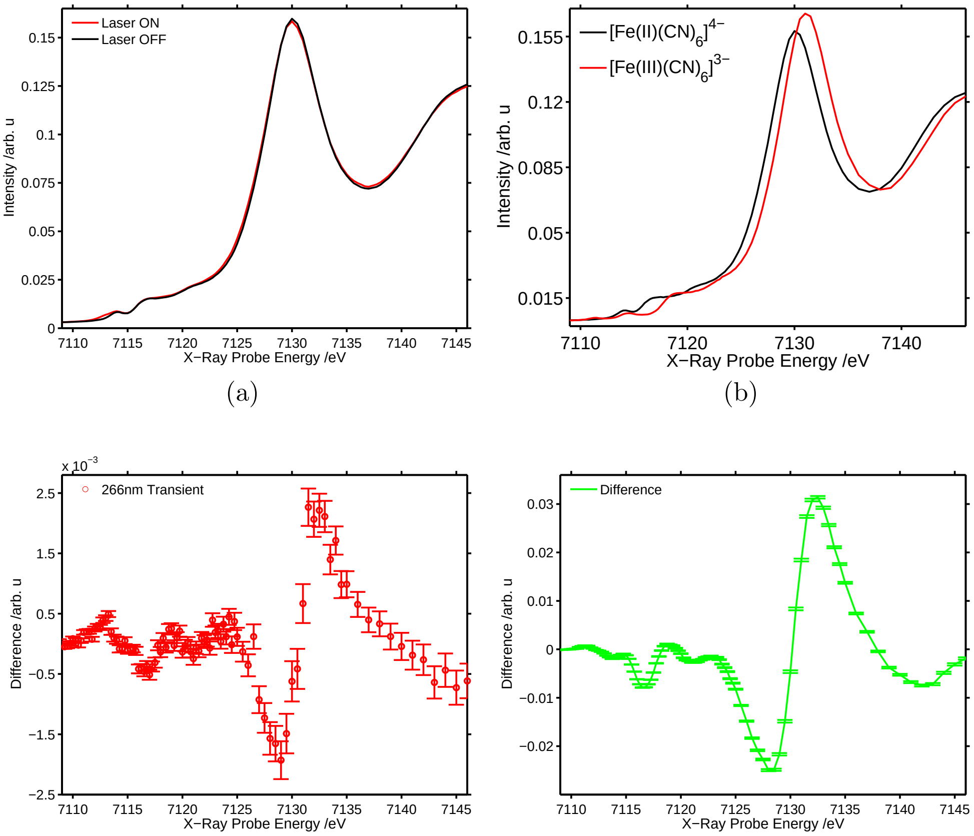

(a) (b)

(c) (d)

Figure 5.2.: Iron k-edge X-ray absorption spectra: a) Picosecond resolved XANES measured after the 266 nm laser excitation and delay of 100 ps. b) Static iron k-edge X-ray absorption spectra of ferricyanide and ferrocyanide molecules. c) Transient spectrum measured at 100 ps following 266 nm laser excitation with intensity of 6.49 GW/cm^2. d) Static difference calculated from ferricyanide and ferrocyanide spectra.

the results in the pump-probe experiments to obtain the excited state fraction and population. Previous studies also reported that excitation of aqueous ferrocyanide with 266 nm laser light predominantly results in a ferricyanide molecule but with additional photoaquated photoproduct [15, 1, 63]. As a result, the transient signal in Fig.5.2(c) measured after 266 nm laser excitation can be loosely compared to the static difference spectrum. For this reason, the solid green line is shown in Fig.5.2(d) has been scaled to the maximum difference feature by a factor of 0.0726 to match the data in Fig.5.2(c) which implies 7.26 % yield of ferricyanide complex formation. Comparison of the transient signal after 266 nm laser excitation and scaled static difference spectrum show a mismatch (see Fig.5.3), which is due to the presence of the additional photoproduct, $[Fe^{II}(CN)_5H_2O]^{3-}$.

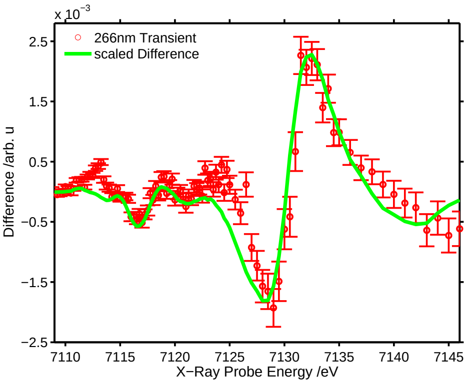

Figure 5.3.: Comparison of transient spectrum measured at 100 ps following 266 nm laser excitation (red dots) and scaled static difference spectrum (green curve).

Next to the rather subtle difference in the region 7125 - 7130 eV one observes a new feature at 7113 eV, which will serve as a fingerprint of the aquated species. The 355 nm transient XANES indeed shows this new feature, which justifies the assumption that the 266 nm transient contains contributions from both the ionized and aquated species. In the following we seek to quantity contributions in order to extract the hitherto unknown XANES of $[Fe^{II}(CN)_5H_2O]^{3-}$ in water.

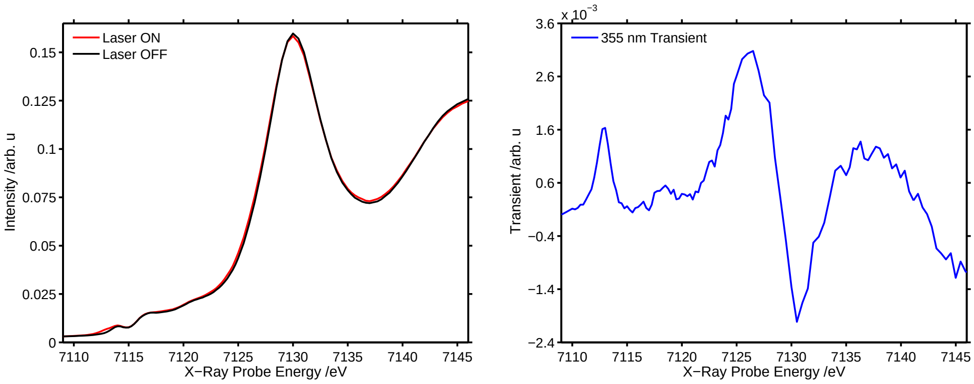

(a) (b)

Figure 5.4.: (a) Time-resolved XANES spectrum of ferrocyanide molecule measured before and after 355 nm laser excitation at 100 ps. (b) Transient spectrum measured after 355 nm laser excitation with intensity of 55 GW/cm^2.

5.2. Disentangling simultaneous reaction channels

Shirom *et al.* concluded from flash photolysis studies that excitation of aqueous ferrocyanide at wavelengths above 313 nm yields no (or only an "insignificant") amount of ferricyanide [1, 37, 2]. As a result, the transient signal measured after 355 nm results solely photoaquated photoproduct and the transient signal, $\Delta\mu_{355nm}$ at 100 ps can be expressed in the following way:

$$\Delta\mu_{355nm} = f_{aq} * ([\mathrm{Fe}^{\mathrm{II}}(\mathrm{CN})_5\mathrm{H}_2\mathrm{O}]^{3-} - [\mathrm{Fe}^{\mathrm{II}}(\mathrm{CN})_6]^{4-}), \tag{5.1}$$

where f_{aq} is the excited state fraction for the aquated photoproduct. The transient signal, $\Delta\mu_{266nm}$ measured after 266 nm laser excitation has a contribution of both photoproducts. Disentangling of both simultaneously occurring reaction channels can be performed via a linear combination of both products.

$$\Delta\mu_{266nm} = \alpha([\mathrm{Fe}^{\mathrm{III}}(\mathrm{CN})_6]^{3-} - [\mathrm{Fe}^{\mathrm{II}}(\mathrm{CN})_6]^{4-}) + \beta([\mathrm{Fe}^{\mathrm{II}}(\mathrm{CN})_5\mathrm{H}_2\mathrm{O}]^{3-} - [\mathrm{F}^{\mathrm{II}}(\mathrm{CN})_6]^{4-}) \tag{5.2}$$

Where α and β are fit parameters for ferricyanide and photoaquated photoproducts respectively. The first term of Eq.(5.2), accounts the ferricyanide formation and can be generated from the static difference between ferrocyanide and ferricyanide spectra (see Fig.5.3). By substituting Eq.(5.1) into 5.2, we can rewrite Eq.(5.2) as:

$$\Delta\mu_{266nm} = \alpha([\mathrm{Fe}^{\mathrm{III}}(\mathrm{CN})_6]^{3-} - [\mathrm{F}^{\mathrm{II}}\mathrm{e}(\mathrm{CN})_6]^{4-}) + \gamma * \Delta\mu_{355nm} \tag{5.3}$$

where α and γ are fitting parameter of the data, with $\gamma = \frac{\beta}{f_{aq}}$. Now we have 2 known spectra to fit the 266 nm transient, with scaled populations as the only fit parameters. To evaluate the statistical goodness of the fit we use the $\chi^2_{reduced}$ test (see Eq.(5.4)).

$$\chi^2_{reduced} = \frac{1}{N}\sum_{i=1}^{N}(\frac{\Delta\mu_{266nm} - (\alpha([\mathrm{Fe}^{\mathrm{III}}(\mathrm{CN})_6]^{3-} - [\mathrm{Fe}^{\mathrm{II}}(\mathrm{CN})_6]^{4-}) + \gamma\Delta\mu_{355nm})}{\delta\Delta\mu_{266nm}})^2 \tag{5.4}$$

Where N is the number of data points and $\delta\Delta\mu_{266nm}$ are the experimental error bars for each data point. The experimental error bars are calculated from the laser on and off error bars as a square root square sum. The $\chi^2_{reduced}$ is evaluated for all possible combinations of α and γ (see Fig.5.5(b)), converges to the best fit parameters corresponding to the global minimum of $\chi^2_{reduced}(\alpha, \gamma)$ point. The fit results are summarised in Table 5.1.

5.2.1. Extracting the excited state fraction

In pump-probe experiments in general, so also in laser-pump X-ray-probe spectroscopy knowledge of the fraction of excited molecules is necessary. Usually, a complementary method is chosen, e.g., ground state bleach. In X-ray pump-probe

Table 5.1.: Fit results of the 266 nm transient data measured at 100 ps with the static difference and 355 nm transient measured at different time delay. The intensity for 355 nm and 266 nm transient data was 55 GW/cm^2 and 6.49 GW/cm^2 respectively. Where α and γ are fit parameters for the ferricyanide and photoaquated photoproducts respectively.

Data/parameter	α	γ
355 nm at 100 ps	0.0726	0.2742
355 nm at 10 ns	0.0726	0.2903
355 nm at 153 ns	0.0726	0.2903
355 nm at 306 ns	0.0726	0.3065

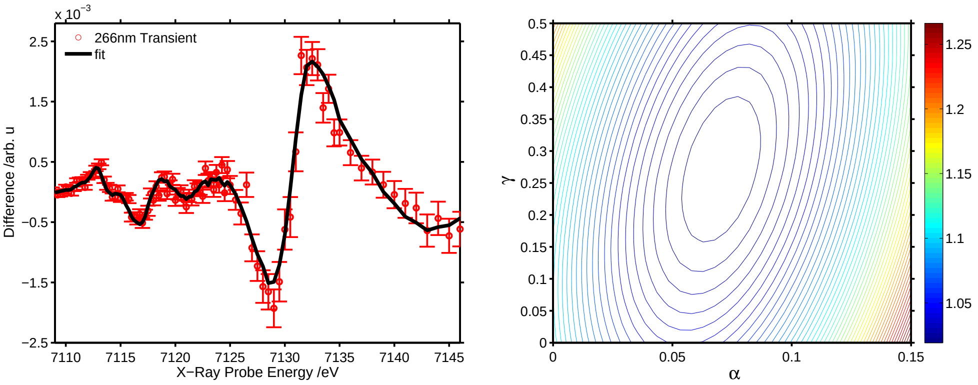

(a) (b)

Figure 5.5.: (a) Fit of the transient signal measured at 100 ps of 266 nm laser excitation (red dots), and the fit reconstructed via 5.3.(b) Calculated reduced χ^2 contour plot versus fitting parameters of α and γ.

experiments not easy to separately do visible pump-probe (ground state bleach) under identical laser pump conditions. Therefore, we exploit time-resolved XES to get the extra information about f, but this relies on reference spectra to aid in quantifying [74, 79]. In this Section, we will present how we quantify the exact value of the excited state fraction using only XANES measurement.

The fit parameters, α and γ extracted from the fit are related to the excited state fraction for ferricyanide and photoaquated formation respectively. To get the excited state fraction from fit results we make the following assumptions:

- We use the quantum yield reported for ferricyanide formation after 265 nm laser light excitation (= 0.52); which should be quite identical to the 266 nm used here.
- Next, the results from ref. [63] shows that the quantum yield for the formation of the photoaquated complex between 365 and 313 nm is constant, and

decreases by half at 253.7 nm, so based on this statement the quantum yield at 365 nm is set to be 0.19 [63].

- Finally, above 313 nm the relaxation channel leading to solvated electron formation is suppressed, thus we only yield the photoaquated product at 355 nm (see Table 5.2) with its reported quantum yield.

Table 5.2.: Quantum yield for ferricyanide and photoaquated formation after excitation of aqueous ferrocyanide at two different wavelengths.

	266 nm	355 nm
Solvated electron	0.52[1]	< 0.02[2]
Photoaquation	0.19[63] or 0.14[63]	0.31

The fraction of photoaquated formation at 266 nm will scale with the quantum yield: $\beta = 0.0726 * (0.19/0.52) = 0.02652$ and ferricyanide formation at 266 nm is $\alpha = 0.0726$. Using the fraction of photoaquated formation at 266 nm, we can scale the photoaquated formation at 355 nm as: f $= \beta/\gamma = 0.02652/0.2710 = 0.0967$, which corresponds to 9.67 % photoaquated formation at 355 nm. Similarly, we report the fit results and the excited state fraction for the different time delay XANES measurements (see Table 5.3). From the result we observe a decrease by 1% of photoaquated complex going from at 100 ps to 306 ns, which is due to the recovery photoaquated complex to the ground state.

Table 5.3.: Summary of fit results using the 355 nm transient measured at different delay with an intensity of 55 GW/cm^2. The 266 nm transient was measured with 6.49 GW/cm^2 intensity. Where f$_{aq.}$ is excited state fraction for the photoaquated complex and f$_{ox.}$ $= \alpha$ is the excited state fraction for ferricyanide complex at 266 nm.

Data/parameter	α	γ	f$_{aq.}$ at 266 nm	f$_{aq.}$ at 355 nm
355 nm at 100 ps	0.0726	0.2742	2.65 %	9.67 %
355 nm at 10 ns	0.0726	0.2903	2.65 %	9.13 %
355 nm at 153 ns	0.0726	0.2903	2.65 %	9.13 %
355 nm at 306 ns	0.0726	0.3065	2.65 %	8.65 %

The 266 nm measurements were done at different pump intensity ranging from 6.5 GW/cm^2 to 30.2 GW/cm^2 (see Fig.5.6). For each measurement we extract the excited state fraction and the results are reported in Table 5.4. The results indicate the fraction of photoaquated complex at 266 nm increases as the pump intensity. For 86 mW (6.49 GW/cm^2) 266 nm laser the fraction of photoaquated complex (f$_{aq}$) is 2.65 % and for 400 mW (30.2 GW/cm^2) 266 nm laser f$_{aq}$ is 8.51 %. The f$_{aq}$ at 355 nm show a slight decrease as 266 nm laser intensity increases. However, the slight change is within the error bars of the estimated f$_{aq}$.

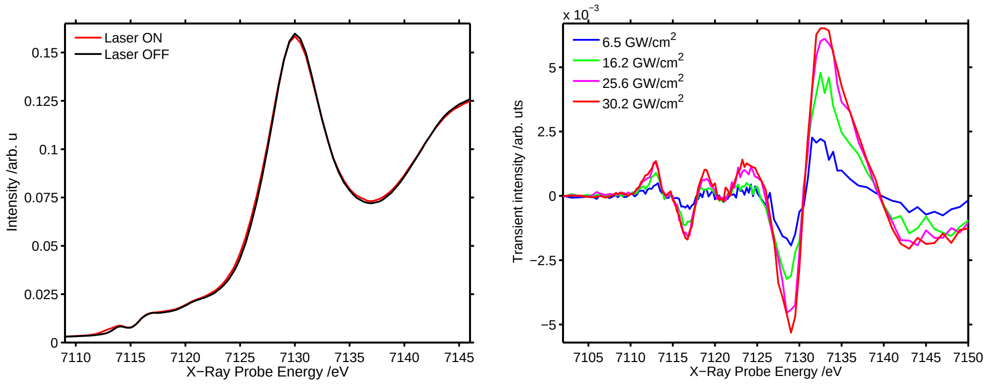

(a) (b)

Figure 5.6.: (a) Time-resolved XANES spectrum of ferrocyanide molecule measured after 266 nm laser excitation at 100 ps. (b) Transient spectrum is measured after 266 nm laser excitation at different laser fluence.

Table 5.4.: Fit results of 266 nm for the different pump intensity measurements. For the 355 nm data, we use the transient at 100 ps, where f$_{aq}$ is the excited state fraction derived form the fit parameters.

266 nm (Power, intensity)	α	γ	f$_{aq}$ at 266 nm	f$_{aq}$ at 355 nm
86 mW, 6.49 GW/cm^2	0.0726	0.2710	2.65 %	9.67 %
215 mW, 16.23 GW/cm^2	0.1471	0.5642	5.37 %	9.53 %
340 mW, 25.67 GW/cm^2	0.2084	0.9745	7.61 %	7.81 %
400 mW, 30.19 GW/cm^2	0.2329	1.1284	8.51 %	7.54 %

5.3. Spectral features of ferricyanide complex

The transient signal measured after 266 nm contains contributions from both the ferricyanide and photoaquated photoproducts (see Sec.5.2). For this reason, we now generate the spectrum only for the ferricyanide formation by subtracting the photoaquated transient contribution via:

$$[\mathrm{Fe}^{\mathrm{III}}(\mathrm{CN})_6]^{3-} = [\mathrm{Fe}^{\mathrm{II}}(\mathrm{CN})_6]^{4-} + \frac{(\Delta\mu_{266nm} - \gamma \cdot \Delta\mu_{355nm})}{\alpha} \tag{5.5}$$

The reconstructed transient spectrum for the ferricyanide complex is also shown in Fig.5.7(a). Shown in Fig.5.7(b) is the ground state and the reconstructed excited state spectrum of ferricyanide formation. Now, we can assign the relevant spectral features of ferricyanide photoproduct: the formation of ferricyanide is evidenced by a blue shift of the edge (C″-feature) which corresponds to the negative signal in the transient signal. The B″-feature is also an indication of the conversion of ferrocyanide to ferricyanide formation. All the relevant features related to ferricyanide formation and the corresponding positions are summarised in Tab.5.5.

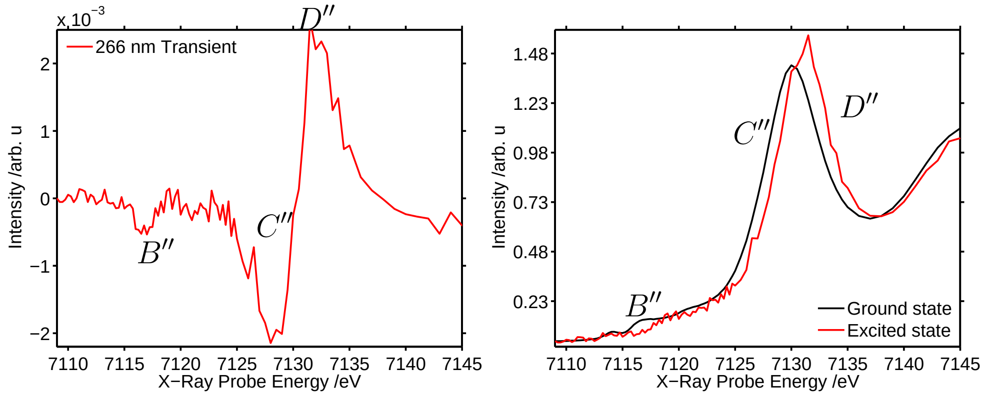

(a)

(b)

Figure 5.7.: (a) The transient signal is reconstructed from the 266 nm transient after subtracting the photoaquated transient. Letters B″, C″ and D″ are used to indicate the relevant spectral features for the ferricyanide formation. (b) Reconstructed $[\mathrm{Fe}^{\mathrm{III}}(\mathrm{CN})_6]^{3-}$ excited state contribution from the data measured after 266 nm laser excitation (red curve) together with the ground state spectrum (black curve).

Table 5.5.: Summary of identified photoaquated features and the corresponding energy positions.

features	B″	C″	D″
Energy (eV)	7117	7129	7132

Comparison of the transient spectrum measured after 266 nm excitation with static difference is shown Fig.5.8 before and after the photoaquated transient is subtraction. Both the reconstructed ferricyanide transient after photoaquated subtraction and scaled static data are in a good agreement within the experimental noise (see Fig.5.8(b)). As indicated in the Fig.5.7 the features B″, C″ and D″ are due to the ferricyanide photoproduct formation. Using these assigned features we can follow the relaxation process of the ferricyanide complex (see Sec.5.4).

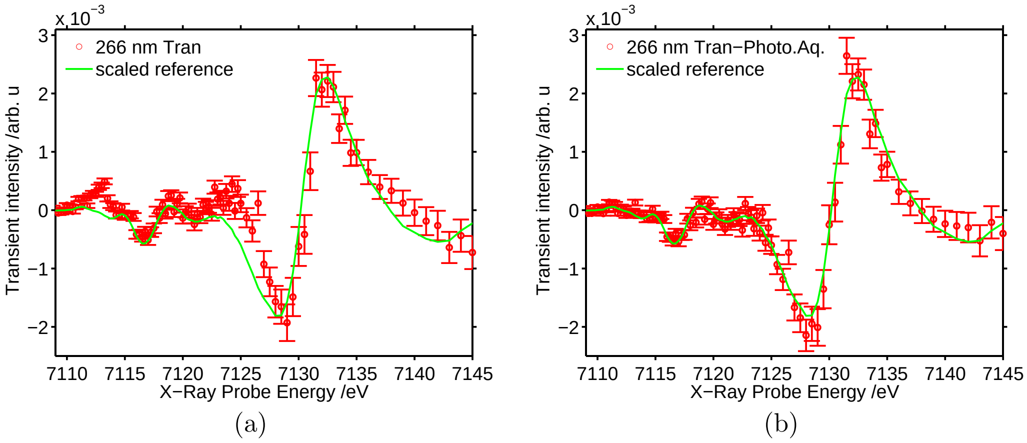

(a) (b)

Figure 5.8.: (a) Comparison of static difference between ferri and ferrocyanide scaled with f=7.26% with XANES transient measured after 100 ps of 266 nm excitation. (b) Comparison of static difference with ferricyanide transient only measured after 266 nm excitation after the photoaquated component is subtracted.

5.4. Reaction kinetics of aqueous ferrocyanide after 266 nm laser excitation

The delay scans reported in Fig.5.9(b) are measured after 266 nm photoexcitation of aqueous ferrocyanide solution. The delay scans are done at three selected energy points shown in Fig.5.9(a). In the delay scan measurements, we observe two different behaviors: B$''$ and D$''$-features show a similar decay whereas the A$'$-feature remains constant over 100 ns, which also agrees with the two expected photoproducts i.e. ferricyanide and photoaquated formation. Similar X-ray studies have been reported recently on the same molecule [25]. This implies the formation of two different photoproducts within the X-ray pulse duration. The B$''$- and D$''$-features show ∼12 ns decay constant and the signal do not converge to zero.

From the fit results, we have observed the ferricyanide complex formation and decay due to the non-geminate electron recombination of the hydrated electron to the ferricyanide molecule within roughly 12 ns. The fit results is summarised in Table 5.6. For the photoaquated complex, we only see the formation of the complex within the experimental resolution and the signal remains constant out to 1.224 μs, which indicates its long lifetime (see also Fig.5.16(a)). The data are shown in Fig.5.10 is fitted with a convolution of a Heaviside ($H(t)$), an exponential decay or rise, experimental error (i.e. integral of Gaussian) functions. We use the Heaviside

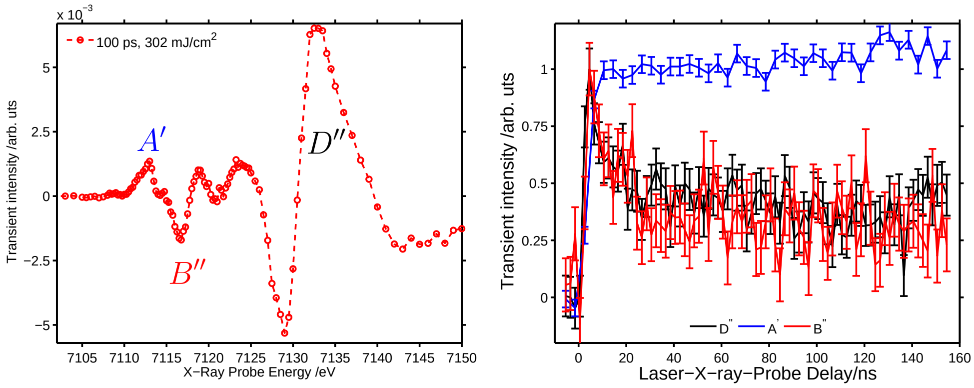

(a)

(b)

Figure 5.9.: (a) The transient signal of 50 mM aqueous ferrocyanide solution measured after 100 ps of 266 nm laser photoexcitation at 302 mJ/cm^2. The arrows indicated to show the positions where the delay scans measured. The negative feature which is marked with the B″ is a signature of the ferricyanide formation. (c) Normalized delay scan measurements at A′ (blue line) and D″ (magenta line) transient spectral features. The signal measured at B″ is multiplied with -1 for comparison. The delay scan measured at position of green arrow show no transient.

function to have a fixed time zero [167].

$$H(t) = \begin{cases} 1, & t > 0 \\ 0, & t < 0 \end{cases} \tag{5.6}$$

$$T_D(t - t_0) = A * e^{-(\frac{t-t_0}{\tau_D})} \tag{5.7}$$

$$T_r(t - t_0) = A * (1 - e^{-(\frac{t-t_0}{\tau_r})}) \tag{5.8}$$

$$G(t - t_0) = \frac{1}{\sigma\sqrt{(2\pi)}} e^{-\frac{(t-t_0)^2}{2\sigma^2}} \tag{5.9}$$

Where FWHM $= 2.355\sigma$ and the fit function is a convolution of the Heaviside, Gaussian and decay or rise exponential functions depending on the data.

$$f(t) = \int_{-t}^{t} H(t') \otimes G(t' - t_0) \otimes T(t' - t_0) \mathrm{d}t' \tag{5.10}$$

The diffusion control electron $\mathrm{e}^-_{\mathrm{aq}}$ recombination process which is estimated roughly 12 ns depends on the diffusion-control rate constant k_D. The diffusion-control rate constant can be obtained via:

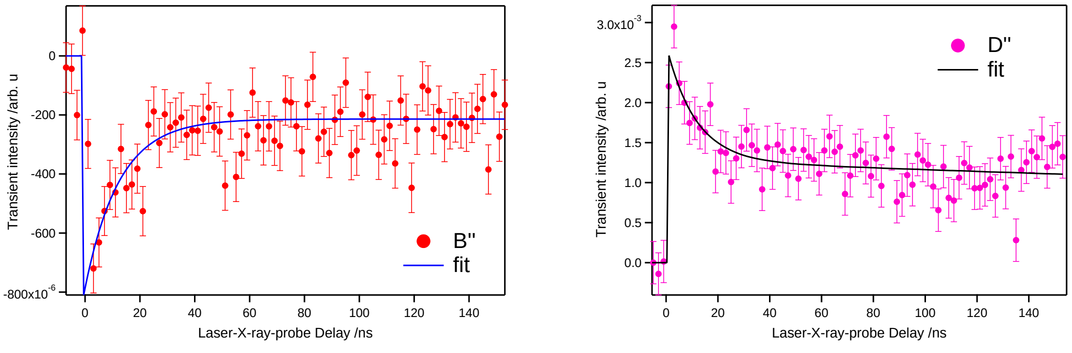

(a) (b)

Figure 5.10.: (a) and (b) Kinetics measured at 7117 eV (B″) and 7133 eV (D″) transient features. The 12 ns decay we see in these features is the non-geminate recombination of the electron to the ferricyanide molecule. The results obtained here are in a good agreement with the reported values by Reinhard *et al.* [25].

Table 5.6.: Fit results of kinetics measured at ferricyanide and photoaquated complex features. The τ_1 reported time is the non-geminate electron recombination to the time scans are done after 266 nm excitation.

features	Energy	σ_{x-ray}(ps)	τ_1 (ns)
A′	7113 eV	34	∞
B″	7117 eV	34	12.34±2.24
D″	7133 eV	34	11.23±3.51

$$k_D = 4\pi N_A r_C D_C, \tag{5.11}$$

where N$_A$ is Avogadro's number, r$_C$ is the sum of the radii of hydrated electron (e^-_{aq}) and the ferricyanide ($[Fe(CN)_6]^{3-}$) complexes. D$_C$ is the sum of diffusion coefficients of $e^-_{aq} = 4.9{\cdot}10^{-5}$cm^2 s^{-1} [172] and $[Fe(CN)_6]^{3-} = 0.9{\cdot}10^{-5}$cm^2 s^{-1} [173]. Using the r$_C$ = 5 Å [173], then k$_D$ becomes $2.546{\cdot}10^7$M^{-1} s^{-1}.

5.5. Spectral features of the photoaquated complex

After the excited state fraction is calculated for the 355 nm XANES measurements as shown in Sec.5.2.1 then we reconstruct the excited state spectrum via:

$$\mu_{aq}(E,\tau) = \mu_{GS}(E) + \frac{\Delta\mu_{355nm}(E,\tau)}{f_{aq}(\lambda)}, \tag{5.12}$$

where $f_{aq}(\lambda)$ is the excited state fraction, $\mu_{aq}(E,\tau)$ is excited state spectrum for aquated complex, and $\Delta\mu_{355nm}(E,\tau)$ is transient measured after 355 nnm laser excitation. The assignment of the important spectral features (Fig.5.11(b)) is the following; the A′, B′, C′, D′ and E′ are assigned for the photoaquated complex produced after 355 nm laser excitation. All listed features and the corresponding position is summarised in Table 5.7.

Table 5.7.: Summary of identified photoaquated features and the corresponding energy positions.

features	A′	B′	C′	D′	E′
Energy (eV)	7113.0	7118.5	7127.0	7130.0	7138.0

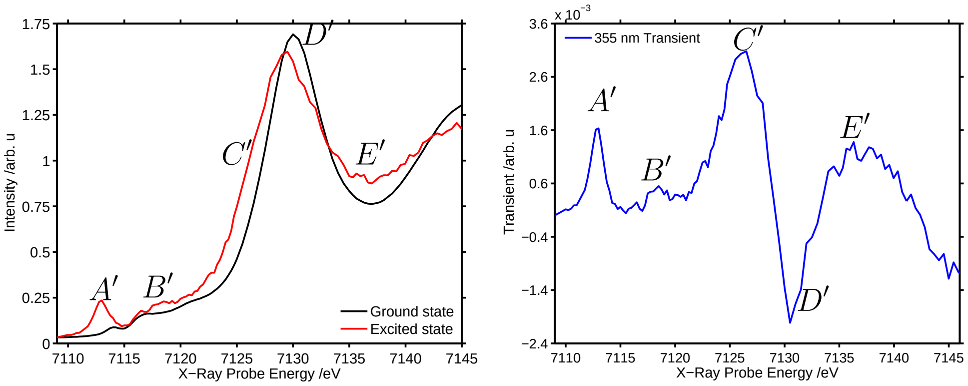

(a) (b)

Figure 5.11.: (a) Reconstructed excited state spectrum with f_{aq}= 9.67% measured at 100 ps after 355 nm laser excitation (red curve) and the ground state spectrum (black curve). (b) The transient signal measured at 100 ps with a laser intensity of at 55 GW/cm^2. Letters A′, B′, C′, D′ and E′ are used to indicate the relevant spectral features.

A′ and B′ are quite intense pre-edge features which are due to the photoaquated formation. As discussed in Section 3.2.4 these pre-edge features originate from dipole-forbidden 1s → 3d transitions, and the peak intensity can be enhanced via intermixing of 3d with 4p orbitals [28, 30, 95]. In addition, for a centrosymmetric molecule these quadrapole-allowed transitions are very weak with little intermixing with 4p orbitals. However, when the inversion symmetry is removed, as discussed by Westre *et al.*, the pre-edge peak intensities increase as a consequence of the increases 4p mixing. The A′-feature has also been observed in previous studies [27], while the B′-feature, centred at ∼7118.5 eV is reported for the first time.

5.5.1. Comparison with static spectra of $[Fe^{II}(CN)_5H_2O]^{3-}$

A 20 mM solution of $[Fe^{II}(CN)_5H_2O]^{3-}$ as a static reference complex was prepared by mixing 0.652 gram $Na_3[Fe^{II}(CN)_5NH_3]$ in 100 ml of water, 0.352 gram ascorbic acid ($C_6H_8O_6$) and 2-3 ml of acetic acid. As a result, the NH_3 is released as a gas and water molecule attached to Fe to form $[Fe^{II}(CN)_5H_2O]^{3-}$ complex. The solution has to be kept in the refrigerator until right before measurements. The integrity of the sample was checked during the experiment by inspecting consecutive laser off scans, and we noticed degradation during the experiment. We did experiments in a neutral condition, and we look at much shorter time scales, but subsequent thermal reactions are reported both in alkaline and acidic condition [174] which does not change our interpretation of the experimental results.

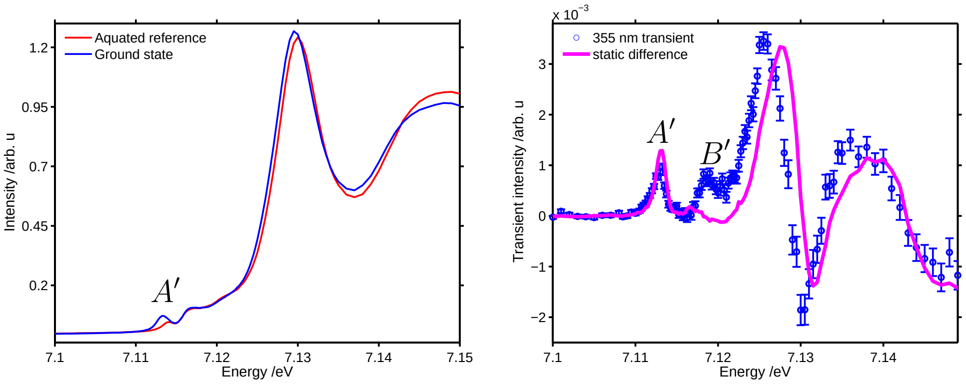

(a)

(b)

Figure 5.12.: (a) Reference spectra measured on $[Fe^{II}(CN)_5H_2O]^{3-}$ reference complex (red curve) and the ground state spectra measured on $[Fe^{II}(CN)_6]^{4-}$ complex. (b) Comparison of static difference with XANES transient measured after 100 ps of 355 nm laser excitation.

Shown in Fig.5.12(a) is the comparison of Fe K-edge static XANES spectra of the aquated and ferrocyanide complexes. The aquated reference spectra show intense A′ pre-edge feature and the edge is blue-shifted with respect to ground state XANES spectra. Shown in Fig.5.12(b) is the comparison of the static difference spectrum with our 355 nm transient. The static difference spectrum is blue-shifted with respect to 355 nm transient and the disagreement between the two data could be due to degradation of the sample both with X-rays and optical laser. Having this in mind, we acquire transient XANES on $[Fe^{II}(CN)_5H_2O]^{3-}$ sample after 100 ps of 355 nm laser excitation, the result is shown in Fig.5.13. We expect that upon photoexcitation of the $[Fe^{II}(CN)_5H_2O]^{3-}$ complex it will photooxidize to form $[Fe^{III}(CN)_5H_2O]^{2-}$ [174].

The transient XANES acquired on $[Fe^{II}(CN)_5H_2O]^{3-}$ complex after 355 nm excitation is not identical to the transient measured on $[Fe^{II}(CN)_6]^{4-}$ complex after 355 nm laser excitation. But the general trend of both transients is similar, the B′-feature is present in $[Fe^{II}(CN)_5H_2O]^{3-}$ transient data. As a result, the B′-feature could be due to a formation of $[Fe^{III}(CN)_5H_2O]^{2-}$ photoproduct but its formation upon excitation of ferrocyanide at 355 nm is unclear, and this will be discussed in depth in a separate Section (see Sec.5.8).

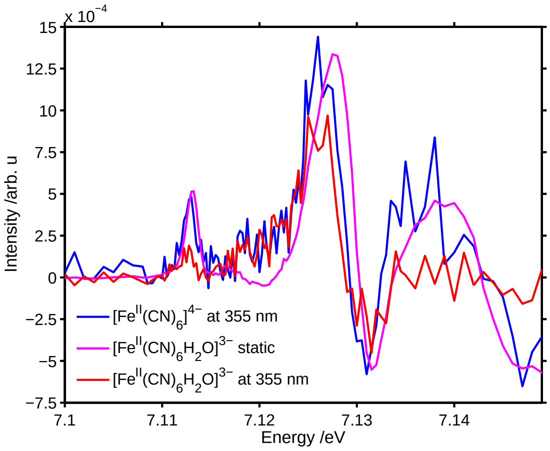

Figure 5.13.: Comparison of the static aquated difference spectrum with the transient XANES of $[Fe^{II}(CN)_5H_2O]^{3-}$ (red curve) and $[Fe^{II}(CN)_6]^{4-}$(blue curve) measured after 100 ps of 355 nm laser excitation.

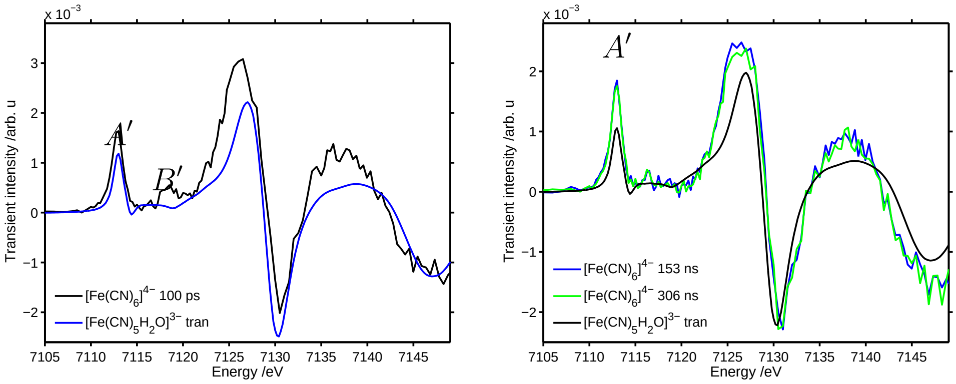

(a) (b)

Figure 5.14.: (a) Comparison of ferrocyanide transient measured at 100 ps after 355nm excitation with simulated difference between $[Fe^{II}(CN)_5H_2O]^{3-}$ and ground state. (b) Comparison of 153 ns and 306 ns transient with simulated difference spectra.

In Fig.5.14(a) we show theoretically calculated differences from the bi-valent aquated complexes with experimental transient measured at 100 ps. The B′-feature which we observe in the 355 nm transient at 100 ps is not reproduced in the calculated difference since it originates from the $[\mathrm{Fe}^{\mathrm{III}}(\mathrm{CN})_5\mathrm{H}_2\mathrm{O}]^{2-}$ complex which is not shown here. Also, we compare the 153 ns and 306 ns transient spectra with the calculated difference as shown in Fig.5.14(b), the result show good agreement in the pre-edge and edge region, which indicates towards the formation of the long-lived photoaquated complex.

5.6. Reaction kinetics of aqueous ferrocyanide after 355 nm laser excitation

To understand the reaction dynamics of the photoaquated complex we looked at the transient signal at different delays (see Fig.5.15). The result shown is measured at 55 GW/cm^2 laser intensity where both A′ and B′-features is clearly visible. The A′-feature does not show decay, however, the B′-feature decays, and the signal disappears after 153 ns. A similar measurement is done at 17.2 GW/cm^2 intensity shown in Fig.5.16(a), where the B′-feature is not clearly visible. This indicates that A′ and B′-features show different behaviour at different pump laser conditions.

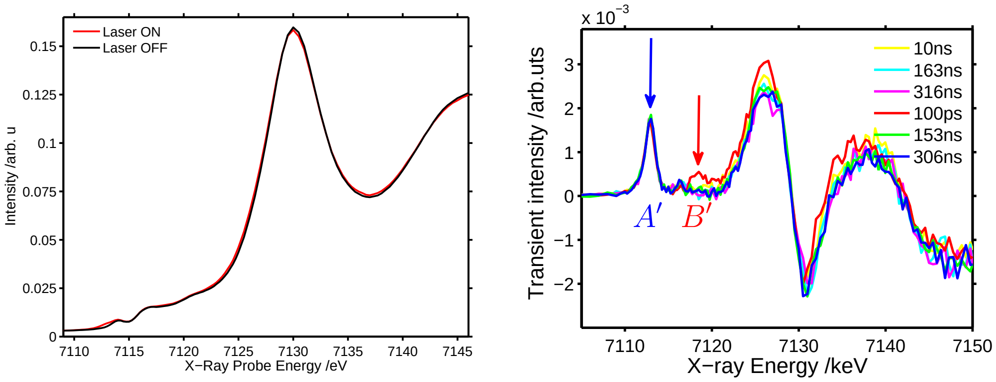

(a) (b)

Figure 5.15.: (a) Time-resolved XANES spectrum of 50 mM aqueous ferrocyanide solution measured before and after 355 nm laser excitation. (b) The transient signal measured at 100 ps with a laser pump intensity of at 55 GW/cm^2. Arrows indicated are positions where delay scans measured which are shown in Fig.5.16(b).

The measurements reported in Fig.5.15(b) were performed at a rather high intensity. For this reason, we added low fluence measurements, as indicated in the Fig.5.16(a). Using the special detection scheme (see Section 4.5), we equally exploit the consecutive X-ray bunches to obtain data at longer time delays out to ∼1

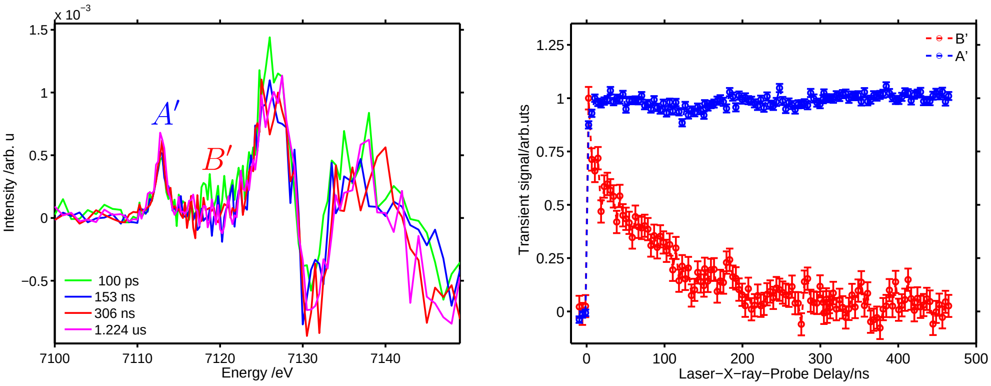

(a) (b)

Figure 5.16.: (a) The transient signal measured at 100 ps after 355 nm laser excitation at 17.5 GW/cm^2 intensity. (b) Delay scans measured at 72.5 GW/cm^2 laser intensity at the A′ and B′-features.

μs. The result confirms the same behaviour of A′-feature as for the high-intensity measurements, while the B′-feature is not clearly visible within the level of noise in the measurement, indicating the intensity-dependence of the B′-feature. As shown in the Fig.5.16(b), the A′-feature indicates the formation of the photoaquated photoproduct within the experimental time resolution and does not change within the 450 ns time window. On the contrary, the B′-feature shows formation within the X-ray pulse width and the signal disappears completely after 153 ns. The behaviour of features is different, indicating that two photoproducts are present. We have fitted the delay scan at the B′-feature using Eq.5.10 with two time constants $\tau_1 \simeq 4.6 \pm 0.5$ ns and $\tau_2 = 105.1 \pm 4.8$ ns (Fig.5.17). The time constant τ_1 and τ_2 are due to the diffusion control electron recombinations to $[Fe^{III}(CN)_5H_2O]^{2-}$ complex from the different areas of solvation shell.

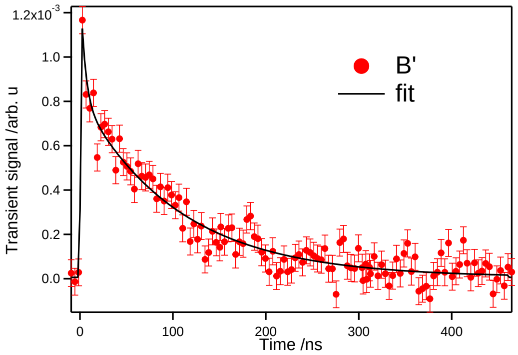

Figure 5.17.: Kinetics fit of the delay scan measured at the B′-features. For the fit two decay time constants were used.

5.7. UV excitation of ferricyanide complex

Similar to the ferrocyanide measurements reported in the previous section, we measured XAS spectra after 266 nm excitation of ferricyanide complex (see Fig.5.18).UV excitation of ferricyanide molecule generates tri-valent aquated complex [175]. Fuller *et al.*[174] reported a quantum yield of 0.02-0.06 for $[\mathrm{Fe^{III}(CN)_5H_2O}]^{2-}$ formation at 254 nm which is roughly five times smaller than that for $[\mathrm{Fe^{II}(CN)_5H_2O}]^{3-}$ formation after excitation $[\mathrm{Fe^{II}(CN)_6}]^{4-}$ at the same wavelength.

$$[\mathrm{Fe^{III}(CN)_6}]^{3-} + \mathrm{H_2O} \xrightarrow{h\nu} [\mathrm{Fe^{III}(CN)_5H_2O}]^{3-} + \mathrm{CN^-} \tag{5.13}$$

In Fig.5.18(b), we observe both A′ and B′-features, implying they could be both fingerprint of the photoaquated product presented in the previous section. We propose that the B′-feature is due to re-excitation of the bi-valent photoaquated product to a tri-valent photoaquated complex. This could happen only if the photoaquated complex is formed within the laser pulse width (10 ps). Indeed, Sec.5.8 will show that indeed the first transition is saturated due to high-intensity results re-excitation within the 10 ps time constant. Thus this process seems possible.

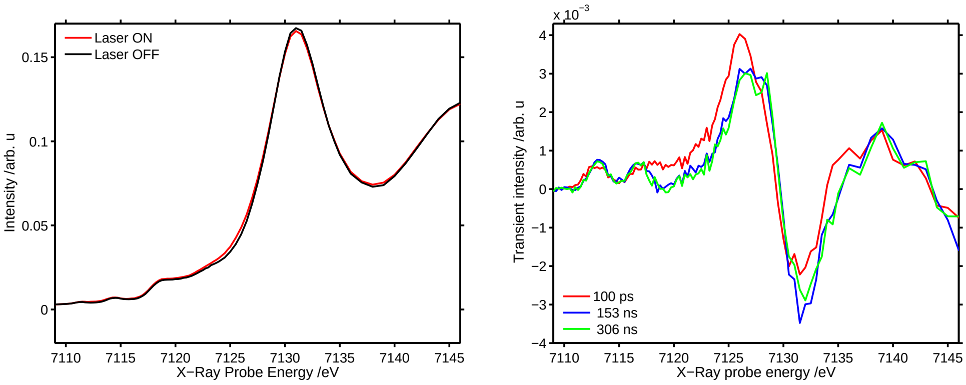

(a) (b)

Figure 5.18.: (a) Time-resolved XANES spectrum of 50 mM aqueous ferricyanide solution measured after 266 nm laser excitation at 100 ps. (b) Transient spectra measured at different time delay at laser intensity of 30.2 GW/cm^2.

5.8. Intensity dependence measurements

In order to inspect the effect of the incident laser pump intensity, the assigned transient peak features A′- and B′ is monitored as a function of incident laser intensities. With 10 ps Duetto laser pulse, we achieve peak intensities of ∼(1.8 -

16.2)*10^{28} photons $\mathrm{cm}^{-2}\mathrm{s}^{-1}$ (~10 - 90 GW cm^{-2}) (see 5.19(a)). The high intensity may lead to multiphoton absorption or step-wise excitation to highly excited states which in return exhibit new deactivation pathways of ferrocyanide molecule. Here we exclude multiphoton absorption by solvent since the peak intensity at the highest fluence used in the data reported is 90 GW cm^{-2} which is much lower than 2 TW cm^{-2} intensity reported for multiphoton absorption in neat water[176].

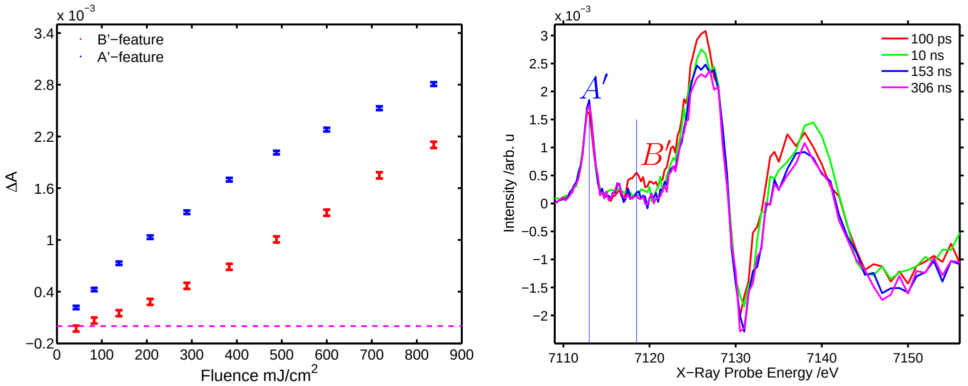

(a) (b)

Figure 5.19.: (a) Fluence dependence of A′- and B′-features measured after 100 ps of 355 nm laser excitation. (b) Transient spectrum measured at a different time delay after 355 nm laser excitation.

High-intensity study with femtosecond pulses by Tarnovsky *et al.* [176] on aqueous $[\mathrm{Ru}^{\mathrm{II}}(\mathrm{bpy})_3]^{2+}$ complex the high peak intensities resulted photoproducts such as $[\mathrm{Ru}^{\mathrm{II}}(\mathrm{bpy})_3]^{+}$, $[\mathrm{Ru}^{\mathrm{III}}(\mathrm{bpy})_3]^{3+}$ next to $\mathrm{e}^-_{\mathrm{aq}}$ which is due to excitation of long-lived ^{3}MLCT excited state. For our experiments we used a 10 ps laser pulse and recent 2D-UV transient absorption spectroscopy results on the aqueous ferrocyanide molecule reported the relaxation of ferrocyanide from the $^1\mathrm{T}_{1g}$ in ~0.5 ps to a transition state before photoaquated formation[25]. As a result during high intensity measurements the second photon absorption can happen from the relaxed photoaquated complex since the $^1\mathrm{T}_{1g}$ state is short-lived. Similar to what has been done on ref.[176], for our case the first transition to ligand-field state is saturated as a consequence the second photon can be absorbed form the relaxed state. For the 10 ps pulse duration (at FWHM), $^1\mathrm{T}_{1g}$ lifetime of τ_{IC} ~0.5 ps and σ_{355nm} = $4.58\cdot10^{-19}$ cm^2, the saturation parameter for the peak intensities of ~(1.8 - 16.2)*10^{28} photons $\mathrm{cm}^{-2}\mathrm{s}^{-1}$ can be calculated as: $\sigma_{355nm}\cdot\mathrm{I}_0\cdot\tau_{IC}$ is less than unity. This indicates we can't have a excitation from $^1T_{1g}$ transient state since it is short lived.

$$[\mathrm{Fe}^{\mathrm{II}}(\mathrm{CN})_6]^{4-}_{\mathrm{aq}} \xrightarrow{h\nu} {}^1\mathrm{T}_{1\mathrm{g}} \tag{5.14}$$

$$[\mathrm{Fe}^{\mathrm{II}}(\mathrm{CN})_5\mathrm{H}_2\mathrm{O}]^{3-}_{\mathrm{aq}} \xrightarrow{\mathrm{h}\nu} [\mathrm{Fe}^{\mathrm{III}}(\mathrm{CN})_5\mathrm{H}_2\mathrm{O}]^{2-}_{\mathrm{aq}} + \mathrm{e}^{-}_{\mathrm{aq}} \tag{5.15}$$

Similarly, the saturation parameter for $[\mathrm{Fe}^{\mathrm{II}}(\mathrm{CN})_5\mathrm{H}_2\mathrm{O}]^{3-}$ is calculated using the lifetime 16 ps reported ref.[25] and it ranges between 0.136 - 1.2. This indicates at higher fluence the re-excitation of primary photoproduct kicks in and Eq.(5.15) can happen resulting hydrated electron. The hydrated electron recombines to tri-valent $[\mathrm{Fe}^{\mathrm{III}}(\mathrm{CN})_5\mathrm{H}_2\mathrm{O}]^{2-}$ complex at different times scales depending on how far the electron is from the complex. For this reason, to avoid the secondary excitation process due to the high intensity laser, the pump intensity should be below ≤ 50 GW cm^{-2}.

As reported in the proceeding Section 5.6 the B′-feature show different behavior at the different laser pump fluence regimes while the A′-feature seems to behave linearly (see Fig.5.19). Combining the saturation parameter calculated above and non-linear behavior observed on the B′-feature: the two-step photon absorption happens as the first photon saturated the photoaquated $(\mathrm{Fe}^{\mathrm{II}}(\mathrm{CN})_5\mathrm{H}_2\mathrm{O}]^{3-})$ transition and the second photon oxidizes and results a tri-valent photoaquated complex $(\mathrm{Fe}^{\mathrm{III}}(\mathrm{CN})_5\mathrm{H}_2\mathrm{O}]^{2-})$ along with hydrated electron. Here we are not excluding the fact that other photoproducts. As a sanity check, we record a transient XAS data by exciting ferricyanide complex at 266 nm which results tri-valent photoaquated complex $(\mathrm{Fe}^{\mathrm{III}}(\mathrm{CN})_5\mathrm{H}_2\mathrm{O}]^{2-})$. Shown in Fig.5.20 is the XAS transient of tri-valent photoaquated complex compared with XAS transient of ferrocyanide measured at 55 GW/cm^2. The figure shows the B′-feature is also present in the XAS transient of tri-valent photoaquated complex which indicates minor presence of tri-valent photoaquated complex in the high intensity XAS data measured on ferrocyanide molecule.

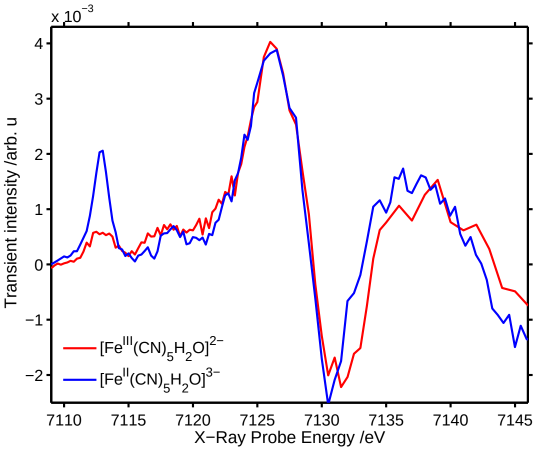

Figure 5.20.: Comparison of transient signal measured after 266 nm laser excitation of aqueous ferricyanide molecule (red spectrum) and transient signal measured after excitation of aqueous ferrocyanide molecule (blue spectrum). Both transient spectra shown are measured at 100 ps.

5.9. Discussion

5.9.1. Excitation at 266 nm

Prior picosecond-resolved XAS studies of ferrocyanide molecule by Reinhard *et al.*, have shown the formation of ferricyanide and photoaquated complex after 266 nm laser excitation [27]. Our study also showed that photoexcitation at 266 nm laser results to two photoproducts i.e. predominantly ferricyanide complex in addition to the photoaquated complex. Using the static reference measurements and previously reported quantum yields we disentangle the two photoproducts. Based on this we extract the excited state the fraction value of the set of measurements. In this respect, we showed a simplified way to disentangle the two photoproducts which were not done in prior studies. Also, we did a time scan after 266 nm photoexcitation of aqueous ferrocyanide molecule which results in ferricyanide molecule, and we observe the formation of the ferricyanide molecule within the experimental resolution and the non-geminate recombination of the electron which takes roughly 12.34 ±2.24 ns. The time scale obtained here is in a good agreement with prior studies on similar system[25]. Based on our experimental data we postulate the relaxation which is shown in Fig.5.21.

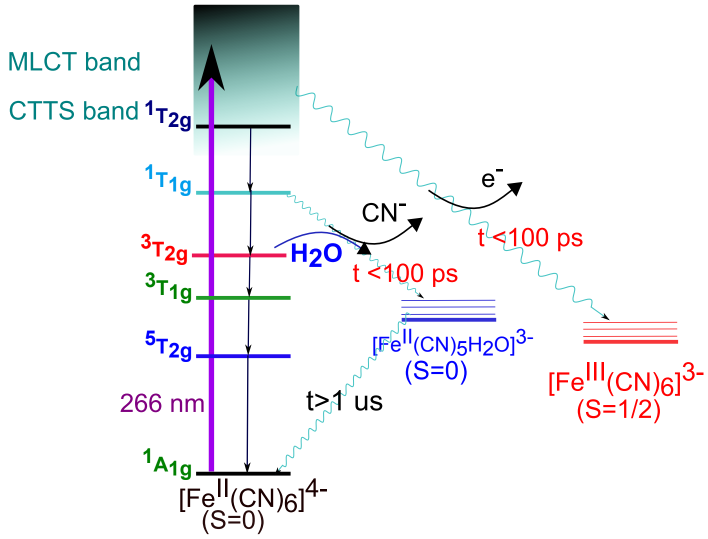

Figure 5.21.: Relaxation pathway of 266 nm excited ferrocyanide molecule in aqueous solution. Based the Picosecond XANES resulted reported earlier in this Chapter, both the ferricyanide and photoaquated complexes are formed within the experimental time resolution of 100 ps. A similar relaxation pathway has been reported by Reinhard *et al.*[25]. In our data we also observe the non-geminate electron recombination to the ferricyanide molecule with ca. 12 ns and the relaxation of photoaquated complex back to ferrocyanide ground state molecule with timescale of $> 1\ \mu$s.

5.9.2. Excitation at 355 nm

Based on the previous studies photoexcitation of aqueous ferrocyanide with 355 nm results bi-valent photoaquated ($Fe^{II}(CN)_5H_2O]^{3-}$) complex [27, 25]. Our low fluence studies conclude similar out come but when we increase the pump laser fluence(intensity) we observe a two-step process. The first laser photon results bi-valent photoaquated ($Fe^{II}(CN)_5H_2O]^{3-}$) complex. Since the bi-valent photoaquated complex is formed within the 10 ps pulse duration; as a result, it can absorb a second laser photon to form a tri-valent photoaquated ($Fe^{III}(CN)_5H_2O]^{2-}$) complex. The B′-feature observed at high laser intensity is assigned to tri-valent aquated complex based the calculated saturation parameter.

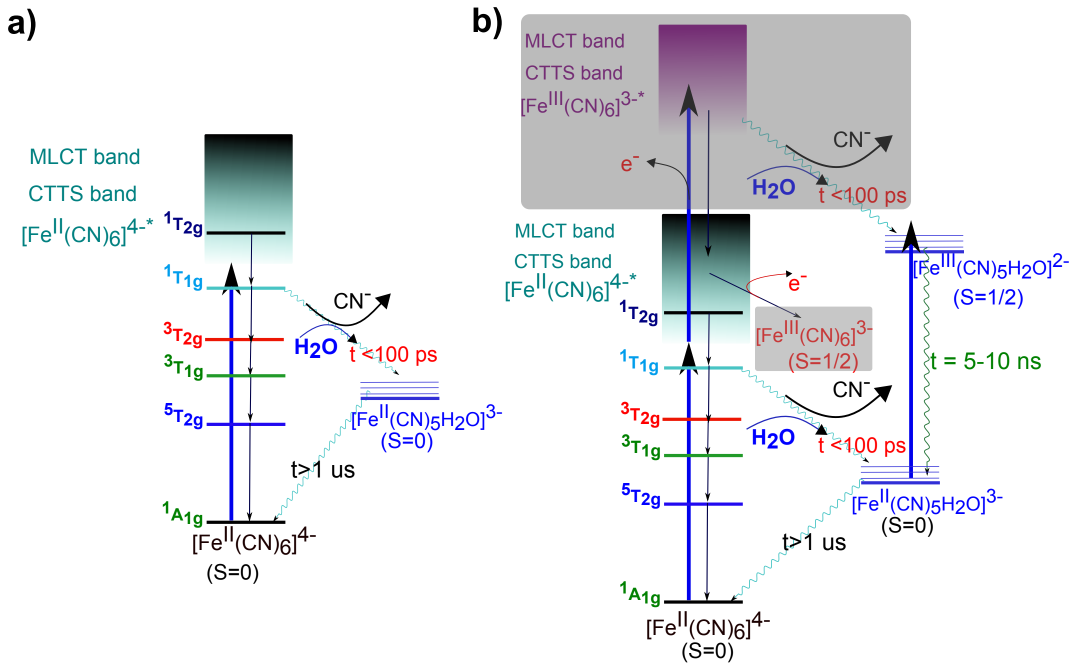

Figure 5.22.: Proposed possible relaxation pathways after 355 nm laser excitation based on the picosecond XANES data measured at the synchrotron. (a) At low laser fluence with 100 ps time resolution we observe the formation of $[Fe^{II}(CN)_5H_2O]^{3-}$ complex. The relaxation back to the ground state takes more than 1 μs. (b) At high laser fluence with 10 ps laser pulse, we think that we re-excite the $[Fe^{II}(CN)_5H_2O]^{3-}$ complex to from $[Fe^{III}(CN)_5H_2O]^{2-}$ complex which relaxes with 5-10 ns by electron recombination. The gray shaded part of the reaction cycle is possible with two 355 nm photon absorption but with 10 ps laser used for this experiment, it is not clear if we have two photon absorption. This scenario will be discussed in detail in Ch.7, when femtosecond laser source is used for the experiment.

According to [175, 174] excitation of aqueous ferricyanide solution with a UV laser undergoes only ligand substitution reaction. As indicated in Eq.(5.13) reaction happens irrespective the energy of the pump (hν). Having said that, as can be seen in Fig.5.20 the pre-edge peak we observe at 7118.5 eV could also be from tri-valent photoaquated formation ($[\mathrm{Fe^{III}(CN)_5H_2O}]^{3-}$). Before answering the question of how this reaction happens, we need to remember that the B′-feature is apparent only at higher intensity measurements. Based on this fact and the saturation parameter calculated above, one possibility is the first laser photon results $\mathrm{Fe^{II}(CN)_5H_2O]^{3-}}$ complex and the second photon can results $\mathrm{Fe^{III}(CN)_5H_2O]^{3-}}$ by photooxidizing the primary photoproduct. The electron recombines with the $\mathrm{Fe^{III}(CN)_5H_2O]^{3-}}$ complex at different time scales ($\tau_1 \simeq 4.6 \pm 0.5$ ns and $\tau_2 = 105.1 \pm 4.8$ ns) through a diffusion control non-geminate recombination.

As a result we conclude that the due to the high laser intensity (≥ 50 GW cm^{-2}) we have a tri-valent photoaquated contribution along with bi-valent photoaquated complex and hydrated electron in our measurements. Based on these results we proposed the ligand dissociation and association reaction will follow the following steps (see Eqs.5.16 and 5.17).

- At low intensity ≤ 50 GW cm^{-2}:

$$[\mathrm{Fe^{II}(CN)_6}]^{4-}_{\mathrm{aq.}} \xrightarrow{\mathrm{h}\nu} [\mathrm{Fe^{II}(CN)_5H_2O}]^{4-}_{\mathrm{aq}} + \mathrm{CN}^{-}_{\mathrm{aq}} \tag{5.16}$$

- At high intensity ≥ 50 GW cm^{-2}:

$$[\mathrm{Fe^{II}(CN)_6}]^{4-}_{\mathrm{aq.}} \xrightarrow{\mathrm{h}\nu} [\mathrm{Fe^{II}(CN)_5H_2O}]^{4-}_{\mathrm{aq.}} + \mathrm{CN}^{-} \xrightarrow{\mathrm{h}\nu} [\mathrm{Fe^{III}(CN)_5H_2O}]^{2-} + \mathrm{CN}^{-} + \mathrm{e}^{-}_{\mathrm{aq.}} \tag{5.17}$$

Finally, based on the XANES results measured after 355 nm excitation of ferrocyanide molecule in aqueous solution is summarised in Fig.5.22.

Chapter 6

Time-resolved X-ray emission results on photoexcited aqueous ferrocyanide molecule

In the preceding Chapter, we showed how we disentangle both the simultaneous photooxidation and photoaquation reaction channels using only picosecond XANES. Our finding suggests that after 266 nm laser excitation the photooxidation channel results roughly twice more excited state fraction compare to the photoaquation channel, similar to the quantum yield results reported by Shirom *et al.*[15, 1] and recently by Reinhard [27]. In addition to XAS, with the XES we can monitor spin state changes to chemical reactions. Both Kα and Kβ XES emission lines can be used to distinguish between $[\mathrm{Fe^{III}(CN)_6}]^{3-}$ and $[\mathrm{Fe^{II}(CN)_6}]^{4-}$, while $[\mathrm{Fe^{II}(CN)_5H_2O}]^{3-}$ photoproduct should exhibit no spin state change.

In this Chapter, we will exploit picosecond-resolved X-ray emission spectroscopy measurements to track the electronic changes that occur during the light-induced reaction sequence. We exploit time-resolved core-to-core (Kβ) and valence-to-core (K$\beta_{2,5}$) emission lines to track chemical reaction of ferrocyanide molecule. In the first Section, we will present the reaction mechanism following 266 nm laser excitation of aqueous ferrocyanide molecule. Part of the results presented in Sec.6 are published in reference [130]. In the second Section, time-resolved Kβ and valence-to-core XES results measured after photoexcitation with 355 nm laser will be presented.

6.1. Picosecond XES results after 266 nm excitation

Fig.6.1 shows the measured Kβ emission spectra for ferricyanide and ferrocyanide complexes in aqueous solution. Each spectrum consist of the main peak K$\beta_{1,3}$ due to a transition from 3p→1s, and a small and broad shoulder at lower energy, Kβ'. If unpaired 3d electrons are present in the ion due to the intra-atomic exchange interaction between the unpaired 3p core electron and unpaired 3d valence electrons transfers intensity into the Kβ' region [177]. A higher spin-state produces more intensity in Kβ' shoulder and a shift of K$\beta_{1,3}$ peak to the higher energy [122]. Fig.6.1(a) we observe ∼1 eV blue shift of $[Fe^{III}(CN)_6]^{3-}$ spectrum with respect to $[Fe^{II}(CN)_6]^{4-}$. The K$\beta_{1,3}$ peak of ferrocyanide ion is at 7057 eV shifts to 7058 eV in ferricyanide ion spectrum which is due to the spin-state change from S = 0 to S=1/2. This is in addition to an intensity increase observed in the Kβ' shoulder.

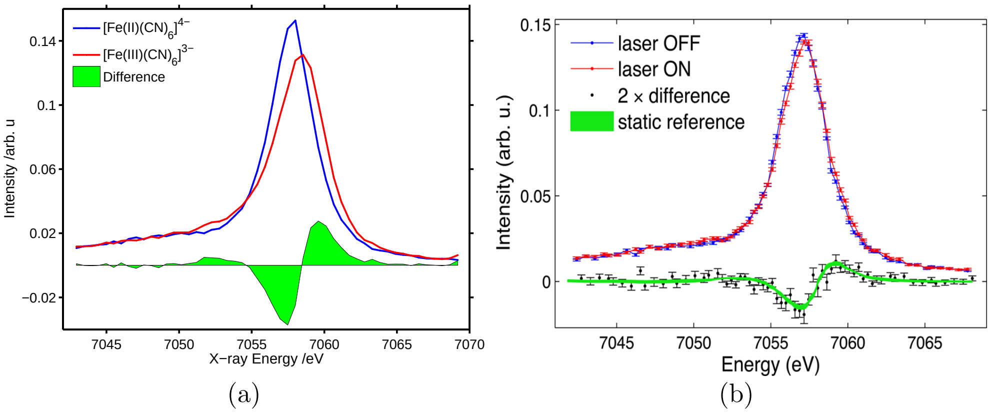

(a) (b)

Figure 6.1.: (a) Kβ (3p→1s) emission spectra measured for 0.4 M aqueous solution of $[Fe^{III}(CN)_6]^{3-}$ (red), $[Fe^{II}(CN)_6]^{4-}$ (blue) and the difference between these spectra. (b) Measured time-resolved Kβ emission spectrum on 50 mM aqueous $[Fe^{II}(CN)_6]^{4-}$ measured before and 120 ps after 266 nm laser excitation. The difference between laser-on and laser-off is compared to the scaled difference between the reference samples discussed in Sec.3.3.1. Fig.6.1(b) from [130].

Excitation of ferrocyanide ion with 266 nm laser generates singly ionised ferricyanide species along with the photoaquated complex [1, 2]. We record Kβ emission spectra before and after 120 ps of laser excitation (see Fig.6.1(b)). We observe a blue-shift of the laser ON the main feature which also indicate the formation of ionised species. It was expected that photoaquated photoproduct does not undergo spin-state change (see Fig.6.3(b)). However, ferricyanide changes its spin-state from S = 0 to S=1/2. The time-resolved transient is compared to the static reference difference signal showing that ferricyanide is the dominant photoproduct, also in agreement with our XANES results (see Chapter 5). However, the observation does not exclude the possibility that other photoproducts are also contributing to the transient signal. Kβ is sensitive to details of the absorbing ion's chemical environment and it is a powerful probe of spin state [178]. Kβ XES spectra of different chemical species with the same spin state look very similar and quite different to those with different spin states (see Section 3.3.1). In the present case, where photoaquation occurs alongside the photooxidation reaction [63], and while the photoaquated product $[Fe^{II}(CN)_5H_2O]^{3-}$, does not a spin change, its XES difference signal could only contribute due to changes in the metal–ligand covalency [178]. Separating contributions from multiple photoproducts in Kβ emission spectra is still a challenge and makes obtaining useful spin-state information for products involved in photoinduced chemical reactions difficult. Detailed studies show that for highly covalent compounds such as $[\mathrm{Fe^{II}(CN)_6}]^{4-}$ the interpretation of the line shapes is more complicated (see [179, 180]).

The Kβ emission line also does not differentiate among the multiple photoproducts which undergo spin change. However, the valence-to-core (vtc) emission lines show greater sensitivity to changes in the chemical environment around the absorbing metal ion [90]. Vtc emission line spectra are dominated by iron np→1s electric dipole-allowed transitions, which has some sensitivity to spin state, ligand identity, ligand ionisation state, hybridization state, and metal-ligand bond lengths [181].

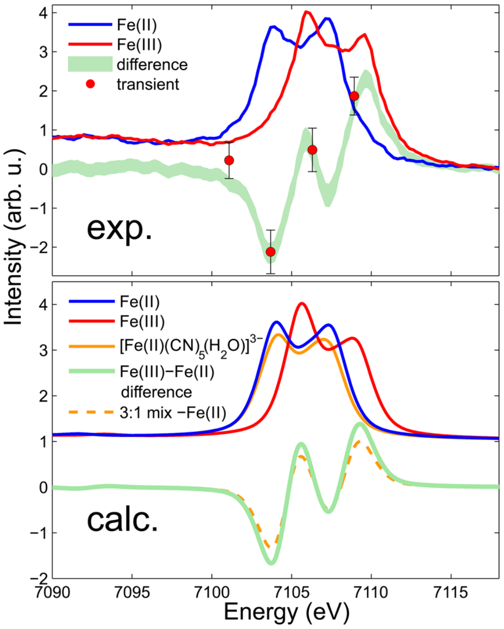

Figure 6.2.: Top panel is measured valence-to-core emission spectra of $[\mathrm{Fe^{II}(CN)_6}]^{4-}$ (blue) and $[\mathrm{Fe^{III}(CN)_6}]^{3-}$ (red) aqueous solutions. Bottom panel is shown the DFT calculated spectra along with the third possible species, the photoaquated product $[\mathrm{Fe^{II}(CN)_5H_2O}]^{3-}$. The differences between the $[\mathrm{Fe^{II}(CN)_6}]^{4-}$ and $[\mathrm{Fe^{III}(CN)_6}]^{3-}$ spectra is shown in green. The red data are the difference between before and after 120 ps of 266 nm laser excitation of $[\mathrm{Fe^{II}(CN)_6}]^{4-}$. The amplitude of the points has been scaled to show the agreement with the reference difference signal. Adapted from [130].

Shown in Fig.6.2 of the top panel is the measured time-resolved vtc XES data. The four data points are the difference between laser OFF and laser ON measured after 120 ps of 266 nm excitation of 50 mM aqueous $[\mathrm{Fe^{II}(CN)_6}]^{4-}$. Each data point results from a total of 2-hour integration. The Johann emission spectrometer was cycled through the four emission energies sitting at each for 2 minutes at a time. The four points are compared to the difference between static measurements of 400 mM aqueous $[\mathrm{Fe^{II}(CN)_6}]^{4-}$ and $[\mathrm{Fe^{III}(CN)_6}]^{3-}$. Since $[\mathrm{Fe^{III}(CN)_6}]^{3-}$ is the dominant photoproduct the time-resolved points seem to follow the difference signal. However, the photoaquated product $[\mathrm{Fe^{II}(CN)_5H_2O}]^{3-}$ is also expected to be present. However, $[\mathrm{Fe^{II}(CN)_5H_2O}]^{3-}$ complex is not stable and difficult to measure alone in a static measurement.

Calculated spectra of $[\mathrm{Fe^{II}(CN)_6}]^{4-}$, $[\mathrm{Fe^{III}(CN)_6}]^{3-}$ and $[\mathrm{Fe^{II}(CN)_5H_2O}]^{3-}$ are shown in the bottom panel of Fig.6.2. The $[\mathrm{Fe^{II}(CN)_6}]^{4-}$ and $[\mathrm{Fe^{III}(CN)_6}]^{3-}$ spectra are in excellent agreement with the experimental spectra. The $[\mathrm{Fe^{III}(CN)_6}]^{3-}$ spectrum is shifted to higher energy with respect to the $[\mathrm{Fe^{II}(CN)_6}]^{4-}$ spectrum due here also to the change in the effective nuclear charge on the metal. The calculated $[\mathrm{Fe^{II}(CN)_5H_2O}]^{3-}$ spectrum is very similar to the $[\mathrm{Fe^{II}(CN)_6}]^{4-}$ spectrum, exhibiting only a loss of signal amplitude. This originates from the fact that the Fe−O distance is rather large in the photoaquated complex (2.19 Å as compared to 1.92 Å for the Fe−C distance in the Fe−CN bonds), leading to little overlap of the O 2s and 2p orbitals with the iron center and therefore negligible contribution to the signal. In effect, the spectrum is due to five CN ligands as opposed to six, and therefore the intensity of the signal is less. The symmetry of $[\mathrm{Fe^{II}(CN)_5H_2O}]^{3-}$ is distorted relative to $[\mathrm{Fe^{II}(CN)_6}]^{4-}$, and this difference in geometrical arrangement of the CN ligands around the Fe centre does not appear to influence the shape of the spectra.

The difference spectra are shown in the lower panel of Fig.6.2 are the difference between ferrocyanide and ferricyanide, compared to the measured difference signal (top panel). For the latter, the relative amounts of $[\mathrm{Fe^{III}(CN)_6}]^{3-}$ and $[\mathrm{Fe^{II}(CN)_5H_2O}]^{3-}$ are taken to be 3 to 1. This has been estimated from the literature quantum yields for the two photoproducts $\phi_e = 0.52$ for the photooxidation reaction at 266 nm as reported by Shirom and Stein [1, 2] and $\phi_{aq} \approx 0.14$ [63]. Detection of the presence of the $[\mathrm{Fe^{II}(CN)_5H_2O}]^{3-}$ photoproduct based on this vtc measurement alone is difficult due to the similarity of its spectral shape to that of the ferrocyanide molecule. The fractions obtained from this technique can then be used as valuable input for EXAFS.

6.2. Picosecond XES results after 355 nm excitation

Shown in Fig.6.3(a) is the Kβ XES measured after 355 nm laser excitation of $[\mathrm{Fe^{II}(CN)_6}]^{4-}$ molecule at ≈18.3 GW/cm^2 intensity. Ferrocyanide excitation at 355 nm laser generates mainly the photoaquated complex, $[\mathrm{Fe^{II}(CN)_5H_2O}]^{3-}$ in its low spin (S=0) state. Shown in the Fig.6.3(b) are the $K\beta$ spectra of $[\mathrm{Fe^{II}(CN)_6}]^{4-}$ and $[\mathrm{Fe^{II}(CN)_5H_2O}]^{3-}$ complex. The $[\mathrm{Fe^{II}(CN)_5H_2O}]^{3-}$ measurements were performed

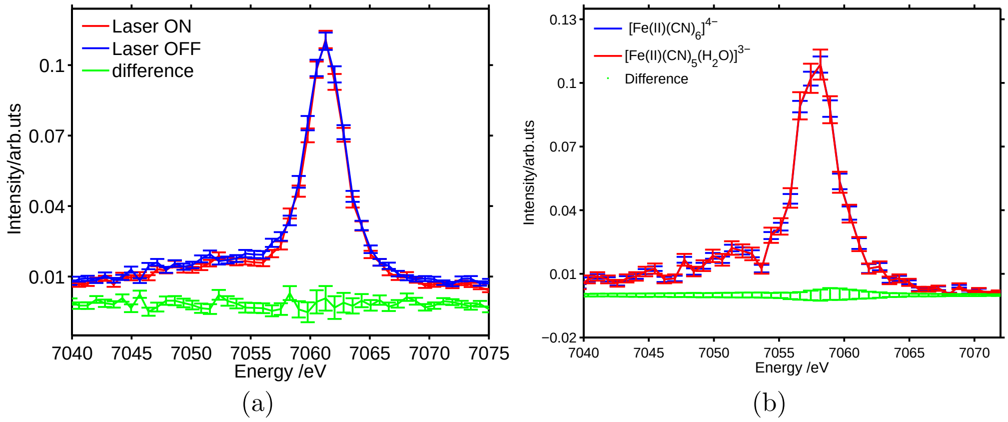

Figure 6.3.: (a) Kβ XES spectra of $[\mathrm{Fe}^{\mathrm{II}}(\mathrm{CN})_6]^{4-}$ measured before and 100 ps after 355 nm laser excitation. The green dots is the transient spectrum measured at laser intensity of ≈18.3 GW/cm^2. (b) Static Kβ emission spectra of $[\mathrm{Fe}^{\mathrm{II}}(\mathrm{CN})_6]^{4-}$, $[\mathrm{Fe}^{\mathrm{II}}(\mathrm{CN})_5\mathrm{H}_2\mathrm{O}]^{3-}$ and the difference.

on the reference sample prepared from a powder of $\mathrm{Na}_3[\mathrm{Fe(II)(CN)}_5\mathrm{NH}_3]._3\mathrm{H}_2\mathrm{O}$, ascorbic acid, acetic acid and mixed in water. The result we get is $[\mathrm{Fe}^{\mathrm{II}}(\mathrm{CN})_5\mathrm{H}_2\mathrm{O}]^{3-}$, which is unstable. For this reason, it was wrapped with Aluminum foil and kept in the refrigerator until right before the experiment. A quick static scan of $K\beta$ measurement does not show a clear difference signal with respect to the grounds state, $[\mathrm{Fe}^{\mathrm{II}}(\mathrm{CN})_6]^{4-}$ complex. This leads us to the conclusion that excitation of ferrocyanide molecule after 355 nm at low intensity results in the photoaquated photoproduct with spin state of S=0. In the previous Chapter high intensity XANES are reported on ferrocyanide molecule, here we did similar experiments by recording Kβ XES spectra (see Sec.6.2.1).

6.2.1. Picosecond XES at high intensity

In the preceding Chapter 5 we showed that due to the high laser intensity we observed tri-valent aquated complex, with a sequential two-step absorption (TSA) process (see Eq.(6.1)).

$$[\mathrm{Fe}^{\mathrm{II}}(\mathrm{CN})_6]^{4-}_{\mathrm{aq.}} \xrightarrow{h\nu} [\mathrm{Fe}^{\mathrm{II}}(\mathrm{CN})_5\mathrm{H}_2\mathrm{O}]^{4-}_{\mathrm{aq.}} + \mathrm{CN}^- \xrightarrow{h\nu} [\mathrm{Fe}^{\mathrm{III}}(\mathrm{CN})_5\mathrm{H}_2\mathrm{O}]^{2-} + \mathrm{CN}^- + e^-_{\mathrm{aq.}} \tag{6.1}$$

We believe that the non-germinate electron recombination to the tr-valent aquated complex to form the bi-valent aquated complex would take up to 5 ns. A similar results are also reported by Reinhard [25] on ferrocyanide complexes, in iodine by Kloepfer [182] and attributed to diffusion control electron recombination. In this

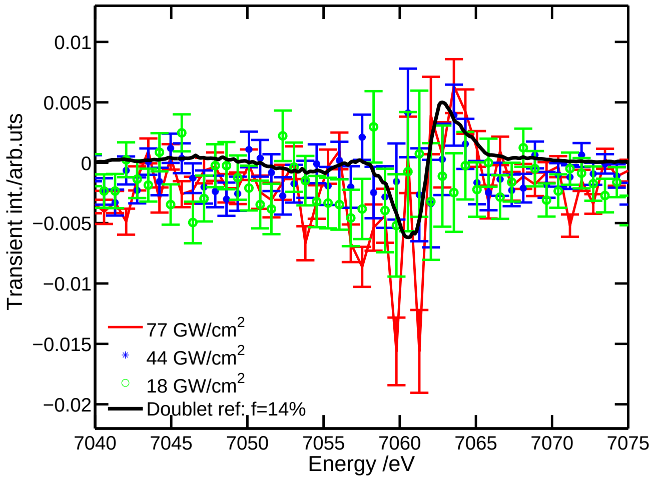

Figure 6.4.: Kβ emission spectra of $[Fe^{II}(CN)_6]^{4-}$, 50 mM measured after 100 ps of 355 nm excitation. (a) Kβ transient spectra measured at different incident laser intensity, the magnitude of transient signal increase with laser intensity. A scaled doublet reference spectrum has been scaled to the f=14% expected signal level.

section, we will present the intensity dependence results to look at the TSA process and the solvated electron non-geminate recombination by looking at the $K\beta$ XES transient.

We repeat the experiment at three different laser intensity, the result is reported in Fig.6.4. As we increase the laser intensity we start to see a transient signal. The transient signal show a shows linear dependence with incident laser intensity. We observe a clear transient at the maximum laser intensity 77 GW/cm^2 but this measurement was done at much higher intensity compare to the XES result measured at 18 GW/cm^2. From the XANES result, we conclude that the high intensity we photooxidized bi-valent photoaquated product which results in tri-valent photoaquated complex $[Fe^{III}(CN)_5H_2O]^{2-}$. The tri-valent aquated complex has one less electron in the iron ion which can give the transient signal. For this reason, we compare the transient signal measured with scaled doublet reference difference (see Fig.6.4).

To look at the time dependence of the transient signal at the high intensity we acquire Kβ emission spectra at difference time delays (i.e 100 ps, 5 ns, and 10 ns), the result is reported in Fig.6.5(a). The IAD signal is then plotted versus time and fitted with the single exponential decay of τ = 4 ns, similar to the results observed in Sec.5.6. The 4 ns decay time is attributed to the time need for the electron recombination to the $[Fe^{III}(CN)_5H_2O]^{2-}$ complex through diffusion-control process (Fig.6.5(b)). A similar time scales also reported in iodine by Kloepfer [182], which is attributed to different recombination processes.

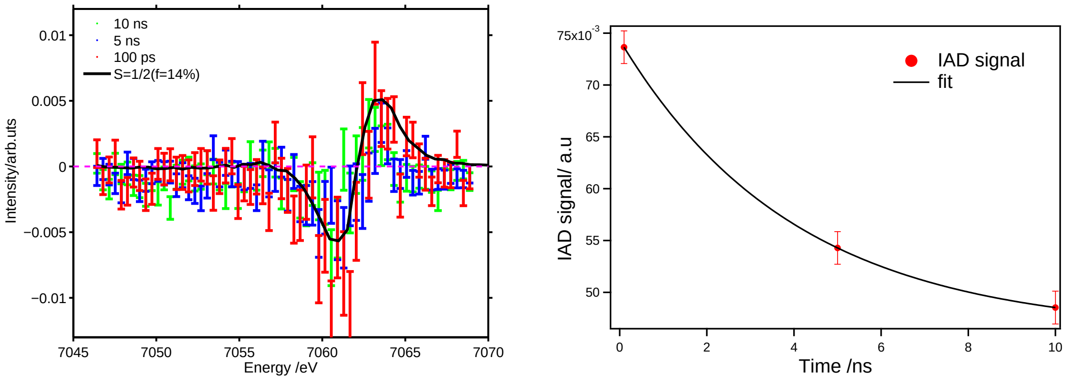

(a) (b)

Figure 6.5.: (a) Core-to-core Kβ emission spectra of $[\mathrm{Fe^{II}(CN)_6}]^{4-}$ before and at 100 ps of after excitation of 355 nm. (b) comparison of Kβ transient spectra measured at 100 ps with 76.7 GW/cm^2 laser intensity and static difference is shown in Fig.6.1(a). (c) Kβ transient spectra measured at different delay with laser intensity, $\mathrm{I}_L \simeq 76.7$ GW/cm^2. (d) IAD signal measured at time different delay.

6.3. Conclusion and interpretation

We showed that photoexcitation at 266 nm laser leads to predominantly ferricyanide and a small part of the photoaquated complex. Having in mind that the photoaquated product does not deliver a transient Kβ XES signal, both the Kβ and K$\beta_{2,5}$ XES emission lines can be a useful tool to identify the different transient species. We also show that the limitation of Kβ emission line in identifying between photoproducts which have a similar spin states whereas, vtc can be used to track the changes of local chemical environment[130].

$$[\mathrm{Fe^{II}(CN)_6}]^{4-}_{\mathrm{aq.}} \xrightarrow{h\nu} [\mathrm{Fe^{II}(CN)_5H_2O}]^{3-}_{\mathrm{aq}} + [\mathrm{Fe^{III}(CN)_6}]^{3-}_{\mathrm{aq}} + \mathrm{CN^-_{aq}} + \mathrm{e^-_{aq}}$$
$$\mathrm{S{=}0} \longrightarrow \mathrm{S{=}0} \qquad \text{and} \qquad \mathrm{S{=}}\frac{1}{2}$$

Excitation of the aqueous ferricyanide molecule at 355 nm generates photoaquated, $[\mathrm{Fe^{II}(CN)_5H_2O}]^{3-}$ complex which exhibits no Kβ XES transient signal. However, at higher intensity 70 GW/cm^2 we observe a clear Kβ XES transient signal which is an indication to the formation of $[\mathrm{Fe^{III}(CN)_5H_2O}]^{2-}$. Similar to the XANES results (see Section 5.8), the $\sim$ 4 ns decay constant of the Kβ XES transient signal can be interpreted as non-geminate recombination of the electron to $[\mathrm{Fe^{III}(CN)_5H_2O}]^{2-}$ molecule to form $[\mathrm{Fe^{II}(CN)_5H_2O}]^{3-}$. This time, constant is similar to earlier works in ferrocyanide [25] and Iodine [182] molecules. As a result, the reaction pathways measured after 355 nm laser excitation will be summarised with the following reactions equations:

- At low intensity $I_L \leq 50$ GW/cm^2:

$$[\mathrm{Fe^{II}(CN)_6}]^{4-}_{\mathrm{aq.}} + \mathrm{h}\nu \longrightarrow [\mathrm{Fe^{II}(CN)_5H_2O}]^{3-}_{\mathrm{aq}} + \mathrm{CN}^{-}_{\mathrm{aq}}$$

$$\mathrm{S{=}0} \longrightarrow \mathrm{S{=}0}$$

- At high intensity (≥ 50 GW/cm^2): with the first photon:

$$[\mathrm{Fe^{II}(CN)_6}]^{4-}_{\mathrm{aq.}} \xrightarrow{h\nu} [\mathrm{Fe^{II}(CN)_5H_2O}]^{3-}_{\mathrm{aq}} + \mathrm{CN}^{-}_{\mathrm{aq}}$$

$$\mathrm{S{=}0} \longrightarrow \mathrm{S{=}0}$$

  With the second photon:

$$[\mathrm{Fe^{II}(CN)_5H_2O}]^{3-}_{\mathrm{aq}} + \mathrm{CN}^{-}_{\mathrm{aq}} \xrightarrow{h\nu} [\mathrm{Fe^{III}(CN)_5H_2O}]^{2-}_{\mathrm{aq}} + \mathrm{CN}^{-}_{\mathrm{aq}} + \mathrm{e}^{-}_{\mathrm{aq.}}$$

$$\mathrm{S{=}0} \longrightarrow \mathrm{S{=}}\frac{1}{2}$$

Chapter 7

Observing short-lived reaction intermediate states

So far we presented picosecond-resolved XANES and XES results on ferrocyanide ions after 266 and 355 nm excitation. The XANES data allows us to disentangle the simultaneous ferricyanide and photoaquated photoproducts formed after 266 nm excitation. We also concluded the photoaquated complex is the only photoproduct at low intensity (< 50 GW/cm^2) but at high intensity, there is a contribution of the tri-valent aquated complex with two-step absorption (TSA) process.

In this chapter, we will present the recent femtosecond resolved X-ray absorption and emission results measured at the SACLA Free-Electron Laser facility, Japan on aqueous ferrocyanide solution after 355 nm laser excitation. The measurements were performed at beamline 4 (BL4) without the later implemented timing tool. As a result, we are limited about 600 fs time resolution because of the XFEL jitter. The setup used for the data collection is similar to the Synchrotron setup described in Ch.4.3, accommodate both XAS and XES techniques. For the XANES measurements, the XFEL beam was monochromatized with a channel-cut monochromator. For XES were measurements, non-monochromatic pink SASE beam was used to have more X-ray flux on the sample (roughly four times more flux than in the monochromatic beam).

7.1. Femtosecond XAS results after 355 nm excitation

Fig.7.1 shows the femtosecond-resolved XAS result measured after 355 nm laser excitation of a 250 mM aqueous ferrocyanide solution. The laser parameters used for this set of experimental data are $\tau = 50$ fs, VxH =50x50 μm^2 (1/e^2), rep. rate of 30 Hz and pulse energy of 38 μJ. The measured XAS transient results are shown in Fig.7.1(b) and similar to the spectral assignments we did for the photoaquated transient measured at 100 ps in Sec.5.5, which labeled as A-, B- and C-features (see Tab.7.1). Simple time traces recorded for each A and B features (Fig.7.1(c)) do not reveal the actual dynamic processes since the A- and B-features consists of two closely lying peaks (see Sec.7.1.2) are riding on the stronger transient changes of the absorption edge itself. Time scans give us a 600 fs time resolution which is due to the X-ray jitter. For the set of measurements reported here timing tool was not available for the jitter correction (which is implemented 2015 at SACLA).

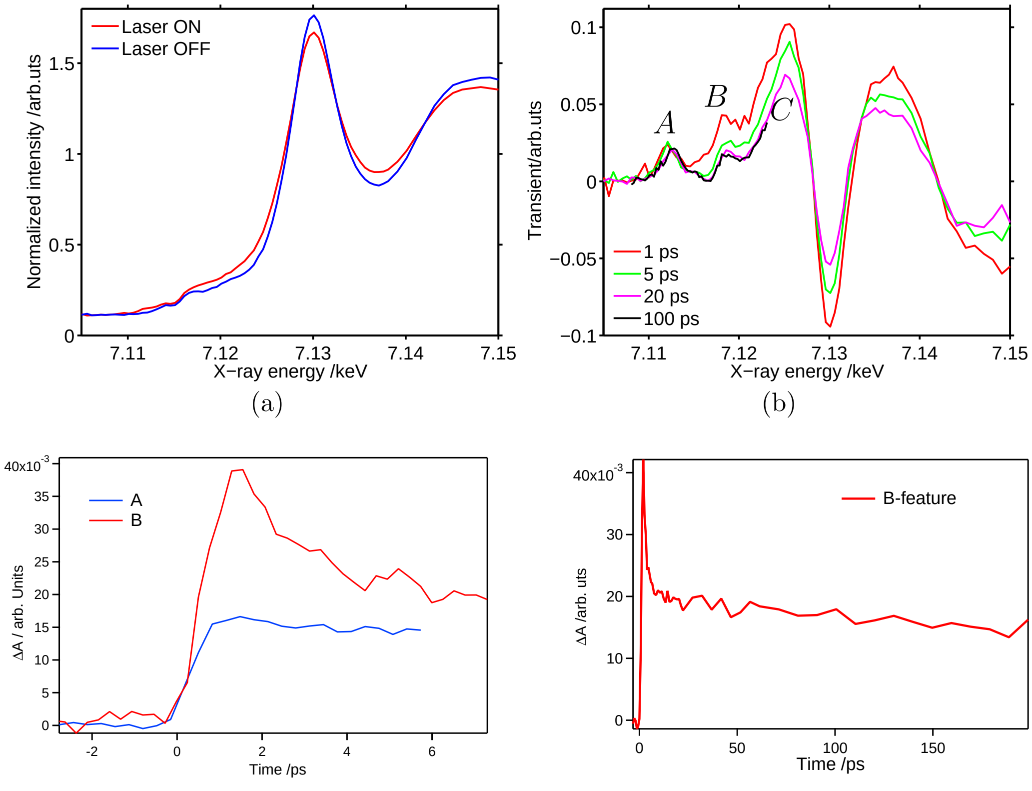

(a) (b)

(c) (d)

Figure 7.1.: Femtosecond resolved XANES of 250 mM $[\mathrm{Fe(II)(CN)_6}]^{4-}$. (a) Laser ON and OFF XANES spectra measured after 355 nm excitation. (b) XANES transient signal measured at different delay time with a laser intensity of $I_L \cong 7.74$ TW/cm^2. (c) Time scans measured at A- and B-features while the X-ray energy is fixed at 7113.0 eV and 7118.5 eV.

Table 7.1.: Summary of pre-edge peaks and edge energy position as shown in Fig.7.1(b).

features	A	B	C
Energy (eV)	7.112	7.1185	7.125

7.1.1. Comparison of XFEL and synchrotron data

Shown in Figs.7.2(a) and 7.2(b) is the comparison of APS and SACLA data, both measured after 100 ps of 355 nm laser excitation. The SACLA XANES transient spectrum is measured at $I_L \cong 7.74$ TW/cm^2 of laser intensity. These two figures shows that both the APS and SACLA data measured at high intensity have the same photoproduct at 100 ps, whereas, the low intensity APS the comparison shows a mismatch in the A-feature.

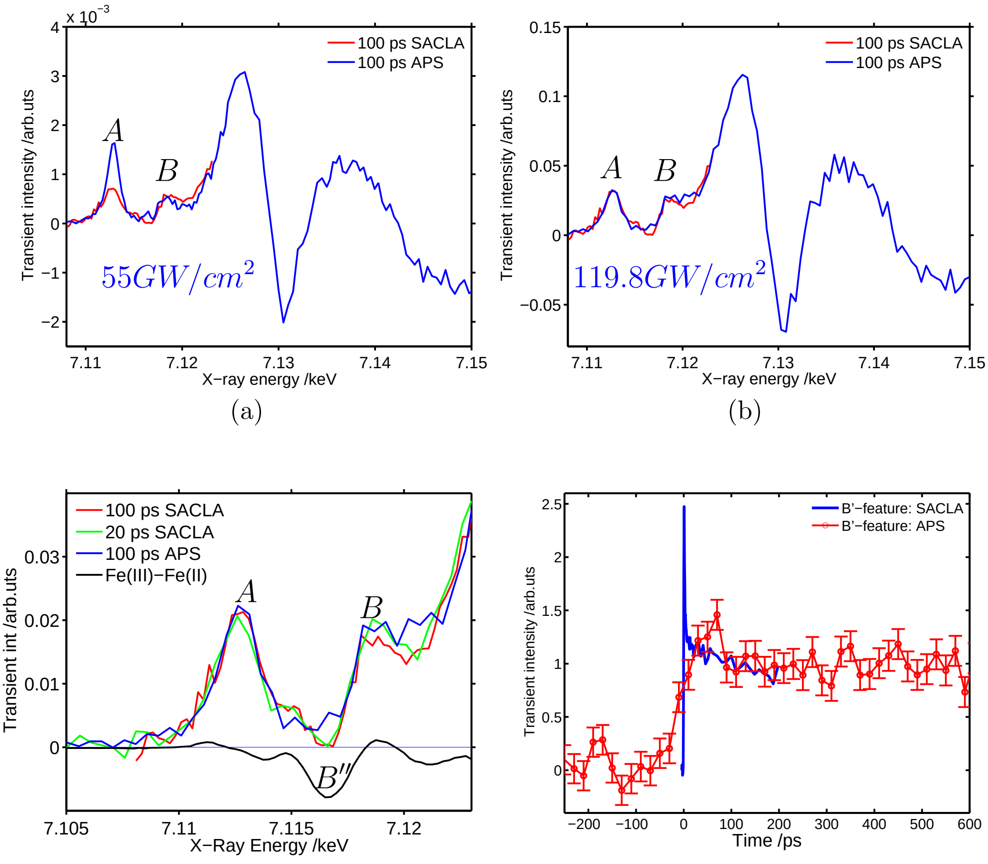

(a) (b)

(c) (d)

Figure 7.2.: Comparison of the APS and SACLA XANES transient data measured after 355 nm laser excitation. The SACLA data is measured at $I_L \cong 7.74$ TW/cm^2. The APS data was measured with: (a) low and (b) high intensity. (c) Zoom comparison of SACLA data measured after 20 ps and 100 ps with APS data and static reference difference between ferricyanide and ferrocyanide. (d) Comparison of time scans measured on the B-feature of XFEL and synchrotron data. The SACLA and APS data is measured at 250 mM and 50 mM concentrations respectively.

As a reminder, in the picosecond resolved APS data presented in Ch.5 we assign

A′-, B′- and C′-features as the fingerprints for the bi-valent photoaquated complex, in addition we noticed the B′-feature is due to the tri-valent photoaquated complex. This indicates in the SACLA data after 100 ps we have only the long-lived photoaquated photoproducts $[\mathrm{Fe^{II}(CN)_5H_2O}]^{3-}$ and $[\mathrm{Fe^{III}(CN)_5H_2O}]^{2-}$. A similar comparison with in Fig. 7.2(c) with the 20 and 100 ps SACLA with 100 ps APS shows that already after 20 ps we have the long-lived photoproducts only, which implies the ligand exchange process is completed. The static difference between ferro and ferricyanide indicates no ferricyanide has been formed.

From the discussion of Ch.5 we learn that due to the high laser intensity we experience a sequential two-step absorption (TSA) process, where the first laser photon creates the bi-valent photoaquated complex ($[\mathrm{Fe^{II}(CN)_5H_2O}]^{3-}$) and the second photon photooxidizes Fe to form tri-valent photoaquated complex, $[\mathrm{Fe^{III}(CN)_5H_2O}]^{2-}$ which exhibits both A′- and B′-features (see 5.9). From this we can learn that due to the high intensity at SACLA measurements have the trivalent photoaquated complex at 20 and 100 ps. Shown in Fig.7.2(d) is the comparison of time scans on B-feature between synchrotron and XFEL experiments. The very fast dynamics we observe on the B-feature is not observed in the synchrotron measurements but the slow dynamics observe in the SACLA data (see Fig. 7.1(d)) is similar the longer decay reported in the synchrotron measurements (see Sec. 5.6).

7.1.2. Observing pentacoordinated intermediate species

We now identify the origin of each pre-edge feature by comparing the experimental data with TD-DFT simulated spectra for all possible intermediate complexes. Shown in Fig.7.3 are calculated spectra (shifted down) together with the experimental data. The simulated spectra represent: i) photoaquated ($[\mathrm{Fe^{II}(CN)_5H_2O}]^{3-}$), ii) pentacoordinated complex ($[\mathrm{Fe^{II}(CN)_5}]^{3-}$) of square pyramidal ($C_{4V}$) and iii) two pentacoordinated complexes with trigonal bipyramidal (D_{3h}) symmetry of different spin states.

The A′ and A-features are due to a quadrupole transition from the 1s core orbital to localized molecular orbitals of mainly 3d character with a dipole contribution from a 3d mixed with the np like states [132, 95]. Depending on the symmetry and geometry of the complex orbital intermixing can increase the peak intensity [30]. The Lack of an inversion center or inversion symmetry leads to such mixing between np and 3d metal centered states [28, 30], explains the large peak intensity observed for the pentacoordinated intermediate complexes (Fig.7.3).

Comparing the calculated with the experimental spectra, we can identify the A-feature being due to the pentacoordinated complex, and the A′-feature due to the bi-valent photoaquated complex. The calculated A-feature is red-shifted with respect to the simulated A′-feature. A similar shift is observed in the experimental data between the 1 ps and 20 ps. Based on the identification above we state that the formation of the photoaquated complex is completed within 20 ps. The other two pre-edge features B'_1 and B'_2 are originated from the tri-valent aquated complex.

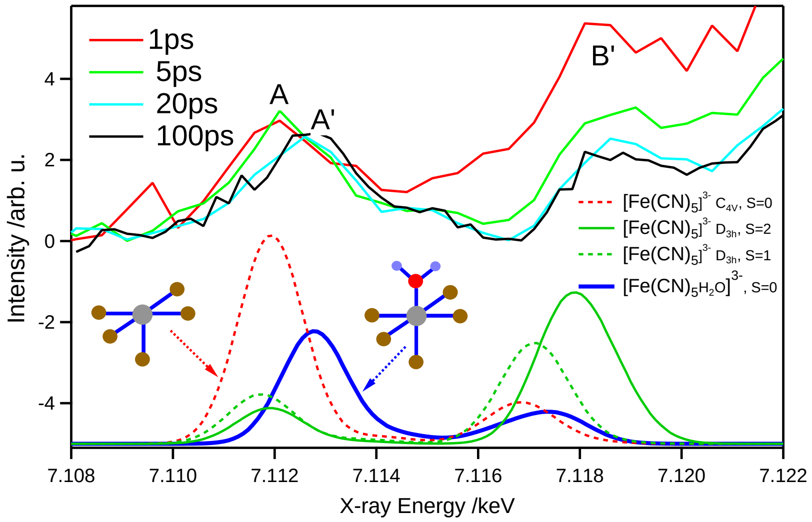

Figure 7.3.: Zoom around the pre-edge region of the experimental data shown in Fig. 7.1(b) shown with solid line. The bottom traces are TD-DFT calculated pre-edge spectra for the possible intermediate molecules. All calculated spectra are shifted by 160 eV to match the position of experimental data. The atomic coordinates of all intermidiate molecules is optimized using ORCA.

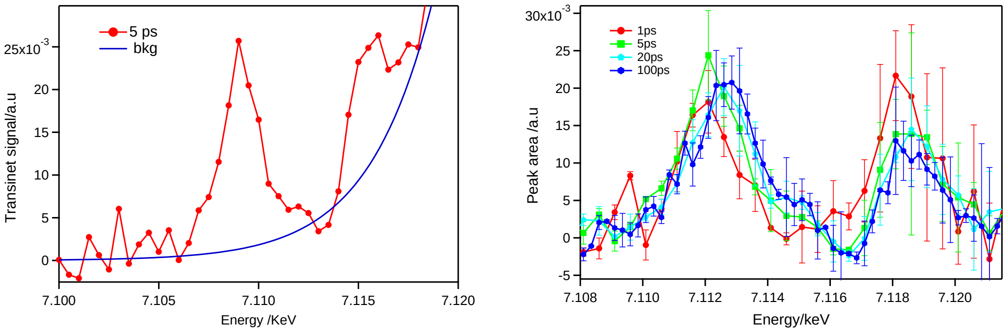

(a) (b)

Figure 7.4.: (a) Experimental transient measured after 5 ps (red dotted line) and the solid blue line is the background function. (b) Pre-edge peaks after the background subtraction in (a).

Table 7.2.: Summary of all experimentally observed pre-edge features.

features	A	A′	B'_1	B'_2
Energy (keV)	7.112	7.113	7.1185	7.1195

The dynamics of the transient pre-edge peaks is extracted by fitting the different scans with a linear combination of four Voigt profiles after background subtraction (See Fig.7.6). The first peak centered at 7.112 keV for the pentacoordinated complex and the second peak centered at 7.113 keV for the photoaquated complex contributions (see Eq.(7.4)). Similarly, two more peaks B'_1 and B'_2 centered at 7.1183 and 7.1195 keV respectively are used to get a reasonable fit. Each peak is fitted with Voigt profile (V(E)) of 1.56 eV broadening, which is a convolution of a Gaussian profile (G(E)) with 1 eV of monochromator broadening and Lorentzian profile(L(E)) with the lifetime broadening of the 1s core hole (1.25 eV) [121] via:

$$V(E) = (L \otimes G)(E) = \int_{-\infty}^{\infty} L(E', \gamma) * G(E', \sigma) dE' \tag{7.1}$$

with

$$G(E) = \frac{1}{\sqrt{2\pi\sigma^2}} e^{\frac{-(E-E_0)^2}{2\sigma^2}} \tag{7.2}$$

and

$$L(E) = \frac{\gamma}{\pi((E - E_0)^2 + \gamma^2)} \tag{7.3}$$

Finally, the fit function can be written as a summation of the all the peaks needed to fit the data as:

$$f(E) = \sum_{i=1}^{4} a_i \cdot V(E_i), \tag{7.4}$$

where a_i intensity for the ith peak and $f(E)$ is the fit function.

Shown in Fig.7.6 is the time evolution of A and A′ peak areas. The A-feature being the fingerprint of the pentacoordinated complex, is formed within the experimental time-resolution (about 600 fs), and its conversion to the photoaquated complex is complete after 20 picoseconds. The A-feature does not disappear completely in the extracted Fig.7.6(a), which indicates other photoproducts such as $[Fe^{III}(CN)_5H_2O]^{2-}$, might contribute at the same energy position. On the other hand, the A′ area signal increases with nearly the same rate as A area decreases indicating a conversion from the pentacoordinated complex to the photoaquated complex.

Table 7.3.: Summary of extracted time scales from each pre-edge and edge features.

features	A	A′	B'_1+B'_2	C
Energy (keV)	7.112	7.113	7.1185	7.125
τ (ps)	15.20±5.18	9.66±2.55	7.53±4.26	7.63±1.19

To have an idea of the time scales of the pentacoordinated decay and photoaquated complex formation we fit the extracted peak areas with single exponential decay and rise times. The summary of the fit result is presented in Tab.7.3. Within the experimental precision we assume both formation and decay times scales to represent the sequence $[Fe^{II}(CN)_6]^{4-} \rightarrow [Fe^{II}(CN)_5]^{3-} \rightarrow [Fe^{II}(CN)_5H_2O]^{3-}$,

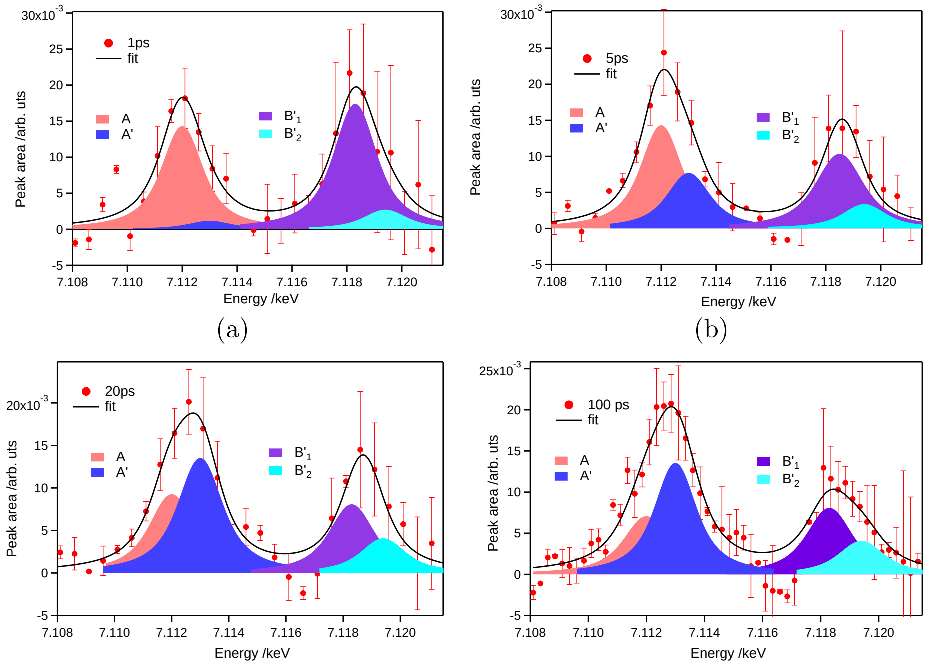

(a) (b)

(c) (d)

Figure 7.5.: (a), (b), (c) and (d) are fit results of the first transient pre-edge peak after background subtraction. The fit is done with four Voigt peaks centered at 7.112, 7.113, 7.1183 and 7.1194 keV for the pentacoordinated and photoauqated complexes.

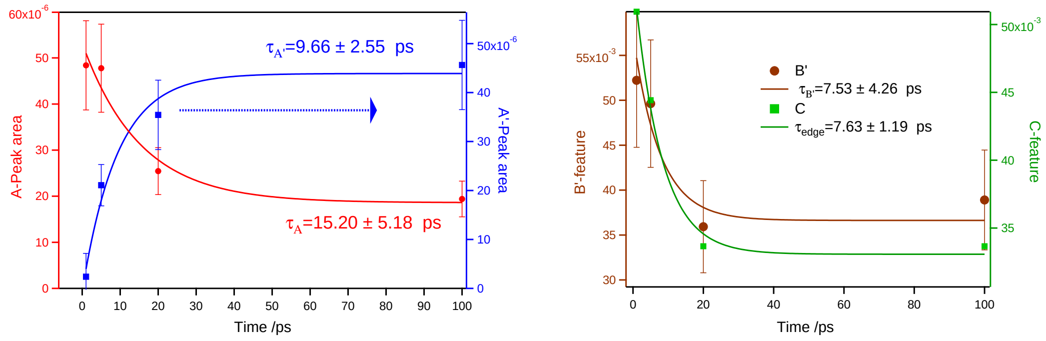

(a) (b)

Figure 7.6.: (a) Extracted dynamics of A and A′ pre-edge peak areas for the different transient data shown in Fig.7.6. (b) Extracted dynamics of C-feature and B′ pre-edge peak area of the different time delay measurements. For the C-feature since we don't have a 100 ps data we take the same value as of 20 ps and based on our comparison in Fig.7.2(c).

and we extract a common time scale of 12.43 ± 5.77 ps. This time scale is similar to previously published results obtained in $[\mathrm{Fe^{III}(CO)_5}]$, which yielded ligation of EtOH to a triplet $\mathrm{Fe^{III}(CO)_4}$ precursor state within 50-100 ps [16], the slow ligation process is explained by presence of a barrier between the triplet precursor state and the final singlet $\mathrm{Fe^{III}(CO)_4(EtOH)}$ state. Ligand exchange reaction in *cis*-$[\mathrm{Ru(bpy)_2(CH_3CN)_2)Cl_2}]$ complex dissolved in water takes 28 and 77 ps for $\mathrm{CH_3CN}$ and $\mathrm{H_2O}$ exchange respectively [183]. In our case, we believe that ligand exchange mechanism can occur from a singlet and triplet pentacoordinated complex. We expect that ligation from a singlet potential surface will be ultrafast, similar to the $\mathrm{Fe^{III}(CO)_4}$ case, which takes 300 fs due to the absence of barrier [16]. The new value (12.43 ps) decay we observe concerns ligation of water from a triplet pentacoordinated potential surface. The $\mathrm{B'}$ area which is the sum of $\mathrm{B'_1}$ and $\mathrm{B'_2}$ area we assign to the $[\mathrm{Fe^{III}(CN)_5H_2O}]^{2-}$ decays with 7.53 ± 4.26 ps time constant, the decay could be electron recombination to form $[\mathrm{Fe^{II}(CN)_5H_2O}]^{3-}$. From comparison of transient data with calculated spectra, at short time delay the $\mathrm{B'}$ could have a contribution of other photoproducts.

We do not exclude the possibility of photoaquated formation from a singlet pentacoordinated complex which should be faster, similar to the 300 fs formation $[\mathrm{Fe^{III}(CO)_4(EtOH)}]$ [16]. The identification of a pentacoordinated $[\mathrm{Fe^{II}(CN)_5}]^{3-}$ complex has not been undertaken in previous studies. Reinhard *et al.* did optical pump-probe spectroscopy and deduced indirectly the formation of $[\mathrm{Fe^{II}(CN)_5H_2O}]^{3-}$ species. Therefore, we performed TR XES to gain another observable in this dynamic process.

7.2. Spin-state of short-lived pentacoordinated complex

Time-resolved Kβ XES measurements were carried out on 250 mM aqueous ferrocyanide solution (see setup in Sec.4.3.2). A single Ge(440) von Hamos crystal allows us to record X-rays emission spectrum in the energy range of 6931 -7230 eV, fixed at an angle of 61.45° to get optimum reflection for the Kβ emission line. Fig.7.7(a) shows the time-resolved X-ray emission spectra measured on 250 mM aqueous $[\mathrm{Fe^{II}(CN)_6}]^{4-}$ solution before and 2 ps after 355 nm laser excitation. Fig.7.7(b) shows the transient spectrum measured after 355 nm laser excitation, for comparison possible static difference spectra i.e. doublet, triplet and quintet spin states are also plotted together. Although the transient signal quality is not great we can clearly see the negative feature 7054 eV, which is present in the triplet and doublet static difference spectra. This means the spin state can be either triplet or doublet spin state, however, the exact assignment whether the spin state is triplet or doublet in C_{4V} or D_{3h} symmetry is hampered by the noisy transient data.

The XES measurement were done at different time delay, to see the time evolution the integrals of the absolute values of the transient spectra (IAD) at different

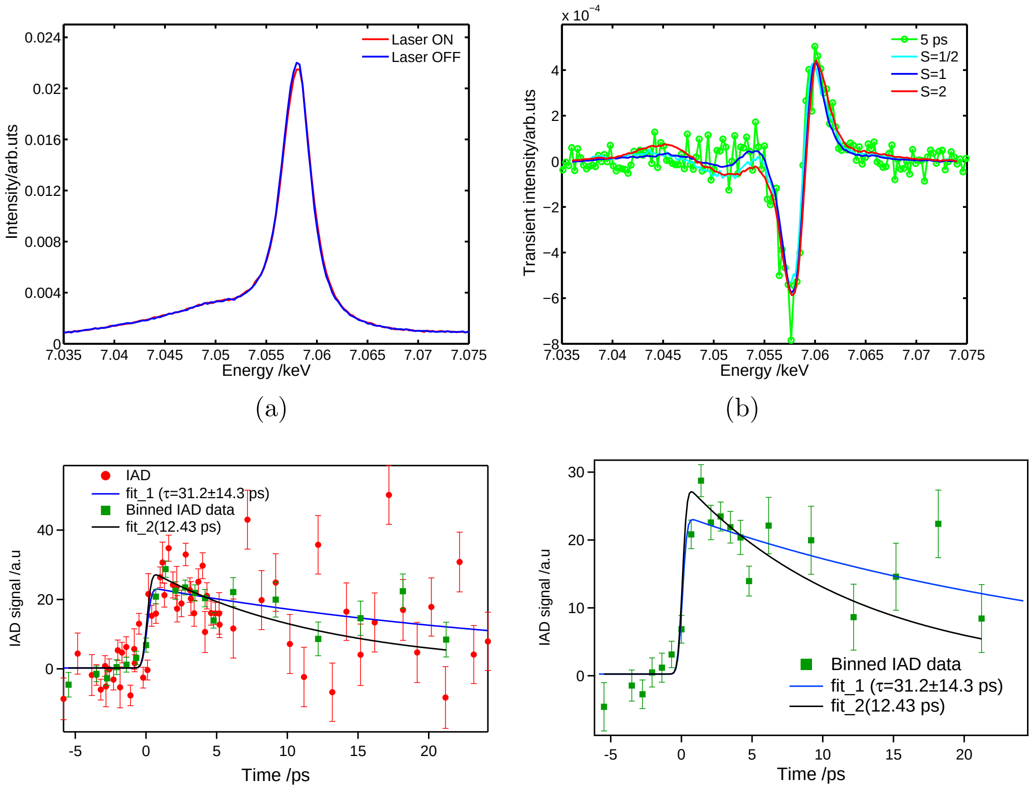

(a) (b)

(c) (d)

Figure 7.7.: Femtosecond resolved XES results of aqueous $[Fe^{II}(CN)_6]^{4-}$ measured at SACLA XFEL facility with a laser intensity of $F_L \cong 7.74$ TW/cm^2. (a) Laser ON and OFF Kβ XES spectra. (b) Transient Kβ XES signal for Δt = 5 ps (green), together with the anticipated difference Kβ XES spectra for quintet, triplet and doublet spin states, taken ref [13]. (c) Red dot data are integrated IAD signal measured at different delay time fitted with a single exponential decay of $\tau = 31.2 \pm 14.3$ ps and with fixed $\tau = 12.43$ ps. The green squares are binned data points extracted from the red dots. (d) Shows only the binned data points fitted single exponential fit of $\tau = 31.2 \pm 14.3$ ps (blue fit) and with fixed $\tau = 12.43$ ps (black fit). The 12.43 ps decay time used here is extracted from pre-edge analysis.

times is shown in Fig.7.7(c). The IAD signal appears within the experimental time resolution of about 600 fs show the formation of a none singlet spin state and decays exponentially with $\tau = 31.2 \pm 14.3$ ps time. The time constant extracted from XES data is different from XAS data which is about 12.43 ps. Here, we speculate that the different decay constant is due to the presence of multiple photoproducts in the XES signal. The difference in the time constants extracted from It is not possible to identify whether Since the XES data is noisy and it is hard to nail down if the decay is a two or one component. Furthermore, previous studies on $Fe^{III}(CO)_5$ [184], indicate that the ligation process would most likely proceed from a dissociative singlet potential towards an associative singlet-type H_2O potential. This would imply that a pentacoordinated complex in C_{4V} symmetry would need to be of singlet character or mixed singlet/triplet character in agreement with Fig.7.3. As a result, in the singlet potential surface, the ligation process would happen fast whereas from the triplet potential surface the ligation process would be slower since it has to go through intersystem crossing.

As we have shown in the Fig.7.7(b) the time-resolved XES signal indicate a spin state change. Prior studies $[Fe^{II}(CN)_6]^{4-}$ and $[Fe^{II}(CN)_5H_2O]^{3-}$ are low spin states[130]. Whereas, $[Fe^{III}(CN)_6]^{3-}$ is doublet and could contribute to the transient signal but as described in Chapter 5 our XANES results doesn't support the formation of ferricyanide formation upon 355 nm laser excitation. So the longer XES transient signal decay could be indicative of the presence of tri-valent photoaquated complex due to the high laser intensity used in this experiment. This implies the measured XES transient signal could be a linear combination of doublet and triplet spin states. As depicted in Fig.7.8, according to ref.[45] due to streric effects the population of d-shells of pentacordinated species are different compared to octahedral complexes.

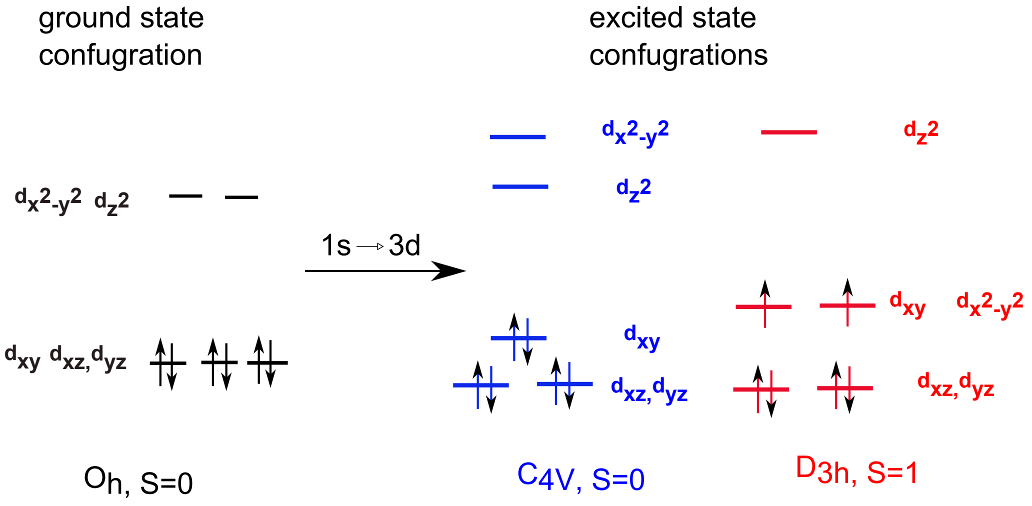

Figure 7.8.: Possible spins multiplicities of Fe(II) with $3d^6$ electronic configuration for the ground state octahedral O_h and two possible intermediate states (i.e. square pyramidal(C_{4V}) and trigonal bipyramidal(D_{3h})) symmetries. The orbital ordering of the excited state symmetries is adapted from [45, 46].

As we describe in Fig.7.2(c) the comparison of transient XAS data measured after 355 nm excitation with the static difference of ferrocyanide and ferricyanide looks significantly different, so we can exclude the ferricyanide formation as a dominating species due to high-intensity excitation. Whereas the sequential two-step absorption (TSA) process is a possibility in the synchrotron data, means the bivalent photoaquated $[Fe^{II}(CN)_5H_2O]^{3-}$ complex absorbs 355 nm photon to form a tri-valent photoaquated $[Fe^{III}(CN)_5H_2O]^{2-}$ complex. Similarly, in the femtosecond XAS transient data, we do not observe the ferricyanide spectral signatures which lead us to the conclusion of two-photon absorption (TPA) reaction channel is highly suppressed. Based on the this result the Kβ XES transient signal measured at 5 ps could be a linear combination of transient signals of triplet $[Fe^{II}(CN)_5]^{3-}$ and of doublet $[Fe^{III}(CN)_5H_2O]^{2-}$ character. From the XAS results of synchrotron studies the $[Fe^{III}(CN)_5H_2O]^{2-}$ takes 5-10 ns to recover and form $[Fe^{II}(CN)_5H_2O]^{3-}$ since it is a diffusion control process. As a result, the longer XES decay we reported ($\tau = 31.2 \pm 14.3$ ps) could explain by the presence of $[Fe^{III}(CN)_5H_2O]^{2-}$ which contributes to the signal along with the triplet contribution from the pentacoordinated complex.

7.3. Femtosecond XES to identify spin state of $[Fe^{II}(CN)_5]^{3-}$ species

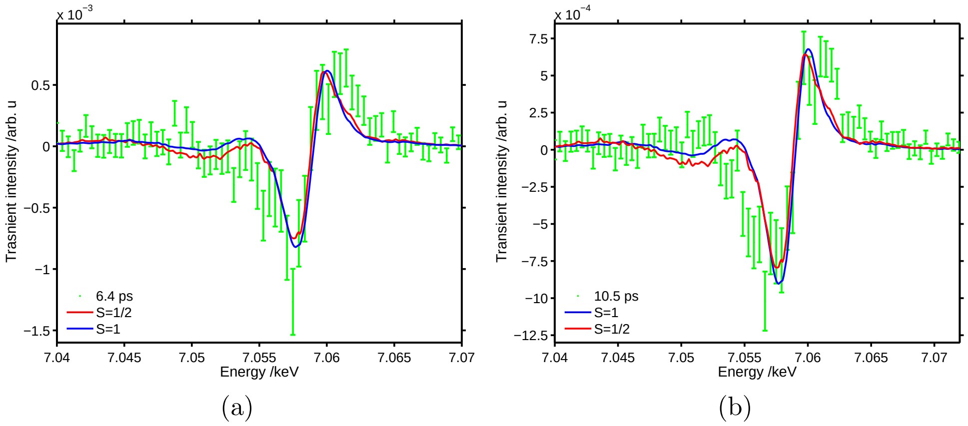

(a) (b)

Figure 7.9.: Femtosecond resolved Kβ XES results of aqueous $[Fe^{II}(CN)_6]^{4-}$ measured after 355 nm laser excitation at SACLA XFEL facility (a) Transient Kβ XES signal measured at 6.4 ps at a laser intensity of $I_L \cong$ 85 GW/cm^2. (b) Transient Kβ XES signal measured after 10.5 ps at $I_L \cong$ 184 GW/cm^2. The blue and red solid lines are anticipated triplet and doublet spin states from [13].

The XES measurements so far in (Fig.7.7) were performed at high laser intensity (7.74 TW/cm^2) and may thus include a two-step absorption (TSA) processes. For this reason we repeated the study at much lower laser intensity, with larger laser spot size of 90 x 100 μm^2 (VxH), pulse duration of 250 fs and 250 mM sample. A single Si(531) von Hamos crystal with 25 cm radius of curvature was used to record the X-ray emission spectra in the energy range of 6931-7230 eV, (at fixed angle of 61.45°) for collecting the Kβ emission line. The measurement shown in Fig.7.9(a) was done at a laser intensity of $I_L \cong 85$ GW/cm^2, whereas the result shown in Fig.7.9(b) was done at twice more intensity $I_L \cong 184$ GW/cm^2.

In this data set we expect only little TSA contribution due to the low laser intensity compared to other time resolved studies [185, 13]. As a result, we state that the transient signal is due to the pentacoordinated complex, although it is difficult to quantify the exact spin state of the nascent pentacoordinated complex. There are no other time-resolved XES results reported on ligand exchange mechanism ferrocyanide molecule to verify the spin state of the intermediate state. At similar intensity we did not observe a transient signal at 100 ps delay, indicates the ligand exchange is completed long before 100 ps.

7.4. Proposed tentative reaction photocycle ferrocyanide molecule after 355 nm photoexciation

The iron K-edge 1s → 3d pre-edge feature has been used as an identifier for the change in the electronic structure of the iron site [30]. The pre-edge intensity for iron complexes shows correlation with the symmetry, according to Roe *et al.*[28, 186, 187] the peak intensity decreases as symmetry deviates from octahedral (see Fig.7.10).

Combining both time-resolved XAS and XES results we conclude that the ligand exchange mechanism in photoexcited aqueous $[\mathrm{Fe}^{\mathrm{II}}(\mathrm{CN})_6]^{4-}$ access via a reduced coordination number intermediate state. Based on the picosecond and femtosecond XAS and XES data presented so far the reaction photocycle of aqueous ferrocyanide molecule after 355 nm laser excitation is summarised in Fig.7.11. The pentacoordinated complex could be either in square pyramidal (C_{4V}) or trigonal bipyramidal (D_{3h}) symmetry. When the molecule rearranges the symmetry from C_{4V} to D_{3h} results in a rearrangement of the molecular 3d orbitals, and as a result, the spin state of the metal centre changes from singlet (S=0) to triplet (S=1) spin state (see Sec.2.3). Since $[\mathrm{Fe(CN)_5H_2O}]^{3-}$ complex has a singlet spin state, photoaquated formation from the pentacoordinated complex with D_{3h} symmetry will be slower because of the presence of a barrier. In contrast photoaquated formation from the pentacoordinated complex C_{4V} symmetry should occur quite promptly since both reactant and product states are on singlet potential surfaces [16].

Although the pre-edge region is sensitive to the geometric structure around the iron centre, we can not differentiate between C_{4V} or D_{3h} symmetries because there is no correlation between the pre-edge peak position and C_{4V} or D_{3h}[30]. Similarly, in our results reported in Fig.7.3 we did not observe possible changes between C_{4V} or D_{3h} symmetries. As a result, the $\mathrm{t}_2 = 12.43$ ps is the time needed for the photoaquated complex formation from the pentacoordinated complex with trigonal

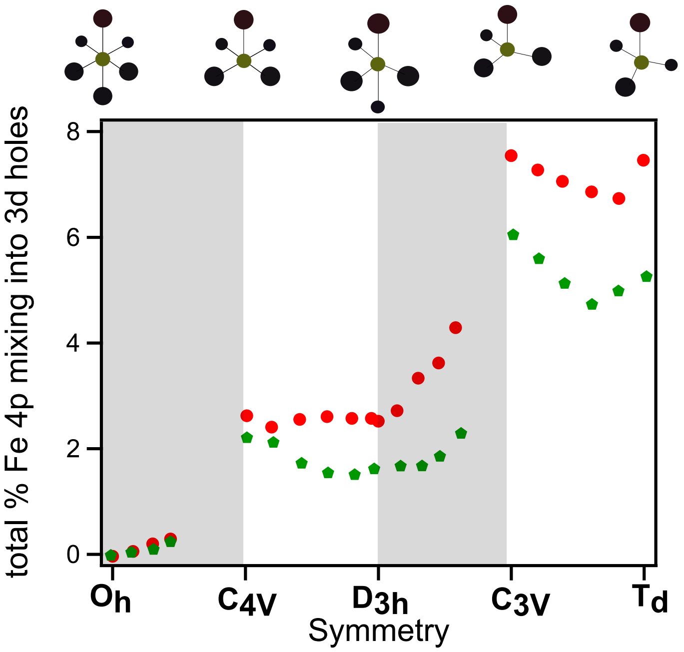

Figure 7.10.: Calculated total 4p mixing into XAS final states for a series of geometries from O_h to T_d. The result shown is for Fe(II), and Fe(III) Chloride ligated complexes with optimised geometries. From [30].

bipyramidal geometry which has a triplet state. However, we cannot disregard the possibility that the photoaquated complex formation from the pentacoordinated precursor in C_{4V} symmetry could happen ultrafast since both are on singlet potential surfaces. Recent optical pump-probe studies of this system claim the formation of the photoaquated complex could happen as fast as 500 fs [25], below our current experimental time resolution.

Although we know that the one laser photon absorption is the dominant channel, at the same time due to the high laser intensity used for this data set, we have either a sequential two-step absorption (TSA) or two-photon absorption(TPA) processes which could contribute to the experimental signal measured. We believe that the TPA would result in ultrashort lived precursor state(MLCT band of $[\mathrm{Fe}^{\mathrm{III}}(\mathrm{CN})_6]^{3-*}$ complex) which could recombine geminately and wouldn't affect the slower process. In the contrary, the highly excited precursor state, $[\mathrm{Fe}^{\mathrm{III}}(\mathrm{CN})_6]^{3-*}$ could undergo ligand substitution resulting $[\mathrm{Fe}^{\mathrm{III}}(\mathrm{CN})_5\mathrm{H}_2\mathrm{O}]^{2-}$ complex. At this point, we can not differentiate between the TPA and TSA processes. In the femosecond XANES spectra reported in this Chapter, due to the high intensity $I_L \cong 7.74$ TW cm^{-2} ($\sim 2.6{\cdot}10^{31}$ photons cm^{-2} s^{-1}) used in this experiment, the saturation parameter($\sigma_{355nm}{\cdot}\mathrm{I}_0{\cdot}\tau_{IC}$) for the first transition $[\mathrm{Fe}^{\mathrm{II}}(\mathrm{CN})_6]^{4-}_{\mathrm{aq}} \xrightarrow{\mathrm{h}\nu} {}^1\mathrm{T}_{1\mathrm{g}}$ is greater than unity, with $\sigma_{355nm} = 4.58{\cdot}10^{-19}$ cm^2 and $\tau_{IC} \cong 500$ fs. This implies we saturate the first transition (see Eq.(7.5)). Here we can have two possibilities, part of the excited stete molecules, $[\mathrm{Fe}^{\mathrm{II}}(\mathrm{CN})_6]^{4-*}$ relax to a ${}^3\mathrm{T}_{1\mathrm{g}}$ which would lead to a CN^- dissociation. The second

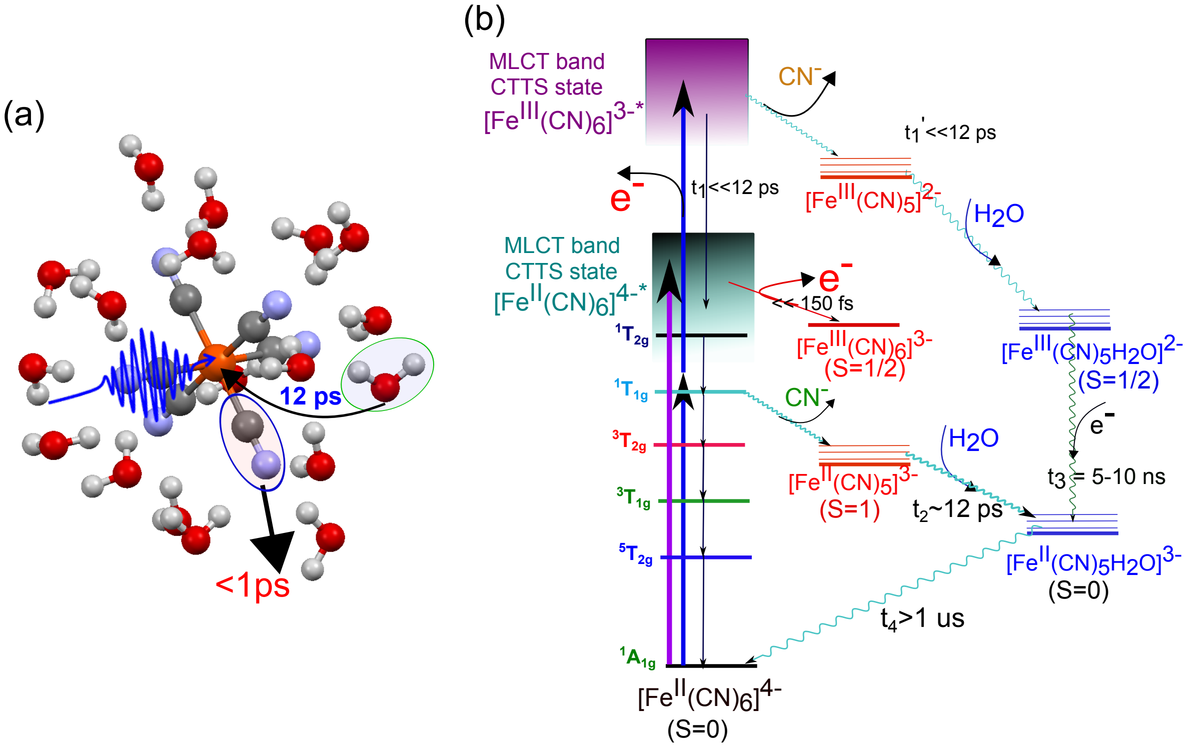

Figure 7.11.: (a) Ferrocyanide molecule in water solution, the time scales indicated here are extracted from femtosecond XAS data. (b) Tentative reaction photocycle of aqueous ferrocyanide molecule after 355 nm laser excitation. The blue and violet arrows are up to scale of 355 and 266 nm laser wavelengths. The solid blue vertical arrows show the two-photon absorption (TPA) processes with 355 nm laser light. The d-d electronic transition states shown are taken from ref.[171] and the position of the CTTS state is as indicated by Reinhard *et al.*[25]. For the details see text.

possibility is the remaining excited state molecules, $[\mathrm{Fe^{II}(CN)_6}]^{4-*}$ absorb a second photon yielding an oxidized excited ferricyanide complex (here MLCT band of $[\mathrm{Fe^{III}(CN)_6}]^{3-*}$) (see Eq.(7.6)).

$$[\mathrm{Fe^{II}(CN)_6}]^{4-}_{\mathrm{aq}} \xrightarrow{h\nu} [\mathrm{Fe^{II}(CN)_6}]^{4-*}_{\mathrm{aq}} \tag{7.5}$$

$$[\mathrm{Fe^{II}(CN)_6}]^{4-*}_{\mathrm{aq}} \xrightarrow{h\nu} [\mathrm{Fe^{III}(CN)_6}]^{3-*}_{\mathrm{aq}} + \mathrm{e^-_{aq}} \tag{7.6}$$

However, assuming the TPA excitation with a pulse duration of ca. 50 fs, we would end up with a mixture of bi-valent pentacoordinated and tri-valent ferricyanide species, which convert to different photoproducts with different time constants. The geminate electron recombination to the parent ferricyanide molecule would happen in competition with CN^- dissociation and aquation process. Both processes would be a take roughly a similar $t_1^{'}$ << 12 ps time scale resulting $[Fe^{III}(CN)_5H_2O]^{2-}$ and $[Fe^{III}(CN)_5]^{2-}$ complex. Here we hypothesis the formation of $[Fe^{III}(CN)_5]^{2-}$ through dissociation before ligation process happens.

A direct two-photon absorption (3.53.5 eV = 7 eV) would directly result in photoionized excited ferricyanide complex. Since the two-photon has 7 eV energy, which is much greater than the 266 nm (4.66 eV) needed the photoionization process to happen, the remaining energy (2.32 eV) would leave the photoionized ferricyanide complex in the MLCT band of ferricyanide complex. Here we propose the excited ferricyanide complex could relax in two competing pathways. The first relaxation pathway is geminate recombination (t_1 << 12 ps) to an excited ferrocyanide electronic state which later relaxed to photoaquated complex with a time constant of roughly 12 ps. The second relaxation pathway is dissociation of CN^{-} from an excited ferricyanide electronic state which leads to a formation of tri-valent aquated complex $[Fe^{III}(CN)_5H_2O]^{2-}$ with a time scale of $t_1^{'}$ << 12 ps. Since only a fraction of the excited ferrocyanide molecules absorb a second laser photon resulting ferricyanide complex, the blue shift of the Iron K-edge expected in the XANES will not be visible in the femtosecond XAS data reported in Sec.7.1(see Fig.7.2(c)). On the other hand, picosecond-resolved XAS and XES analysis indicate the conversion from tri-valent photoaquated complex to bi-valent photoaquated would take 5-10 ns because of the diffusion control electron recombination process (see Ch.5 and 6). The pre-edge analysis of the femtosecond XAS data suggests photoaquation from the bi-valent pentacoordinated complex takes about 12 ps. As a result, both the bi-valent pentacoordinated and tri-valent photoaquated complexes convert to the final bi-valent photoaquated complex with different time scales.

Chapter 8

Characterizing excited state molecular structures with picometer spatial resolution using new time-resolved EXAFS techniques

EXAFS provides structural information of bond distance and bond angles around absorbing atom. Unlike, crystallography it can be applied to resolve structures which are both in ordered and disordered medium. After describing the EXAFS basics in Sec.4.3 it is applied to extract the relevant information from the measured experimental results. To connect the experimental data with the theory, one has to extract the EXAFS oscillations, $\chi(k)$. In this chapter, the steady state EXAFS data reduction steps to extract the structural information from a given EXAFS spectra will be described. To the present these steps the experimental data measured on aqueous ferrocyanide ($[\mathrm{Fe(CN)_6}]^{4-}$) solution will be used. Next, the details the energy-space EXAFS fitting to analyse time-resolved data will be described. This new novel approach will be applied to light-induced spin-cross over systems: $[\mathrm{Fe(terpy)_2}]^{2+}$ and $[\mathrm{Fe(bpy)_3}]^{2+}$. Portions of the data have already been published [74, 79].

8.1. EXAFS Data reduction

There are several ways to extract the $\chi(k)$ function, in this Section the description and used procedures implemented in the data analysis software Athena [106, 188] will be explained. Before the starting EXAFS data reduction process, preprocessing procedures are required to refine the recorded spectrum. Refining includes rebinning, deglitching, truncation, calibration, and averaging of several scans to obtain a good quality EXAFS spectrum. After all these pre-requisite steps we start the EXAFS data reduction. Fig.8.1 shows the consecutive steps of data reduction to yield the EXAFS function $\chi(k)$:

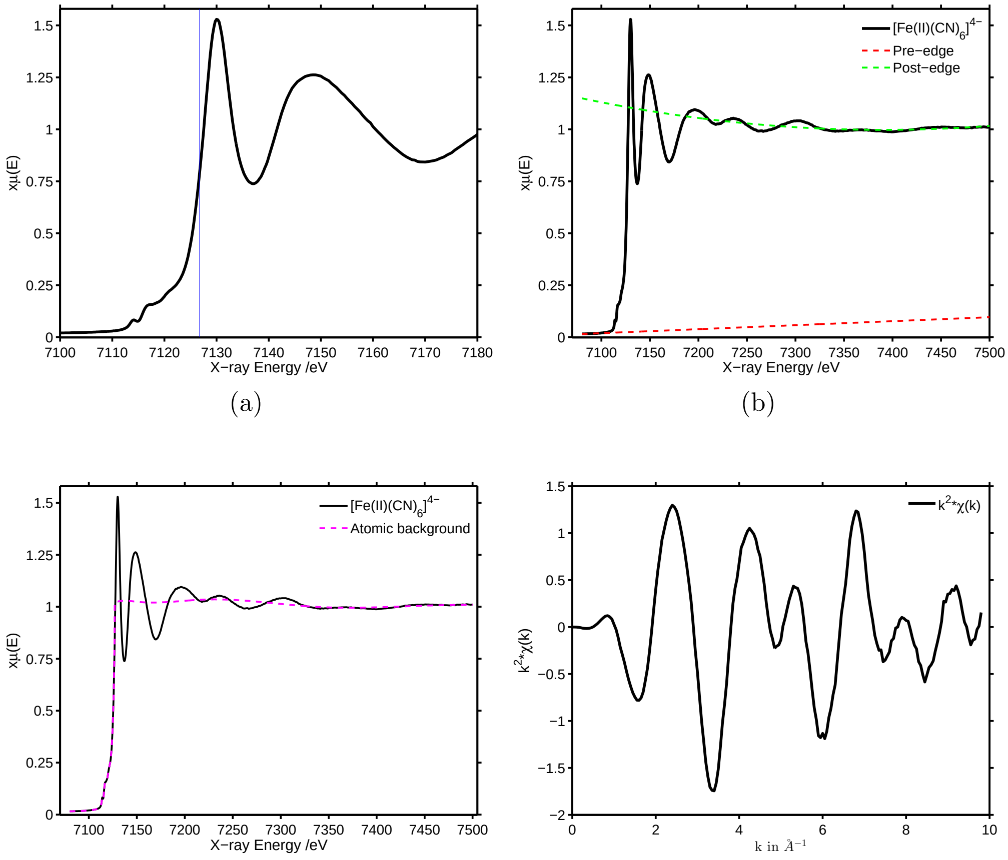

(a)

(b)

(c)

(d)

Figure 8.1.: EXAFS analysis sequence shown on aqueous $[\mathrm{Fe^{II}(CN)_6}]^{4-}$ solution around the Fe K-edge. (a) Shows the extrapolated pre-edge (red dashed line) and post-edge (green dashed line) used for background removal. (b) Shows the energy position (E_0) determined from the inflection point at the edge position. (c) Atomic background determined using Athena software of IFEFFIT package using a spline function. (d) Post edge oscillations scaled by k^2 with $k = 0$ determined by E_0.

1. **Determining $\mathbf{E_0}$**(Fig.8.1(b)): The choice of edge energy value E_0 is rather arbitrary. The most common way to determine E_0 is by using the first maximum of the derivative of the X-ray absorption spectrum itself. This definition is meant to reflect the Fermi level, which is defined as the energy right between HOMO and LUMO state. But to $k = 0$ of the free electron is otherwise found via its ionization potential IP. This is difficult to observe in XAFS, as life-time broadened bound-bound transitions already deliver a sizable rise in

absorption cross-section. Overall, the definition of E_0 via the inflection point systematically places E_0 at lower energies than IP, but this error accounts to only a few eV, which is much less than the EXAFS oscillations extending to several 100 eV above the edge. However, in the energy space fitting routine presented later (Sec.8.3), we show that we can actually determine IP quite precisely with this novel method [9]. But for now the position of the half height of the normalized XAS spectrum will define the E_0 value [92]. After determining E_0 we calculate k of the photoelectron wavevector in Å^{-1} see step 4.

2. **Pre-edge subtraction and post-edge determination** (Fig.8.1(b)): The photoelectric absorption cross-section scales with incident energy via $\mu(E) \propto E^{-3}$ above the absorption edge (see Sec.3.1), as a result, below the edge, $\mu(E)$ is also non-zero and can be removed by appropriate pre-edge subtraction. In Athena the pre-edge subtraction is done by selecting two energy points well below the edge jump and fitted with a polynomial line between the two energy points. Then the fit is subtracted from the data. Similarly, the post-edge is determined by selecting two energy points well above the edge jump and fitted with a polynomial line between the two energy points.

3. **Atomic background determination** (Fig.8.1(c)): Athena models the atomic background $\mu_0(E)$ using a cubic spline function [189]:

$$\mu_0(k) = \sum_{i=1}^{N} \frac{\mu x_i - BCK_i}{SM \cdot e^{-WEK_i^2}} \leq 1, \tag{8.1}$$

   where SM is a smoothing parameter, W is a weighting factor and N is the number of points. The number of data points determines the goodness of the spline function.

4. **Edge-jump normalization and EXAFS determination** (Fig.8.1(d)): In order to arrive at the EXAFS function $\chi(k)$ the spectrum needs to be normalized. The difference between the pre-edge and the post-edge polynomial functions gives us the $\Delta\mu_0(E)$ is the normalization factor. Having all the above steps allows us to calculate the EXAFS function $\chi(E)$.

   After all these steps the EXAFS function is ready for further analysis (see Sec.8.2). With E_0 we can transform from energy space into k-space of the photoelectron wave via:

$$k = \sqrt{\frac{2m}{\hbar^2}(E - E_0)}, \tag{8.2}$$

   with m is being the mass of the electron and $\hbar$ is Planck's constant. We weight the $\chi(k)$ with k, k^2 or k^3 to enhance the visibility of the EXAFS oscillations.

The Fourier transformation of the EXAFS function $\chi(k)$ results in a pseudo-radial distribution function according to Sayers *et al.* [97], delivering bond distances between the absorber and the different neighboring scatterers together with the number of atoms (or coordination number)(see (Eq.8.3)).

$$\chi(R) = \frac{1}{\sqrt{2\pi}} \int_{k_{min}}^{k_{max}} k^n \chi(k) e^{i2kR} dk \tag{8.3}$$

The bond distances we extract are approximately 0.5 Å shorter than the actual distance, due to the energy dependence of the phase factors in the sine function of Eq.(3.19) [101, 100]. The pseudo-radial distribution function contains the scattering contribution from all atoms in the material measured. The two peaks shown in Fig.8.2 represent the first and the second shell atom distances for the ground state $[\mathrm{Fe^{II}(CN)_6}]^{4-}$. The first shell contains six relevant paths due to the six carbon atoms and the second shell is due to the nitrogen atoms. We select only k > 3Å^{-1} since the resulting pseudo-radial distribution only depends on single scattering paths (see Sec.3.2.1). The k-range is chosen as input to the forward Fourier transform (from k- to R-space), and depends on the signal quality in the high k range and on the reliability of the data for lower k-values which may also be obscured due to non-structural XANES effects and insufficient background treatment.

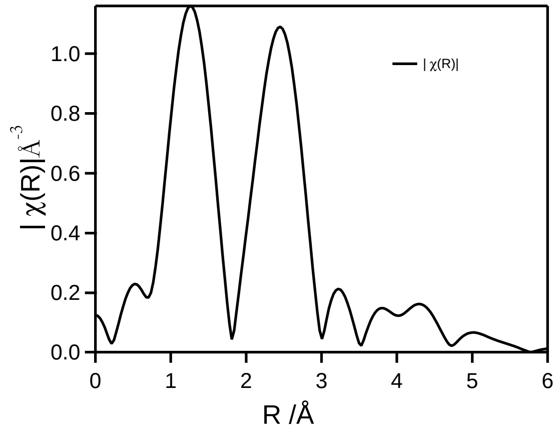

Figure 8.2.: Pseudo-radial distribution function after Fourier transformation of $\chi(k)$ from 3 - 8.5 Å^{-1} of aqueous $\mathrm{Fe(CN)_6^{4-}}$ molecule. Phase correction is applied to the R-axis.

The Fourier transformation can be taken by different multiplication factors of k^n to distinguish between the high and low atomic number scatters in the atom. D. C. Koningsberger *et al.* [92] described how the weighting with different k values will emphasize the different scatterers in a specific region of the EXAFS spectrum. As an example by selecting only the first shell Fe-C EXAFS spectrum which is between 0.7 - 1.8 Å in the R-space, we can do inverse Fourier transform which results in $\chi(k)$ of Fe-C single scattering shell. By Selecting a specific region of the

EXAFS spectrum and allows us to analyze a specific part of the spectrum [92].

8.2. Ground state EXAFS structural analysis

We will now introduce the EXAFS fitting routine with the ARTEMIS program package. The fitting analysis starts with a choice of model structure as the starting point for the FEFF calculation. This input structure is used to calculate the Muffin-tin potentials, self-energy, scattering amplitudes (S_0^2) and phases (ϕ_i) which are necessary to generate the fine structure χ(k) according to EXAFS equation [190, 191]. The input model should be reasonably close to the structure of interest. The input model can either contain DFT optimized coordinates or X-ray crystallographic data. The molecular structure of $K_4[Fe(CN)_6.3\,H_2O]$ has been determined with neutron powder diffraction [51]. However, in an aqueous solution the four potassium (K^+) ions are rather disconnected from the $[Fe(CN)_6]^{4-}$ ion. For this reason we used DFT optimized input atomic coordinates (the feff.inp file is shown in Appendix A).

The Artemis EXAFS fitting program (based on FEFF 8.20) generates a list of single- and multiple-scattering paths in sequence of their effective bond distance R_{eff} up to the maximum path length of R_{max}. The first 17 calculated scattering paths with amplitudes higher than >3.34% are used in our example (see Tab.8.1).

For the fit shown in Figs.8.3 and 8.4 we used only the first four dominating paths listed in the Tab.8.1. The scattering pathways considered for the fit are also shown in Fig.8.4. In EXAFS the number of independent fitting parameters (N_{ind}) is limited by the utilized data window considered for the fit and determined according to the Nyquist theorem [100]:

$$N_{ind} = \frac{2\Delta k \Delta R}{\pi} + 1, \tag{8.4}$$

where Δk and ΔR are the data range selected in k- and R-space. For the chosen data window (Δk = 5.5Å^{-1} and ΔR = 5Å) we can have at most 17 fitting parameters. We used in total only 5 parameters are used: S_0^2, E_0, ΔR_1, ΔR_2 and σ. To reduce the number of free fitting parameters, we have categorized the paths as the first and the second shell. As a result, ΔR_1 is used for the first shell and ΔR_2 is used for the second shell paths. The squared DW factor for all paths is assumed to be the same, although we know it is not the case.

The Artemis EXAFS fitting is done in R-space using a Hanning window over the k-range of 3 - 8.5Å^{-1}. The phase-correlated fit to the data using only first four paths are shown in Fig.8.4. The fitted values and fit statistics using only 4 (refereed as model 1) and 17 (refereed as model 2) paths respectively deliver nearly identical results given in Tab.8.2 and 8.3.

The contribution of the first four paths is shown in Fig.8.4. The peak at 1.9 Å is due to the scattering from the six nearest neighbor C atoms. The other peak at 3.125 Å is composed of the scattering from N atoms. For this peak, since

Table 8.1.: Summary FEFF 8.20 calculated paths using the input file of Appendix A. Only paths with with amplitude >3.34% relative to the strongest path (No. 1) are listed. N = path degeneracy; R_{eff} = effective path distance (in Å); Ampl. = amplitude (in %), SS = single scattering and MS = multiple scattering events.

No.	N	$R_{eff.}$	Ampl.	type	Pathway
1	6	1.924	100	SS	Fe−C−Fe
2	6	3.125	35.69	SS	Fe−N−Fe
3	12	3.125	98.93	MS	Fe−C−N−Fe
4	6	3.125	68.13	MS	Fe−C−N−C−Fe
5	24	3.275	12.10	MS	Fe−C−C−Fe
6	6	3.837	13.59	MS	Fe−C−C−Fe
7	6	3.837	16.31	MS	Fe−C−C−Fe
8	6	3.837	4.08	MS	Fe−C−C−Fe
9	24	3.837	11.36	MS	Fe−C−C−Fe
10	6	4.332	9.38	MS	Fe−N−C−N−Fe
11	48	4.355	10.02	MS	Fe−C−N−Fe
12	48	4.355	10.95	MS	Fe−C−N−C−Fe
13	24	4.631	11.65	MS	Fe−C−C−C−Fe
14	24	4.631	11.76	MS	Fe−C−C−C−Fe
15	12	5.044	13.00	MS	Fe−C−N−Fe
16	12	5.044	16.13	MS	Fe−C−N−Fe
17	12	5.044	3.34	MS	Fe−C−C−N−Fe

the Fe−C≡N is linear due to focusing effect other multiple scattering pathways contribute to this peak [52]. EXAFS fitting in Artemis can be done either in k- or R-space and the statistical goodness of the fit are evaluated by minimizing the statistical χ^2. Combining each shell reduces the number of fitting parameters and already lead to reasonable fit results. In our case, the fit is done in R-space and after back-FT of the R-space fit and the data in the range of 1 - 6 Å, χ_{fit}(k) is shown in Fig.8.3.

Table 8.2.: Fit results after the fit using the two different models, Model 1: only considering the first four paths with higher calculated scattering amplitude and Model 2 is considering all the ranked paths. Where each of Model 1 and Model 2 contain 4 and 17 scattering paths.

	S_0^2	E_0	ΔR_1	ΔR_2	σ^2
Model 1	0.78±0.07	-2.25±0.76	-0.029±0.001	-0.024±0.007	0.0015±0.0013
Model 2	0.65±0.04	0.499±1.150	-0.058±0.012	-0.056±0.014	0.003

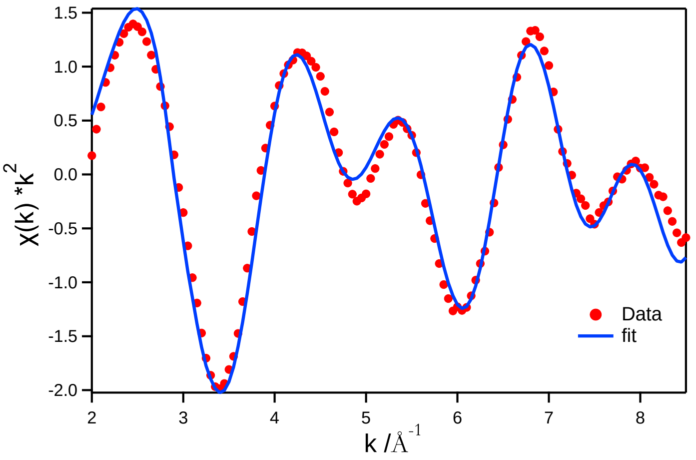

Figure 8.3.: The EXAFS spectrum χ(k) weighted with k^2 (red dots) obtained from the data of Fig.8.1 after data reduction such as edge-jump normalization and background subtraction, together with the χ(k) fit (solid blue line).

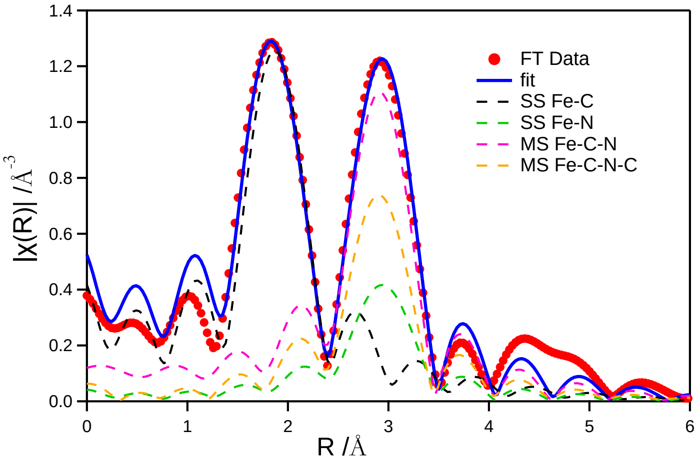

Figure 8.4.: The Magnitude of the Fourier transform of $k^2 \cdot \chi(k)$ (red dots) and the fit (solid line), and the contributions from different scattering paths (dashed lines). SS = single scattering path; MS = multiple scattering paths; Fe = iron atom; C = carbon atom; N = nitrogen atom. The data shown is phase corrected.

Tab.8.4, is Fe−C and C≡N bond length and compared with neutron diffraction measurements, DFT calculation and other EXAFS analysis. The Fe−C bond length obtained is in good agreement with neutron diffraction measurements and previously EXAFS results, but the DFT result is slightly overestimating the bond length. The C≡N bond length obtained in our analysis is slightly larger than all other measurements. One possible explanation is we assume the Fe−C≡N bond

Table 8.3.: Fit statistics for the different number of paths considered for the fit. Model 1: only considering the first four paths with higher calculated scattering amplitude and model 2 is considering all the ranked paths. N_{para} number of fit parameters considered, χ^2_R is the reduced χ^2 and R-factor is the square of the difference between fit and data points. For the details how the reported χ^2_R values calculated refer to [192].

	Model 1	Model 2
N_{indp}	17.56	17.56
N_{para}	5	5
No. paths	4	17
χ^2_R	367	1225
R-factor	0.016	0.04

angle to be 180 deg but in a solution it is slightly distorted or less than 180 deg, this distortion is not considered in our fitting procedure [52].

Table 8.4.: Summary of fit results and comparison between bond lengths in Å determined in this work with previously published values. The numbers in brackets are standard deviation values. ND = neutron diffraction.

	EXAFS	EXAFS[52]	ND [51]	DFT
Fe−C	1.918(3)	1.92(2)	1.924	1.970
C≡N	1.207(2)	1.18(2)	1.167	1.191

8.3. Time-resolved EXAFS analysis: applying a new approach

This Section contains the description of time-resolved EXAFS data fitting procedure using DFT optimised atomic coordinates. This method can be applied to different spin-crossover complexes. Unlike Fourier transform k-space fitting, it is not needed to know the excited state fraction of the measurement since it is determined directly from the fit via:

$$T = f(ES - GS), \tag{8.5}$$

where T is the experimental transient EXAFS spectrum between laser on and off at fixed time delay, f is the fraction of excited state molecules by the laser, ES is excited state spectrum, and GS is the measured ground state or laser off EXAFS spectrum. Eq.(8.5) has two unknown i.e. ES and f which is impossible to solve analytically with two unknowns. For this, we exploit prior knowledge of the reaction coordinate of excited state molecules, in this case, the structural distortion. Based on this we can construct models starting from the GS structure along the reaction coordinate in small steps. Then using FEFF we calculate EXAFS spectrum for each model which allows us to reconstruct different transient models and using a scaling factor f we compare to transient experimental data. Depending the steps used to reconstruct the various structural models the fitting procedure can be sensitive upto a picometer changes.

Parameters such as excited state fraction (f), bond length change (ΔR) and high spin (HS) low spin (LS) energy shift (ΔE) will be extracted with little prior knowledge (see flow chart 8.5). This analysis scheme is useful since it also allows extracting the excited state fraction (f) of the experiment from the fit. The method works for any structural modification; however, with the spin transition systems treated here, the variation to each distance (e.g. six Fe−N bond distances) treated into one ΔR for all (or at most two - 1 axial and one equatorial for terpy, etc.). This method of analysis is applied to two different samples, such as $[\mathrm{Fe(terpy)_2}]^{2+}$ and $[\mathrm{Fe(bpy)_3}]^{2+}$. The procedure of fitting transient EXAFS as follows:

1. First the experimental ground state spectrum using the DFT optimized atomic coordinates is fitted. Once a reasonable fit is achieved, the fit is exported and parameters to generate $\chi_{GS}= \chi_0^{fit}(R_0, E_0)$.

2. Next, we identify the reaction coordinate which changes during the dynamics of the photoexcited molecule. Then we start from the ground state molecule atomic coordinates and start altering the structure in small steps towards the possible excited state structure. For each step, we obtain new molecular coordinates. During this structural change we respect the chemical bonding of unchanged structures (e.g. the pyridine rings are kept constant in shape and size). Hence, we prepare feff.inp input files to calculate the EXAFS spectrum using FEFF. For each structural model generated we calculate the EXAFS spectrum ($= \chi_i(R', E')$) using FEFF 8.20. For this calculation, the amplitude and Debye-Waller factors are fixed to the ground state values (obtained in step 1). We save the output file which contains the EXAFS spectrum.

3. As we recall from Eq.(3.15) the relation between the EXAFS and the absorption coefficient is given by:

$$\mu(E) = \Delta\mu_0(E_0).\chi(E) + \mu_0(E_0) \tag{8.6}$$

The above formula is slightly different from the definition $\chi(E)$ because we have an edge-jump normalization factor $\Delta\mu_0(E_0)$ instead of the atomic background normalization $\mu_0(E_0)$. Assuming the atomic background function between the ground and excited state is similar we can write the change in the absorption coefficient $\Delta\mu(E)$ between the excited and ground state as:

$$\Delta\mu(E) = \Delta\mu_0(E).[\chi_{ES}(E_0') - \chi_{GS}(E_0)] = \Delta\mu_0(E).\Delta\chi(E) \tag{8.7}$$

where $\chi_{ES}(E_0^{'})$ and $\chi_{GS}(E_0)$ are the EXAFS spectrum for the excited and ground state respectively. E_0 and $E_0^{'}$ are the energy which corresponds to k=0 for the ground and excited state spectra. E_0 is determined in Athena and roughly assigned as the first maximum of the derivate of the $\mu_0(E)$. Using all this input the normalized measured EXAFS transient signal ($\Delta\chi_{exp}(E)$) can be written as:

$$\Delta\chi_{exp}(E) = f(t).\Delta\chi(E) \tag{8.8}$$

Using FEFF we simulated excited state EXAFS signals $\chi_i(R^{'}, E^{'})$ for a series of i possible excited states (ES) structures generated with FEFF 8.20 code [91]. With the ground state Artemis fit results $\chi_0^{fit}(R_0, E_0)$ we can calculate theoretical transient EXAFS (after converting the photoelectron wavevector space to energy space) via:

$$\Delta\chi_i(\Delta R_i, \Delta E_i) = \left[\chi_i(R_i, E_i) - \chi_0^{fit}(R_0, E_0)\right], \tag{8.9}$$

with $\Delta R_i = R_i - R_0$ and $\Delta E_i = E_i - E_0$, the bond distance changes and chemical energy shifts between the possible excited states and ground state spectra respectively. This comes from the assumption that each Fe−N bond distance changes by the same amount.

4. At this step we have a collection of theoretical transients ($\Delta\chi_i(\Delta R_i, \Delta E_i)$) with the experimental transient ($\Delta\chi_{exp}(E)$) measured at a fixed time delay. Since $\Delta\chi_i(\Delta R_i, \Delta E_i)$ is a transient with 100% excited state we scale $\Delta\chi_i(\Delta R_i, \Delta E_i)$ by $f(t)$ (the excited state fraction of excited molecules) which will be equally fitted below.

5. **Statistical analysis**: The calculated EXAFS spectra have some remaining uncertainty in E_0 (k=0) so we shift each spectrum in energy in order to optimize E_0 during the fit (but keeping the ground state model locked). Each possible model ($= \chi_i$) is thus shifted in energy with respect to the ground state and for each step the transient EXAFS is calculated. Then each model is multiplied by $f(t)$ (which varies between 0 and 100 %) and the results is compared with the experimental data via the statistical goodness of the fit, $\chi^2_{stat.}$ according to:

$$\chi^2_{stat.} = \frac{1}{N-1}\sum_{j=1}^{N}\left[\frac{f(t).\Delta\chi_i(\Delta E_i, \Delta R_i) - \Delta\chi^j_{exp}(\Delta E, \Delta R)}{\sigma^j_{\Delta\chi_{exp}}}\right]^2, \tag{8.10}$$

$\chi^2_{stat.}(\Delta E_i, \Delta R_i, f(t))$ is now a function of ΔE, ΔR and $f(t)$ only since non structural parameters (listed here) are kept constant to the ground state value. $\sigma^j_{\Delta\chi_{exp}}$ represent are the experimental error bars (standard deviation) for each data point.

6. Having extracted 3D representation of $\chi^2_{stat.}$ as a function of ΔE, ΔR and

$f(t)$, the best fit parameters will be determined from the global minimum of $\chi^2_{stat.}$ and we yield $f(t)$, the HS-LS bond length change (ΔR_{HS-LS}) and energy shift (ΔE).

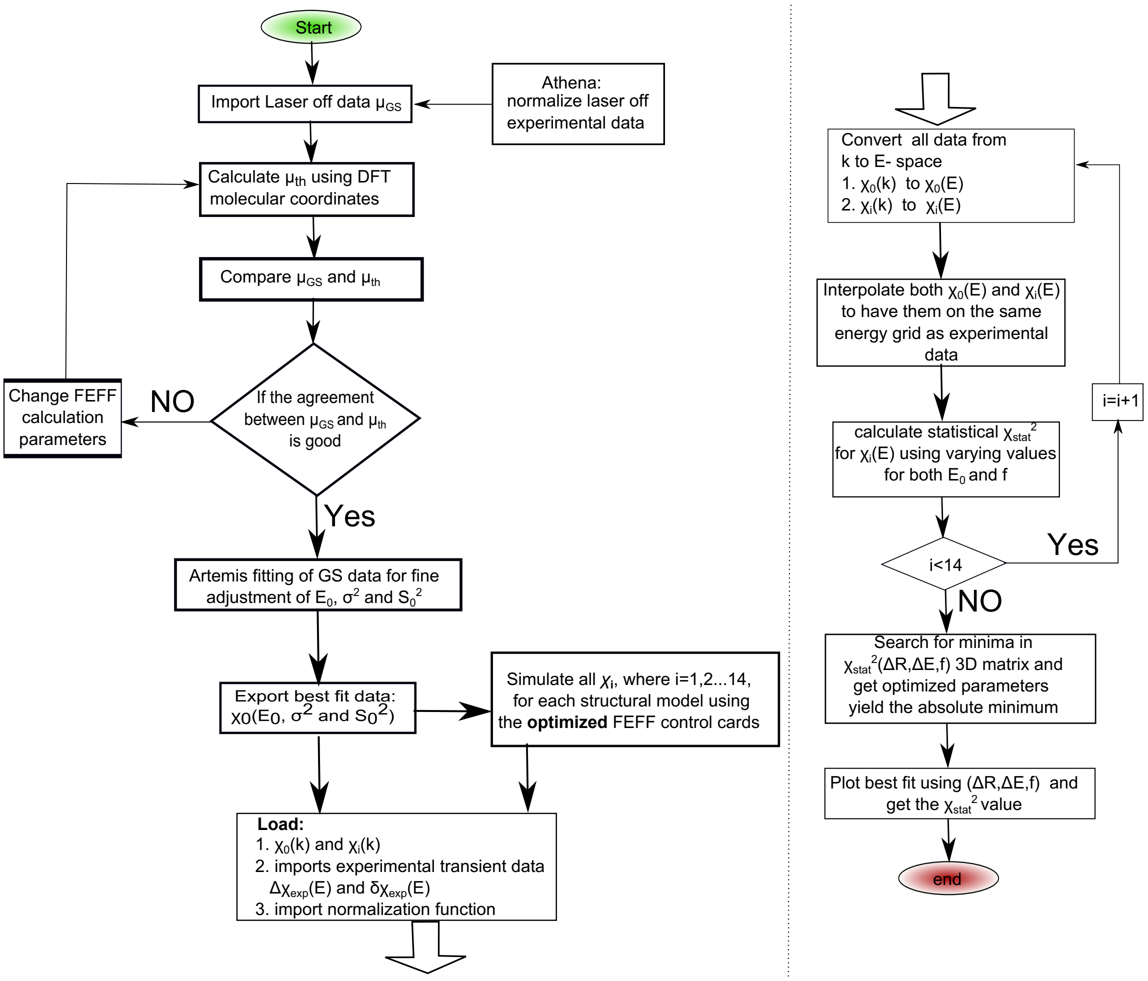

Figure 8.5.: Flowchart for the procedure of energy space EXAFS fitting. For details see text.

8.4. Case examples:

This strategy was applied to measure the structural changes in the time-resolved EXAFS data measured for two spin-crossover complexes $[Fe(bpy)_3]^{2+}$, $[Fe(terpy)_2]^{2+}$ and the former treated as a cross check to the method since the data has already been reported in ref [79].

8.5. Excited state EXAFS of $[Fe(bpy)_3]^{2+}$

Photoexcitation of $[Fe(bpy)_3]^{2+}$ by visible light, first populates the ^{1}MLCT manifold states, which eventually decays to the lowest-lying quintet state (HS), $^5T_2$, by a cascade of intersystem crossing steps through intermediate states [34, 13]. At room temperature, the HS state relaxes non-radiatively to the LS ground state with a lifetime of 1 ns in acetonitrile solution. The structure of HS state has been characterized by EXAFS fitting of the reconstructed excited state spectrum in Fourier transform space using no energy shift $\Delta E = E_0(HS)-E_0(LS)$ and a fixed value of excited state fraction $f = 20\%$ [193]. Later the structure was also analyzed by fitting the transient EXAFS data directly in energy space using the methodology presented here [75]. Hereby, f was varied from 10 to 30% and ΔE in steps of 0.6 eV from 0 to -2.4 eV and global minimum was found for $\Delta E = -1.8$ eV and $f = 17\%$, which was slightly lower than the 20% used in the Fourier transform fitting. As a result, they stated having achieved sub-picometer resolution. We perform a improved time-resolved EXAFS analysis in energy space on the same data published in ref [79].

In order to fit the transient EXAFS data uniformly expanded models are used. For each uniformly expanded model the $\chi^2_{stat}(\Delta R, \Delta E, f)$ values are calculated for all possible energy shifts and excited state fractions. The global minimum is found for an excited state fraction of f=38% (Fig.8.6). The excited state fraction f reported here 38% show a good agreement with the value 34% estimated from XES method [79].

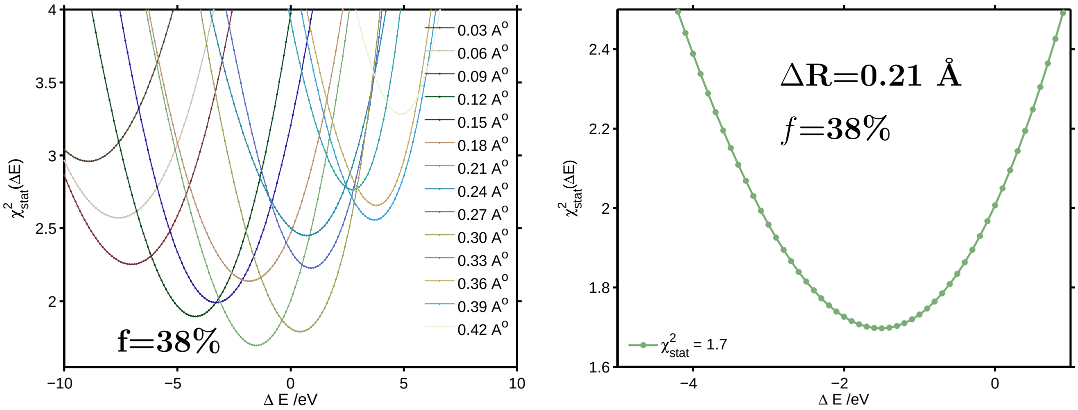

(a) (b)

Figure 8.6.: (a) Calculated $\chi^2_{stat}(\Delta E)$ for all the possible structural models at fixed excited state fraction, $f = 38\%$. (b) Calculated $\chi^2_{stat}(\Delta E)$ values for $\Delta R = 0.21$ Å and $f = 38\%$.

Fig.8.7 shows the best fit in energy and photoelectron wavevector space reconstructed using the fit parameters ΔR = 0.21 Å, ΔE = -1.5 eV and f = 38% are extracted from the global minimum value of the calculated χ^2_{stat}. The error bars for each fitting parameter were estimated by inspecting the change of χ^2_{stat} around the global minimum: we accept all values which do not increase the least square value by more than 5%.

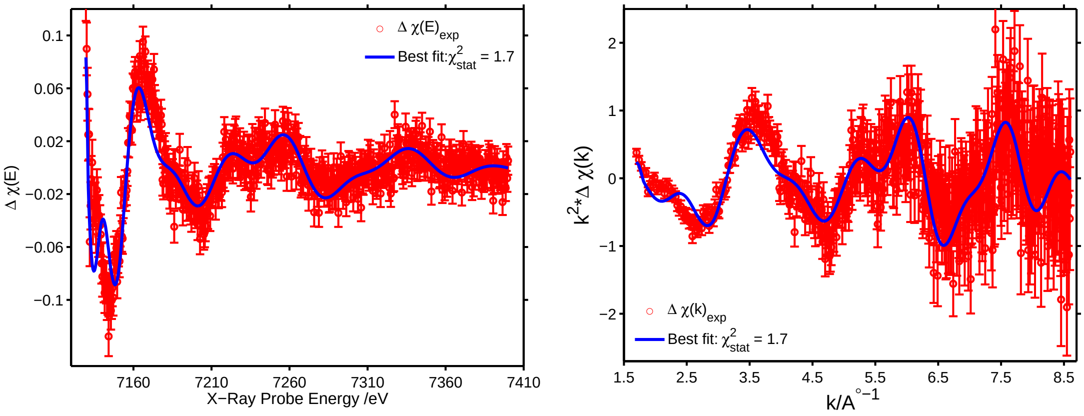

(a) (b)

Figure 8.7.: Best transient EXAFS fit with ΔE = -1.5 eV, ΔR = 0.21 Å and f = 38% fit parameters of the uniformly expanded model. (a) EXAFS fit in energy space and (b) in photoelectron wavevector space to amplify the higher energy part of the spectrum.

The result of this analysis delivers a value f = 38% for the HS population, which lies in between those previously extracted [79] (see Tab.8.5), albeit with a larger uncertainty (see (Tab.8.6)).

Table 8.5.: Comparison of excited state fraction obtained by complementary X-ray techniques of data set measured at the same laser fluence. The error bars for XES and XDS are with 95% confidence limits.

Technique	f(%)
XES [79]	34±4
XDS [79]	43±3
EXAFS (this work)	38±5

The structural result for ΔR is tabulated together with the optimum fit values for f and ΔE, and the result from [75] is displayed, in order to compare the relevant values for ΔE and ΔR. The reported values agree well within uncertainty and uncertainty is determined by looking at the nearest neighbor models(see Fig.8.8)[75].

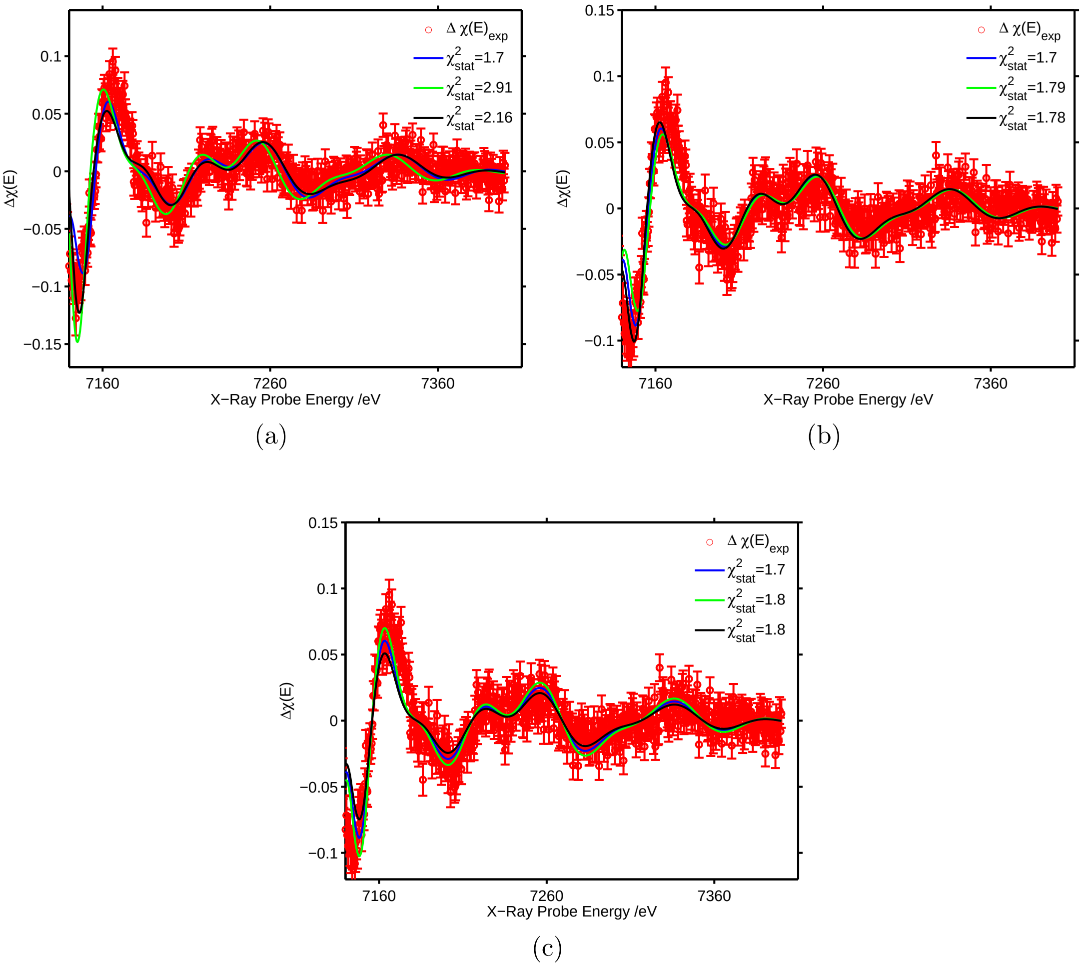

(a) (b) (c)

Figure 8.8.: (a) Best EXAFS transient fit together with next neighbor theoretical models i.e $\Delta R_{eq.} = 0.18$ Å and $\Delta R_{eq.} = 0.24$ Å. (b) Best EXAFS transient fit together with next neighbor theoretical models i.e. $\Delta E =$ -2.3 eV and $\Delta E =$ -0.7 eV. (c) Best EXAFS transient fit together with next neighbor theoretical models i.e. $f = 32\%$ and $f = 44\%$.

However, the uncertainty derived from the current analysis is larger than previously reported value. This is due to larger data range used in [75] and underlines the need for high quality data in order to extract precise structural changes, such data was recorded for $[\mathrm{Fe(tery)_2}]^{2+}$ and will be analysed in the next section.

Table 8.6.: Best fit results extracted after χ^2_{stat} analysis. The best fit results from [75] are shown to compare the structural changes.

	ΔE (eV)	ΔR_{HS-LS} (Å)	f (%)	χ^2_{stat}
Best fit	-1.5±1.0	0.21±0.03	38±5	1.7
Best fit [75]	-1.8±0.6	0.2003±0.008	17±1	1.35

8.6. Excited state EXAFS of $[Fe(terpy)_2]^{2+}$

As introduced in Sec.2.5.3 $[Fe(terpy)_2]^{2+}$ molecule has six nitrogen atoms bonded to the central iron atom (Fig.8.9). The nitrogen atoms are categorised into two groups according to their different Fe−N bond distances, as axial and equatorial, with two and four nitrogen atoms respectively [81].

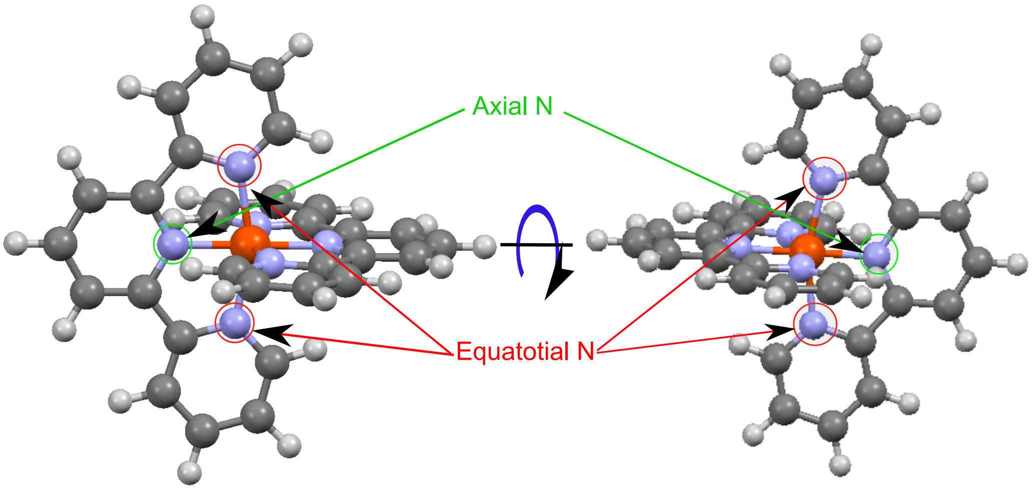

Figure 8.9.: Ground state molecule of $[Fe(terpy)_2]^{2+}$ molecular structure. For clarity, we show we rotated along the duplicated the $[Fe(terpy)_2]^{2+}$ molecule and plotted side-by-side to show both terpy ligands. Green and red circles indicate the equatorial and axial nitrogen atoms.

The DFT-calculated bond distances for the ground and both possible excited states are summarised in the Tab.8.7. While the 4 $Fe-N_{eq}$ distances are quite identical, there is a striking difference for the two $Fe-N_{ax}$ elongations. However, overall this is a challenging task to distinguish between both ^5E and $^5B_2$) states which requires an extraordinary precision to determine the Fe−N bond distances for each subgroup $Fe-N_{ax}$ and $Fe-N_{eq}$ bond distances.

Excitation of $[Fe(terpy)_2]^{2+}$ with light yields $^1A_{1g} \rightarrow {}^{1,3}$ MLCT transition, which in later time relaxes to the excited HS state (either ^5E or $^5B_2$). The lifetime of the HS excited state is 2.6 ns. A 13 mM aqueous solution of $[Fe(terpy)_2]^{2+}$ was measured, and the EXAFS spectrum before and 100 ps after 532 nm laser excitation

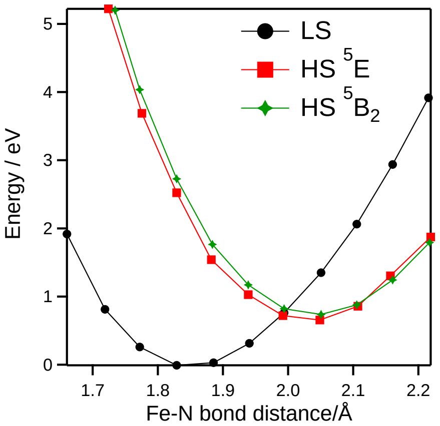

Figure 8.10.: CASPT2-calculated potential energy surfaces for $[Fe(terpy)_2]^{2+}$ molecule: for ground state (LS) and for ^{5}E or $^5B_2$ high spin states. The zero value of the energy scale is set to the minimum of the ground state potential. Adopted from [81].

Table 8.7.: DFT predicted results for the ground state that is LS and two possible excited HS (HS) states. $R_{ax.}$ is the axial bond distance for Fe−N and $R_{eq.}$ is for equatorial nitrogen atoms. The DFT predicted Fe−N bond distance change with respect to the ground state for both HS states are indicated with $\Delta R_{ax.}$ and $\Delta R_{eq.}$.

	$R_{ax.}$ (Å)	$R_{eq.}$ (Å)	$\Delta R_{ax.}$ (Å)	$\Delta R_{eq.}$ (Å)
LS	1.889	1.984	-	-
HS: ^{5}E	2.107	2.202	0.218	0.218
HS: $^5B_2$	2.160	2.191	0.271	0.207

used to generate the transient EXAFS (Fig.8.11). The refined ground state EXAFS spectrum is fitted by starting using the DFT optimized atomic coordinates, allowing only the non-structural parameters to vary while the structural parameters of the ground state are kept fixed. This fit function then represents the ground state model χ_0 (Fig.8.12).

DFT predicts that the ^{5}E excited HS state experiences a symmetric 0.218 Å bond distance change for both the axial and equatorial nitrogen atoms, while $^5B_2$ should exhibit a 0.271 Å and 0.207 Å bond distance change for the axial and equatorial nitrogen atoms respectively. Thus, the ^{5}E excited state structure shows a uniform expansion around the Fe center, while the $^5B_2$ excited state structure exhibits two groups.

The EXAFS data presented here analysed with Fourier transform analysis starting with two possible excited states i.e. ^{5}E and $^5B_2$ predicted by DFT/CASPT2 calculations. The EXAFS analysis reported in [74] was done on the reconstructed

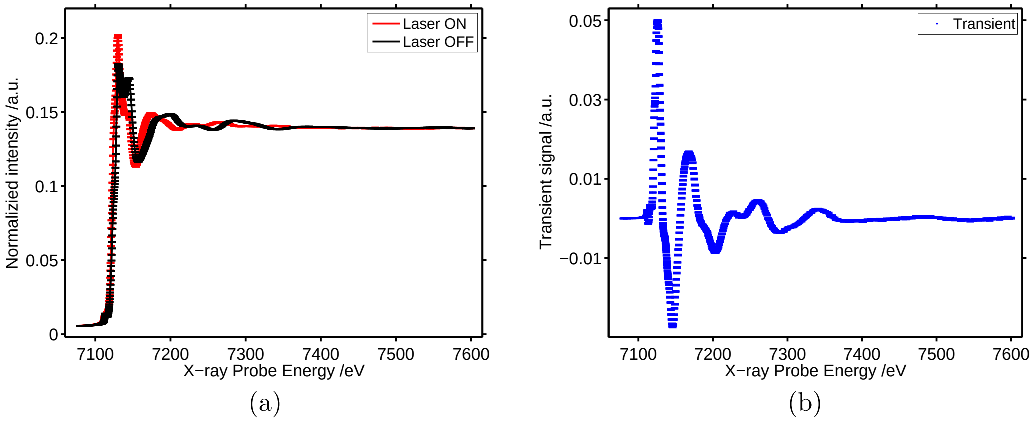

(a)

(b)

Figure 8.11.: Fe K-edge EXAFS spectra of a 13 mM aqueous solution of [Fe(terpy)$_2$]$^{2+}$. (a) EXAFS spectra measured before and 100 ps after 532 nm laser excitation (laser repetition rate of 1.3 MHz) and 3.356 GW/cm^2 laser fluence. (b) Transient EXAFS spectrum difference between laser ON and OFF.

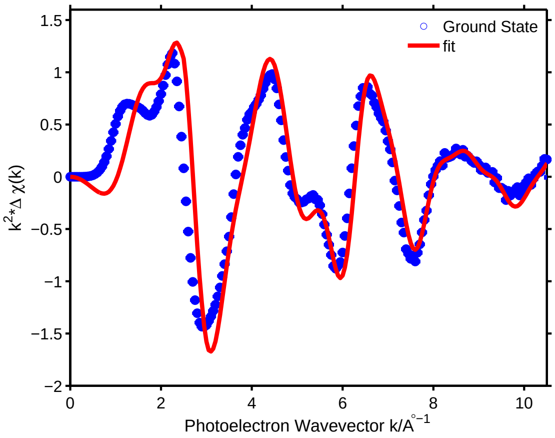

Figure 8.12.: Ground state EXAFS Artemis fit using DFT optimized ground state atomic coordinates of [Fe(terpy)$_2$]$^{2+}$ molecule. The fit range is between 3-10.5 Å^{-1}. The fitting is done in Artemis using only non-structural parameters.

excited state spectrum. The results show that the atomic coordinates of ^{5}E fits the data better [74]. However, the Fourier transform EXAFS fitting does not comply the chemistry the final product, since it use one parameter for different paths considered in the fit, which will distorts the structure of pyridine rings. With superior data quality measured at APS, 7ID-D beamline (Fig.8.11) we examine, whether we can distinguish between two closely-spaced HS excited states of $[\mathrm{Fe(terpy)_2}]^{2+}$ by fitting directly the transient data.

For the analysis, we prepared 14 models of uniformly expanded ligands in steps of 0.02 Å ^{5}E like. Using this input we calculated the EXAFS spectrum and each spectrum is listed as χ_i, i=1,2, 3,...14. For the $^5B_2$ structure, we also prepared 14 models (= χ_i, i=1, 2, 3,...14) of such non-uniformly expanded ligands in steps of 0.027 Å and 0.02 Å, for 4 equatorial and 2 axial nitrogen atoms respectively. In all cases we kept the pyridine rings constant in shape and structure. Then steps 3 to 6 (Sec.8.3) are applied (via home-written MATLAB script). Parameters including excited state fraction f, the $\Delta R_{eq.}$, $\Delta R_{ax.}$ and the chemical energy shift ΔE_0 are extracted from this fitting procedure.

Uniformly expanded model ^{5}E

The best fit yields a least square value of $\chi^2_{stat}(\Delta R, \Delta E, f) = 5.13$ with $\Delta R = 0.2 \pm 0.02$ Å for all six Fe−N bond lengths, f= 66 ±3 % excited state fraction and an energy shift of ΔE = - 1.5±0.3 eV. Shown in Fig.8.13 is the result of the best transient EXAFS fit, with the parameters (8.8). Fig.8.13(b) shows the same result in k-space of the photoelectron wavevector and weighted with k^2.

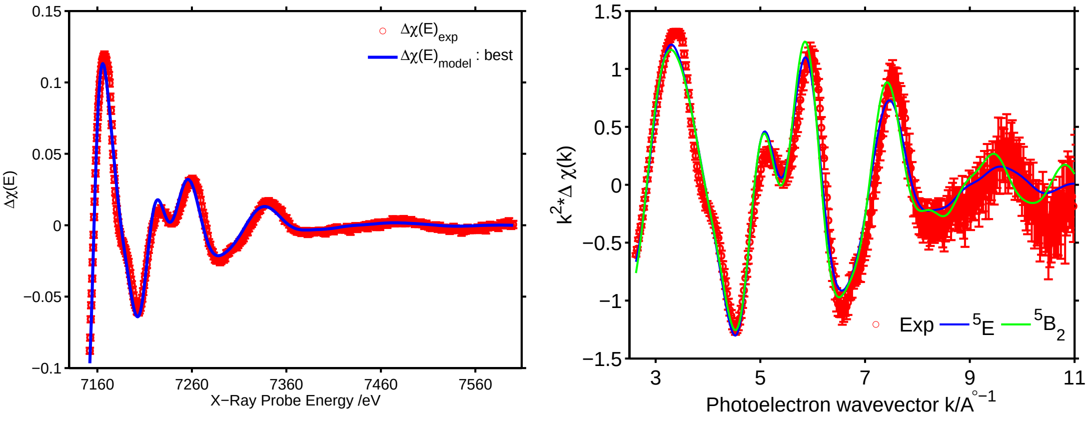

(a)

(b)

Figure 8.13.: Best transient EXAFS fit with ΔE = -1.5 eV, ΔR = 0.2 Å and f = 66% fit parameters of the uniformly expanded model where (a) in energy space and (b) in photoelectron wavevector space to see more the higher energy part of the fit.

Fig.8.14 shows the calculated χ^2_{stat} values via Eq.(8.10) for each 0.02 Å step in Fe−N bond distance change and for energy shifts varying between -10 and +10 eV in 0.1 eV steps. Each step of Fe−N bond length change (or structural distortion) has a local minimum at a different energy shift values, indicating the strong correlation between energy shift and bond distance (see also Fig.8.15(a)). The global minimum is located at ΔR = 0.2 Å, f= 66% and ΔE = -1.5 eV (see also Fig.8.14(b)).

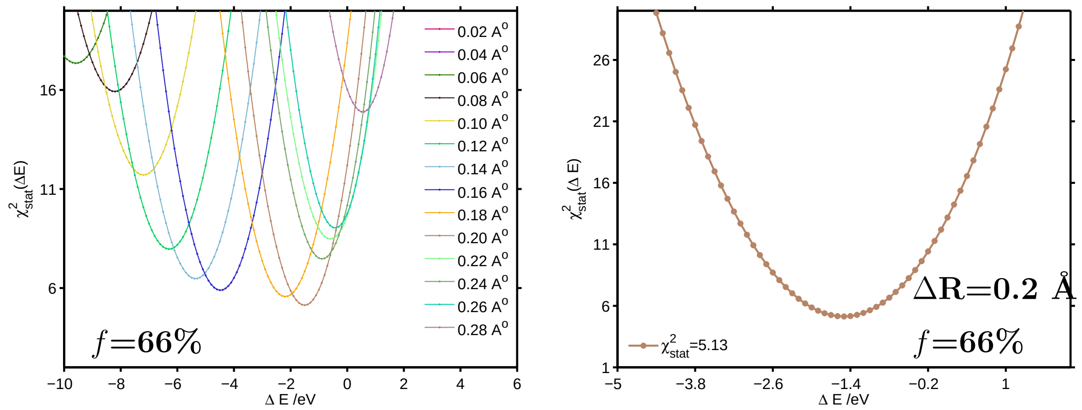

(a) (b)

Figure 8.14.: (a) Calculated $\chi^2_{stat}(f,\Delta E)$ values for all the possible structural models versus the energy shift, ΔE at fixed excited state fraction, f=66%. (b) Calculated $\chi^2_{stat}(\Delta E)$ values for ΔR = 0.2 Å and f = 66%.

This result shows all structural distortions yield a local minimum at different values of energy shift (Fig.8.15(a)). In other words, as the structural distortion ΔR increases the minimum of the calculated χ^2_{stat} value is also located at a higher value of ΔE, showing a strong correlation. Similar results have been obtained in previous studies [75, 168]. We have also shown calculated $\chi^2_{stat}(\Delta R,f)$ values at fixed energy shift, ΔE= -1.5 eV (Fig.8.15(b)), the negative correlation between the structural distortion and excited state fraction. In this analysis we did not observe a correlation between ΔE and excited state fraction f (Fig.8.15(c)).

Estimating the uncertainty in determining the HS structure

The error bars are determined by the condition that all calculated χ^2_{stat} values are acceptable, which do not increase the least squares value by more than 5% [194, 9]. With this definition, for ΔR the error bars range from 0.18 and 0.22 Å. The calculated $\chi^2_{stat}(\Delta R,\Delta E,f)$ value for the transient model with ΔR = 0.22 Å is 11.03 and with ΔR = 0.18 Å is 6.85. The two adjacent theoretical transient models do not fit the first EXAFS oscillation resulting a higher χ^2_{stat} value compare to the best fit value. As a result, the error bar for the structural distortion ±0.02 Å is the limit and we cannot estimate better than this value. Similarly, the error bars for the excited state fraction and energy shift are estimated to be ± 3 % and ± 0.3 eV respectively. These are rather optimistically small uncertainties, since the transient

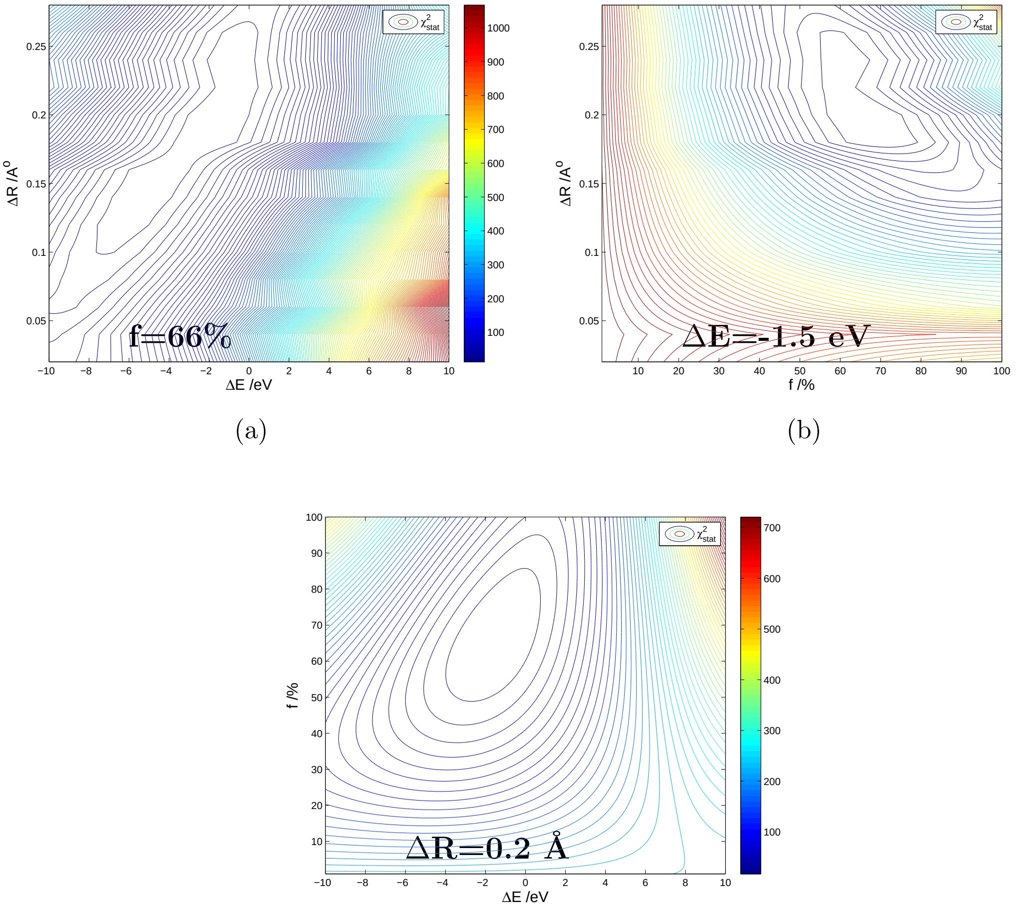

(a)

(b)

(c)

Figure 8.15.: Surface plot to visualize the correlation between fit parameters considered. (a) between energy shift, ΔE and Fe−N bond length change, ΔR at fixed excited state fraction, f = 66%. (b) between excited state fraction, f and Fe−N bond length change, ΔR at a fixed ΔE = -1.5 eV, and (c) between energy shift, ΔE and excited state fraction, f at a fixed Fe−N bond length change, ΔR = 0.2 Å.

EXAFS models for the upper and lower boundaries already look very similar to the optimum transient EXAFS. Nevertheless, relying on the least squares evaluation of these parameters deliver the accuracy reported here(see Fig.8.16).

Non-uniformly expanded model: $^5B_2$ like

Similar to the preceding Sec.8.6, 14 non-uniformly expanded structural models were constructed by applying steps of 0.02 Å and 0.027 Å for the $\Delta R_{eq.}$ and $\Delta R_{ax.}$ atoms

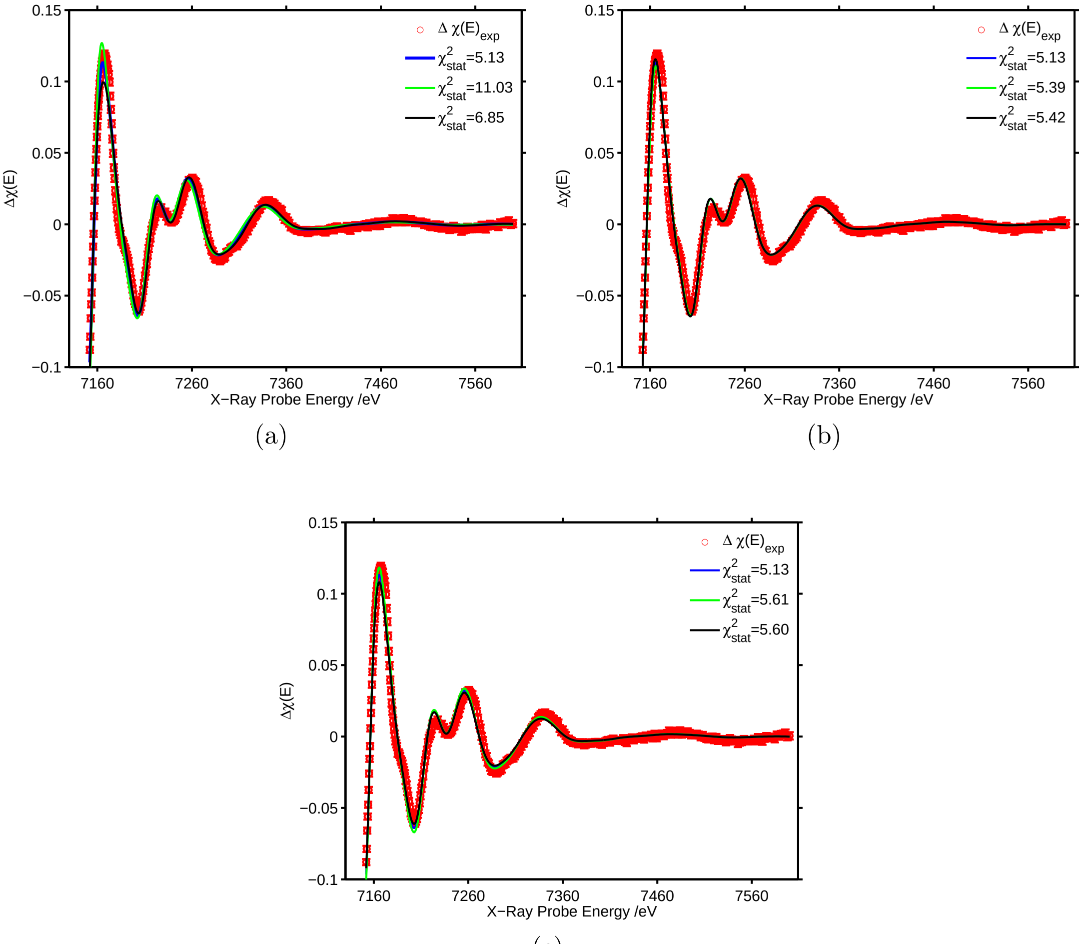

(a)

(b)

(c)

Figure 8.16.: (a) EXAFS transient fit together with next neighbor theoretical models i.e ΔR = 0.18 Å and ΔR = 0.22 Å together with best fit. (b) Best EXAFS transient fit together with next neighbor theoretical models i.e. ΔE = -1.2 eV and ΔE = -1.8 eV. (c) Best EXAFS transient fit together with next neighbor theoretical models i.e. f = 63% and f = 69%.

respectively. This expansion should cover the possible $^5B_2$ excited state structure. The structural distortion delivers a global minimum $\chi^2_{stat}(\Delta R,\Delta E,f) = 7.36$ at $\Delta R = 0.18 \pm 0.02$ Å and 0.243 ± 0.027 Å for the equatorial and axial Fe−N bond distances, excited state fraction $f = 57 \pm 3$ % and energy shift $\Delta E = -3.5 \pm 0.4$ eV. Fig.8.17 shows the best fit in energy and photoelectron wavevector space using the above parameters. Parameters for the best fit are summarized in Table (8.8).

Fig.8.18(a) shows the $\chi^2_{stat}(\Delta R,\ \Delta E)$ values calculated for fixed f = 57 %, for each structural distortion, energy shift variation between -10 and 5 eV in 0.1 eV

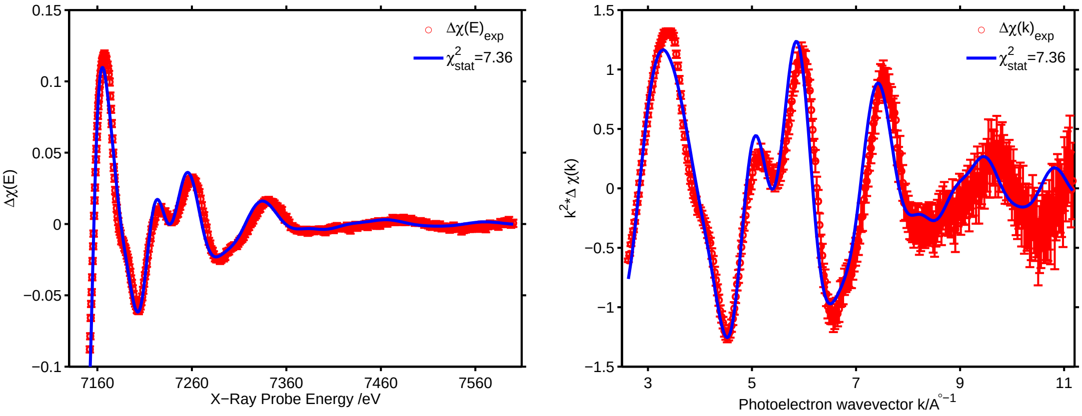

(a) (b)

Figure 8.17.: Best transient EXAFS fit with ΔE = -3.5 eV, $\Delta R_{eq.}$ = 0.18 Å, $\Delta R_{ax.}$ = 0.216 Å and f = 57% fit parameters of the non-uniformly expanded model. (a) fit in energy space and (b) in photoelectron wavevector space multiplied by k^2 to amplify the higher energy part of the spectrum.

steps. Each structural model has a relative local minimum at a different energy shift value, indicates strong positive correlation between structural change and energy shift (Fig.8.19(a)). Similarly, the contour plot between structural distortion and excited state show a correlation, this means each local minimum for the different structural distortions is at a different excited state fraction (Fig.8.19(b)), where as the excited state fraction and energy shift show less correlation and the contour plot yields the more localized global (Fig.8.20).

Estimating the uncertainty in the excited state structure

Similar to the ^{5}E excited state we have plotted the model spectra representing the upper and lower bound values for each fit parameter (Tab.8.4), together with the best fit result. Again, the adjacent models look very similar to the best transient EXAFS model, implying that only the statistical goodness defines the uncertainty. This may also hint to a stringent(small) definition of the error bar sizes(see Fig.8.21).

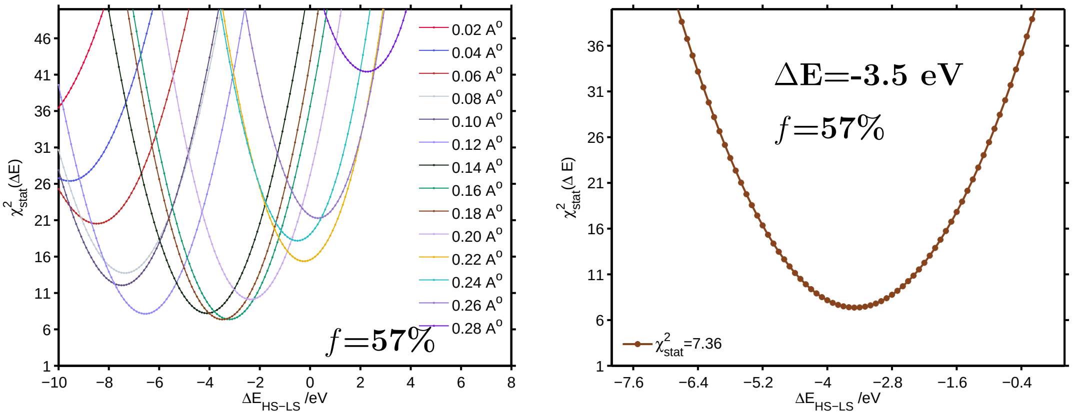

(a) (b)

Figure 8.18.: (a) Calculated $\chi^2_{stat}(\Delta\text{E})$ curves for all the possible structural distortions at single value of excited state fraction f = 57%. (b) Calculated $\chi^2_{stat}(\Delta\text{E})$ values for $\Delta\text{R}_{eq.}$ = 0.18 Å, $\Delta\text{R}_{ax.}$ = 0.243 Å, and f = 57%.

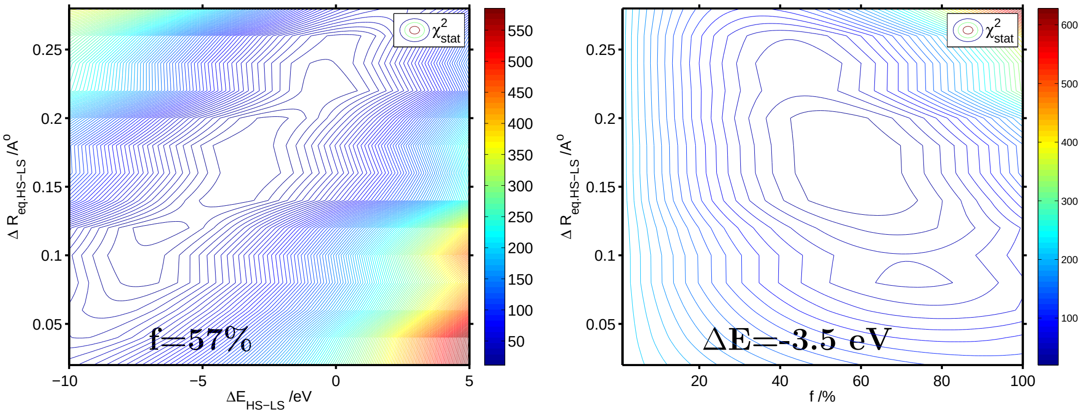

(a) (b)

Figure 8.19.: Surface plot to visualize the correlation between fit parameters considered. (a) between energy shift, ΔE and Fe−N bond length change, $\Delta\text{R}_{eq.}$ at fixed excited state fraction, f = 57% and (b) between excited state fraction, f and Fe−N bond length change, $\Delta\text{R}_{eq.}$ at a fixed ΔE = -3.2 eV.

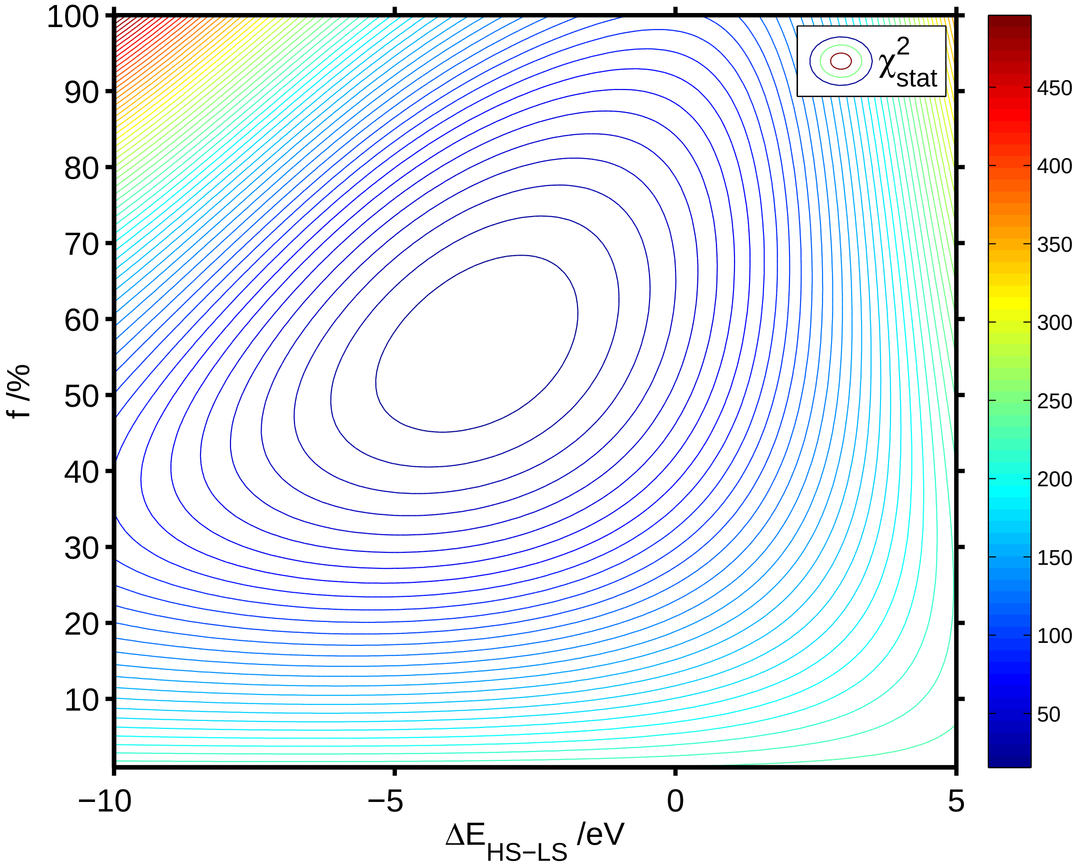

Figure 8.20.: Surface plot to visualize the correlation between fit parameters considered between energy shift, ΔE and excited state fraction, *f* at a fixed Fe−N bond length change, $\Delta R_{eq.} = 0.18$ Å. The plot clearly shows the global minimum for the χ^2 is at ΔE of 1.5 eV and $f = 66\%$.

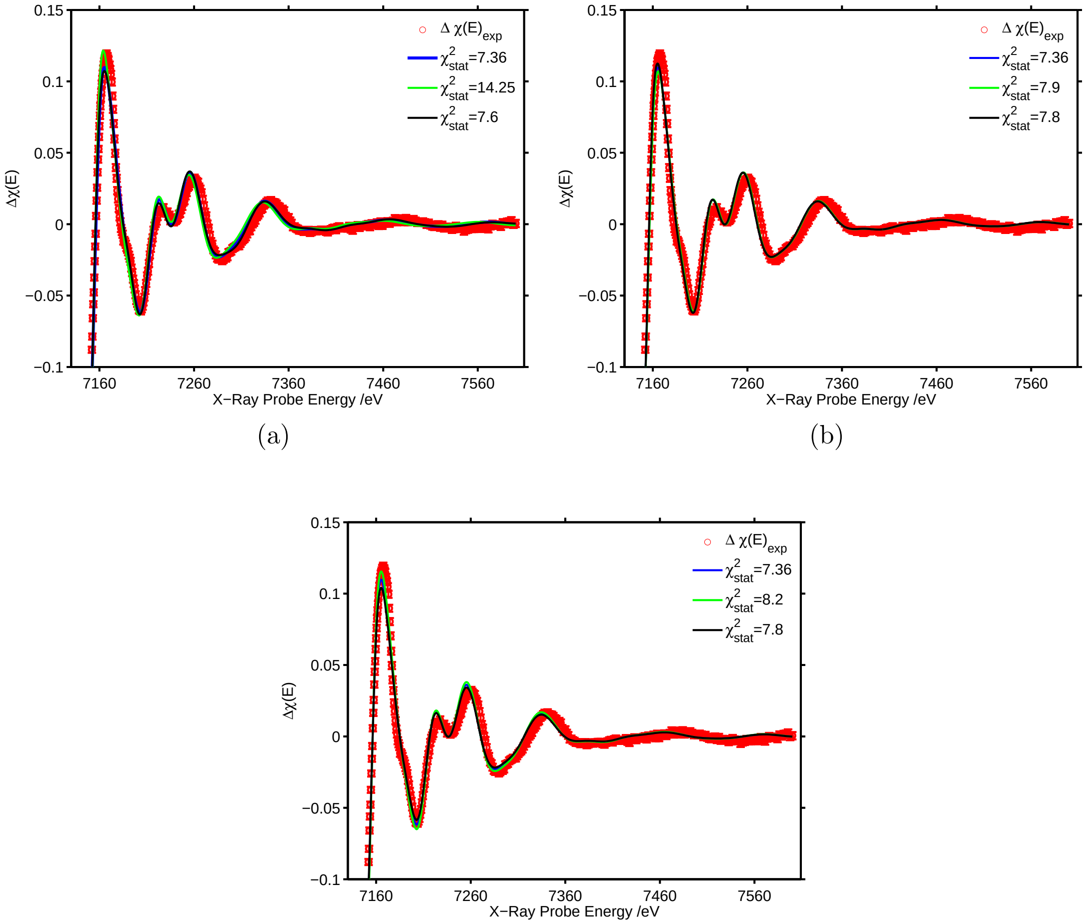

(a) (b)

(c)

Figure 8.21.: Best EXAFS transient fit together with adjacent theoretical models: (a) for $\Delta R_{eq.} = 0.18$ Å and $\Delta R_{eq.} = 0.22$ Å, (b) for ΔE = -3.1 eV and ΔE = -3.9 eV and (c) for $f = 53\%$ and $f = 60\%$.

8.7. Discussion on HS of $[Fe(terpy)_2]^{2+}$

Recent studies by Canton *et al.*[86] indicated $^5B_2$ state results close-lying degenerate ^5E state through pseudo-Jahn−Teller coupling. These two excited states are optimized in DFT yielding slightly different bond lengths(Tab.8.7). Energy space EXAFS fitting is done to extract the excited state structure. Unlike Fourier transform (FT) EXAFS fitting, in the fitting approach used here, it is not needed to know the HS population f, since it is determined during the fit. For the FT EXAFS fitting reported [74] f=71% is used to analyses the experimental data. The analysis predicted the excited state structure to be ^5E. In the analysis reported here, the excited state fraction is refined to f=66± 3%, which is smaller than the value used in the FT fitting. According to our fit results the most probable high spin state for the $[Fe(terpy)_2]^{2+}$ molecule is ^5E with uniformly expanded model which yields the lower χ^2_{stat} value compared to $^5B_2$ (see Tab.8.8). The Fe−N high-spin to low-spin bond distance change ΔR_{HS-LS}= 0.2±0.02 Å show a good agreement with the 0.218 Å predicted from the DFT (see Tab.8.7) but the structural values obtained here show slight difference with respect to FT fitting analysis. In FT EXAFS fitting the scattering paths are categorized as the first and second shells each with one structural fitting parameter, this leads distortion of molecules (such as distorting the pyridine rings). The distortion doesn't respect the angle, however in the analysis done her we overcome this problem by changing only the Fe−N bond distance but keeping intact the pyridine rings. Finally, this method could be used as an alternative EXAFS analysis for similar spin crossover complexes.

Table 8.8.: Fit parameters extracted after convergence of Eq.(8.10) for non-uniformly expanded model. FT = Fourier transform.

models	f(%)	$\Delta R_{ax.HS-LS}$ (Å)	$\Delta R_{eq.HS-LS}$ (Å)	ΔE(eV)	χ^2_{stat}
Best fit: $^5B_2$	57±3	0.243±0.027	0.18±0.02	-3.5±0.4	7.36
Best fit: ^5E	66±3	0.2±0.02	0.2±0.02	-1.5±0.3	5.13
FT fit: ^5E[74]	71	0.206±0.020	0.231±0.010	-	

Chapter 9

Conclusion and outlook

This thesis presents time-resolved X-ray absorption and emission spectroscopy results measured upon photoexcitation of ferrocyanide, $[\mathrm{Fe(bpy)_3}]^{2+}$ and $[\mathrm{Fe(terpy)_2}]^{2+}$ ions in aqueous solution.

Picosecond-resolved XAS results measured upon 266 nm photoexcitation of ferrocyanide ions results in two simultaneous photoproducts namely $[\mathrm{Fe(CN)_5H_2O}]^{3-}$ and $[\mathrm{Fe^{III}(CN)_6}]^{3-}$ complexes. These two photoproducts are disentangled only with time-resolved XANES data, and the ratio of estimated excited state fraction is consistent with quantum yield measurements reported in prior studies. Also, time-resolved XES is used to characterise the transient species formed after photoexcitation [130]. The photoaquation process has been investigated in detail upon photoexcitation with 355 nm laser and comparison of picosecond-resolved XANES results with calculated spectra suggest the formation of photoaquated complex within 100 ps experimental time resolution. Furthermore, we did not observe decay of the photoaquated product until 1.226 microseconds.

We investigated the ligand exchange mechanism happens upon 355 nm excitation of ferrocyanide ($[\mathrm{Fe^{II}(CN)_6}]^{4-}$) ions. Based on the comparison of simulated pre-edge peaks of 1s→3d transition with our data, we conclude that the reaction pathway commences via ligand detachment followed by the formation of the long-lived photoaquated complex. TR Kβ XES results also reveal the spin state of the intermediate complex. Unfortunately, due to the poor-quality of the XES data, we could not nail down the exact spin state of the intermediate state. Combining these findings we interpret that the aquation process happens from a pentacoordinated precursor state with non-singlet spin state, and takes roughly 12 ps. In our data we did not observe Berry pseudorotation (conversion from square pyramidal to trigonal bipyramidal symmetries) similar to what has been seen in $[\mathrm{Fe^{III}(CO)_5}]$ [195] and $[\mathrm{Cr(CO)_5}]$ [196].

High-quality time-resolved EXAFS measured $[\mathrm{Fe(terpy)_2}]^{2+}$, and $[\mathrm{Fe(bpy)_3}]^{2+}$ complexes after 100 ps of 532 nm laser excitation allows us to characterise the excited state structures with sub-angstrom spatial resolution. A new novel approach is implemented i.e. fitting directly the time-resolved transient EXAFS data in energy space to extract the excited state structure of photoexcited molecules. This method can be used to extract structural information from time-resolved EX-

AFS data collected over different transition metal complexes given that we know the reaction coordinate of the molecule. Although the transient EXAFS fitting approach rely on DFT atomic coordinates it allows us to have control over the parameters involved in the fitting procedure, unlike Fourier transform fitting. The TR-EXAFS data on $[\mathrm{Fe(bpy)_3}]^{2+}$ has been re-analysed, and we show that the excited state fraction estimated (f=38±5%) from this method is in good agreement with other complementary tools such as XES (f=34±4%). Another set of TR EXAFS data measured on $[\mathrm{Fe(terpy)_2}]^{2+}$ molecule has been analysed to identify the excited state structure among the two possible high spin state complexes. The estimated statistical χ^2 values for both HS structures is very close, with the ^{5}E which is uniformly expanded model resulting lower χ^2 value. Based on this we concluded the photoexcited $[\mathrm{Fe(terpy)_2}]^{2+}$ molecule have ^{5}E high spin state after 100 ps.

In this thesis, ferrocyanide molecule was used as a model system to understand ultrafast ligand dissociation mechanism. Unfortunately, the low optical cross section (about 100 times less than spin crossover complexes) hinders the signal quality of TR XAS and XES techniques which makes our interpretation difficult. However, the quest for understanding the ligand exchange process will continue by analysing the time-resolved X-ray diffuse scattering data collected along with the results reported. Since the scattering data is more sensitive to the solvation shell, additional information about the solvation shell will be extracted from the XDS data which we are not sensitive with XAS and XES techniques. In addition, photon hungry experiments such as X-ray Raman and valence-to-core XES can be realised at Femtosecond X-ray Experiments (FXE) instrument (will be ready for user in 2017) and will provide a complementary information about photoinduced chemical changes.

Appendix A

FEFF input file

The FEFF 8.20 is ab initio based computer package uses an input file (saved with name feff.inp) to start the calculation of the X-ray absorption spectra. The first two blocks contain the input cards, the values of each card can be changed, and it gives an opportunity to determine the outcome of the calculation (refer [197] for the explanation of the input cards). The last block contains the xyz atomic coordinates of the atoms in the complex. The source of xyz coordinates can be X-ray crystallographic, Neutron diffraction, EXAFS and DFT optimised. The atomic coordinates are shown here and all other calculations reported in this thesis uses DFT optimised geometries provided by György Vankó group. The file shown here contains the coordinates of $[\mathrm{Fe}^{\mathrm{II}}(\mathrm{CN})_6]^{4-}$ complex.

```
 CONTROL     1      1      1      1     1   1
  PRINT      1      0      0      1     0   3
  EDGE       K
   S02       1
   SCF      4.5     1     30    0.05   10
  EXAFS     12
  RPATH      6
EXCHANGE     0      0    0.04     0
  SIG2     0.003
CRITERIA   10.0   0.05
```

```
POTENTIALS
      ipot          Z   element  l-scmt  l-fms  stoichiometry
       0           26     Fe        2      2          1
       1            6      C        1      1          6
       2            7      N        1      1          6
```

```
ATOMS
 * X          Y           Z          IPOT   Element
 0.000000   -0.000000   -0.000000     0       Fe
 0.000000    0.000000    1.969611     1       C
-0.000000   -1.969611   -0.000000     1       C
-1.969611   -0.000000    0.000000     1       C
 0.000000   -0.000000   -1.969611     1       C
-0.000000    1.969611   -0.000000     1       C
 1.969611   -0.000000    0.000000     1       C
-0.000000   -3.160259   -0.000000     2       N
 0.000000    0.000000    3.160259     2       N
 3.160259   -0.000000    0.000000     2       N
-3.160259    0.000000    0.000000     2       N
 0.000000   -0.000000   -3.160259     2       N
-0.000000    3.160259   -0.000000     2       N
 END
```

Appendix B

ORCA input file

The ORCA is ab initio based Quantum Chemistry Program can be used to calculate XAS, XES, UV-vis, IR, Raman, etc. spectra. The program is used DFT and semiempirical SCF-MO packages, and it does self-consistent calculations. An input file for ORCA calculation contains keywords which can be given any order and are not case sensitive. The keywords allow the user to define the outcome of the calculation (for the details of other keywords please refer[108]). The last block contains xyz atomic coordinates, the complex charge and the total spin state of the metal centre. The atomic coordinates shown here are DFT optimised geometries provided by György Vankó group and Alexander Guda from Southern Federal University, Rostov-on-Don, Russia. The input files used for the pre-edge calculation of the different complexes is given below.

B.1. $[\mathrm{Fe^{II}(CN)_6}]^{4-}$ with S=0

```
    !SP         UKS       B3LYP       RIJCOSX   def2-TZVP   def2-TZVP/JK
 !TightSCF   Grid4   NoFinalGrid   LargePrint

   % method
   ScalHFX    = 0.15
      end

     % maxcore       2024
       % tddft
        NRoots           20
       MaxDim          150
   OrbWin[0] = 0,      0,     -1,   -1
   OrbWin[1] = 0,      0,     -1,   -1
    DoQuad true
         end
```

```
*xyz      -4          1
 Fe    0.000000    0.000000    0.000000
 C     0.000000    0.000000    1.969611
 C    -0.000000   -1.969611   -0.000000
 C    -1.969611   -0.000000    0.000000
 C     0.000000   -0.000000   -1.969611
 C    -0.000000    1.969611   -0.000000
 C     1.969611   -0.000000    0.000000
 N    -0.000000   -3.160259   -0.000000
 N     0.000000    0.000000    3.160259
 N     3.160259   -0.000000    0.000000
 N    -3.160259    0.000000    0.000000
 N     0.000000   -0.000000   -3.160259
 N    -0.000000    3.160259   -0.000000
 *
```

B.2. $[\mathrm{Fe}^{\mathrm{III}}(\mathrm{CN})_6]^{3-}$ with S=1/2

```
*xyz      -3          2
 Fe    0.000000   -0.000000   -0.000003
 C    -0.000573   -0.000537    1.973330
 C     0.042710   -1.964503    0.000526
 C    -1.964503    0.042710    0.000485
 C     0.000573    0.000536   -1.973336
 C    -0.042709    1.964503   -0.000532
 C     1.964503   -0.042710   -0.000491
 N     0.055719   -3.144475    0.000818
 N    -0.000665   -0.000780    3.152723
 N     3.144475   -0.055718   -0.000739
 N    -3.144474    0.055720    0.000752
 N     0.000665    0.000780   -3.152729
 N    -0.055718    3.144474   -0.000803
 *
```

B.3. $[\mathrm{Fe}^{\mathrm{II}}(\mathrm{CN})_5]^{3-}$ with D_{3h} symmetry and S = 1

```
*xyz     -3          3
 Fe    0.026980   -0.000114   -0.000286
 C    -2.072451    0.000259   -0.000374
 C     1.081725   -1.817056   -0.000368
 C     0.025998   -0.000178   -1.992698
 C     1.081515    1.817071   -0.000369
 C     0.025993   -0.000177    1.992138
 N    -3.244402    0.000502   -0.000378
 N     1.666338   -2.832796   -0.000360
 N     0.024542   -0.000211   -3.166067
 N     1.665950    2.832914   -0.000360
 N     0.024530   -0.000213    3.165505
 *
```

B.4. $[\mathrm{Fe}^{\mathrm{II}}(\mathrm{CN})_5]^{3-}$ with D_{3h} symmetry and S = 2

```
*xyz     -3          5
 Fe    0.038542    0.000062   -0.000280
 C    -2.192761   -0.000525   -0.000336
 C     1.221308   -1.851164   -0.000296
 C    -0.054639    0.000655   -2.389277
 C     1.222424    1.850736   -0.000293
 C    -0.054710    0.000654    2.388630
 N    -3.361982   -0.000830   -0.000354
 N     1.833662   -2.848269   -0.000383
 N    -0.090156    0.000585   -3.561083
 N     1.835311    2.847508   -0.000380
 N    -0.090281    0.000589    3.560435
 *
```

B.5. $[\mathrm{Fe^{II}(CN)_5}]^{3-}$ with C_{4V} symmetry and S=1

```
*xyz       -3            3
 Fe    0.018579000   0.282831000  -0.505426000
 C     0.014849000  -0.786797000   1.299578000
 C    -2.190956000   0.231690000  -0.436464000
 C     0.019621000  -0.665453000  -2.313843000
 C     2.232376000   0.213216000  -0.429789000
 N     0.007384000  -1.373385000   2.317592000
 N    -3.369174000   0.228992000  -0.442725000
 N     0.018874000  -1.223143000  -3.350544000
 N     3.410509000   0.197003000  -0.423992000
 C     0.027091000   2.317697000  -0.457282000
 C     0.020612000   3.492664000  -0.382404000
 *
```

B.6. $[\mathrm{Fe^{II}(CN)_5H_2O}]^{3-}$ with S=0

```
*xyz       -3            1
 Fe    0.000000000   0.000000000   0.000000000
 O     2.186943000  -0.099655000  -0.017811000
 C    -1.839940000   0.092971000   0.015102000
 C     0.089813000   1.088997000  -1.566668000
 C     0.137040000   1.556180000   1.099337000
 C    -0.043539000  -1.564498000  -1.093932000
 C    -0.001886000  -1.100584000   1.560301000
 N    -3.025479000   0.155773000   0.024920000
 N     0.170675000   1.761351000  -2.538541000
 N     0.249634000   2.518549000   1.780718000
 N    -0.056084000  -2.535037000  -1.772314000
 N     0.010806000  -1.783632000   2.527535000
 H     2.456774000   0.559903000   0.648715000
 H     2.439146000   0.307535000  -0.868144000
 *
```

Appendix C

Physical constants

Some of the most commonly used physical constants in this thesis. The values given here are taken from CODATA of 2014 [198].

Avogadro constant	N_A	6.022 140 857(74)x 10^{23} mol^{-1}
Boltzmann constant	K_B	1.380 648 52(79)x 10^{-23} JK^{-1}
Electron mass	m_e	9.109 383 56(11) x 10^{-31} kg
Planck's constant	h	6.626 070 040(81) x 10^{-3k} Js
Speed of light	c	2.99 792 458 x 10^{8} ms^{-1}
Elementary charge	e	1.602 176 6208(98) x 10^{-19} C

Acknowledgments

First and foremost, I want to express my sincere gratitude to my boss, Prof. Dr. Christian Bressler, for the invaluable learning opportunity he gave me to work under his supervision. Dear Christian, I cannot thank you enough for your tireless efforts to stimulate my research activity, sharing your brilliant ideas and for encouraging me to look forward in all situations. Moreover, I am very lucky and grateful for the challenges and opportunities you presented to me. Your guidance and continuous support equipped me with knowledge and experience that will help me in my career. In addition, I would like to extend my gratitude to Prof. Dr. Markus Drescher for agreeing to be my University thesis supervisor. I am exceedingly grateful for the generous time given to discuss my research activities and for the insightful comments and advice.

A special thank you goes to Dr. Wojciech Gawelda who introduced me to the field of X-ray science. Dear Wojciech, I am grateful for your precious advice, discussions during beamtimes and your immense support since the very beginning. Above all, I would like to show my gratitude for the lengthy scientific discussions we had regarding our results and for all your advice both at the scientific and personal level. Another special thank you goes to Dr. Andreas Galler, also regarding his contribution to the results. I am privileged to thank Andreas for his tireless support during the XFEL beamtime with the data reduction and data analysis. In addition, Andreas has read part of my thesis and has provided me with invaluable comments.

My heartfelt appreciation goes to the SFB 925 graduate school program for funding the PhD project and for providing me with the necessary travel support, which has allowed me to participate in the various X-ray experiments. The program opened a significant opportunity for me to live and study in Germany. Residing and conducting research in a foreign country has enabled me to immerse myself in a new culture, broaden my worldview and expose me to many invaluable opportunities, some of which do not exist in an Ethiopian cultural setting. Another special thank you goes to the PIER Helmholtz Graduate School for their generous travel grants, which allowed me to participate in essential X-ray experiments.

I also want to thank Mr. Alexander Britz, Dr. Dmitry Khahulin and Dr. Peter Zalden for being an integral part of both the synchrotron and XFEL experiments. Dear Alexander, I want to extend my gratitude to you for all the fun time we shared during beamtimes, conferences, workshops and discussions regarding our results. In addition, I am especially grateful to Micheal Diez, Manuel Harder, Maria Naumova, Dr. Dennis Goeries and Christina Boemer for proofreading parts my thesis. Dear Manuel, I thank you as well for the translation of the abstract into German. And I want to thank Dr. Alexander Guda for his support with the simulation of the XAS spectra and discussion of my results.

A debt of sincere gratitude also goes to the AMO group members: Dr. Anne Marie March, Dr. Gilles Doumy and Dr. Stephen H Southworth who were instrumental, kind and supportive during the Synchrotron measurements included in this thesis. Dr. Gyorgy Vanko who introduced me to the X-ray emission spectroscopy, encouraged me, and put me at ease with his well-crafted jokes during beamtimes also has my heartfelt appreciation. Gyorgy and his group members, Dr. Zoltan Nemeth and Dr. Rozsalyi Emese, are to be specially acknowledged for providing me with invaluable preparation of the sample and DFT optimised coordinates. I also want to thank the Prof. Martin Meedom Nielsen group members, and particularly Dr. Tim Brandt van Driel who helped me during the SACLA beamtime data analysis of TR XES and TR XDS measurements. I would like to extend the same gratitude to Dr. Marcin Klepka, Dr. Anna Wolska, Dr. Keisuke Hatada and Prof. Dr. Serena DeBeer for giving me a chance attend conferences and offering me ample time for discussing my results.

Of all those who have continuously supported me with their encouragement and advice, I am especially grateful to my good friends Meseret Bisirat, Yewedalem Tesfaye and to my colleagues Jones Amir Rafippor and Alexander Achner. I extend this same loving gratitude to my friends Birhanu Mekuanint and his wife, Dagnachew Amare, Yohannes Birhanu and his wife, Mona Rafipoor, Sadegh Bakhtiarzadeh, Dr. Yeshambel Tesfa, Dr. Lorenzo Galli and my friends from University of Groningen; Jorge, Eric and Daniel.

And last, but not in anyway least, it is my privilege and my very great pleasure to thank my uncle Dagnachew Atinkut and his family, my brothers and sisters, namely Alebel, Sefinesh, Banchamlak, Assefa, Birhanu, Teshager, Meseret, Daniel, Yonannis, Ermias, Robel, and my brothers-in-law Agmasie and Wasie, all of whom have shown me their unwavering love and support in all aspects of my life.

Bibliography

[1] Miriam Shirom and Gabriel Stein. Excited state chemistry of the ferrocyanide ion in aqueous solution. i. formation of the hydrated electron. *The Journal of Chemical Physics*, 55(7):3372–3378, 1971. v, vii, 6, 7, 9, 20, 22, 23, 24, 87, 88, 89, 91, 93, 111, 112, and 114

[2] Miriam Shirom and Gabriel Stein. Excited state chemistry of the ferrocyanide ion in aqueous solution. ii photoaquation. *The Journal of Chemical Physics*, 55(7):3379–3382, 1971. v, vii, 6, 7, 9, 18, 19, 20, 23, 24, 88, 91, 93, 112, and 114

[3] Ahmed H Zewail. Femtochemistry : Atomic-scale dynamics of the chemical bond. *Journal of physical chemistry A*, 104:5660–5694, 2000. 5

[4] Friedrich Schotte, Hyun Sun, Ville R I Kaila, Hironari Kamikubo, Naranbaatar Dashdorj, and Eric R Henry. Watching a signaling protein function in real time via 100-ps time-resolved Laue crystallography. 2012. 5

[5] Friedrich Schotte, Hyun Sun Cho, Jayashree Soman, Michael Wulff, John S. Olson, Anfinrud, and Philip A. Real-time tracking of CO migration and binding in the α and β subunits of human hemoglobin via 150-ps time-resolved Laue crystallography. *Chemical Physics*, 422:98–106, 2013. 5

[6] Matteo Levantino, Giorgio Schiro, Henrik Till Lemke, Grazia Cottone, James Michael Glownia, Diling Zhu, Mathieu Chollet, Hyotcherl Ihee, Antonio Cupane, and & Marco Cammarata. Ultrafast myoglobin structural dynamics observed with an X-ray free-electron laser. *Nature communications*, 6, 2015. 5

[7] Marco Cammarata, Matteo Levantino, Friedrich Schotte, Philip A Anfinrud, Friederike Ewald, Jungkweon Choi, Antonio Cupane, Michael Wulff, and Hyotcherl Ihee. Tracking the structural dynamics of proteins in solution using time-resolved wide-angle X-ray scattering. 5(10):881–887, 2008. 5

[8] Lin X. Chen, Wighard J. H. Jager, Guy Jennings, David J. Gosztola, Anneli Munkholm, and Jan P. Hessler. Capturing a Photoexcited Molecular Structure Through Time-Domain X-ray Absorption Fine Structure. *Science*, 292(5515):262–264, 2001. 5, 63, and 76

[9] Ch. Bressler, C. Milne, V. Pham, A. ElNahhas, R. M. van der Veen, W. Gawelda, W. Johnson, P. Beaud, D. Grolimund, M. Kaiser, C. N. Borca, G. Ingold, R. Abela, and M. Chergui. Femtosecond XANES Study of the Light-Induced Spin Crossover Dynamics in an Iron(II) Complex. *Science (New York, N.Y.)*, 323(January):489–492, 2009. 5, 6, 137, and 153

[10] Christian Bressler and Majed Chergui. Ultrafast x-ray absorption spectroscopy. *Chemical Reviews*, 104(4):1781–1812, 2004. PMID: 15080712. 5, 9, 38, 41, 76, 77, and 79

[11] György Vankó, Pieter Glatzel, Van-Thai Pham, Rafael Abela, Daniel Grolimund, Camelia N Borca, Steven L Johnson, Christopher J Milne, and Christian Bressler. Picosecond time-resolved X-ray emission spectroscopy: ultrafast spin-state determination in an iron complex. *Angewandte Chemie (International ed. in English)*, 49(34):5910–2, aug 2010. 5

[12] Sophie E Canton, Kasper S Kjær, György Vankó, Tim B van Driel, Shin-ichi Adachi, Amélie Bordage, Christian Bressler, Pavel Chabera, Morten Christensen, Asmus O Dohn, Andreas Galler, Wojciech Gawelda, David Gosztola, Kristoffer Haldrup, Tobias Harlang, Yizhu Liu, Klaus B Møller, Zoltán Németh, Shunsuke Nozawa, Mátyás Pápai, Tokushi Sato, Takahiro Sato, Karina Suarez-Alcantara, Tadashi Togashi, Kensuke Tono, Jens Uhlig, Dimali A Vithanage, Kenneth Wärnmark, Makina Yabashi, Jianxin Zhang, Villy Sundström, and Martin M Nielsen. Visualizing the non-equilibrium dynamics of photoinduced intramolecular electron transfer with femtosecond X-ray pulses. *Nature communications*, 6:6359, 2015. 6

[13] Wenkai Zhang, Roberto Alonso-Mori, Uwe Bergmann, Christian Bressler, Matthieu Chollet, Andreas Galler, Wojciech Gawelda, Ryan G Hadt, Robert W Hartsock, Thomas Kroll, Kasper S Kjær, Katharina Kubiček, Henrik T Lemke, Huiyang W Liang, Drew a Meyer, Martin M Nielsen, Carola Purser, Joseph S Robinson, Edward I Solomon, Zheng Sun, Dimosthenis Sokaras, Tim B van Driel, György Vankó, Tsu-Chien Weng, Diling Zhu, and Kelly J Gaffney. Tracking excited-state charge and spin dynamics in iron coordination complexes. *Nature*, 509(7500):345–8, may 2014. 6, 9, 55, 127, 129, 130, and 146

[14] Wojciech Gawelda, Andrea Cannizzo, Van-Thai Pham, Frank van Mourik, Christian Bressler, and Majed Chergui. Ultrafast nonadiabatic dynamics of $[\mathrm{Fe(bpy)_3}]^{2+}$ in solution. *Journal of the American Chemical Society*, 129(26):8199–206, 2007. 6 and 27

[15] Miriam Shirom and Gabriel Stein. Phosphate-mediated dehydrogenation of alcohol in the photochemistry of ferrocyanide in aqueous solution. *Nature*, 204(21):778 – 779, 1964. 6, 9, 20, 24, 87, 88, 89, and 111

[16] Ph Wernet, K. Kunnus, I. Josefsson, I. Rajkovic, W. Quevedo, M. Beye, S. Schreck, S. Grubel, M. Scholz, D. Nordlund, W. Zhang, R. W. Hartsock, W. F. Schlotter, J. J. Turner, B. Kennedy, F. Hennies, F. M. F. de Groot, K. J. Gaffney, S. Techert, M. Odelius, and A. Fohlisch. Orbital-specific mapping of the ligand exchange dynamics of Fe(CO)5 in solution. *Nature*, 520(7545):78–81, 2015. 6, 9, 16, 126, and 130

[17] Henrique E Toma and John M Malin. Properties and Reactivity of Some Pentacyanoferrate(II) Complexes of Aromatic Nitrogen Heterocycles. *Inorganic chemistry*, 12(5):1039–1045, 1973. 6

[18] Henrique E Toma and John M Malin. Kinetics of Formation and Stability Constants of Some Pentacyanoferaate (II) Complexes of Aromatic Nitrogen Heterocycles. *Inorganic chemistry*, 12(9):2080–2083, 1973. 6

[19] By Zdravko Bradic, Dusanka Pavlovic, Ivo Murati, and Rudjer Bobkovic. Kinetics and Mechanism of Replacement of Sulphite in the Pentacyano- (sulphito)ferrate(ii) Ion by Cyanide Ion. *Journal of the Chemical Society, Dalton Transactions*, (344):1973–1975, 1973. 6

[20] D Pavlovib, I Murati, and S. ASperger. Mechanism of octahedral substitutions .9. Grunwald-Winstein treatment of spontaneous aquation of trans-chloronitro-dichlorobisethylenediaminecobalt(III) and trans-dichlorobisethylenediaminecobalt(iii) ions in mixed aqueous solvents. *Journal of the Chemical Society-Dalton Transactions*, (602):1972–1973, 1972. 6

[21] M. I. Finston and H. G. Drickamer. Photoconductivity Studies of the Ferrocyanide Ion under High Pressure. *The journal of physical chemistry*, 619(1):50–55, 1981. 6

[22] S. Le Caër, G. Vigneron, J. P. Renault, and S. Pommeret. First coupling between a linac and FT-IR spectroscopy: The aqueous ferrocyanide system. *Chemical Physics Letters*, 426:71–76, 2006. 6 and 23

[23] Stanislas Pommeret, Ryszard Naskrecki, Peter van der Meulen, Marjorie Menard, Georges Vigneron, and Thomas Gustavsson. Ultrafast events in the electron photodetachment from the hexacyanoferrate(ii) complex in solution. *Chemical Physics Letters*, 288:833 – 840, 1998. 6 and 23

[24] Max S. MATHESON, W. A MULACA, and JOSEPRHA BAKI. Formation of the hydrated electron in the flash photolysis of aqueous solutions. *Journal Of Physical Chemistry*, 1089(10), 1963. 6

[25] Marco Eli Reinhard. *Ultrafast X-Ray and 2-Dimensional UV Spectroscopic Studies of Hexacyanoferrate Ions in Solution.* PhD thesis, École polytechnique Fédérale de Lausanne, 2014. 6, 22, 88, 96, 98, 105, 106, 107, 108, 115, 117, 131, and 132

[26] Taewoo Lee, Yan Jiang, Christoph G Rose-Petruck, and Frank Benesch. *The Journal of chemical physics*, 122(8):84506, 2005. 7, 19, 23, and 88

[27] M Reinhard, T J Penfold, F A Lima, J Rittmann, R Abela, I Tavernelli, C J Milne, and M Chergui. *Structural Dynamics*, 024901:0–12, 2014. 7, 23, 87, 88, 99, 107, 108, and 111

[28] A L Roe, D J Schneider, R J Mayer, J W Pyrz, J Widom, and L Que. X-ray absorption spectroscopy of iron-tyrosinate proteins. *Journal of American Chemical Society*, 106(22):1676–1681, 1984. 7, 39, 99, 122, and 130

[29] A L Roe, D J Schneider, R J Mayer, J W Pyrz, J Widom, and L Que. X-ray absorption spectroscopy of iron-tyrosinate proteins. *Journal of American Chemical Society*, 106(22):1676–1681, 1984. 7

[30] Tami E Westre, Pierre Kennepohl, Jane G Dewitt, Britt Hedman, Keith O Hodgson, and Edward I Solomon. A multiplet analysis of fe k-edge 1s f 3d pre-edge features of iron complexes. *Journal of the American Chemical Society*, 7863(20):6297–6314, 1997. 7, 39, 99, 122, 130, and 131

[31] A. Hauser, C. Enachescu, M. L. Daku, A. Vargas, and N. Amstutz. Low-temperature lifetimes of metastable high-spin states in spincrossover and in low-spin iron(II) compounds: The rule and exceptions to the rule. *Coordination Chemistry Reviews*, 250:1642–1652, 2006. 9, 10, 27, 28, and 29

[32] K. Kalyanasundaram. Photophysics, photochemistry and solar energy conversion with tris(bipyridyl)ruthenium(ii) and its analogues. *Coordination Chemistry Reviews*, 46:159 – 244, 1982. 9

[33] Atkins Peter, Overton Tina, Rourke Jonathan, Weller Mark, and Armstrong Fraser. *Inorganic Chemistry.* Oxford University Press, 5th ed. edition, 2010. 9

[34] Gerald Auböck and Majed Chergui. Sub-50 fs photoinduced spin crossover in $[Fe(bpy)_3]^{2+}$. *Nature Chemistry*, 7(August):629–633, 2015. 9, 27, and 146

[35] Frederico a Lima, Thomas J Penfold, Renske M van der Veen, Marco Reinhard, Rafael Abela, Ivano Tavernelli, Ursula Rothlisberger, Maurizio Benfatto, Christopher J Milne, and Majed Chergui. Probing the electronic and geometric structure of ferric and ferrous myoglobins in physiological solutions by Fe K-edge absorption spectroscopy. *Physical chemistry chemical physics : PCCP*, 16:1617–31, 2014. 9

[36] Frederico a Lima, Christopher J Milne, Dimali C V Amarasinghe, Mercedes Hannelore Rittmann-Frank, Renske M van der Veen, Marco Reinhard, Van-Thai Pham, Susanne Karlsson, Steven L Johnson, Daniel Grolimund, Camelia Borca, Thomas Huthwelker, Markus Janousch, Frank van Mourik, Rafael Abela, and Majed Chergui. A high-repetition rate scheme for synchrotron-based picosecond laser pump/x-ray probe experiments on chemical and biological systems in solution. *The Review of scientific instruments*, 82(6):063111, jun 2011. 9

[37] Miriam Shirom and Stein Gabriel. Phosphate-mediated dehydrogenation of alcohol in the photochemistry of ferrocyanide in aqueous solution. *Nature*, 201:1212–1213, 1964. 9 and 91

[38] Franz Renz, Hiroki Oshio, Vadim Ksenofontov, Markus Waldeck, Hartmut Spiering, and Philipp Gtlich. Strong field iron(II) complex converted by light into a long-lived high-spin state. *Angewandte Chemie - International Edition*, 39(20):3699–3700, 2000. 10, 25, 27, and 29

[39] Peter Atkins and Julio de Paula. *Physical Chemistry.* Oxford University Press, 9th ed. edition, 2010. 10 and 21

[40] By J S Griffith and L E Orgel. Ligand field theory. *Quarterly Review of the Chemical Society*, 11(4):381–393, 1957. 11

[41] J. S. Griffith and L. E. Orgel. Ligand-field theory. *Q. Rev. Chem. Soc.*, 11:381–393, 1957. 11

[42] M a Halcrow. Interpreting and controlling the structures of six-coordinate copper (ii) centers: When is a compression really a compression? *ChemInform*, 35(15):4375–4384, 2004. 12

[43] J. Franck. Elementary processes of photochemical reactions. *Trans. Faraday Soc.*, pages 536–542, 1924. 13

[44] Perrin jablonski diagram. `http://www.texample.net/tikz/examples/the-perrin-jablonski-diagram/`. Accessed: 2016-03-24. 14

[45] L. G. Vanquickenborne and K. Pierloot. Role of spin change in the stereomobile reactions of strong-field d6 transition-metal complexes. *Inorganic chemistry*, 20(1), 1981. 15, 16, and 128

[46] Steven T Spees, Jayarama R Perumareddi, and Arthur W Adamsonlb. Substitution reactions of inorganic complexes. concerning the prediction of activation energies and reaction mechanisms by crystal field theory. *Journal of American Chemical Society*, pages 6626–6635, 1968. 15, 22, and 128

[47] John J. Alexander and Harry B. Gray. Electronic structures of hexacyanometalate complexes. *Journal of the American Chemical Society*, 1900(3576):4260–4271, 1968. 17, 18, 19, 20, and 22

[48] Harry B. Gray and N. A. Beach. The electronic structures of octahedral metal complexes. i. metal hexacarbonyls and hexacyanides. *Journal of American Chemical Society*, 8:2922–2927, 1963. 17, 18, and 19

[49] C. S. Naiman. Interpretation of the absorption spectra of $K_3Fe(CN)_6$. *The Journal of Chemical Physics*, 35(1):323, 1961. 18 and 19

[50] Arthur W. Adamson, William L. Waltz, Edoardo. Zinato, Donald W. Watts, Paul D. Fleischauer, and Robert D. Lindholm. Photochemistry of transition-metal coordination compounds. *Chemical Reviews*, 68(5):541–585, 1968. 18

[51] J. C. Taylor, M. H. Mueller, and R. L. Hitterman. A neutron diffraction study of ferroelectric KFCT, $K_4Fe(CN)_6 \cdot {}_3D_2O$, above the curie temperature. *Acta Crystallographica Section A*, 26(5):559–567, September 1970. 18, 20, 139, and 142

[52] Kuniko Hayakawa, Keisuke Hatada, Paola D'Angelo, Stefano Della Longa, Calogero R Natoli, and Maurizio Benfatto. Full quantitative multiple-scattering analysis of x-ray absorption spectra: application to potassium hexacyanoferrat(ii) and -(iii) complexes. *Journal of the American Chemical Society*, 126(47):15618–23, 2004. 18, 19, 20, 140, and 142

[53] B. N. Figgis, M. Gerloch, and R. Mason. The crystallography and paramagnetic anisotropy of potassium ferricyanide. *Proceedings of the Royal Society A: Mathematical, Physical and Engineering Sciences*, 309(1496):91–118, February 1969. 18 and 20

[54] Keith J. Laidler and M. Christine King. The development of the transition-state theory. *Journal Of Physical Chemistry*, 87(15):2657–2664, 1983. 20

[55] Chmouel R. Goldschmidt and Gabriel Stein. Fast formation of the hydrated electron by dissociation of excited beta-naphtholate. *Chemical Physics Letters*, 6(4):299–303, 1970. 20

[56] Shin-ichi Ohno. The photochemistry of aqueous hexacyanoferrate (II) solutions . i photoaquation reaction at 366 nm. *Bulletin of the Chemical Society of Japan*, 40:1765–1769, 1967. 20 and 24

[57] Cooper H Langford and Thomas R Stengle. Ligand substitution dynamics. *Ann. Rev. Phys. Chem*, (December), 1968. 21

[58] P. L. Airey and F S Dainton. The photochemistry of aqueous solutions of fe(ii). i . photoelectron detachment from ferrous and ferrocyanide ions.

Proceedings of the Royal Society A: Mathematical, Physical and Engineering Sciences, 291:340–352, 1966. 22 and 24

[59] W. L. Waltz and Arther W. Adamson. Photochemistry of complex ions. viii. photoelectron production. *Journal of Chemical Physics*, 3(1967):4250–4255, 1969. 22 and 24

[60] Stein Gabriel. Photochemstry of the ferrocyanide ion in aqueous solution: hydrated electron formation and aquation. *Isreal Journal of Chemistry*, 8:691–697, 1970. 23

[61] Y. Gauduel, a. Migus, J.P. Chambaret, and a. Antonetti. Femtosecond reactivity of electron in aqueous solutions. *Revue de Physique Appliquée*, 22:1755–1759, 1987. 23

[62] Shin-ichi Ohno. The photochemistry of aqueous hexacyanoferrate (ii) solutions . ii photooxidation reaction at 253.7 nm. *Bulletin of the Chemical Society of Japan*, 40:1770–1775, 1967. 23 and 24

[63] G Emschwiller and J Legros. Lhydrolyse photochimique des solutions de ferrocyanure de potassium - influence de la frequence de lintensite d irradiation et de la concentration sur le rendement quantique. *Comptes rendus hebdomadaires des seances de l academie des sciences*, 261:1535, 1965. 24, 89, 92, 93, 112, and 114

[64] P. Gutlich and H. A. Goodwin. *Topics in Current Chemistry: Spin Crossover in Transition Metal Compounds I.* Springer-Verlag Berlin, Heidelberg, Germany, 2004. 24 and 26

[65] Ballhausen C.J. *Introduction to ligand field theory.* Springer-Verlag Berlin, McGraw-Hill, New York, 1962. 24 and 25

[66] David N. Bowman, Alexey Bondarev, Sriparna Mukherjee, and Elena Jakubikova. Tuning the Electronic Structure of Fe(II) Polypyridines via Donor Atom and Ligand Scaffold Modifications: A Computational Study. *Inorganic Chemistry*, 54(17):8786–8793, 2015. 25 and 29

[67] HN Russell and FA FA Saunders. New regularities in the spectra of the alkaline earths. *Astrophysical Journal*, 61(1):1–28, 1925. 24

[68] Y Tanabe and S Sugano. On the absorption spectra of complex ions. 2. *Journal of the Physical Society of Japan*, 9(5):766–779, 1954. 24

[69] Y Tanabe and S Sugano. On the absorption spectra of complex ions. 1. *Journal of the Physical Society of Japan*, 9(5):753–766, 1954. 24

[70] Philipp Gütlich, Andreas Hauser, and Hartmut Spiering. Thermal and optical switching of iron (II) complexes. *Chemie International Edition*, 33:2024–2054, 1994. 25, 26, and 27

[71] S Decurtins, P Gutlich, C P Kohler, and H Spiering. New examples of light-induced excited spin state trapping (LIESST) in Iron(II) Spin-crossover systems. *Journal of the Chemical Society-Chemical Communications*, (7):430–432, 1985. 26

[72] S. Decurtins, P. Gutlich, K. M. Hasselbach, a. Hauser, and H. Spiering. Light-Induced Excited-Spin-State Trapping in Iron(11) Spin-Crossover Systems. Optical Spectroscopic and Magnetic Susceptibility Study. *Inorganic chemistry*, 24:2174–2178, 1985. 26

[73] A. Hauser, J. Jeftic, H. Romstedt, R. Hinek, and H. Spiering. Cooperative phenomena and light-induced bistability in iron (II) spin-crossover compounds. *Coordination Chemistry Reviews*, 190-192:471–491, 1999. 26

[74] György Vankó, Amélie Bordage, Mátyás Pápai, Kristoffer Haldrup, Pieter Glatzel, Anne Marie March, Gilles Doumy, Alexander Britz, Andreas Galler, Tadesse Assefa, Delphine Cabaret, Amélie Juhin, Tim B van Driel, Kasper S Kjær, Asmus Dohn, Klaus B Møller, Henrik T Lemke, Erik Gallo, Mauro Rovezzi, Zoltán Németh, Emese Rozsályi, Tamás Rozgonyi, Jens Uhlig, Villy Sundström, Martin M Nielsen, Linda Young, Stephen H Southworth, Christian Bressler, and Wojciech Gawelda. Detailed Characterization of a Nanosecond-Lived Excited State: X-ray and Theoretical Investigation of the Quintet State in Photoexcited $[\mathrm{Fe(terpy)}_2]^{2+}$. *The journal of physical chemistry. C, Nanomaterials and interfaces*, 119(11):5888–5902, 2015. 26, 28, 29, 30, 54, 77, 92, 135, 150, 151, and 160

[75] W Gawelda, V Pham, R M Van Der Veen, D Grolimund, and R Abela. Structural analysis of ultrafast extended x-ray absorption fine structure with subpicometer spatial resolution : Application to spin crossover complexes Structural analysis of ultrafast extended x-ray absorption fine structure with subpicometer spatial resolution. *Journal of Chemical Physics*, 124520, 2009. 26, 146, 147, 148, 149, and 153

[76] E. Buhks, G. Navon, M. Bixon, and J. Jortner. Spin conversion processes in solutions. *Journal of the American Chemical Society*, 102(9):2918–2923, 1980. 26

[77] Chuan Liang Xie and David N. Hendrickson. Mechanism of spin-state interconversion in ferrous spin-crossover complexes: direct evidence for quantum mechanical tunneling. *Journal of the American Chemical Society*, 109(23):6981–6988, 1987. 27

[78] Yu Zhang, Shaul Mukamel, , Munira Khalil, and Niranjan Govind. Simulating Valence-to-core X-ray emission spectroscopy of transition metal complexes with time-dependent density functional theory. *Journal of Chemical Theory and Computation*, 11:5804–5809, 2015. 27 and 54

[79] K. Haldrup, G. Vanko, W. Gawelda, a. Galler, G. Doumy, a. M. March, E. P. Kanter, a. Bordage, a. Dohn, T. B. Van Driel, K. S. Kjae r, H. T. Lemke, S. E. , J. Uhlig, V. Sundstrom, L. Young, S. H. Southworth, M. M. Nielsen, and C. Bressler. *Journal of Physical Chemistry A*, 116:9878–9887, 2012. 27, 92, 135, 145, 146, and 147

[80] Anthony T Baker and Harold A Goodwin. Crystal Structure of Bis(2,2' :6',2"-terpyridine)iron(II) Bis(perchlorate) Hydrate. *Australian Joournal Chemistry*, 38:207–214, 1985. 28

[81] Matyas Papai, György Vankó, Coen De Graaf, and Tamas Rozgonyi. Theoretical Investigation of the Electronic Structure of Fe(II) Complexes at Spin-State Transitions. *Journal of Chemical Theory and Computation*, 9:509–519, 2013. 28, 29, 149, and 150

[82] Carmen Sousa, Coen de Graaf, Andrii Rudavskyi, Ria Broer, Jörg Tatchen, Mihajlo Etinski, and Christel M. Marian. Ultrafast deactivation mechanism of the excited singlet in the light-induced spin crossover of $[\mathrm{Fe}(_{2,2}{}'-\mathrm{bipyridine})_3]_{2+}$. *Chemistry – A European Journal*, 19(51):17541–17551, 2013. 28

[83] Jun Chang, A. J. Fedro, and Michel Van Veenendaal. Ultrafast cascading theory of intersystem crossings in transition-metal complexes. *Physical Review B - Condensed Matter and Materials Physics*, 82(7):1–5, 2010. 28

[84] Michel Van Veenendaal, Jun Chang, and A. J. Fedro. Model of ultrafast intersystem crossing in photoexcited transition-metal organic compounds. *Physical Review Letters*, 104(6):1–4, 2010. 28

[85] Latévi Max Lawson Daku, Alfredo Vargas, Andreas Hauser, Antony Fouqueau, and Mark Earl Casida. Assessment of density functionals for the high-spin/low-spin energy difference in the low-spin iron(II) tris(2,2′-bipyridine) complex. *ChemPhysChem*, 6(7):1393–1410, 2005. 29

[86] Sophie E. Canton, Xiaoyi Zhang, Latovi M. Lawson Daku, Amanda L. Smeigh, Jianxin Zhang, Yizhu Liu, Carl Johan Wallentin, Klaus Attenkofer, Guy Jennings, Charles A. Kurtz, David Gosztola, Kenneth Wernmark, Andreas Hauser, and Villy Sundstrom. Probing the anisotropic distortion of photoexcited spin crossover complexes with picosecond X-ray absorption spectroscopy. *Journal of Physical Chemistry C*, 118(8):4536–4545, 2014. 30 and 160

[87] H. Nikjoo, S.Uehara, and D. Emfietzoglou. *Interaction of Radiation with Matter*. CRC Press, New York, USA, 2012. 31

[88] Stefan P. Hau-Riege. *Nonrelativistic Quantum X-Ray Physics*. WILEY-VCH, Livermore, CA, USA, 2015. 31

[89] M.J. Berger, J.H. Hubbell, S.M. Seltzer, J. Chang, J.S. Coursey, R. Sukumar, D.S. Zucker, and K. Olsen. Xcom: Photon cross sections database. *National Institute of Standards and Technology (NIST)*, 2010. 32

[90] Glatzel and Pieter U. Bergmann. High resolution 1s core hole x-ray spectroscopy in 3d transition metal complexes-electronic and structural information. *Coordination Chemistry Reviews*, 249:65–95, 2005. 34, 51, 52, and 113

[91] J. J. Rehr and R. C. Albers. Theoretical approaches to x-ray absorption fine structure. *Reviews of Modern Physics*, 72(3):621–654, jul 2000. 34, 38, 41, 42, 43, 45, and 144

[92] D C Koningsberger, B L Mojet, G E Van Dorssen, and D E Ramaker. Xafs spectroscopy ; fundamental principles and data analysis. *Topics in Catalysis*, 10:143–155, 2000. 34, 137, 138, and 139

[93] Frank De Groot. Multiplet effects in x-ray spectroscopy. *Coordination Chemistry Reviews*, 249:31–63, 2005. 34, 45, 51, and 52

[94] Als-Nielsen J. *Elements of Modern X-Ray Physics*. John Wiley and Sons, Inc, 8th ed. edition, 2001. 35 and 58

[95] G Drager and R Frahm. On the multipole character of the x-ray transitions in the pre-edge structure of fe k absorption spectra. an experimental study. *Physica Status Solidi (b)*, 287(1988):287–294, 1988. 39, 99, and 122

[96] James E. Hahn, Robert a. Scott, Keith O. Hodgson, Sebastian Doniach, Sylvia R. Desjardins, and Edward I. Solomon. Observation of an electric quadrupole transition in the X-ray absorption spectrum of a Cu(II) complex. *Chemical Physics Letters*, 88(6):595–598, 1982. 39

[97] Dale E Sayerst, Edward A Stern, and Farrel Lytle. New technique for investigating noncrystalline structures: Fourier analysis of the extended x-ray absorption fine structure. *Physical Review Letters*, 2(18), 1971. 39 and 138

[98] P. A. Lee and J. B. Pendry. Theory of the extended x-ray absorption fine structure. *Physical Review B*, 11(8):2795–2811, 1975. 39

[99] J.J. Rehr and R.C. Albers. Scattering-matrix formulation of curved-wave multiple-scattering theory: Application to x-ray-absorption fine structure. *Physical Review B*, 41(12):8139–8149, 1990. 40 and 42

[100] Edward A. Stern. Theory of the extended x-ray-absorption fine structure. *Phys. Rev. B*, 10:3027–3037, Oct 1974. 40, 138, and 139

[101] Edward A Stern. Number of relevant independent points in x-ray-absorption fine-structure spectra. *Physical Review B*, 48(13):9825–9827, 1993. 40 and 138

[102] R. D. Cowan. *The theory of Atomic Structure and Spectra.* The University of California, Berkley, USA, 1981. 42 and 52

[103] A. L. Ankudinov, J. J. Rehr, and S. D. Conradson. Real-space multiple-scattering calculation and interpretation of x-ray-absorption near-edge structure. *Physical Review B*, 58(12):7565–7576, 1998. 43

[104] J. L. Beeby. Heisenberg exchange hamiltonian from narrow energy band theory. *Proceedings of the Royal Society A: Mathematical, Physical and Engineering Sciences*, 765, 1967. 43

[105] B. Ravel. A practical introduction to multiple scattering theory. *Journal of Alloys and Compounds*, 401:118–126, 2005. 44

[106] B. Ravel and M. Newville. Athena, artemis, hephaestus: Data analysis for x-ray absorption spectroscopy using ifeffit. *Journal of Synchrotron Radiation*, 12(4):537–541, 2005. 44 and 135

[107] John J. Rehr, Joshua J. Kas, Fernando D. Vila, Micah P. Prange And, and Kevin Jorissena. Parameter-free calculations of x-ray spectra with feff9. *Physical chemistry chemical physics : PCCP*, 12(21):5647–5652, 2010. 44

[108] Frank Neese, Frank Wennmohs, Ute Becker, Dmitry Ganyushin, Andreas Hansen, Dimitrios G Liakos, Christian Kollmar, Simone Kossmann, Taras Petrenko, Christoph Reimann, Christoph Riplinger, Kantharuban Sivalingam, Edward Valeev, and Boris Wezisla. Orca: An ab initio, dft and semiempirical scf-mo package. pages 1–489, 2010. 45 and 165

[109] List of quantum chemistry packages. `https://en.wikipedia.org/wiki/List_of_quantum_chemistry_and_solid-state_physics_software`. Accessed: 2016-06-06. 45

[110] Frank Neese. The orca program system. *Wiley Interdisciplinary Reviews: Computational Molecular Science*, 2:73–78, 2012. 45

[111] Núria Aliaga-Alcalde, Serena DeBeer George, Bernd Mienert, Eckhard Bill, Karl Wieghardt, and Frank Neese. The geometric and electronic structure of [(cyclam-acetato)Fe(N)] +: A genuine iron(v) species with a ground-state spin S = 1/2. *Angewandte Chemie - International Edition*, 44(19):2908–2912, may 2005. 46

[112] Michael Roemelt, Martha a Beckwith, Carole Duboc, Marie-Noëlle Collomb, Frank Neese, and Serena DeBeer. Manganese K-edge X-ray absorption spectroscopy as a probe of the metal-ligand interactions in coordination compounds. *Inorganic chemistry*, 51(1):680–7, jan 2012. 46

[113] John F Berry, Eckhard Bill, Eberhard Bothe, Serena DeBeer George, Bernd Mienert, Frank Neese, and Karl Wieghardt. An octahedral coordination complex of iron(VI). *Science (New York, N.Y.)*, 312(Vi):1937–1941, 2006. 46

[114] Serena DeBeer George, Taras Petrenko, and Frank Neese. Prediction of iron K-edge absorption spectra using time-dependent density functional theory. *The journal of physical chemistry. A*, 112(50):12936–43, dec 2008. 46 and 47

[115] Kendra Getty, Mario Ulises Delgado-jaime, and Pierre Kennepohl. Assignment of Pre-edge Features in the Ru K-edge X-ray Absorption Spectra of Organometallic Ruthenium Complexes. *Inorganica Chimica Acta*, 361(4):1–13, 2010. 46

[116] A. D. Becke. Density-functional exchange-energy approximation with correct asymptotic behavior. *Physical Review A*, 38(6):3098–3100, 1988. 46

[117] Ansgar Schäfer, Christian Huber, and Reinhart Ahlrichs. Fully optimized contracted Gaussian basis sets of triple zeta valence quality for atoms Li to Kr. *The Journal of Chemical Physics*, 100(8):5829, 1994. 46

[118] A Klamt and G Schüürmann. Cosmo - a New Approach To Dielectric Screening in Solvents With Explicit Expressions for the Screening Energy and Its Gradient. *Journal of the Chemical Society-Perkin Transactions 2*, pages 799–805, 1993. 46

[119] P. A. M. Dirac. The quantum theory of the emission and absorption of radiation. *Proceedings of the Royal Society A: Mathematical, Physical and Engineering Sciences*, 114, 1927. 51

[120] M.O. Krause Oliver and J.H. Natural widths of atomic k and l levels, kalpha x-ray lines and several kll auger lines. *Journal of the American Chemical Society*, 8(2):329–338, 1979. 51

[121] M.O. Krause. Atomic radiative and radiationless yields for K and L shells. *Journal of Physical Chemistry*, 8(2):307–327, 1979. 51, 77, and 124

[122] György Vankó, Thomas Neisius, Gábor Molnár, Franz Renz, Szilvia Kárpáti, Abhay Shukla, and Frank M F De Groot. Probing the 3D spin momentum with X-ray emission spectroscopy: The case of molecular-spin transitions. *Journal of Physical Chemistry B*, 110:11647–11653, 2006. 53, 54, and 112

[123] Ö Söğüt, E Buyukkasap, and H Erdogan. Chemical-effect variation of K beta/K alpha X-ray intensity ratios in 3d elements. *Radiation Physics and Chemistry*, 64(5-6):343–348, 2002. 52

[124] Ö Söğüt, S. Seven, E. Baydaş, E. Büyükkasap, and A. Küçükönder. Chemical effects on Kβ/Kα X-ray intensity ratios of Mo, Ag, Cd, Ba, La, Ce compounds and total mass attenuation coefficients of Fe and Cu. *Spectrochimica Acta - Part B Atomic Spectroscopy*, 56(8):1367–1374, 2001. 52

[125] Erik Gallo and Pieter Glatzel. Valence to Core X-ray Emission Spectroscopy. *Advanced Materials*, 26:7730–7746, 2014. 52

[126] Marko Petric and Matjaž Kavčič. Chemical speciation via X-ray emission spectroscopy in the tender X-ray range. *J. Anal. At. Spectrom.*, 2016. 52

[127] S.I. Salem, S.L. Panossian, and R.a. Krause. Experimental K and L relative x-ray emission ratess. *Atomic Data and Nuclear Data Tables*, 14(2):91–109, 1974. 53

[128] Jun Kawai, Chikashi Suzuki, Hirohiko Adachi, Tokuzo Konishi, and Yohichi Gohshi. Charge-transfer effect on the linewidth of Fe Kα x-ray fluorescence spectra. *Physical Review B*, 50(16):11347–11354, 1994. 53 and 54

[129] Pieter Glatzel. *X-Ray Fluorescence Emission Following K Capture and 1s Photoionization of Mn and Fe in Various Chemical Environments.* PhD thesis, Universität Hamburg, 2001. 54, 73, and 74

[130] Anne Marie March, Tadesse A. Assefa, Christian Bressler, Gilles Doumy, Andreas Galler, Wojciech Gawelda, Elliot P. Kanter, Zoltán Németh, Mátyás Pápai, Stephen H. Southworth, Linda Young, and György Vankó. Feasibility of Valence-to-Core X-ray Emission Spectroscopy for Tracking Transient Species. *The Journal of Physical Chemistry C*, 119(26):14571–14578, 2015. 54, 55, 111, 112, 113, 117, 128, and 161

[131] Gyorgy Vanko, Amelie Bordage, Pieter Glatzel, Erik Gallo, Mauro Rovezzi, Wojciech Gawelda, Andreas Galler, Christian Bressler, Gilles Doumy, Anne Marie March, Elliot P. Kanter, Linda Young, Stephen H. Southworth, Sophie E. Canton, Jens Uhlig, Grigory Smolentsev, Villy Sundstrom, Kristoffer Haldrup, Tim Brandt Van Driel, Martin M. Nielsen, Kasper S. Kjaer, and Henrik T. Lemke. Spin-state studies with xes and rixs: From static to ultrafast. *Journal of Electron Spectroscopy and Related Phenomena*, 188:166–171, 2013. 54

[132] P E Best. Electronic Structure of the MnO^{4-}, CrO_4^{2-}, and VO_4^{3-} Ions from the Metal K X-Ray Spectra. *Journal of Chemical PhysicsChemical Physics*, 44(9):3248–3253, 1966. 55 and 122

[133] U Bergmann, C R Horne, T J Collins, J M Workman, and S P Cramer. Chemical dependence of interatomic X-ray transition energies and intensities – a study of Mn Kβ'' and Kβ2,5 spectra. *Chemical Physics Letters*, 302(1-2):119–124, 1999. 55

[134] Janine C. Swarbrick, Yaroslav Kvashnin, Karina Schulte, Kalaivani Seenivasan, , Carlo Lamberti, and Pieter Glatzel. Ligand Identification in Titanium Complexes Using X-ray Valence-to-Core Emission Spectroscopy. *Inorganic chemistry*, 49(18):8323–8332, 2010. 55

[135] Mario Ulises Delgado-Jaime, , Serena DeBeer, and Matthias Bauer. Valence-to-Core X-Ray Emission Spectroscopy of Iron-Carbonyl Complexes: Implications for the Examination of Catalytic Intermediates. *Chemistry-A European Journal*, 19(47):15888–15897, 2013. 55

[136] Samantha N Macmillan, Richard C Walroth, Demetra M Perry, Thorbjørn J Morsing, and Kyle M Lancaster. Ligand-Sensitive But Not Ligand-Diagnostic: Evaluating Cr Valence- to-Core X-ray Emission Spectroscopy as a Probe of Inner-Sphere Coordination. *Inorganic chemistry*, 54:205–214, 2015. 55

[137] Australian synchrotron facility. `http://www.synchrotron.org.au/`. Accessed: 2016-01-20. 58

[138] Philip Willmott. *An Introduction to Synchrotron Radiation: Techniques and Applications.* John Wiley and Sons, Ltd, first edition edition, 2011. 58

[139] Linac coherent light source. `http://lcls.slac.stanford.edu/`. Accessed: 2016-03-24. 58, 67, and 68

[140] Spring-8 compact sase source. `http://www-xfel.spring8.or.jp/`. Accessed: 2016-03-24. 58 and 67

[141] Swiss free-electron laser. `http://www.psi.ch/swissfel/`. Accessed: 2016-03-24. 58, 67, and 68

[142] European xfel facility. `http://xfel.desy.de/technical_information/photon_beam_parameter/`. Accessed: 2016-01-20. 58, 67, and 68

[143] W Ackermann and *et al.* Operation of a free-electron laser from the extreme ultraviolet to the water window. *Nature Photonics*, 1(6):336–342, 2007. 59

[144] Advanced photon source. `https://www1.aps.anl.gov/`. Accessed: 2016-03-24. 60, 61, and 62

[145] Advanced photon source machine parameters. `http://www.aps.anl.gov/Accelerator_Systems_Division/Accelerator_Operations_Physics/SRparameters/node1.html`. Accessed: 2016-03-24. 61

[146] European synchrotron radiation facility machine parameters. `http://www.esrf.eu/UsersAndScience/Publications/Highlights/2007/XRS/XRS1`. Accessed: 2016-03-24. 61

[147] Petra III machine parameters. `http://photon-science.desy.de/facilities/petra_iii/machine/parameters/index_eng.html`. Accessed: 2016-03-24. 61

[148] Eric M. Dufresne, Bernhard Adams, Dohn A. Arms, Matthieu Chollet, Eric C. Landahl, Yuelin Li, Donald A. Walko, and Jin Wang. Time-resolved research at the advanced photon source beamline 7-ID. *AIP Conference Proceedings*, 1234(2010):181–184, 2010. 62

[149] 7ID-D beamline parameters. `https://www1.aps.anl.gov/sector-7/7-id/techniques-and-facilities`. Accessed: 2016-03-24. 63

[150] Anne Marie March, Andrew Stickrath, Gilles Doumy, Elliot P Kanter, Bertold Krassig, Stephen H Southworth, Klaus Attenkofer, Charles a Kurtz, Lin X Chen, and Linda Young. Development of high-repetition-rate laser pump/x-ray probe methodologies for synchrotron facilities. *The Review of scientific instruments*, 82(7):073110, 2011. 63, 64, 65, and 76

[151] Michael Wulff, Friedrich Schotte, Graham Naylora, Dominique Bourgeois, Keith Moffat, and Gerard Mourou. Time-resolved structures of macromolecules at the ESRF: Single-pulse Laue diffraction, stroboscopic data collection and femtosecond flash photolysis. *Nuclear Instruments and Methods in Physics Research, Section A: Accelerators, Spectrometers, Detectors and Associated Equipment*, 398(1):69–84, 1997. 63

[152] Melanie Saes, Frank Van Mourik, Wojciech Gawelda, Maik Kaiser, Majed Chergui, Christian Bressler, Daniel Grolimund, Rafael Abela, Thornton E. Glover, Philip A. Heimann, Robert W. Schoenlein, Steven L. Johnson, Aaron M. Lindenberg, and Roger W. Falcone. A setup for ultrafast time-resolved x-ray absorption spectroscopy. *Review of Scientific Instruments*, 75(1):24–30, 2004. 63

[153] W. Gawelda, C. Bressler, M. Saes, M. Kaiser, A. N. Tarnovsky, D. Grolimund, S. L. Johnson, R. Abela And, and M. Chergui. Picosecond Time-Resolved X-Ray Absorption Spectroscopy of solvated organometallic complexes. *Physicca Scripta*, 102, 2005. 63

[154] Winick H and *et al.* Short wavelength FELs using the SLAC linac. *Nuclear instruments & methods in physics research section A*, 347(13):199–205, 1994. 66

[155] D. A. G. Deacon, L. R. Elias, J. M. J. Madey, G. J. Ramian, H. A. Schwettman, and T. I. Smith. First operation of a free-electron laser. *Phys. Rev. Lett.*, 38:892–894, Apr 1977. 66

[156] Deutsches elektronen-synchrotron(desy). `http://photon-science.desy.de/facilities/flash/the_free_electron_laser/how_it_works/high_gain_fel/index_eng.html`. Accessed: 2016-05-02. 67

[157] Parc Yong Woon, Han Jang-Hui, Kang Heung Sik, Kim Ilyou, Yang Haeryong, and Hwang Ilmoon. Radiation size and divergence at the hard x-ray beamline in the PAL-XFEL. *Journal of the Korean ...*, 64(7):976–981, 2014. 67 and 68

[158] Y Otake. Overview of SACLA Machine status. *Proceedings of LINAC*, pages 427–431, 2012. 68

[159] Tsumoru Shintake. Spring-8 Compact SASE source and XFEL project in Japan. *Proceedings of LINAC*, pages 813–816, 2006. 68

[160] M. Harmand, R. Coffee, M. R. Bionta, M. Chollet, D. French, D. Zhu, D. M. Fritz, H. T. Lemke, N. Medvedev, B. Ziaja, S. Toleikis, and M. Cammarata. Achieving few-femtosecond time-sorting at hard X-ray free-electron lasers. *Nature Photonics*, 7(3):215–218, 2013. 68

[161] Wojciech Gawelda. *Time-resolved X-ray Absorption Spectroscopy of Transition metal Complexes.* PhD thesis, École polytechnique Fédérale de Lausanne, 2006. 70

[162] K. Hämäläinen, D. P. Siddons, J. B. Hastings, and L. E. Berman. Elimination of the inner-shell lifetime broadening in x-ray-absorption spectroscopy. *Physical Review Letters*, 67(20):2850–2853, 1991. 71

[163] Matthew Newville. Fundamentals of XAFS, 2004. 71

[164] Isabelle Llorens, Eric Lahera, William Delnet, Olivier Proux, Aurélien Braillard, Jean Louis Hazemann, Alain Prat, Denis Testemale, Quentin Dermigny, Frederic Gelebart, Marc Morand, Abhay Shukla, Nathalie Bardou, Olivier Ulrich, Stéphan Arnaud, Jean Franois Berar, Nathalie Boudet, Bernard Caillot, Perrine Chaurand, Jérôme Rose, Emmanuel Doelsch, Philippe Martin, and Pier Lorenzo Solari. High energy resolution five-crystal spectrometer for high quality fluorescence and absorption measurements on an x-ray absorption spectroscopy beamline. *Review of Scientific Instruments*, 83(6), 2012. 72 and 74

[165] Roberto Alonso-Mori, Jan Kern, Dimosthenis Sokaras, Tsu Chien Weng, Dennis Nordlund, Rosalie Tran, Paul Montanez, James Delor, Vittal K. Yachandra, Junko Yano, and Uwe Bergmann. A multi-crystal wavelength

dispersive x-ray spectrometer. *Review of Scientific Instruments*, 83(7):1–9, 2012. 72 and 76

[166] Lars Anklamm, Christopher Schlesiger, Wolfgang Malzer, Daniel Grotzsch, Michael Neitzel, and Birgit Kanngieoer. A novel von Hamos spectrometer for efficient X-ray emission spectroscopy in the laboratory. *Review of Scientific Instruments*, 85(5):0–5, 2014. 72

[167] C. Bressler, W. Gawelda, A. Galler, M. M. Nielsen, V. Sundström, G. Doumy, a. M. March, S. H. Southworth, L. Young, and G. Vankó. Solvation dynamics monitored by combined X-ray spectroscopies and scattering: photoinduced spin transition in aqueous $[Fe(bpy)_3]^{2+}$. *Faraday Discuss.*, 171:169–178, 2014. 77 and 97

[168] Renske Marjan van der Veen. *Ultrafast X-ray and Optical Spectroscopy of Binuclear Molecular Complexes*. PhD thesis, École polytechnique Fédérale de Lausanne, 2010. 77 and 153

[169] Thompson Albert C, Vaughan Douglas, and *et al.* *X-Ray data booklet*. Lawrence Berkeley National Laboratory, University of California, second edition, 2001. 82

[170] Victor Lenchenkov, Jeremiah Kloepfer, Victor Vilchiz, and Stephen E. Bradforth. Electron photodetachment from $[Fe(CN)_6]^{4-}$:photoelectron relaxation and geminate recombination. *Chemical Physics Letters*, 342:277 – 286, 2001. 88

[171] Helen Bolvin. d-d Spectrum and High-Spin/Low-Spin Competition in d6 Octahedral Coordination Compounds : ab Initio Study of Potential Energy Curves. *Journal of physical chemistry A*, 5639(98):7525–7534, 1998. 88 and 132

[172] Farhataziz. Diffusion of the solvated electron ln mixtures of polar solvents and the two absorber model. *Chemical Physics Letters*, 7(1):4–6, 1980. 98

[173] E. Hankiewicd and D. Schulte-Frohlinde. The Rate of Hydrated Electron Reaction with Neutral and Anionic Scavengers in Concentrated Salt Solutions. *The journal of physical chemistry*, 7(1):4–6, 1980. 98

[174] Michael W. Fuller, Kim Maree F. Le Brocq, Elizabeth Leslie And, and Ivan R. Wilson. The Photolysis of Aqueous Solutions of Potassium Haxacyanoferrate (III). *Australian Joournal Chemistry*, 39:1411–1419, 1986. 100, 104, and 108

[175] L. Moggi, F. Bolletta, V. Balzani, and F. Scandola. Photochemistry of coordination compounds—xv. *Journal of Inorganic and Nuclear Chemistry*, 28(11):2589 – 2597, 1966. 104 and 108

[176] A N Tarnovsky, W Gawelda, M Johnson, C Bressler, and M Chergui. Photoexcitation of Aqueous Ruthenium(II)-tris-(2,2′-bipyridine) with High-Intensity Femtosecond Laser Pulses. *Journal of Physical Chemistry B*, 110:26497–26505, 2006. 105

[177] Mauro Rovezzi and Pieter Glatzel. Hard x-ray emission spectroscopy: a powerful tool for the characterization of magnetic semiconductors. *Semiconductor Science Technology*, 023002:17, 2013. 111

[178] Christopher J Pollock, Mario U Delgado-Jaime, Mihail Atanasov, Frank Neese, and Serena Debeer. Kβ Mainline X-ray Emission Spectroscopy as an Experimental Probe of Metal-Ligand Covalency. *J. Am. Chem. Soc*, 136:9453, 2015. 112 and 113

[179] Rosalie K. Hocking, Erik C. Wasinger, Frank M. F. de Groot, Keith O. Hodgson, Britt Hedman, and Edward I. Solomon. Fe L-Edge XAS Studies of K4[Fe(CN)6] and K3[Fe(CN)6]: A Direct Probe of Back-Bonding. *Journal of American Chemical Society*, 128(32):6648–6652, 2006. 113

[180] Marcus Lundberg, Thomas Kroll, Serena Debeer, Uwe Bergmann, Samuel A Wilson, Pieter Glatzel, Dennis Nordlund, Britt Hedman, Keith O Hodgson, and Edward I Solomon. Metal-Ligand Covalency of Iron Complexes from High-Resolution Resonant Inelastic X-ray Scattering. *Journal of the American Chemical Society*, 45(135):17121–17134, 2013. 113

[181] Nicole Lee, Taras Petrenko, Uwe Bergmann, Frank Neese, and Serena Debeer. Probing valence orbital composition with iron K-beta x-ray emission spectroscopy. *Journal of the American Chemical Society*, 132(28):9715–9727, 2010. 113

[182] Jeremiah A Kloepfer, Victor H Vilchiz, Victor A Lenchenkov, and Stephen E Bradforth. Femtosecond dynamics of photodetachment of the iodide anion in solution : resonant excitation into the charge-transfer-to-solvent state. *Chemical Physics Letters*, 298(December):120–128, 1998. 115, 116, and 117

[183] Yao Liu, David B Turner, Tanya N Singh, Alfredo M Angeles-boza, Abdellatif Chouai, Kim R Dunbar, and Claudia Turro. Ultrafast Ligand Exchange : Detection of a Pentacoordinate Ru (II) Intermediate and Product Formation. *Journal of American Chemical Society*, 131(1):26–27, 2009. 126

[184] Peter Portius, Jixin Yang, Xue-Zhong Sun, David C. Grills, Pavel Matousek, Anthony W. Parker, Michael Towrie, and Michael W. George. Unraveling the Photochemistry of $Fe(CO)_5$ in Solution: Observation of $Fe(CO)_3$ and the Conversion between $2\,Fe(CO)_4$ and $Fe(CO)_4$(Solvent). *Journal of American Chemical Society*, 126(34):10713–10720, 2004. 128

[185] Kristoffer Haldrup, Wojciech Gawelda, Rafael Abela, Roberto Alonso-mori, Uwe Bergmann, Marco Cammarata, Sophie E Canton, Asmus O Dohn, Tim Brandt Van Driel, David M Fritz, Andreas Galler, Pieter Glatzel, Tobias Harlang, Kasper S Kjær, Henrik T Lemke, Klaus B Møller, Norbert Sas, Jens Uhlig, Diling Zhu, Gyo Vanko, Villy Sundstro, Martin M Nielsen, and Christian Bressler. Observing Solvation Dynamics with Simultaneous Femtosecond X -ray Emission Spectroscopy and X-ray Scattering. *The journal of physical chemistry B*, 120(6):1158–1168, 2016. 130

[186] Clayton R Randall, Lijin Shu, Yu-Min Chiou, Karl S. Hagen, Masami Ito, Nobumasa Kitajima, Rene J Lachicotte, Yan Zang, and Lawrence Que. X-ray Absorption Pre-Edge Studies of High-spin Iron(II) Complexes. *Inorganic Chemistry*, 34:1036–1039, 1995. 130

[187] G R Shulman, Y Yafet, P Eisenberger, and W E Blumberg. Observations and interpretation of x-ray absorption edges in iron compounds and proteins. *Proceedings of the National Academy of Sciences*, 73(5):1384–1388, 1976. 130

[188] Matthew Newville. Ifeffit: Interactive xafs analysis and feff fitting. *Journal of Synchrotron Radiation*, 8:322–324, 2001. 135

[189] J W Cook Jr and D E Sayers. Criteria for automatic x-ray absorption fine structure background removal. *Journal of Applied Physics*, 52(5024), 1981. 137

[190] J.J. Rehr, S.I. Zabinsky, a. Ankudinov, and R.C. Albers. Atomic-xafs and xanes. *Physica B: Condensed Matter*, 208-209:23–26, 1995. 139

[191] S. I. Zabinsky, J. J. Rehr, a. Ankudinov, R. C. Albers, and M. J. Eller. Multiple-scattering calculations of x-ray-absorption spectra. *Physical Review B*, 52(4):2995–3009, 1995. 139

[192] D E Sayers. Report of the International XAFS Society Standards and Criteria Committee. 539(1983):1–15, 2000. 142

[193] Wojciech Gawelda, Van-Thai Pham, Maurizio Benfatto, Yuri Zaushitsyn, Maik Kaiser, Daniel Grolimund, Steven Johnson, Rafael Abela, Andreas Hauser, Christian Bressler, and Majed Chergui. Structural Determination of a Short-Lived Excited Iron(II) Complex by Picosecond X-Ray Absorption Spectroscopy. *Physical Review Letters*, 98(5):6–9, feb 2007. 146

[194] John R. Taylor. *An Introduction to Error Analysis: The Study of Uncertainties in Physical Measurements.* University Science Books Sausalito, California, second edition, 1997. 153

[195] Erik P a Couzijn, J Chris Slootweg, Andreas W Ehlers, and Koop Lammertsma. Stereomutation of pentavalent compounds: validating the Berry

pseudorotation, redressing Ugi's turnstile rotation, and revealing the two-and three-arm turnstiles. *Journal of the American Chemical Society*, 132(51):18127–40, dec 2010. 161

[196] Jeremy Burdett, Joseph M Grzybowski, Robin N Perutz, Martyn Poliakoff, James J Turner, and Robert F Turner. Photolysis and Spectroscopy with Polarized Light: Key to the Photochemistry of Cr(C0)S and Related Species'. *Inorganic chemistry*, 17(1):147–154, 1978. 161

[197] J.J. Rehr, A. Ankudinov, B. Ravel, , and K. Jorissen. The FEFF Project, 2012. 163

[198] Codata internationally recommended physical constants. `http://physics.nist.gov/cuu/Constants/`. Accessed: 2016-08-21. 169